Characterization of the structure and precipitation process in Al-Mg-Si and Al-Mg-Ge casting alloys

vorgelegt von

Viktoriya Boyko, M.Sc.

aus Kiew, Ukraine

von der Fakultät III – Prozesswissenschaften
der Technischen Universität Berlin
Zur Erlangung des akademischen Grades
Doktor der Ingenieurwissenschaften
- Dr. - Ing. -

genehmigte Dissertation

Promotionsausschuss:

Vorsitzender:	Prof. Dr. J. Banhart
Gutachter:	Prof. Dr. rer. nat. W. Reimers
Gutachter:	Prof. Dr.-Ing. W. Schneider

Tag der wissenschaftlichen Aussprache: 19. August 2014

Berlin 2014
D83

Zusammenfassung

Die Al-Mg-Si-Legierungen, welche neuerdings in der Gießerei verwendet werden, weisen eine exzellente Kombination aus Härte und Duktilität auf, aber es liegen kaum Informationen über ihre Zusammensetzung, Struktur und Phasen sowie die Ausscheidungsprozesse bei der Wärmebehandlung vor. Für das Al-Mg-Ge-System trifft dies in noch stärkere Maße zu. Das Ziel der vorliegenden Dissertation ist darum die Erweiterung des Wissensstands bezüglich Struktur, Zusammensetzung und Ausscheidungen in Al-Mg-Si- und Al-Mg-Ge-Legierungen sowie nach Zulegierung von Mangan und Lithium sowie Scandium in Verbindung mit Zirkon. Diese Untersuchungen wurden für 9 experimentelle Legierungen nach dem Guss, der Lösungsglühung und der Auslagerung durchgeführt und mit 3 kommerziellen Legierungen verglichen. Die eutektischen Temperaturen von Al-Mg-Si und Al-Mg-Ge wurden kalorimetrisch ermittelt und ergaben 587.0°C bzw. 629.0°C. Für die Legierung der nominalen Zusammensetzung AlMg7Si besteht die Struktur im Gusszustand aus den 4 Bestandteilen: Al-Mischkristall, Al/Mg_2Si-Eutektikum, primäre Mg_2Si-Kristalle und Al(Mn,Fe)Ge-α-Phase. Nach zwei Tagen natürlicher Alterung traten im Mischkristall aller Legierungen Ausscheidungen auf, welche zebrastreifenartig angeordnet sind. TEM Untersuchungen ergaben, dass es sich dabei um heterogene Nukleation an Versetzungen handelt. Die Lösungsglühung bei 575.0°C führt zur Sphärodisierung des Eutektikums, der Auflösung der Ausscheidungen und der Entstehung von -Al(Mn,Fe)Si-Dispersoiden an den Oberflächen von Mg_2Si und Mg_2Ge-Lamellen. In den Legierungen mit Sc+Zr Zusätzen wurde nach 120 min Glühung die Bildung von $Al_3(Sc_{1-x}Zr_x)$-Ausscheidungen beobachtet, welche im weiteren Verlauf wachsen. Die Auslagerung der Al-Mg-Si- und Al-Mg-Ge-Legierungen bewirkt einen Anstieg ihrer Härte, hauptsächlich durch Ausscheidungshärtung. Die Entmischung der α −Matrix führt in Al-Mg-Si-Legierungen zur β"-Phase, in Al-Mg-Ge-Legierungen zur $U1_{Ge}$-Phase. In Legierungen mit Lithiumzusatz trat eine plattenförmige Mg_2Si-β-Phase auf zusammen mit kleinen würfelförmigen δ'-Al_3Li-Ausscheidungen. Die Ergebnisse wurden verglichen mit denen dreier kommerzieller Legierungen, nämlich Magsimal 59 (Al-Mg-Si System), A201.0 (Al-Cu-System) und A356.0 (Al-Si-Mg-System). Die Makro- und Mikrohärte der neuentwickelten Legierungen liegen unter denen der hochfesten A201-Legierung, sind aber besser als von A356.0. Damit wurde gezeigt, dass das Al-Mg-Si und Al-Mg-Ge-System erfolgversprechend sind für das Design neuartiger Gusslegierungen und für die Entwicklung Li-haltiger Gusslegierungen mit reduzierter Dichte.

Abstract

The Al-Mg-Si alloys recently applied in foundry show an excellent combination of strength and plasticity, but information about composition structure phases and the effect of heat treatment on the precipitation process are rather scanty. Even less information is available for the Al-Mg-Ge system. Therefore, the aim of this thesis is to provide the knowledge about structure, composition and precipitates in nine Al-Mg-Si and Al-Mg-Ge casting alloys with and without Mn, Li and Sc+Zr additions. Three conditions, as cast, solution treated and aged, were investigated and the results were compared with those of three commercial alloys. The eutectic melting temperatures for both systems were recorded by differential scanning calorimetry and gave for Al-Mg-Si – 587.0°C, for Al-Mg-Ge – 629.0°C. It was shown that in as-cast state, the structure of an alloy having the nominal composition AlMg7Si3 consists of four phases: first - the Al based solid solution, second - the (Al)+(Mg_2Si) eutectic, third - the primary Mg_2Si crystals and fourth – the α-Al(Mn,Fe)Si phase. Similar phases were observed in the AlMg4.3Ge6.49 alloy: Al based solid solution, (Al)+(Mg_2Ge) eutectic, primary Mg_2Ge crystals and α-Al(Mn,Fe)Ge. After two days of storing in an as-cast condition, the solid solution in all tested alloys decomposes and forms zebra-crossing shaped precipitates. TEM examinations revealed that these precipitates nucleate heterogeneously on dislocations. The solution treatment at 575.0°C results in spheroidization of the eutectic, dissolution of the precipitates and formation of α-Al(Mn,Fe)Si dispersoids, nucleating on the surfaces of Mg_2Si and Mg_2Ge lamellas. In the Sc+Zr containing alloys, the formation of $Al_3(Sc_{1-x}Zr_x)$ was detected after 120 min soaking. Further heating resulted in the growth of these precipitates. Aging of the Al-Mg-Si and the Al-Mg-Ge alloys leads to an increase of hardness in all studied alloys. This effect is mainly related to precipitation strengthening, via solid solution decomposition and formation of β"-phase in the Al-Mg-Si alloys and $U1_{Ge}$ phase in the Al-Mg-Ge alloys. Additionally, in Li-alloyed specimens, plates of β Mg_2Si phase were observed together with small cubic-shaped δ' Al_3Li precipitates. The obtained results were compared with those of three commercial casting alloys, namely Magsimal 59 (Al-Mg-Si system), A201.0 (Al-Cu system) and A356.0 (Al-Si-Mg system). The macro and microhardness properties of the developed alloys are lower than those of the high strength A201.0 alloy, but higher than those of A356.0 casting alloy. This demonstrates the promising potential of the Al-Mg-Si and the Al-Mg-Ge system for the design of novel casting alloys and the development of the first Li-containing casting alloys with reduced density.

Acknowledgements

This research project was carried out from October 2010 to December 2013 at the Department of Metallic Materials, Institute of material Science and Technology of Technical University Berlin, Germany with financial support of Germany Academic Exchange Service (DAAD) (DAAD code number A/09/81040).

First and foremost I am extremely grateful to my supervisors**,** Professor Dr. rer. nat. Walter Reimers and Dr.-Ing. Thomas Link, for their guidance though my PhD.: not only has they guided my scientific development by imparting much wisdom and displayed great patience and tact, they also allowed my academic curiosity to flourish. Their cool and optimistic attitude towards my research progress was always encouraging.

The financial support from the German Academic Exchange Service is gratefully acknowledged and personally Sebastian Feicht and Katja Hamann.

I am grateful to Alexander Epishin, Bettina Camin and Melanie Paulisch whose collaboration on some of the work in this thesis was essential. I won't forget big laughs and discussions about materials we had during these years. I also greatly appreciated Michael Hill and all cooperators from metallographic laboratory for research related discussions.

Last but not least I would like to express my deep gratitude to my parents who encouraged and supported me in all respects.

I would also like to thank the industrial partners Norsk Hydro Germany for supplying aluminum for alloys preparation, KBM AFFILIPS B.V. (Netherlands) for supplying aluminum-magnesium and aluminum-lithium master alloys.

I also would like to thank my research supervisor from Ukrainian side – Professor Kostiantyn Mykhalenkov from National Technical University of Ukraine (Kiev, Ukraine) for providing scientific cooperation, valuable suggestions and fruitful discussion throughout my PhD.

Table of Contents

Introduction

Rationale of research

In 1828 Friedrich Wöhler, a German scientist, produced the first aluminum ingot, which was more expensive than gold *[RIC08]* in this time. Following the availability of high voltage supplies of electricity, independent discoveries by Charles Hall in the United States and Paul Heroult in France in 1886 led to the development of an economic method for extracting aluminum (Hall-Herault process) and nowadays the annual aluminum production has reached nearly 45 million tons.

The majors sectors in which aluminum is used worldwide are building and construction, transportation, containers and packaging, and electrical applications. Wrought products dominate, traditionally accounting for some 85% of all aluminum used, although the steady replacement of cast iron components in motor cars by lighter aluminum alloy castings is changing this wrought-to-cast alloy ratio.

There are *three mainstreams* of scientific and engineering evolution in the area of aluminium, in particular casting alloys:

- (i) designing of new and improvement of well-established casting processes. The last 30 years brought to life and to practice the usage of thixo- and rheocasting processes which deal with the semisolid state of alloys. This involved the demand for new alloys suitable for these processes;
- (ii) improvement of degassing and cleaning techniques of aluminium wrought and casting alloys which satisfy the requirements for new high performance products and also meet environmental needs. The most successful and common method to remove impurities in foundry is rotary degassing;
- (iii) development of new alloys providing subsequently the basis for new design products. This line of investigation is especially important for casting alloys because Al is one of the few metals that can be cast by all of the processes used in casting metals.

In spite of the fact that the first and the second point are of vital importance for improvement of casting properties and quality, there is a great demand for the third one, because it allows to elaborate new cost-effective casting processes and designing of principally new highly integrated components for the next generation of vehicles, trains, ships and airplanes.

A large number of aluminium alloys for casting has been developed, but most of them

are varieties of six basic types, such as Al-Cu, Al-Cu-Si (or Mg), Al-Si, Al-Mg, Al-Zn-Mg and Al-Sn. In contrast to wrought alloys, where the Al-Mg-Si series alloys are the most popular ones, for casting alloys Al-Mg-Si is still not in use.

The last years brought to life several Al-Mg-Si casting alloys, namely Hydronalium 511 *[PIR90]*, *[PIR93]*, Magsimal®59 *[KOC98]*, *[WUT00]*, *[STE06]*, Maxxalloy and Maxxalloy Ultra *[JOR08]*, Aural11 *[JOR08]*. The nominal chemical composition of Hydronalium 511 (AlMg5Si2Mn), Magsimal 59 and Maxxalloy Ultra are the same and contains about 5.00 wt.% Mg, 2.00 wt.% Si and 0.60 wt.% Mn. Similar to the successful alloy AlSi7Mg0.3 (A356.0), this composition demonstrates the high strength and ductility which can be achieved in as-cast state. Despite of the increased usage of the AlMg5Si2Mn alloy in foundry shops, the origins of its high mechanical properties are still not adequately explained and only few publications exist on the topic of structure characterisation and phase composition in this alloy.

For Al-Mg-Ge casting alloys there were only a few results published until now. These alloys based on the Al-Mg-Ge system, are very attractive candidates for further development because they have a high eutectic melting point (629.0°C) and good mechanical properties. Preliminary trials performed on Al-1.8 mol%Mg_2Ge show that the yield strength of this alloy is on the level of 470 MPa and the ultimate tensile strength exceeds 560 MPa.

From this analysis of the actual industrial state of art in the field of aluminum casting alloys and the scientific background, follow the aims of the present work.

- analysis of the structure of Al-Mg-Si and Al-Mg-Ge casting alloys in as-cast state together with its change during solution treatment and aging;
- determination of the composition of the solid solution in as-cast state and its variation during solution treatment and artificial aging;
- finding out the origins of the high mechanical properties of Al-Mg-Si casting alloys in as-cast state and tracing their changes during solution treatment and aging;
- investigation of the morphology and type of secondary precipitates formed in Al-Mg-Si and Al-Mg-Ge during heat treatment.

The thesis splits into 6 major chapters:

- Chapters 1 and 2 contain a review of the most common casting methods applied for the production of aluminum casting alloys and the fundamentals of solidification. It also considers the effect of alloying elements on the properties of aluminum-based casting alloys and the strengthening mechanisms operating in aluminum alloys, in particular castings. On base of this overview the research goals are formulated.

- Chapter 3 discusses the ternary Al-Mg-Si and Al-Mg-Ge phase diagrams in connection with the composition of the experimental alloys. Metallographic techniques applied for structural investigations, such as specimen's preparation, thin foils preparation and applied equipment are presented too.

- Chapter 4 considers the as-cast state of the alloys of the research program. Results of DSC heating and cooling experiments, structural studies and EDX measurements of the different phases are presented, as well as the characterization of precipitates formed during natural aging of Al-Mg-Si and Al-Mg-Ge alloys.

- Chapter 5 reports and discusses the results obtained from solution treated specimens. It contains hardness measurements for different times of solution treatment, light microscope of the phase morphology, TEM micrographs of the solid solution and precipitates as well as EDX measurements of the local chemical composition of solid solution grains.

- Chapter 6 reports hardness and microhardness measurements of alloys after artificial aging for different times and results of transmission electron microscopy examinations after ageing times between 30 and 1440 min.

1 Fundamentals of structure formation of aluminum alloys

1.1 Application of aluminum alloys

The phase transformation from liquid to solid, the solidification, has fundamental importance for the resulting properties of the alloys. According to the classical theory of phase transformations, the formation of the final structure of a casting is the result of two processes. The first one is the nucleation of crystals out of the melt and the second one is the growth of such crystals and the formation of eutectic or peritectic phases. Both processes are of high interest, but still controversial views are present due to their complexity and interconnections. This chapter represents an overview of established casting processes and the fundamentals of structure formation of Al-based alloys and points out their effects on the properties of the final product.

Aluminum is one of the most abundant metals, available in the earth crust as bauxite, *[POL95]*. It has a wide range of applications in the modern world and there are many reasons for a continuous expansion into newer and wider fields of application, namely light weight, excellent specific strength, high thermal and electrical conductivity, high reflectivity, good corrosion resistance, excellent workability and attractive appearance. Al alloys are available in both forms cast and wrought. The major fields of application are *[ALU12], [CON92]*:

- transportation;
- packaging / consumer market;
- building / construction / infrastructure;
- electrical engineering.

Wrought products dominate, traditionally accounting for some 80% of all aluminum used *[KAU04]*, *[ALU12]*. The steady replacement of cast iron components in automotive industry by lighter aluminum alloy castings is increasing this cast-to-wrought alloy ratio. Figure 1.1 shows the steady growth of aluminum production in the world and Figure 1.2 represents the consumption of aluminum alloys by different production sectors.

Use of aluminum alloys in the transportation sector is rapidly increasing due to the strong need for fuel-efficient, environment friendly vehicles. Today aluminum is the second most used material of the total weight of the car. It is used to produce components of the suspension, the chassis, cylinder blocks and other engine components. Roughly estimated, 1 kg of aluminum can replace up to 2 kg of steel and cast iron in many areas of application. In 2012 the automotive industry output reached 67 million vehicles. If the bodies, engines and other components of these

vehicles would have been made out of aluminum instead of steel, the CO_2 emissions into the air would have been reduced by 140 million tones, and the total fuel economy during the lifetime of all vehicles would have allowed saving 60 billion liters of crude oil.

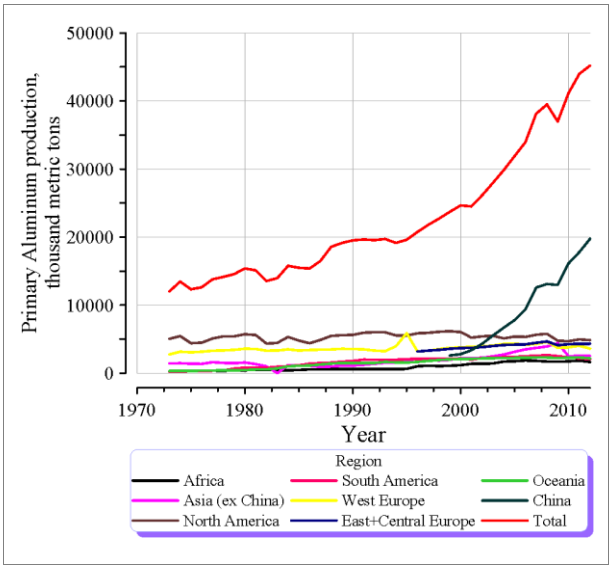

Fig. 1.1: World aluminum production, [BRO12]

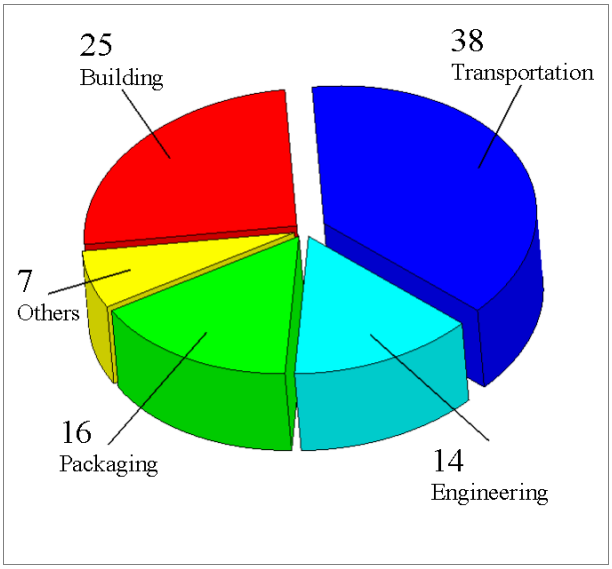

Fig. 1.2: Main end-use markets in % for Aluminum products, [ALU12]

Today, between 110 and 145 kg aluminum are used in the production of a car, *[MIL00]*. However, contrasting with all enthusiastic prognoses for making cars lighter, the average weight of compact class vehicles gradually increases as shown on Figure 1.3.

A step to counter this trend is the design of new alloys with high performance and strength-to-weight ratio, such as new aluminum casting alloys.

The first well-known application of aluminium alloys in the building sector dates back to the end of the 19th century. Aluminum is now used there in a host of applications, such as curtain walling, window frames and other glazed structures. The aluminum can was invented in 1972. Its weight was ten times less than the weight of a glass bottle. In modern cans even 40% less metal is used than 35 years ago. Since 1972 the popularity of aluminium alloys in packaging industry has steadily grown. Right now it uses 7.2 million tones from the total aluminium production of 45 million tons per year.

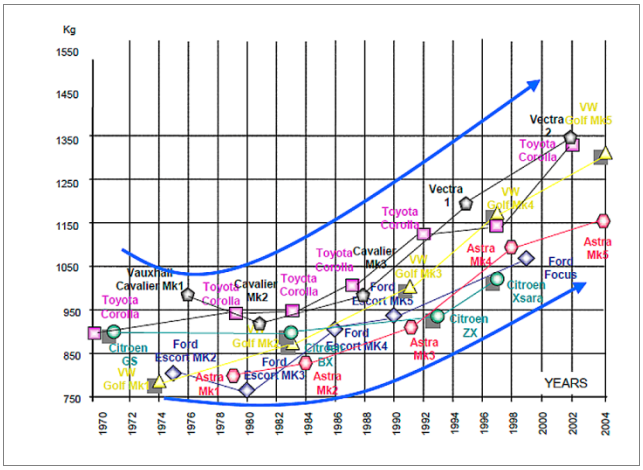

Fig. 1.3: Evolution of weight in compact class cars from 1970 to 2004 shows the steady-state growth of weight in spite of a general demand of weight and fuel consumption reduction, [ALU12]

1.2 Casting of aluminum alloys

Aluminium castings have played an integral role in the growth of aluminium industry since its inception in the late 19th century. The first commercial aluminium products were castings, such as cooking utensils and decorative parts, which exploited the novelty and utility of the new metal. Those early applications rapidly expanded to address the requirements of a wide range of engineering specifications, *[ZOL07]*. The hierarchy of the established casting processes used in foundry shops is represented in Figure 1.4.

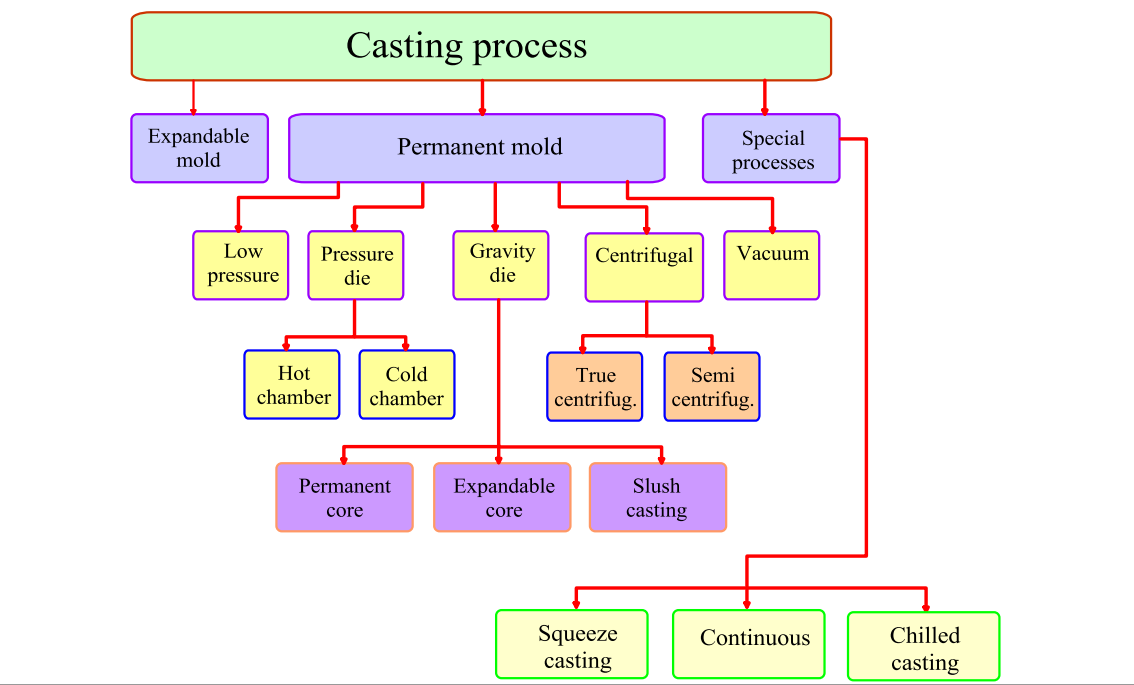

Fig. 1.4: Hierarchy of the most important casting processes used in Al foundry, (present work)

For each casting technique it is important to consider the effect of cooling rate on structure formation and resulting properties. In this paragraph the most important shape casting techniques of Al-based alloys will be presented. A unique property of these alloys is that they can be cast by all established processes. In future, scientific and engineering evolution of aluminium casting will follow the three mainstreams:

- (i) designing of new and improvement of well-established casting processes. In the last 30 years thixo- and rheocasting processes were developed, which deal with the semisolid state of the material. This generated a demand for new alloys suitable for these processes *[HIR04]*, *[SAU06]*, *[PAT08]*;
- (ii) improvement of degassing and cleaning techniques of wrought and casting aluminium alloys, in order to satisfy the requirements for new high performance products and environment protection, *[NEF04]*. The most successful and common method to remove impurities in foundry is rotary degassing;

- (iii) development of new alloys providing the basis for new high integrity casting part. This line of investigation is especially important for Al casting alloys because they can be cast by all of the processes as mentioned above.

The following processes are listed by increasing cooling rate.

1.2.1 Sand casting

Sand casting is the most important and most frequently used casting technique, because it is least expensive. Here a pattern, i.e. a model with the positive shape of the desired part is made out wood, plastic or metal. The pattern is intentionally made larger than the cast part to allow for shrinkage during cooling. Simple designs can be made as a single piece, more complex designs in several parts. The pattern is then packed in sand with a binder, which helps to harden the sand into a semi-permanent shape. Once the sand is cured, the pattern is removed leaving behind its negative shape in the sand. This is the mold. For hollow castings sand cores can be inserted. Simple molds are open on top and the liquid metal is directly poured in.

The pouring temperature of an alloy should be somewhat higher than the melting point to ensure good fluidity, thereby avoiding premature cooling, which causes voids and porosity. When the metal is solidified, the sand mold is removed and the next operations, such as machining and plating, follow. As an example for a sand mould casting, in Figure 1.5 the body of an oil pump for a modern aircraft is presented, made from A201.0 (Al-Cu-Mn-Ag) high strength alloy, *[MYK96]*. Specimens cut from the castings in heat treated condition showed an ultimate tensile strength (UTS) of 430 MPa at a relative elongation of 9%.

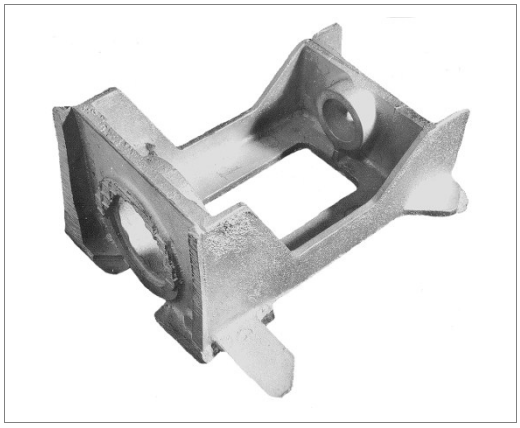

Fig. 1.5: Oil pump body for heavy-weight aircraft produced via sand casting techniques. High strength A201.0 casting alloy (AlCu4.5MnAg), [MYK96]

The advantages of sand mould casting are:

- least expensive casting process;
- castings can be up to several tons;
- less expensive than machining shapes from bar stock;
- intricate shapes possible.

However, several disadvantages must be taken into account:

- Only basic parts can be cast because of the impossibility to form thin sections of the casting;
- Casting requires secondary machining because of the rough surface;
- Poor dimension accuracy;

- Limitations on mechanical properties because of the low cooling rate, resulting in a coarse grained structure of the casted part. Sand casting gives a very slow cooling rate of 0.1-2.0 K s^{-1} prior to solidification and is therefore suitable for aluminum alloys with a tendency to hot tearing. The shrinkage porosity forming in thick sections of the castings can be avoided by using special cooling devices, called metal chills. They are inserted in such sections into the mould wall, in order to provide uniform cooling rates all over the specimen, which helps to prevent cracks.

1.2.2 Investment casting

Investment castings using the so-called "lost mould" process can be performed with all aluminum alloys. It is also characterized as precision casting, because it is used to produce intricate castings with very tight tolerances. However, the method is also used for mass-produced parts, because near net dimensions and good surface quality are attained without additional machining.

To produce such a mold, first a pattern has to be made from material with low melting point, usually wax or plastic. A filling funnel is added at the top of the pattern. Next this assembly is coated with several millimeters of refractory slurry (watery paste of silica and a binder), which gives the mold. After hardening, the mold is turned upside down and heated above the melting point of the wax or plastic, such that the material of the pattern can leave the mold via the funnel. Such a mold is known as shell. After cleaning and heating of the mold, liquid metal can be cast into the funnel. Finally, after solidification the shell must be destroyed for uncovering the casting. Such an investment casting process is more expensive than the other casting methods; therefore it becomes economical only for parts with complex geometries, where the post processing cost would be higher than the shell production costs. In many cases investment castings can be used in "as cast" condition. Advantages of investment casting can be summarized as follows:

- complex shapes possible;
- thin wall section possible;
- highest dimensional accuracy;
- minimum surface treatment.

The disadvantages are:

- weight of castings limited up to 1 kg;
- expensive dies for wax pattern;
- many production steps.

Due to high production cost, investment casting techniques are not often employed in foundry shops for aluminum alloys. In general the cooling rate of the melt is similar to that of sand casting.

1.2.3 Permanent mould casting (PM)

Instead of using sand as the mould material, metal is used as mould material. Typically, it is cast iron, whereas the core of the casting is made from metal or sand. The surfaces of the mold are coated with a thin layer of heat resistant material such as clay or sodium silicate. The mould is pre-heated up to 200ºC before the metal is poured into the cavity. A typical mould construction for permanent mould casting is shown in Fig. 1.6.

For the cavity design, the shrinkage of the casting plays a minor role compared with sand casting because the metal moulds heat up and expand during the pour, i.e. the volume loss at the liquid-solid transition is mostly compensated. Typically, the parts have a mass between 50 g and 70 kg and are used as gears, splines, wheels, gear housings, pipe fittings, fuel injection housings and automotive engine pistons. Advantages of permanent mold casting in comparison to sand mould casting can be summarized as follows:

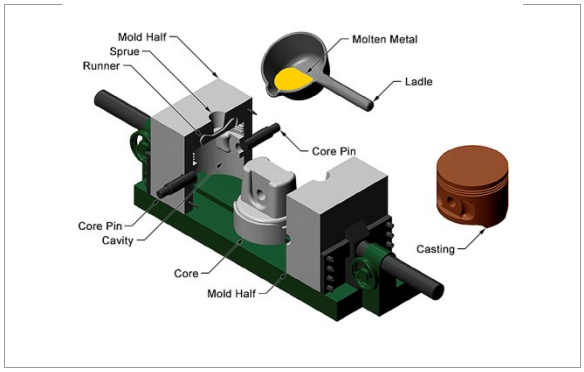

Fig. 1.6: Schematic drawing of a permanent mould casting process, [CAM04]

- complex shapes and designs possible;
- fine grain structure, good for isotropic mechanical properties;
- high as-cast surface finish;
- high number of shares;
- precise and consistent control over dimensional attributes;
- increased repeatability of casting per life time of mold;
- low wall thickness possible;
- cheaper casting production;

Disadvantages of permanent mould casting:

- higher cost of tooling requires a higher volume production of castings.

Complex castings such as aluminium engine blocks and heads are now commonplace.

1.2.4 Pressure die casting (PDC)

Die casting is a process for producing metal parts by forcing molten metal under high or low pressure into reusable steel molds. These molds, called dies, are usually designed to produce

complex shapes with a high degree of accuracy and repeatability *[AND04], [VIN03]*. The earliest examples of die casting by pressure injection dates back to the mid-19th century, mass production began in the early 20th century.

The die casting process has evolved from the original low-pressure injection method to techniques including high-pressure casting and also squeeze casting and semi-solid die casting, which is described in the following section. These modern processes are capable of producing high integrity, near net-shape castings with excellent surface finishes.

Basically, die casting means to inject molten metal under high pressure into a mould. Die casting machines are typically rated in clamping tons equal to the amount of pressure they can exert on the die. Two methods to inject molten metal into the die are now applied: hot chamber or cold chamber, resulting in different cooling rates of the melt. For aluminum alloys cold chamber methods are usually utilized.

High pressure die casting is the most widely used, representing about 50% of the total light alloys casting production. It has traditionally been utilized in the production of housings etc, but this has changed. Presently, feasible products are automotive front end structures and instrument panels in magnesium alloys.

However, for HPDC to be competitive for extended automotive applications and attractive for new market segments the crash worthiness and fatigue properties must be improved and a scientific comprehension of the process and metal behavior is required. The most common HPDC aluminum alloy is the A380 (AlSi9Cu3) alloy, but a generally more utilized foundry alloy is the A356 Al-Si-Mg alloy which possesses good fluidity.

Recently, another group of casting alloys experiences its renaissance. Being long time in the shadow, in 1996 alloys of the system Al-Mg-Si-Mn returned into the market. It was reported by Koch et al. *[KOC96], [KOC03]* and *[HUZ13]* that an Al-alloy with the nominal composition AlMg5Si2Mn subjected to high pressure die casting shows one of the best properties regarding ductility (up to 18%), yield strength (up to 220 MPa) and ultimate tensile strength (up to 350 MPa) compared with other casting alloys.

Another variation of pressure die casting is squeeze casting, also known as liquid metal forging, a combination of the processes casting and forging. Molten metal is poured into the bottom half of a pre-heated die. As the metal starts solidifying, the upper half closes the die and applies pressure during the solidification process. The amount of pressure thus applied is significantly less than used in forging, but enough to produce parts with fine structures. The squeeze casting process (i) prevents the formation of shrinkage defects (ii) and removes dissolved gases from the melt. This method was originally developed in Russia and has undergone considerable improvement in the U.S.A. It is carried out in metal molds, resembling

the punch and die sets used, for example, in car-body presses. Squeeze casting produces very low gas entrapment and castings exhibit shrinkage volumes approximately one half of those one gets in sand castings. Additionally, the production rates are very high, comparable to die casting but with considerably lower die costs. The process produces high quality surfaces typical for permanent mould casting, with good reproduction of details. Rapid solidification results in a fine grain size, which strongly improves mechanical properties.

1.2.5 Semisolid metal processing (SSM)

Two casting technologies have been developed which use semi-solid metal (SSM) in form of feedstocks, namely thixocasting and rheocasting. In the thixocasting process, a solid billet, with a fine-grained equiaxed microstructure is partially remelted to the semi-solid state *[FLE91], [CZE06], [FAN02]*. The billet is then transferred to the shot chamber of a die cast machine and injected into a die. Rheocasting involves stirring the alloy during solidification to produce a semi-solid slurry, then injecting the slurry directly into the die.

Currently, there is little choice in commercially available feedstock materials, and alloys are usually limited to aluminum based materials, mostly A356.0 and A357.0 (Al-Si-Mg) type cast alloys with 76.2 – 152.4 mm billet diameter, produced by magneto-hydrodynamic stirring. However, there are a number of other production techniques and alloys compositions which are at different stages of research and development.

The above-mentioned processes can be described on the basis of their effects on microstructural features. Different casting processes induce on the casting different thermal field conditions and this information is summarized in Table 1.1.

1.3 Solidification of aluminum alloys

Almost each processing of technologically important metals includes the liquid-solid phase transition. It is very common, for example, to take into account, that the concentrations of the components of an alloy in the melt are different from those in the casting after solidification. In order to form a solid from parent melt we need the formation of crystalline nuclei and growth of these nuclei to form a solid structure. Transformations which occur during these two processes, nucleation and growth, are examples of first order phase transitions. Before discussing nucleation and growth of pure materials, general characteristics of phase transitions are pointed out, *[FRE12]*.

The thermodynamic equilibrium of a system is reached when its energy has reached its minimum. For processes at constant pressure P, this system energy is called Gibbs free energy G:

$$G=H-TS \tag{1.1}$$

where H is the enthalpy, S is the entropy, and T is the absolute temperature. When the state of the system changes at constant temperature the change of G equals:

$$dG=dH-TdS \quad (1.2)$$

Table 1.1: Characteristic ranges of cooling rate and minimum wall thickness for various casting processes utilized for producing aluminum castings

	casting process	cooling rate, ($K\ s^{-1}$ *) and thermal gradient $K\ mm^{-1}$	minimum wall thickness, mm	reference
1.	dry sand mould (rarely applied for Al casting)	0.05 – 0.20 0.05	2.00 – 5.00	*[TOT03]*
2.	green sand mould (applied for high strength Al-Cu and Al-Zn-Mg casting alloys)	0.10 – 1.00 0.05	2.00 – 5.00	*[TOT03]*
3.	investment casting (applied for all Al-based casting alloys)	0.50 – 2.00 n.a.	1.00 – 2.00	*[TOT03]*
4.	permanent mould (mainly applied for Al-Si, Al-Si-Mg alloys)	0.50 – 10.00 n.a.	2.00 – 5.00	*[SHI11]*
5.	die casting (mainly applied for Al-Si, Al-Si-Mg alloys and novel Al-Mg-Si-Mn)	20 – 100 n.a.	1.00 – 2.50	*[AND04]*
	- high pressure die casting	20 – 100	1.00 – 2.50	*[YAM08]*
	- low pressure die casting	10 - 40	1.00 – 2.50	*[AND04]*

* - cooling rate is the temperature change per time prior solidification

Each metal has its own characteristic values of the thermodynamic quantities. The values of the molar enthalpy and the molar entropy of the solid metal are different from those of the liquid metal. The values of H are fairly constant but S varies with temperature for each phase, *[KAU02]*. At solidification, the system emits heat, i.e. the phase transition is exothermic. In this case the enthalpy change is negative and the entropy change is negative. The system changes from a disordered state (liquid) to a more ordered state (solid), so the disorder decreases. In case of melting the opposite is valid. The phase transition is endothermic and the entropy change is positive. Heat has to be added to the system and its disorder increases.

Solidification processes in metals and alloys are controlled by kinetic laws and depend on the driving force of the process. The driving force of solidification equals the change in Gibbs' free energy when the system is transferred from a liquid to a solid state. Solidification takes

place at the equilibrium fusion temperature T_e, mostly called melting point. At T_e in Figure 1.7, the molar Gibbs' free energies of the melt and the solid are equal.

Below the melting point the solid has a lower free energy than the melt and is therefore the stable phase. Above the melting point the reverse is true and the liquid is more stable than the solid. The difference in molar Gibbs' free energy between liquid and solid at the same temperature below the melting point acts as a driving force for solidification of the undercooled liquid. The greater the driving force is, the stronger will be the tendency of the melt to solidify.

During the solidification process, the Gibbs' free energy change $\Delta G_{L\to S}$:

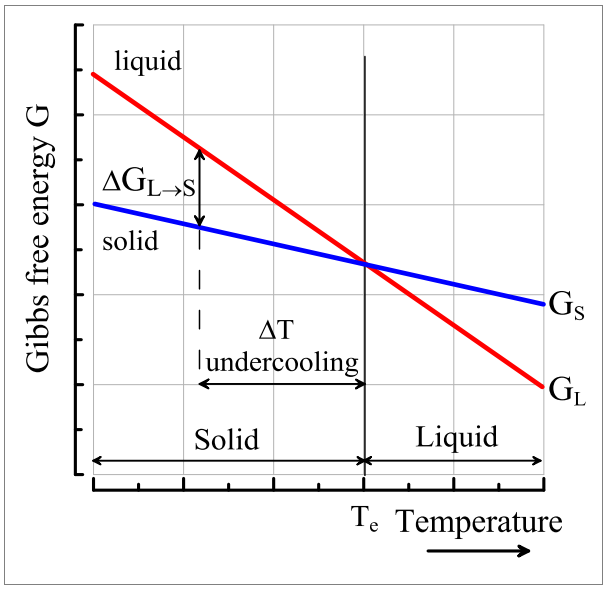

Fig. 1.7: Gibbs free energy as function of temperature
T_e– equilibrium melting temperature
ΔT – undercooling
$\Delta G_{L\to S} = G_S - G_L$, (present work)

$$\Delta G_{L\to S} = G_S - G_L \tag{1.3}$$

is negative because heat is lost to the surroundings, where G_L is the Gibbs free energy of the liquid phase, G_S of the solid phase. The convention is, to have a positive driving force for a spontaneous process and for this reason it is defined as:

Driving force = the negative change of the Gibbs' free energy at solidification

$$-\Delta G_{L\to S} = G_L - G_S \tag{1.4}$$

To derive an expression, where the driving force of solidification is given as a function of the temperature difference ΔT between actual temperature and melting point, equation (1.2) is slightly changed:

$$-\Delta G_{L\to S} = -(\Delta H_{L\to S} - T\Delta S_{L\to S}) \tag{1.5}$$

At the melting point $T=T_e$, the liquid and solid phases are in equilibrium with each other, which can be expressed as $\Delta G_{L\to S} = 0$. Inserting these values into equation (1.5), we obtain:

$$\Delta S_{L\to S} = \frac{\Delta H_{L\to S}}{T_e} \tag{1.6}$$

Inserting expression (1.6) into equation (1.5):

$$-\Delta G_{L\to S} = -(\Delta H_{L\to S} - T\frac{\Delta H_{L\to S}}{T_e}) \tag{1.7}$$

After rearrangement of equation (1.7), the driving force for solidification can be written:

$$-\Delta G_{L\to S} = \frac{T_e - T}{T_e}(-\Delta H_{L\to S}) = \frac{\Delta T}{T_e} H_m \qquad (1.8)$$

where $-\Delta G_{L\to S}$ is the driving force for solidification, $T_e$is the equilibrium melting point temperature, ΔT the undercooling $(T_e - T)$ and $-\Delta H_{L\to S}$=H_m the heat of fusion. Therefore the driving force of solidification close to melting point is proportional to the undercooling ΔT and the heat of fusion H_m. Accordingly, the higher the undercooling, the larger is the driving force for solidification. From classical solidification theory *[FLE74]*, *[KUR84], [STE09]* the undercooling is the sum of four individual undercoolings:

$$\Delta T=\Delta T_t+\Delta T_c+\Delta T_r+\Delta T_k \qquad (1.9)$$

where ΔT_t is the thermal undercooling, which originates from the temperature difference between melt and mould wall. For pure metals ΔT_t is the main driving force, leading to so-called thermal dendrites, nucleating at the mould walls and growing towards the center until the tips of the dendrites touch each other. ΔT_c describes the constitutional undercooling, which is the main driving force for the growth of the solid phase in alloys. It has to do with a change of the composition and ergo the melting temperature at the liquid-solid interface, as will be explained more in detail in section 1.3.2. ΔT_r takes into account the so-called curvature undercooling or known as Gibbs-Thomson undercooling originating from the curvature of the solid-liquid interface, defined as:

$$\Delta T_r = \frac{2\Gamma}{R} \qquad (1.10)$$

where R is the radius of the curvature at the dendrite tip or spherical crystal and Γ the Gibbs-Thomson coefficient, given as:

$$\Gamma = \frac{\gamma^{L/S} T_L}{H_f} \qquad (1.11)$$

where T_L is the liquidus temperature, H_f the latent heat of fusion and $\gamma^{L/S}$ the interfacial energy between liquid and solid phase *[KUR84]*, *[PER05]*. The Gibbs-Thomson coefficient is a measure of the energy required to form a new surface. For most metals, Γ is of the order of 10^{-7} Km. Using equation (1.10), it follows that for $\Delta T_r = 2^{\circ}$ R is 0.1 μm and for $\Delta T_r = 0.2^{\circ}$ R is 1 μm. Hence the effect of the solid-liquid interface energy, $\gamma^{L/S}$, becomes important for morphologies which have a radius less than 10 μm. This includes nuclei, interface perturbations, dendrite tips growing at high rate and eutectic phases. ΔT_k is the kinetic undercooling arising from the propagation of the dendrite tip during growth. It is given by:

$$\Delta T_k = \frac{V}{\mu} \tag{1.12}$$

where V is solid-liquid interface velocity and μ the kinetic undercooling parameter, *[TUR61]*. For solidification to occur, more atoms must jump from liquid to solid than from solid to liquid. Consequently, the solidifying interface must be at lower temperature than T_e by an amount that is called kinetic undercooling, ΔT_k. Typically, for metals the kinetic undercooling is of the order of 0.01 to 0.05 K and becomes significant only for rapid solidification.

Therefore under normal solidification conditions, the coupling condition can be written:

$$\Delta T = \Delta T_c + \Delta T_r \tag{1.13}$$

Historically, the first systematic investigations of crystal growth from the melt were carried out by G. Tamman, *[TAM25]* and co-workers. Working with transparent organic melts (succinonitrile, succinonitrile–acetone, *[JAC65]*) they measured the growth rate as a function of undercooling and heat transfer characteristics of liquid and solid. On basis of such experiments Tamman introduced the main solidification concept as the combined action of nucleation and crystal growth and quantified them as functions of undercooling and energy gain at the liquid-solid transition, called liberated heat. He explained the three zones of a casting regarding nucleation and preferred crystal growth as follows: when molten metal is poured into a cold container, the extraction of heat will take place through the container walls. Thus the layer of melt closest to the wall will solidify first. A large number of grains will nucleate at random along the walls (so-called chill-zone) and grow into the melt. Because the crystal growth rate is anisotropic, such grains having their axis of maximum growth rate parallel to the direction of the heat-flow will grow faster (columnar crystal zone). In case of a pure metal there are only these two zones formed. Since heat can be extracted only by the mold walls, there is no possibility to undercool the residual melt in the center and hence no nucleation of grains can take place there. If, however, impurities are present, they will accumulate in this residual melt and change its solidification temperature. The resulting undercooling will permit nucleation of new grains in the ingot center. This general presentation will be specified for Al casting in the following sections.

1.3.1 Initiation of α-Al grains. Homogeneous and heterogeneous nucleation

The structures of cast materials are very much influenced by the density of crystals growing in the melt. That is why nucleation is very important. Normally, there are two different mechanisms:

a. homogeneous nucleation;
b. heterogeneous nucleation.

Another kind of phase formation is spinodal decomposition, which can take place in alloy systems with low miscibility. Inside the spinodal curve, the initially homogeneous distribution of solved atoms becomes instable against concentration fluctuations. By uphill diffusion such fluctuations grow spontaneously, which can result in a regular arrangement of precipitates. This process is called spinodal decomposition. In between the spinodal and the coexisting curve, however, a free–energy barrier must be overcome, and this requires the formation of a "nucleus" of a new phase: this mechanism is termed nucleation, *[FAV08]*. In the general discussion of nucleation of a new phase in a molten material, it is assumed that the new phase is formed as clusters. The clusters vary in size owing to statistical fluctuations. A cluster that reaches a minimum critical size can continue to grow. Clusters in a new phase, which exceed the critical size required for continuous growth, are usually called nuclei. Clusters of subcritical size are often called embryos in order to distinguish them from the nuclei. The size of an embryo changes because of thermal fluctuations. A nucleus is unlikely to arise directly from occasional thermal fluctuations. It is rather formed out of an embryo, which gradually increases its size by assimilation of atoms from its surroundings. Alternatively, an embryo can lose atoms to its surroundings and disappear, *[FRE12]*.

In classical homogeneous nucleation theory represented by Chalmers *[CHA64]*, Turnbull *[TUR61],* Flemings *[FLE86]*, initially solid particles form clusters throughout the bulk of an undercooled liquid as clusters. These occasional solid conglomerates are called embryos. Their shapes, compositions, structures and sizes vary. In order to analyze the nucleation process, some simplifications are used. The first one is that the equilibrium shape is spherical, as for a solid body with an isotropic surface tension, surrounded by a liquid. The second one is that composition and structure of all embryos are equal. The only remaining variable is the size of the particle, the embryo radius r. Nucleation occurs when the undercooling is such that there are sufficient embryos with a radius larger than the critical radius r_{crit}.

To study the nucleation process theoretically, we have to consider the Gibbs' free energy of the system. The majority of the embryos decay shortly after their formation. Some of them pertain and increase in size. The larger the embryo radius is and the difference in Gibbs' free energy between the melt and the embryo the more unlikely will be the persistence of the embryo. The opposite is true below the melting point. For each temperature a stable statistical equilibrium distribution is developed, i.e. nucleation and decay of embryos is balanced. It can be shown that the distribution is the well-known Boltzmann distribution:

$$n_r = n e^{-\frac{\Delta G_r}{k_B T}} \tag{1.14}$$

where ΔG_r is the difference in Gibbs' free energy between the embryo and the melt. ΔG_r depends on the radius embryo r, n_r is the equilibrium number of embryos with radius r per unit volume of the melt, n the total number of sites where embryos can form per unit volume in the melt and T the temperature. ΔG_r consist of two parts, a volume part corresponding to the Gibbs' free energy of the embryo 'in bulk' and an area part owing to the interface energy between the melt and the embryo.

$$\Delta G_r = -\frac{\frac{4\pi r^3}{3}}{V_m}[-\Delta G_{L\to S}] + 4\pi r^2 \gamma^{L/S} \tag{1.15}$$

where V_m is the molar volume of the material, $-\Delta G_{L\to S} = G_L - G_S$ is the driving force of solidification, $\gamma^{L/S}$ the interface energy of the interface melt/embryo.

For a small particle, the reduction in bulk energy ΔG_r caused by its formation is lower than the energy consumption for the generating particle/surrounding interface. Small particles can form only via random thermal fluctuations of atoms and are more likely to decay than to grow. Because the relation bulk energy/surface energy is proportional to $r^3/r^2 = r$, beyond a critical particle size r_{crit} the particle continues to grow. Calculating the maximum of ΔG_r, one gets:

$$r_{crit} = \frac{2\,\gamma^{L/S}\,V_m}{\Delta G_{L\to S}} \tag{1.16}$$

and

$$\Delta G_r = \frac{16\pi}{3}\,\frac{(\gamma^{L/S})^3 V_m^2}{(\Delta G_{L\to S})^2} \tag{1.17}$$

With (1.17) and (1.14) the number of embryos of critical size can be calculated. For growing the embryo has to incorporate atoms from the liquid. These atoms must overcome the Gibbs' free-energy barrier or the activation energy U^I to reach the surface of the embryo. The number of atoms per unit volume, which have an energy high enough to fulfill this condition, is proportional to $Pe^{-\frac{U^I}{k_B T}}$, where P is the probability related to the entropy ($S = k_B \ln P$).

The nucleation rate J can be described by the equation:

$$J = \text{const} \times n_r P\, e^{-\frac{U^I}{k_B T}} \tag{1.18}$$

which gives with (1.14)

$$J = \text{const} \times P\, e^{-\frac{\Delta G_{L\to S} + U^I}{k_B T}} \tag{1.19}$$

In contrary to the homogeneous nucleation in an infinite medium, in real systems, where the melt touches the mold walls and contains certain insoluble impurities, sites for precipitation exist *ab initio*, i.e. heterogeneous nucleation is the dominant mechanism. It requires undercooling in the order of a few degrees, *[FRE12]*. For example, it was reported by Quested and Greer, *[QUE04]* that the measured undercooling of pure aluminium after addition of TiB_2 particles is only in the range 0.18-0.22 K.

The principal of the heterogeneous nucleation theory *[GLI11], [FRE12]*, *[CAN79]* is that the surface of a catalyst (inoculation particle) reduces the energy barrier of nucleation. A solid nucleus forms as a spherical cap at a flat catalyst-liquid surface. The energy barrier ΔG_r is then given by

$$\Delta G_r = \frac{16\pi}{3} \frac{(\gamma^{L/S})^3 V_m^2}{(-\Delta G_{L\to S})^2} \frac{(2+\cos\Theta)(1-\cos\Theta)^2}{4} \tag{1.20}$$

with Θ as contact angle at the catalyst-solid-liquid triple point. In order not to confuse the homogeneous nucleation Gibbs energy in (1.17) with the heterogeneous nucleation in (1.20), the first one is called ΔG_{hom}, the second one ΔG_{het}. With this definition (1.20) can be written as:

$$\Delta G_{het} = \Delta G_{hom} \frac{(2+\cos\Theta)(1-\cos\Theta)^2}{4} \tag{1.21}$$

Heterogeneous nucleation on a flat substrate model is illustrated in Figure 1.8. The higher $\gamma_{L/C}$ - $\gamma_{C/S}$, the smaller becomes Θ. So drops with small Θ indicate a good wettability of the surface.

The higher the wettability of the catalyst, the higher is its efficiency. However, when Θ approaches zero, liquid-solid interface and catalyst-solid interface fuse and r_{crit} becomes infinite, *[KIM94]* i.e. the model fails (see Table 1.2). For that case, a so-called adsorption model was developed by Cantor, *[KIM94]* where heterogeneous nucleation takes place by adsorption of the solidifying atoms on the catalyst surface. The crystal structure at the surface determines how this adsorption takes place in detail. Recently, such an adsorption mechanism was studied using high-resolution transmission electron microscopy (HR TEM) by Schumacher and Greer, *[SCH94]*. In Al–Si–P alloys the nucleation of Si on Al crystals, covered by a monolayer of catalytic AlP, *[CAN03]* was investigated. Additionally, they

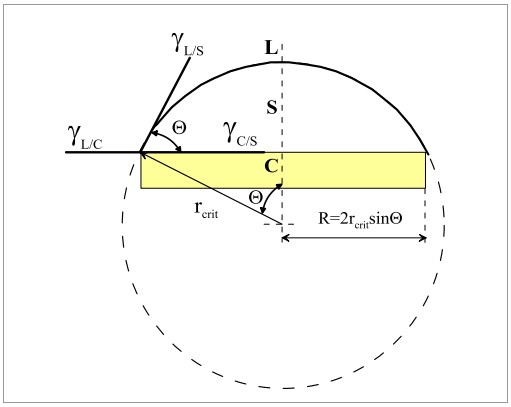

Fig. 1.8: Spherical-cap model of heterogeneous nucleation
L – liquid, S – solid, C – catalyst, (present work)

investigated in Al-based glasses the nucleation of Al on TiB_2, covered by a monolayer of catalytic $TiAl_3$. They showed that nucleation at a catalyst surface can slowed down by replacing a liquid with high diffusivity by a glass with low-diffusivity.

Solidification of Al alloys is well known to take place by heterogeneous nucleation on TiB_2 particles. In Al based glasses, first Al is adsorbed onto the TiB_2 particle surfaces, to form a catalytic Al_3Ti layer, then the crystallization of primary Al starts. This sequence can be seen in Figure 1.9. Zr additions 'poison' this process, because they partially substitute Ti in the catalytic Al_3Ti layer, which leads to a $Al_3(Ti,Zr)$ layer, which is less effective for the following Al adsorption, *[BUN99]*. In presence of Si, the catalytic Al_3Ti interface is replaced by an ineffective Ti_2Si layer. This is the reason, why the addition of Ti or Ti+B does not result in grain refinement of Al-based casting alloys, as soon as they contain a high amount of Si (7.00 - 9.00 wt.%).

Table 1.2: Nucleation undercoolings ΔT_n, contact angles Θ and nucleation site densities N_c obtained from kinetic analysis of the solidification of embedded B-rich liquid droplets in an A-rich solid matrix, using the classical spherical cap model of heterogeneous nucleation, [KIM94]

alloy	nucleation undercooling ΔT_n, K	contact angle Θ, °	nucleation sites density per droplet N_c
Al-Pb	22.00	21	10^{-6}
Al-In	13.00	27	10^{-7}
Al-Cd	56.00	42	30
Al-Sn	104.00	59	100

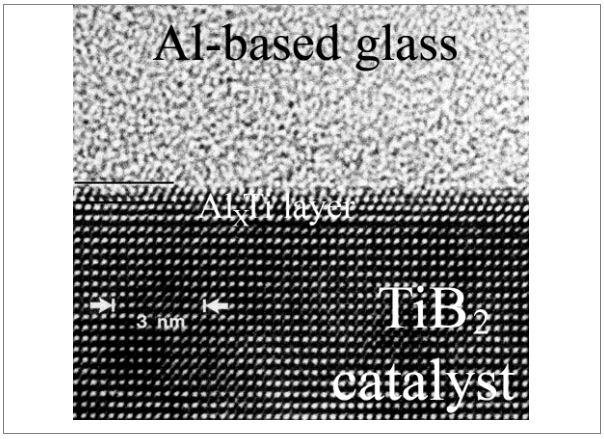

Fig. 1.9: High resolution transmission electron micrograph of the surface of a TiB_2 particle embedded in an Al-based matrix. The boride particle is first covered with a layer of Al_XTi, then Al follow, [CAN03]

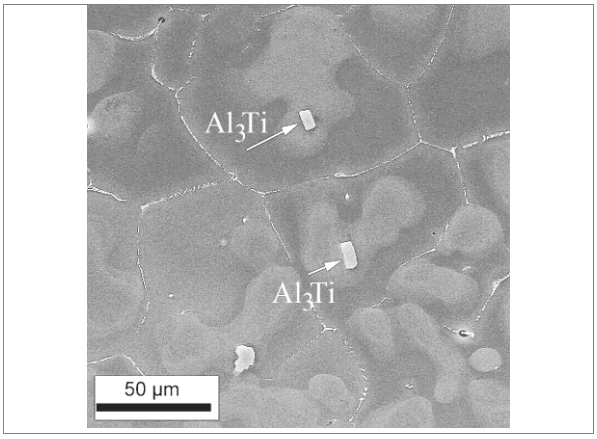

Fig. 1.10: Particles of $TiAl_3$ in grain centers of Al+0.23 wt.% Ti alloy (marked by arrows), [MYK99]

In an attempt to understand the formation of fine equiaxed grains in Al alloys after addition of Ti or Zr, Maxwell and Hellawell, *[MAX75]* took into account, that in this case

adsorption does not take place on a infinite planar surface but on faceted Al_3Ti or Al_3Zr particles.

First spherical-cap nuclei form on the different facets, and then wettability causes the fusion of theses nuclei, resulting in a spherical envelope around the particle. The radius of this nucleus has about this size, which one gets for the critical nucleus size of aluminum at low undercooling. Examples of such intermetallic particles acting as nucleation sites of Al grains are shown in Figure 1.10. Al-Ti alloys belong to the class of peritectic systems. This means, that a new solid α-phase is formed out of the properitectic β solid phase (Al_3Ti) and the liquid, as soon as the peritectic temperature T_p is reached. The nucleation in Ti or Zr containing Al alloys as described by Maxwell and Hellawell, *[MAX75]* is the peritectic reaction $L+\beta(\text{solid})=\alpha(\text{solid})$ on a atomistic level.

Significant changes in the nucleation behavior were observed when the aluminum melt was subjected to intensive shearing, *[FAN09]* e.g. melt agitation or electromagnetic stirring.

The microstructural studies in the present work confirmed that in aluminum casting alloys some phases can nucleate in this multi-step way: first a new phase nucleates on the surface of a preexisting particle and then the new phase nucleates on the surface of the precipitate, which had formed just before.

As an example Figure 1.11 shows the agglomeration of TiB_2 particles surrounded by Ti-enriched phase observed in the center of Al grain. Additional prove for such a multi-step nucleation operating in Al-based casting alloys will be given in Chapter 4, where the formation of Mg_2Si primary crystals in Al-Mg-Si alloys is described. Once a solid nucleus has formed and reached a critical radius r_{crit}, it will grow stably into the surrounding liquid. This growth of the solid phase is the second part of structure formation and will be described in the following chapter.

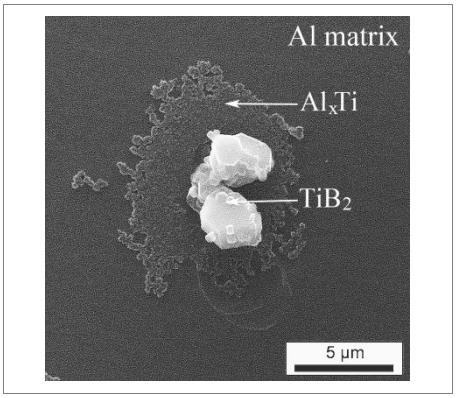

Fig. 1.11: Agglomeration of TiB_2 *particles surrounded by* Ti *-enriched phase. It acts as catalyst for the α-Al grain. Material: A99.7 purity Al with additions of* TiB_2 *and* Ti*, (present work)*

1.3.2 Growth of the solid phase

During the growth of a solid from its undercooled parent melt a number of microstructural changes may occur, when the undercooling ΔT is increased. In all aluminum casting processes, solidification usually starts on the mold walls, resulting in a columnar crystals zone close to mold wall, as shown in Figure 1.12 for an Al-Mg-Si alloy.

The direction of the temperature gradient determines the orientation of the columnar dendrite axis, its steepness the dendrite arm spacing. During growth the heat of fusion is released. Consequently, the temperature increases and thermal undercooling ΔT_t is no longer the main driving force. Growth is no more thermally controlled, but becomes diffusion controlled, which what is represented by the constitutional undercooling ΔT_c. This undercooling will be briefly discussed.

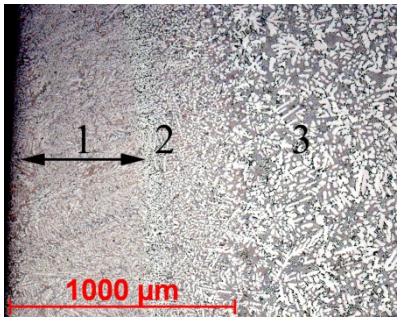

Fig. 1.12: Columnar crystals zone (1) in AlMg7Si3Mn alloy cast into permanent mould. Intermediate zone (2) and equiaxed crystal zone (3), (present work)

Considering a hypothetical A+B alloy, the constitutional undercooling ΔT_c is proportional to the concentration C_0 of the alloying element B, the slope m of the liquidus line and the relative partitioning of the element (k-1)/k:

$$\Delta T_c = \frac{C_0 m(k-1)}{k} \qquad (1.22)$$

$k = \frac{C_S}{C_L}$ is the equilibrium partition coefficient of solute element B, where C_S is the concentration of B in solid and C_L in liquid.

When the alloy melt solidifies, the concentration of solute in the solid will differ from that of the melt. If $k < 1$, which is true for eutectic-type alloys, an excess of solute atoms arises in the solid, close to the interface. Solute atoms become rejected from the interface into the melt. The higher concentration of solute atoms at the solidification front, compared to the rest of the melt, leads to diffusion of solute atoms from the interface into the melt and an equilibrium distribution of solute atoms in the melt develops.

The concept of constitutional undercooling was first introduced by Chalmers, *[TIL53]*. Based on this, the theory expanded in new topic, for example, the break down of a planar solid-liquid interface and the columnar to equiaxed transition (CET) during solidification of metallic alloys. These are the fundaments of the recent understanding of the mechanism of grain refinement in Al-based alloys.

Chalmers showed *[CHA64], [JAC04]* that constitutional undercooling causes an instability of the planar front of solidification and results in the formation of cellular or dendritic structures.

Initially, solid nuclei, formed on the mold wall or potent substrates, have planar interfaces with the surrounding liquid. The condition necessary for the instability of a planar interface is

that undercooling increases with distance from the interface. In Figure 1.13 a, the actual temperature shows a linear increase, starting at the solid-liquid interface, expanding with $y > 0$ into the liquid.

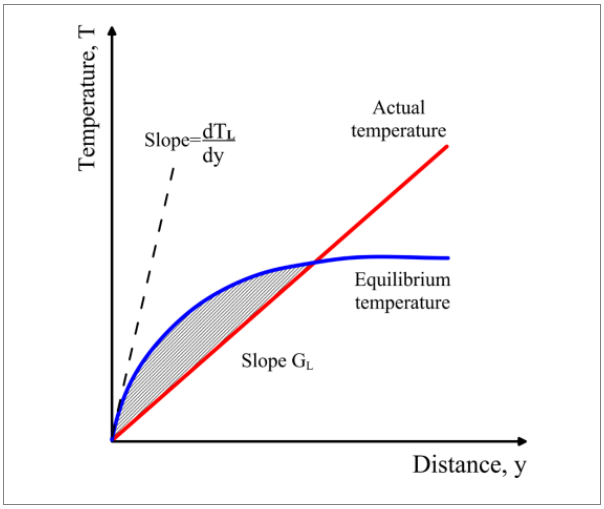

a. undercooling in front of a planar interface, [CHA64]

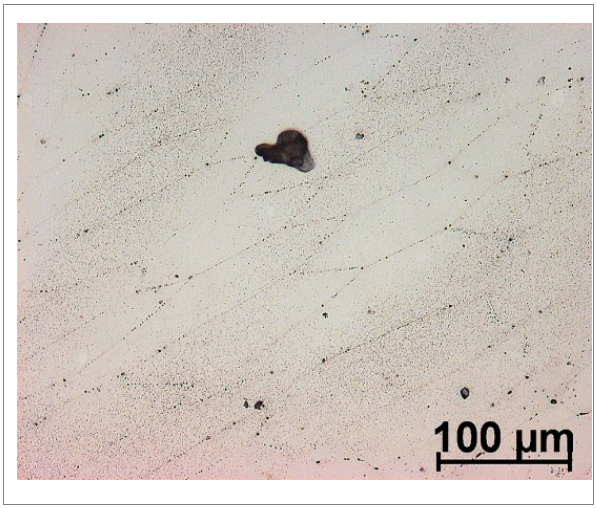

b. cellular structure in Al-0.60 wt.% Mn alloy, (present work)

Fig. 1.13: Actual and equilibrium temperatures on the solidification front (a) and cellular structure of low alloyed Al-base alloy (b)

The equilibrium temperature in the hatched area is higher than the actual temperature, i.e. we have undercooling. This is fulfilled in case of constitutional undercooling - ΔT_c. This undercooling leads to a breakdown of the planar interface in favor of the cellular and further dendritic structure. As an example in Figure 1.13 b a cellular structure is shown, obtained in low alloyed Al-0.60 wt.% Mn alloy after solidification.

Experiments performed by Chalmers *[CHA64]*, Sekerka *[SEK68]* and such described in books of Glicksman *[GLI11]* and Fredriksson *[FRE12]*, confirmed that a cellular structure appears below a critical value of the ratio $\frac{G_L}{V_{growth}}$, namely if

$$\frac{G_L}{V_{growth}} \leq \frac{m}{D_L}\frac{1-k}{k}C_0 = -\frac{1}{D_L}\Delta T_c \qquad (1.23)$$

where G_L is the temperature gradient in liquid phase (K m^{-1}), V_{growth} the growth rate, which is equal to the velocity of the solidification front (m min^{-1}) and D_L the diffusion constant of solute atoms in the melt. It is worth noting that the term $\frac{m}{D_L}\frac{1-k}{k}C_0$ in the equation represents the solidification temperature range of the alloy at C_0 composition, *[CHA64]*.

The size of the constitutionally undercooled zone is equal to the length of the diffusion boundary layer δ_C which is in direct proportion to the D_L:

$$\delta_C = \frac{D_L}{V_{growth}}, \textit{[KUR92]} \qquad (1.24)$$

Figure 1.14 shows the changes of the solidification mode from planar to columnar dendritic, and finally to equiaxed dendritic for increasing constitutional undercooling.

For small constitutional undercooling, the instabilities will only grow in the solidification direction, and a cellular interface will result. This is shown schematically in Figure 1.14 b.

However, if the constitutional undercooling increases because of the lower thermal gradient of the actual temperature (Fig. 13 a), the spacing between the cells increases. Instabilities will develop on the sides of the cells, resulting in the formation of dendrites (Fig. 1.14 c).

This is the cellular-to-dendrite transition. Both cellular and dendritic growth, starting from the wall into the opposite direction of the heat transport, can be described as columnar growth. If constitutional undercooling is even higher, equiaxed grains can be nucleated in the liquid in some from the interface (Fig. 1.14 d), i.e. the dendritic-to-equiaxed transition occurs. If the thermal gradient is more flat, the driving force for the columnar front will be extremely small. A complete equiaxed structure is expected because of the large width of the zone where nucleation of equiaxed grains can occur. Formation of equiaxed grains restricts the development of columnar grains.

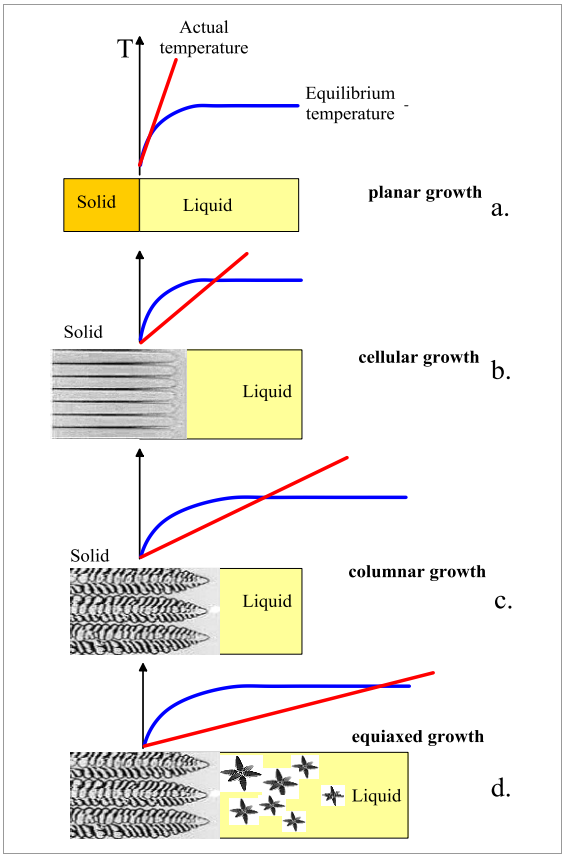

Fig. 1.14: Effect of constitutional undercooling on solidification mode: a- planar interface (no constitutional undercooling); b – cellular (small undercooling); c – columnar dendritic; d – equiaxed dendritic (large undercooling), (present work)

The morphology of the dendritic structure is of technological importance, as many important materials properties are intimately related to their morphology. In nearly all systems dendrites begin coarsening immediately upon formation.

1.3.3 Eutectic solidification

The dendritic structure is a preferential morphology for single-phase alloys. It is the structure of Al-based solid solution grains in all commercial casting techniques, covering cooling

rates from 10^{-6} K s^{-1} for large ingots up to 10^{9} K s^{-1} for surface treatments such as electron beam or laser glaze processing. It takes place in Al-Mg or Al-Cu casting alloys and has been well investigated (section 1.3.2). As an example, in Figure 1.15 the dendritic structure of AlCu4.5MnAg (A201.0) casting alloy, cast into a sand mould, is shown.

Fig. 1.15: Dendrites and grains of the commercial AlCu4.5MnAg (A201.0) alloy cast in a permanent mold, (present work)

In contrast to single-phase alloys, eutectic growth involves the nucleation and cooperative growth of two or more solid phases within one liquid phase ($L \leftrightarrow \alpha + \beta$). Since eutectic alloys play a very important role in foundry production, it has attracted extensive attention. The reason for their widespread use can be found in the unique combination of good castability (comparable to that of single-phase alloys), relatively low melting point (minimizing the energy required for production), and interesting behavior as "composite" materials.

A typical eutectic-type phase diagram is given in Figure 1.16. Two distinctive features characterize the diagram: (i) there is complete miscibility in the liquid state and incomplete miscibility in the solid state; (ii) The temperatures of the pairs of liquidus and solidus lines are monotonically decreasing from T_A, respectively T_B towards T_E. The point E in the diagram represents the eutectic point. The eutectic alloy with the composition C_E has a lower freezing point than any other composition C. So when a liquid with eutectic composition C_E is cooled to the temperature T_E, solidification proceeds with the simultaneous crystallization of both phases α and β with the compositions D and F. Under equilibrium conditions, in the eutectic point E two solid phases and the liquid phase coexist. According to Gibbs phase rule:

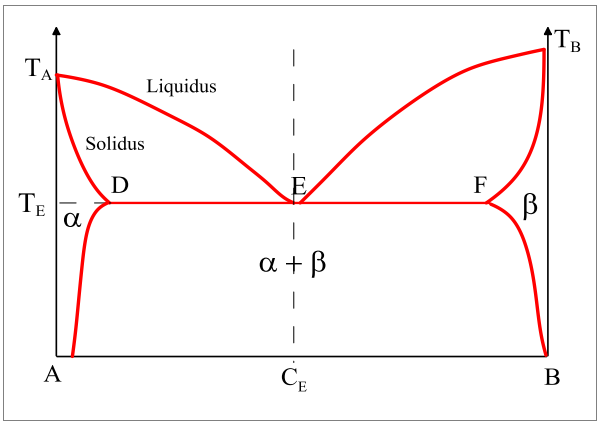

Fig. 1.16: Typical eutectic phase diagram, (present work)

$$f = C - \varphi + 1 \qquad (1.25)$$

where f is the degree of freedom, C the number of components and φ the number of phases present. For a binary system, e.g. Al-Si alloys, C=2 with three conjugate phases, so subsequently,

$f = 0$. This is the reason, for the statement the "eutectic equilibrium is invariant" which means, it occurs at a fixed temperature, pressure and composition for each of the three participating phases. The solid formed by the reaction consists of a mixture of the phases α and β, with their proportion given by the lever rule as:

$$\frac{\text{Portion of } \alpha - \text{phase}}{\text{Portion of } \beta - \text{phase}} = \frac{\text{FE}}{\text{DE}}, \textit{[CHA63]} \tag{1.26}$$

From a morphological point of view, eutectic alloys exhibit a wide variety of microstructures, which can be classified as:

(i) continuous microstructures. Continuous means that both phases can be traced along an unbroken path from the beginning of the solidification process to the space of its completion, i.e. both phases are continuous in the growth direction. The lamellar structures and the rod-like structures apparently fulfill this criterion;

(ii) discontinuous microstructures. In this group, one of the phases of the alloy is dispersed in the second phase as discrete particles, i.e. there is no continuity of the included phase in any direction. A characteristic example of this type of structure is the A1-Si eutectic system, in which the silicon is finely dispersed in the aluminum matrix (Fig. 1.17);

(iii) Spiral structures. According to *[CHA63]* it is a unique microstructure for two alloy systems, namely Al-Si and Mg-Zn. Therefore it will be described in detail.

According to *[FRE12]*, eutectic reactions in melts often result in very different morphologies. Owing to their appearances, descriptive names have been given to them such as lamellar, rod, Chinese script, spiral and nodular eutectic structures. As two or three of these morphologies can appear in the same system, there are other ways to classify eutectic structures. One way is to classify the eutectic as normal or degenerate regarding the interaction between the two phases during precipitation.

(i) At a normal eutectic reaction, there is a close cooperative interaction between the two phases. They grow with a common interface in the melt. The two phases form lamellar- or rod-shaped aggregates, which grow perpendicularly to the interface.

(ii) Normal eutectic growth implies that the two phases grow at the same rate.

(iii) Characteristic of degenerate eutectic growth is a competitive interaction, i.e. one of

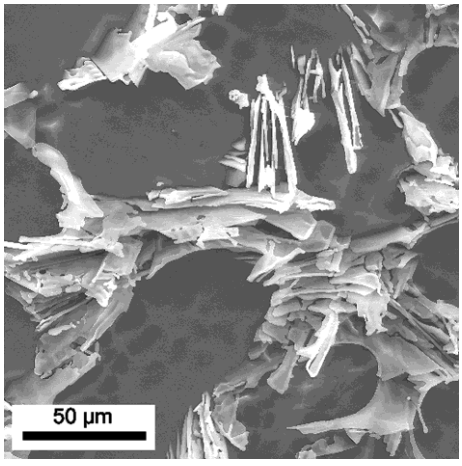

Fig. 1.17: Microstructure of the commercial A356 (AlSi7Mg) casting alloy after deep etching, (present work)

the two phases grows faster than the other one. A lamellar or rod eutectic cannot be formed if one phase always grows ahead of the other. Consequently, the growth mechanisms of the two phases determine the structure of the eutectic.

Nucleation of eutectic phases from the melt was studied in detail by Sundquist and Mondolfo *[SUN61], [GLI11]*. For Al-Si casting alloys eutectic nucleation was carefully studied by Nogita and Dhale *[NOG01]*, *[MCD04]*. Sundquist and Mondolfo's main findings are summarized below:

(i) non-reciprocal nucleation catalysis: If the nucleation of phase β is easy in the melt α, i. e. with little undercooling, then the nucleation of α in β is difficult. Specifically, Sundquist and Mondolfo observed in the common Pb-Sn eutectic solder, that the Pb-phase is efficiently nucleated from the eutectic melt;

(ii) phases that act as effective nucleation catalysts tend to have 'complex', noncentrosymmetric, crystal structures;

(iii) the crystalline phase, which does not nucleate easily from the eutectic melt, provides an efficient substrate for the subsequent nucleation of a more symmetric conjugate phase.

Dahle and Nogita, *[NOG01]* observed three eutectic nucleation modes in Al-Si alloys of different purities, such as:

(i) with mode I, the eutectic nucleates on or directly adjacent to the primary dendrites. The nucleation frequency is very high and the eutectic evolves with a very irregular interface. An intermediate porosity is therefore expected;

(ii) with mode II, the eutectic nucleates on potent nuclei in the interdendritic areas;

(iii) with mode III, the eutectic solidification involves nucleation at or adjacent to the wall and the growth front is opposite to the thermal gradient. The growth front of the eutectic is expected to be relatively flat and gradually move toward the centre of the casting.

In frame of these findings, one can state that in Al-Si hypoeutectic alloys ($\leq 12.60\text{wt.}\%$) eutectic nucleates on primary $\alpha-\text{Al}$ as well as on the mould walls. A similar nucleation mode might be expected for Al-Mg-Si hypoeutectic alloys. In case of hypereutectic alloys eutectic may nucleate on the surface of primary Si crystals in case of Al-Si alloys, and on primary Mg_2Si in Al-Mg-Si alloys.

Eutectic growth is a typical diffusion-controlled process and the first diffusion model of eutectic growth was published by Tiller in 1957, *[TIL58]*. In 1966 Jackson and Hunt (JH model) expanded the method to solve the coupled diffusion problem at a regular eutectic interface, *[JAC66], [MAG91]* which is now accepted as the classical model. The relationship between undercooling ΔT at the solid-liquid interface and the eutectic spacing λ, was obtained as:

$$\Delta T = K_1 \lambda V_{growth} + \frac{K_2}{\lambda} \qquad (1.27)$$

where V_{growth} is the growth rate, and K_1 and K_2 are constant parameters which express the constitutional undercooling effect and the Gibbs-Thompson effect of the solid-liquid interface, respectively. Equation (1.27) shows that λ depends not only ΔT, but also on V_{growth}.

The solution of this problem was found by Tiller, *[TIL58]*. According to their extremum criterion, eutectic growth occurs with the minimum liquid undercooling at the solid/liquid interface or with the maximum growth rate. So, if the first derivative of the total undercooling is set equal to zero, the following relationships among ΔT, λ and V_{growth}, are obtained, *[KUR92]*:

$$\lambda^2 V_{growth} = \frac{K_2}{K_1} \qquad (1.28)$$

$$\frac{\Delta T}{\sqrt{V_{growth}}} = 2\sqrt{K_1 K_2} \qquad (1.29)$$

The JH model was developed for normal lamellar or rod eutectic according to (i) and (ii) on page 16. However, the most important cast alloys, e.g. Fe-C and Al-Si, have irregular eutectic structures. Al-Si casting alloys usually contain from 7.00 to 10.00 wt.% Si.

Conventional casting applications are sand casting, permanent mould casting and investment casting, where V_{growth} varies from $0.01 - 0.10\ \mathrm{mm\,s^{-1}}$ and the thermal gradient G between $1 - 10\ \mathrm{K\,mm^{-1}}$. Here the eutectic structure is characterized by long acicular plates of silicon, a diamond structure phase in which the solubility of aluminum is essentially zero (Figure 1.18).

Experiments of Liu, *[LIU92]* on Al-Si eutectic growth showed that the interface undercooling is an approximately linear function of the term λV_{growth} which means, that it is according to (1.27) mainly a constitutional undercooling ΔT_c. The interface profile as a function of the temperature gradient G_L becomes

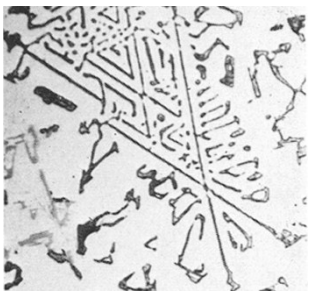

a. x450, *[MIN74]*

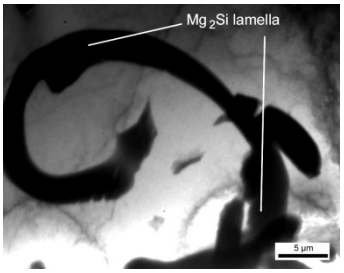

b.

Fig. 1.18: Morphology of $(Al)-(Mg_2Si)$ *eutectic observed by [MIN74] (a), and* $(Al)-(Mg_2Si)$ *eutectic found in AlMg7Si3 alloy (b), (present work) showing spiral growth of eutectic*

more planar when G_L increases and hence the interface undercooling decreases with increasing G_L.

Another eutectic morphology, the so-called spiral structure (see above, *[FRE12]*) has to be considered because the Al-Mg-Si quasibinary alloys are the main subject of the present work.

Right now they are increasingly used in automotive and aerospace industries for critical structure applications because of their excellent castability and corrosion resistance and, in particular, high mechanical properties in as-cast state.

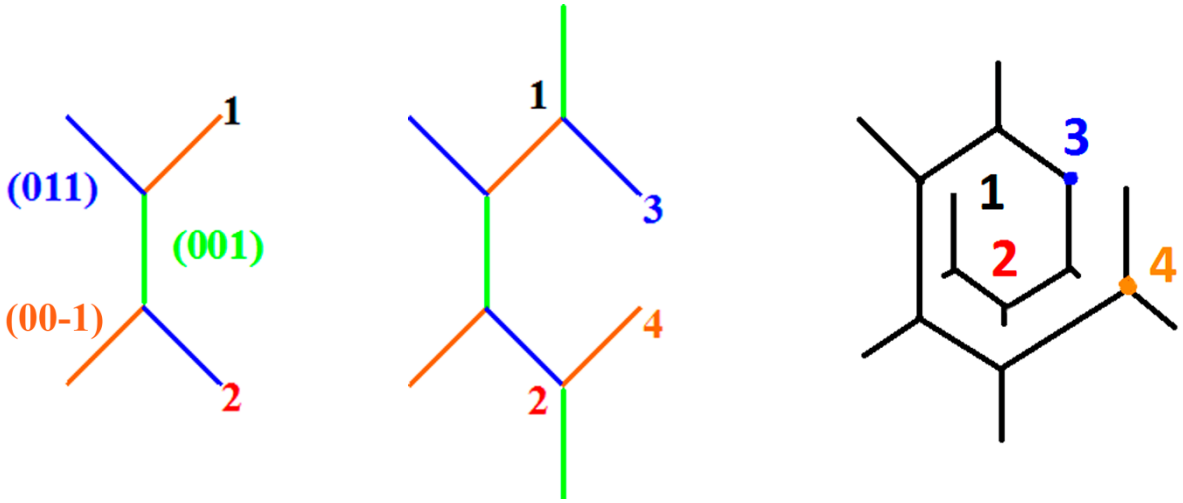

a. b. c.

Fig. 1.19: Schematic Mg_2Si plates on (001), (011), (01-1) *planes at cuts on the (100), (a); continued branching in point 1 and 2, (b); spiral-formation by continuation in point 3 and 4 and interaction of the plates (c), (present work)*

In contrast to (Al)+(Si) eutectic, the (Al)+(Mg_2Si) eutectic system shows under normal solidification conditions lamellar structure and spiral growth. This growth mode is not obvious from the light microscopy images (Figure 1.18 a) but can be clearly seen in a bright field TEM image (Figure 1.18 b) where the first turn of Mg_2Si lamella is shown. According to Minkoff, *[MIN74]* Mg_2Si eutectic plates grow as {100} and {110} oriented plates. The different growth steps are shown in Fig. 1.19. When the plates grow, they branch into different direction (Figure 1.19 a). This branching continues (Figure 1.19 b). When different plates meet each other, growth continues into the "free" direction. The result is a spiral. In contrast to the normal solidification conditions, for an increased cooling rate of 60 - 90 K s^{-1}, as in the case of the high pressure die casting, the morphology of the $(Al)+(Mg_2Si)$ eutectic changes. It becomes short fibrous (Chapter 4), illustrating the effect of cooling rate on eutectic growth.

1.4 Conclusion

- For the casting processes in the production of aluminum parts, the cooling rate plays an essential role. Highest cooling rates are attained in the HPDC process. This has two effects: the morphology of the primary phase $\alpha - \mathrm{Al}$ changes from long dendrites to the spherical ones. The eutectic shape transforms them from plates to short fibers.
- The nucleation of the primary $\alpha - \mathrm{Al}$ phase takes place heterogeneously on the mold walls in the initial stage of solidification and equiaxed grains are heterogeneously nucleated inside the constitutionally undercooled zone ahead of the columnar crystal zone. Such a complex nucleation is possible not only for the formation of $\alpha - \mathrm{Al}$ but also for intermetallic phases, (see Chapter 4).
- The morphology of eutectic either for $(\mathrm{Al}) + (\mathrm{Si})$ or $(\mathrm{Al}) + (\mathrm{Mg_2Si})$ systems depends on the cooling rate. Higher cooling rate gives a finer eutectic structure and smaller interlamellar spacing. Under normal solidification conditions, $(\mathrm{Al}) + (\mathrm{Mg_2Si})$ eutectic tends to spiral growth whereas high cooling rate results in a short fibrous eutectic morphology.

2 Strengthening mechanisms and their effects in aluminum alloys

2.1 Classification of aluminum alloys. Casting alloys

The low strength of pure aluminum limits its commercial usefulness. A major aim of alloying is to overcome this drawback. For structural use, the additional selection criteria for an alloy are corrosion resistance, ductility and toughness. Consequently, composition is first selected for strength.

Specifications for casting alloys are clearly distinguished from those of wrought aluminum alloys and are defined by their chemical compositions *[DAV93], [ALU98], [ASM88]*. Each country has developed its own aluminum casting alloy nomenclature and designation and so far no internationally accepted system has been adopted for identification yet.

Alloy systems are classified by a number systems (ANSI) or by names indicating their main alloying constituents (DIN and ISO). As a major step towards alignment of Aluminum and Aluminum Alloy compositions on an international basis, most countries have agreed to adopt the 4 digit classification for wrought alloy composition designation. The European reference for the alloys will be identified with the prefaces EN and AW which indicate European Normative and Aluminum Wrought alloys, respectively. In all other respects, the alloy numbers and composition limits are identical to those registered by the Aluminum Association.

Wrought aluminum is identified with a four digit number which identifies the alloying elements, followed by a dash, a letter identifying the type of heat treatment and a 1 to 4 digit number identifying the specific temper (e.g. 6061 - T6, the most common free-machining aluminum alloy). The Aluminum Association (AA) has adopted a nomenclature of cast aluminum alloys similar to that of wrought alloys. Cast aluminum alloys use a four to five digit number with a decimal point. The main alloying elements in the AA system are shown in Table 2.1. A five digit numbers system is used to characterize the casting process, such as: D - Pressure die casting, K - Chill or permanent mould casting, L - Investment casting, and S - Sand casting.

The meaning of the four designation digits are as following:

- first digit: Principal alloying element(s);
- second and third digits: Specific alloy designation (“identification number”);
- fourth digit: casting (0) or ingot (1, 2) designation.

Table 2.1: Classification of casting aluminum alloys EN AB, EN AC, EN AM according to Aluminum Association (AA) and European Norms (EN = European Norm A = Aluminum, B = Ingot, C = Cast Alloy, M = Master Alloy)

AA	major alloying elements, wt.%	atoms in solid solution	precipitation hardening	heat treatment
1XX.X	min 99.00% Al			non heat treatable alloys
4XX.X	Si	+		
5XX.X	Mg (<7.00%)	+		
2XX.X	Cu (up to 5.00%)	+	+	heat treatable alloys
3XX.X	Si+Mg (Cu)	+	+	
6XX.X**	Mg+Si	+	+	
7XX.X	Zn+Mg	+	+	
8XX.X	Sn	+	+	

** - 6XX.X series is not used in AA designation system but included into DIN EN 1706

The new European reference for alloys will be identified with the preface EN followed by a blank space followed by A which indicates aluminum then B, C, or M which indicate respectively ingots for re-melting, casting or master alloys.

Until now, casting aluminum based alloys with silicon additions are probably the most important once for engineering applications. This is because of the high fluidity provided by alloys with near eutectic composition. The castings have high corrosion resistance, combined with a low coefficient of thermal expansion and good weldability.

In Table 2.1, the 6XX.X series is given in cursive letters and was inserted by the author. In the original AA designation system for casting alloys, this position is designated as a place holder. The reason for addressing these alloys, represented in DIN EN 1706 as EN AC-AlMg5(Si), is that they possess high strength and ductility in as-cast state and the ability to be strengthened by heat treatment. It is still the matter of many controversies and will be discussed in Chapters 5 and 6.

Five classes of casting alloys, namely Al-Cu (2XX.X), Al-Si-Mg (3XX.X), Al-Zn (7XX.X) and Al-Sn (8XX.X) are usually subjected after casting to heat treatment. In some cases Al-Mg alloys with Mg content higher than 8.00wt.% are appointed to homogenisation and quenching.

Heat treatment of aluminum alloys can significantly influence properties such as strength, ductility, fracture toughness, thermal stability, as well as residual stresses, dimensional stability and resistance to corrosion and stress corrosion cracking.

The main heat treatment procedures are homogenization, annealing and precipitation hardening, involving solution heat treatment, quenching and aging. A heat treatment and temper designation system has been developed by the Aluminum Association to describe the processing of wrought and cast aluminum alloys, (See Table 2.2).

Table 2.2: Designation system of the heat treatment of aluminum alloys

suffix		treatment
F		as-fabricated (in case of casting alloys – as-cast state)
O		annealed (seldom applied for casting alloys)
H		strain hardened by cold work
T		heat treated to stable condition, excluding annealing (O)
	T1	cooled from an elevated temperature forming process (partial solution) followed by natural aging (for wrought alloys only)
	T2	cooled from an elevated temperature forming process, cold worked and naturally aged (for wrought alloys only)
	T3	solution heat treated, quenched, cold worked and naturally aged (for wrought alloys only)
	T4	solution heat treated, quenched and naturally aged (for both – wrought and casting alloys)
	T5	rapidly cooled from elevated temperature and then artificially aged
	T6	solution heat treated, quenched and than artificially aged (applied mainly for casting alloys)
	T7	solution heat treated, quenched and overaged (applied mainly for casting alloys)

Homogenization

The as-cast microstructure of direct chill (DC) cast ingots or shape casting shows normally a significant segregation of the alloying elements caused by the growth of the solid phase during solidification (section 1.3.2). Examples for microsegregation in shape castings are the gradual change in composition from the center to the edge of dendrites and grains. On Figure 2.1 the inhomogeneous distribution of Ti in Al - 0.12 wt.% Ti is shown. The darker area in the grain center contains a higher Ti concentration, gradually

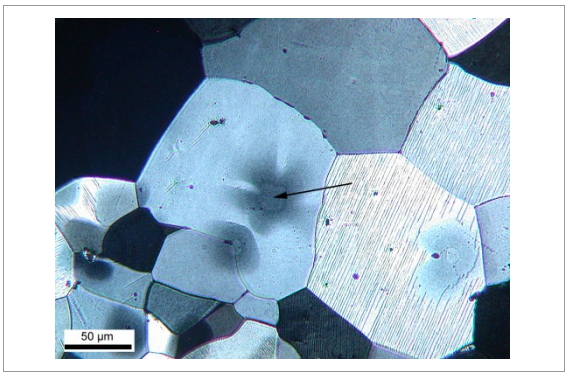

Fig. 2.1: Coring in Al - 0.12 wt.% Ti alloy. Darker area in the grain center (marked by arrow) contains a higher Ti concentration than dendrite tips, (present work)

decreasing towards the ends of dendrite arms.

The main aim of homogenization is to improve workability and mechanical properties by dissolving the non-equilibrium brittle interdendritic constituents and by providing a more homogeneous structure throughout the ingot. Homogenization is carried out at temperatures between the solvus and the solidus, ~ 450.0 – 570.0°C (for casting alloys), for times between 2 and 10 h.

Annealing

Different types of annealing treatments with different objectives exist depending on the alloy system and prior processing. Full annealing (O temper) produces the softest, most ductile and workable conditions for both heat-treatable and non-heat-treatable wrought alloys. Reduction or elimination of the strengthening from cold working is accomplished by heat treatment at a temperature between ~ 250.0°C and 450.0°C for times ranging from a few seconds up to several hours. The annealing temperature should not exceed 415.0°C to avoid oxidation and grain growth. Heating and cooling rates must be controlled to avoid precipitation hardening or softening in heat-treatable alloys. Relatively slow cooling is recommended for all alloys to minimize distortion. However, for heat treatable alloys, a slow cooling rate will result in the formation of coarse precipitates. Annealing of castings is not common. However, it may be used to provide the maximum dimensional stability for elevated temperature service and additionally a high ductility. When used, the treatment involves 2 - 4 hours at 315.0°C – 345.0°C to provide the optimum relaxation of residual stresses and the formation of phases formed by any excess solute retained in solid solution in as-cast state.

Solution heat treatment

The solution treatment serves three roles:

- homogenization of the as-cast structure (similar to the homogenization);
- dissolution of certain intermetallic phases such as primary Al_2Cu and Mg_2Si;
- change of the morphology of eutectic silicon for Al-Si alloys and, as it was established in present work, the morphology of $(Al)+(Mg_2Si)$ eutectic.

It is carried out at a sufficiently high temperature for long times (from 1 to 20 hours) to produce a nearly homogeneous solid solution. The applied temperature depends on the composition and maximum solid solubility, i.e. normally heat treating slightly below the eutectic temperature. In order to avoid local melting (grain boundary melting), heating has to be sufficiently slowly to redissolve nonequilibrium precipitates and the solution heat treatment temperature must not be too high.

For instance, Al-Cu high strength casting alloys changes their two phase structure in as cast state ($\alpha - Al + \text{primary } CuAl_2$) to one phase ($\alpha - Al$) during solution treatment at 530.0°C for 20 h as it is shown in Figure 2.2.

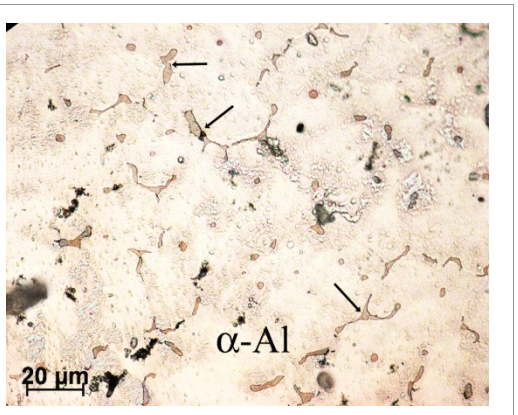

a. as-cast state, primary $CuAl_2$ *marked by arrows*

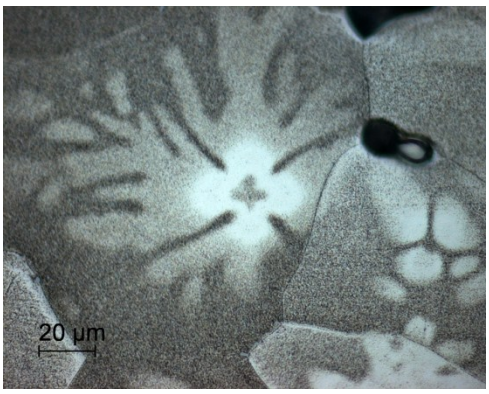

b. after solution treatment at 530 °C for 20 hours

Fig. 2.2: Microstructure of A201.0 (AlCu4.5MnAg) in as-cast state (a) and after solution treatment (b). Primary $CuAl_2$ *phase, present in cast sample, has been dissolved during solution treatment, (present work)*

Underheating results in incomplete solution and reduces the strengthening potential of the alloy while overheating leads to grain boundary melting or incipient melting and drastically reduces strength and plasticity. The solution heat treatment time depends on microstructure, section thickness and furnace loading and can vary from less than a minute to 20 hours for Al-Cu casting alloys. Generally, the soaking time for castings is longer than for wrought products due to coarser microstructures. Al-Si casting alloys with addition of strontium, sodium or antimony, undergo a rapid spheroidization of the silicon particles. For Al-Mg-Si casting alloys, solution treatment may result in $(Al) + (Mg_2Si)$ eutectic spheroidization too (see Chapter 5). However, this effect is not experimentally confirmed yet.

Quenching

Subsequent to solution heat treatment the material must be cooled at a sufficient rate to retain the solute in solid solution and to retain a high number of vacancies at room temperature. Precipitation during cooling could result in coarse particles that are detrimental for mechanical and corrosion properties. It also reduces the level of supersaturation and, therefore, the response to subsequent age hardening. Generally, the highest attainable strength levels, the best combination of strength and toughness, the best corrosion resistance and the best resistance to stress corrosion cracking are associated with the most rapid quenching rates. Quench sensitivity is generally higher for high solute levels and in alloys containing dispersoids which can act as

nucleation sites for coarse precipitates. Water is normally used as quenching agent. Components with complex shapes and with different thicknesses, such as castings and forgings, are often cooled at slower rates to avoid distortion and excessive residual stresses.

Aging

Aging is the controlled decomposition of the supersaturated solid solution to form finely dispersed precipitates in heat-treatable alloys, usually by soaking for convenient times at one or sometimes two temperature levels.

The decomposition is normally complicated and occurs through several precipitate stages which are considered in the next section for Al-Cu and Al-Mg-Si systems. These finely dispersed precipitates have a dominant effect in raising yield and tensile strengths and may also affect other properties such as corrosion resistance and dimensional stability. The age hardening response of some alloys is significantly improved by introducing a controlled amount of cold work prior to ageing, but this operation is not used for casting alloys. Some alloys retain a supersaturated solid solution and high vacancy concentration, without quenching, by rapidly cooling the material after mechanical working at elevated temperatures.

Natural aging

Natural ageing refers to the decomposition of the solid solution that occurs at room temperature. Most alloys age harden at room temperature and some alloys decompose over a few days to yield stable and adequate properties for many applications. Natural ageing is practiced industrially with alloys that display the most significant changes in microstructure and properties over a period of a few days (< 4 days), while the subsequent changes are minor. Other alloys can continue to naturally age for many years. During natural ageing the high level of supersaturation and the high vacancy concentration causes a rapid formation of clusters or coherent stable Guinier-Preston (G-P) zones. In some alloys, notably the 2XX.X series alloys, the ageing response is strongly improved, when the recently quenched material is cold worked, i.e., T3 and T4 treatments are common for these alloys.

2.2 Effect of alloying elements on the properties of aluminum casting alloys

Silicon

Binary Al-Si alloys are widely used in castings (see Table 2.1), as they possess many desirable qualities for casting, such as high fluidity (castability), low melting points, light weight,

rapid heat transfer and good surface finish. The addition of silicon increases fluidity, decreases the melting point and reduces hot tearing during solidification. The amount of silicon added depends on the casting process. Slow cooling processes such as sand and investment casting (see Chapter 1) can use alloys with silicon concentrations of 5.00 wt.% to 7.00 wt.%, while fast cooling processes, such as HPDC, utilize silicon contents of 8.00 wt.% to 12.00 wt.%. The latter alloy has a higher fluidity and lower melting point than the former. However, the strength of binary Al-Si alloys is not very high and can not be improved significantly by heat treatment. According to *[ASM04], [ASK87]*, the ultimate tensile strength of pure Al (99.9999) is 78 MPa. When 7.00 wt.% Si is added to Al, UTS increases up to 210 MPa. For alloy AlSi9, UTS is only 240 MPa after T6 heat treatment.

The commercial attraction of Al-Si cast alloys is mainly attributed to the discovery of a modification in the (Al)+(Si) eutectic system made by Aladar Pacz around 1920, *[PAC21] and [PAC35]*. He found that the brittle (Al)+(Si) eutectic changes its morphology from undesirable long plates to fine acicular fibers when small amounts of alkali fluoride, sodium or potassium are added to the melt. This ability of improving the eutectic morphology was the starting point of the popularity of Al-Si alloys.

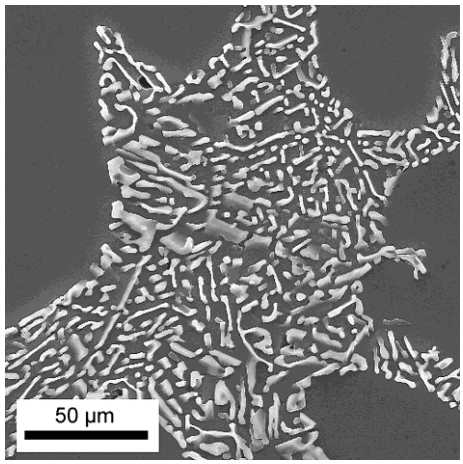

Fig. 2.3: Morphology of eutectic Si in AlSi7 alloy after addition of 0.05 wt.% Sr (deep etching), (present work)

Now foundry shops add Sr to Al-Si alloys which produces a similar modification effect as Na. As an example, in Figure 2.3 the morphology of eutectic Si in AlSi7 alloy is shown after addition of 0.05 wt.% Sr. The eutectic changes its morphology during growth from coarse plate-like (see Figure 1.17) to fine fibrous networks. According to *[TIM12a], [FAR10]* this effect is associated with the adsorption of Sr at the Al/Si eutectic interfaces on the side of the eutectic Al region. Formation of ternary Sr-Al-Si compounds and their segregation within the eutectic Si phase has been recently presented by *[TIM12b]*.

After the accidental discovery of age hardening in Al-Cu-Mg alloys by Alfred Wilm, *[WIL11]* it was proposed to add 0.20 - 0.50 wt.% Mg to Al-Si alloys for making them age-hardenable, *[WAN01]*. It was found then that the yield strength of such Al-Si-Mg alloys in T6 condition increases more than two times compared with the binary Al-Si alloy of the same Al-Si composition. After these advances, until now casting alloys of the Al-Si system are the most widespread materials in foundry shops and the A356.0 alloy containing 7.00 wt.% Si and 0.30 wt.% Mg is entitled as the ‘work horse’ for aluminum casting industry. Some details of the

microstructure of the Al-Si alloy and the solubility of Si at different temperatures are given in Appendix 2.

Copper

The aluminum-copper casting alloys typically contain between 2.00 to 5.00 wt.% Cu, with smaller additions of other elements (Mn, Ti, Ag, Mg). Addition of copper has the greatest impact of all alloying elements on strength and hardness of aluminium casting alloys. Copper provides a substantial increase in strength and facilitates precipitation hardening by the formation of $\Theta - CuAl_2$ or intermediate phases (Θ'', Θ') during the decomposition of the $\alpha - Al$ solid solution (Figure 2.4, see also Figure 2.2). In preliminary investigations performed with commercial A201.0 casting alloy, cast in permanent mold, the formation of plate-like precipitates was detected after artificial aging.

There it was found that after artificial aging at 150.0°C for 7 hours, Brinell hardness of A201.0 alloy reached 150 HB.

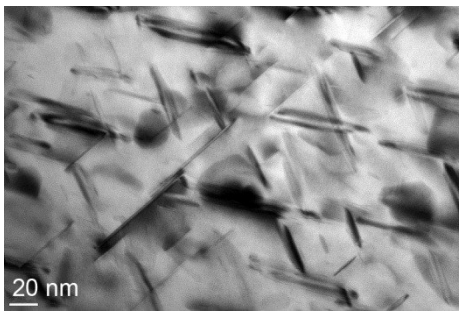

Fig. 2.4: Bright field image of plate-like precipitates of $\Theta - CuAl_2$ phase observed in A201.0 casting alloy after T6 heat treatment, (present work)

The introduction of copper can also reduce ductility and corrosion resistance, while keeping the UTS on the level of 420 - 450 MPa. The susceptibility to solidification cracking of aluminum-copper alloys is increased after additional alloying. Another drawback of Cu addition is the reduction of the corrosion resistance of Al-based alloys. Al-Cu alloys have relatively poor fluidity and resistance to hot tearing during solidification.

Manganese

The addition of manganese to aluminum increases strength somewhat by solution strengthening. In contrast to wrought alloys, where Al-Mn alloys are attributed to the 3XX.X class, the casting alloys designation system does not contain an individual position for Al-Mn alloys. The main reason to add Mn, except solution strengthening, is to change the morphology of Fe-containing phases in Al-Si or Al-Si-Mg alloys.

Fe forms with Al, Si and Mg intermetallic compounds such as $\beta(Al_5FeSi)$, $\alpha(Al_8Fe_2Si)$ and $\pi(Al_8FeMg_3Si_6)$. These iron rich phases affect the mechanical behavior, corrosion resistance and machinability of the castings, depending on their chemical composition, morphology and distribution. Especially the β-phase (Al_5FeSi) is considered to be detrimental

for the ductility of the material. This phase is appearing as needles in the interdendritic regions. They act as a stress raiser thus decreasing the mechanical properties of the cast part.

To neutralize the harmful effect of Fe-rich phases, the addition of Mn is considered the most effective and is therefore commonly used. It intensifies the formation of α-phase, which forms in the interdendritic regions as well in the $\alpha - \mathrm{Al}$ matrix and leads to the formation of quaternary $(\mathrm{Al} - \mathrm{Fe} - \mathrm{Mn} - \mathrm{Si})$ intermetallics.

It was reported by Lodgaard and Ryum, *[LOD00]* that in Al-Mg-Si wrought alloy addition of Mn results in the formation of fine-scale dispersoids. These dispersoids form during heat treatment and the proposed mechanism of their formation is heterogeneous nucleation on the so-called 'u-phase' precipitates, which also contain Mn and Si. The type of Mn-containing dispersoids is identical to the $\alpha - \mathrm{Al(MnFe)Si}$ phase. This result shows that presence of Mn in solid solution in Al-Mg-Si-type alloys may produce not only a solution strengthening effect but also the formation of Mn- and Fe-containing dispersoids. It can be expected that such a Mn behavior take place in casting alloys too but it was not reported yet.

Magnesium

The addition of magnesium to aluminum increases strength by solid solution strengthening. It is established that each weight percent of Mg added to Al increase the UTS by 50 MPa. Commercial casting alloys contain usually up to 10.00 wt.% Mg. They are corrosion resistant materials and used in marine constructions. A low level of thermal expansion is retained.

Among casting alloys, Al-Mg are not as popular as Al-Si due to certain metallurgical factors (mainly hydrogen contamination and strong tendency to oxidation). Mg addition is usually applied to make Al-Si heat treatable as mentioned above. Al-Mg alloys have a poor castability, when the magnesium content is small (2.00 - 4.00 wt.%), but becomes better with higher magnesium content (up to 12.00 wt.%).

The addition of magnesium to Al-Si alloys leads to an extremely important and useful family of compositions that combines outstanding casting characteristics with excellent properties after heat treatment. Mg is the basis for strength and hardness development in heat treated Al-Si alloys additionally alloyed with copper, nickel and other elements with the same purpose. The hardening-phase Mg_2Si displays a low solubility limit of about 0.70 wt.% Mg, beyond which either no further strengthening occurs or matrix softening takes place. The sequence of events taking place during aging of Al-Si-Mg casting alloys will be considered more in detail in the following section.

Zinc

The addition of zinc to aluminum (in conjunction with some other elements, primarily magnesium and/or copper) produces heat-treatable aluminum alloys with highest strength. Zinc substantially increases strength and permits precipitation hardening. The composition of Zn-containing casting alloys is in the range of 4.00 - 8.00 wt.% Zn and 1.40 - 2.50 wt.% Mg.

Iron

Iron is the most common impurity found in aluminum and is intentionally added to some pure (1XX.X series) alloys to provide a slight increase in strength. For casting alloys, increased Fe content is usually desirable in order to prevent die sticking. But in most cases, Fe is considered as undesired impurity, which crucially reduces alloys plasticity by formation of needle-shaped intermetallics.

Nickel

Nickel is added to aluminum-copper and to aluminum-silicon alloys to improve hardness and strength at elevated temperatures and to reduce the thermal expansion.

Transition metals (Cr, Ti, Zr) and B

Chromium is added to aluminum in order to control the grain structure, to prevent grain growth in aluminum-magnesium alloys and to prevent recrystallization in aluminum-magnesium-silicon or aluminum-magnesium-zinc alloys during heat treatment. Chromium also reduces stress corrosion susceptibility and improves toughness. It was reported by Leis *[LEI07],* that the recently developed Maxxalloy-Ultra alloy (SAG Aluminium Lend GmbH&Co) containing 0.10 - 0.30 wt.% Cr, possesses in as-cast state one of the highest strength (UTS – up to 350 MPa) among all established casting alloys.

Titanium is added to aluminum primarily as a grain refiner (see Figure 1.10). In case of hyperperitectic Ti concentrations (>0.15 wt.%), primary Al_3Ti crystals act as catalyst for the nucleation of α-Al.

Now in foundry shops, a separate addition of Ti is not utilized, because especially in Al-Si or Al-Si-Mg alloys brittle Ti-containing silicides are formed. Even if Ti is added to the Al-Si alloy in combination with B in order to produce TiB_2 or the intermediate compound AlTiB, the grain refinement effect is weak. The reason is that Si deactivates the surface of the catalyst, *[QIU07]*.

In preliminary studies, the individual addition of B to ASi7Mg alloy showed the most efficient grain refinement. Addition of 0.15 wt.% B causes a reduction of grain size more than three times and changes the morphology of $\alpha-Al$ dendrites from needle-shaped to rosette-like (Figure 2.5). In this case particles of AlB_2 act as nucleation sites for $\alpha-Al$. It was observed that addition of B to AlMg7Si3Mn alloys provides grain refinement, too.

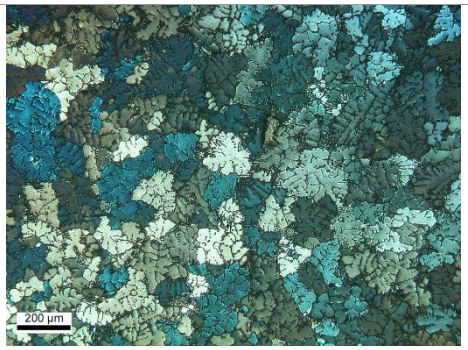

Fig. 2.5: Morphology of $\alpha-Al$ *dendrites in AlSi7Mg casting alloy after addition of 0.15 wt.% B, (present work)*

A zirconium addition is usually applied for Al-Zn-Mg and Al-Mg wrought alloys. The purpose of its addition is to replace Ti as a grain refiner and to increase the recrystallization temperature. In casting alloys, Zr addition is rarely applied because of it has a lower grain refinement potential than Ti or B.

Scandium or Scandium+Zirconium

Recently, the aluminum industry began to use scandium as a strengthening addition, mostly for Al-Mg alloys and some authors consider the Al-Mg-Sc system as a promising candidate for developing casting alloys.

Similar to other transition metals, Sc can form a supersaturated solid solution ($\alpha-Al$) upon solidification. After its decomposition during aging above 300.0°C, highly dispersed coherent cubic-shaped precipitates of Al_3Sc will be formed. Examples of such precipitates will be given in Chapter 6 for the AlMg7Si3Mn+(Sc+Zr) casting alloy.

In spite of the small amounts of Sc in aluminum alloys (not more than 0.20 - 0.30 wt.%), scientists believe it to be a "principal'' alloying element, since it can make a very significant contribution to the strengthening processes, comparable, for example, with several percentage of magnesium.

Additional to its strengthening action, Sc can effectively refine the grain structure of Al and its alloys. As an example, Figure 2.6 shows an AlScZr particle in the center of a grain in AlMg7Si3Mn alloy observed in preliminary investigations. It can be seen that the nucleation particle (marked by arrow) exhibits a cubic shape and is not homogeneous. It consists of two distinguished areas (Figure 2.6 b). The inner part is visible as dark grey, the outer shell is lighter and has a fibrous structure as known from eutectic structures. In the center of some particles, inclusions were observed thus confirming a multi-step nucleation mechanism (sections 1.3.1 and 4.4.1).

According to Kaiser, *[KAI11]* and Patakham, *[PAT12]* the addition of Sc to the Al-Si-Mg casting alloy effectively refines the $\alpha-Al$ grains.

It was found that the $\alpha-Al$ grains were initiated from the Al-Sc-Si compound. The appearance of the ternary Al-Sc-Si phase is undesirable because it reduces the Sc concentration in the α-Al solid solution and subsequently the fraction of precipitates after aging.

Currently, Al–Sc master alloys are available for the production of Sc-containing Al alloys, however, the price of Sc is high, approximately US$ 2000 per kg. This means, that the addition of 0.20 wt.% Sc, which is a fairly common content for wrought alloys, increases the price per kg alloy by US$ 4. Depending on the alloy type, Sc addition triples or quadruples the price.

A reduction of the Sc addition can be achieved by partially substituting it by Zr. This lead to an effective grain refinement at a lower Sc level, but the most prominent effect is that a refinement of the dispersoids distribution can be achieved.

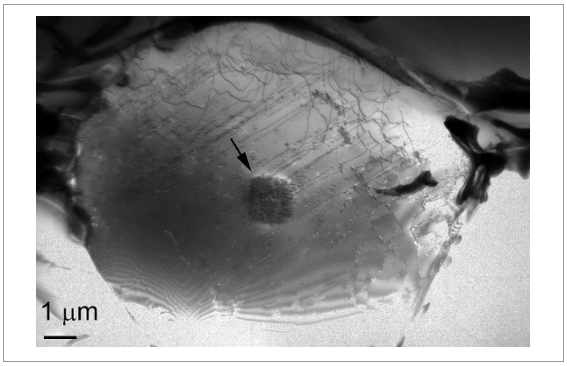

a.

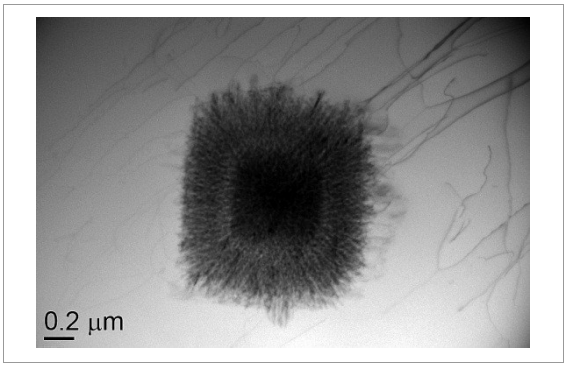

b.

Fig. 2.6: Bright field images of a $\alpha-Al$ grain in AlMg7Si3Mn casting alloy where a AlScZr particle is located in the center (a) and of the particle morphology showing two distinguished areas (b), (present work)

Lithium

The addition of lithium to aluminum can substantially increase strength and Young's modulus, provide precipitation hardening and decrease density. The density of aluminium is reduced by about 3% for each weight percent of lithium, while Young's modulus is increased by about 6%, *[LAV87]*. The reason for the improvement of the mechanical properties of Al-based alloys containing Li is precipitation hardening, caused by a large volume fraction of a metastable, ordered and coherent $\delta'(Al_3Li)$ phase with Ll_2 type superlattice structure, *[WAN05], [NIE98]*. This δ' phase has been observed in Al-Li, A1-Mg-Li, and Al-Cu-Li alloys, *[GAL87]*. In A1-Cu-Li alloys, additional strengthening is achieved by the co-precipitation of copper-rich phases' independent of the $\delta'(Al_3Li)$ precipitation, *[SAT03]*. In high copper - low lithium alloys (3.00 to 4.50 wt.% Cu, 1.00 to 2.00 wt.% Li), the decomposition of the

supersaturated solid solution (α_{SS}) occurs by the reactions:

$$\alpha_{SS} \rightarrow \delta'(Al_3Li) \rightarrow \delta(AlLi) \tag{2.1}$$

simultaneously with

$$\alpha_{SS} \rightarrow G-P\ Zone's \rightarrow \Theta'' \rightarrow \Theta' \rightarrow \Theta(Al_2Cu) \tag{2.2}$$

In A1-Mg-Li alloys, Mg not only acts as a solid solution strengthener, but it also decreases the solubility of lithium in aluminum, resulting in an increase of the volume fraction of $\delta'(Al_3Li)$. It has been found, *[LAV87]* that the ageing sequence for A1-Mg-Li alloys is:

$$\alpha_{SS} \rightarrow \delta'(Al_3Li) \rightarrow S_1(Al_2MgLi) \tag{2.3}$$

According to *[NIE98]*, the subsequent formation of Al_2MgLi consumes nearby $\delta'(Al_3Li)$ particles and therefore the reaction $\delta'(Al_3Li) \rightarrow \delta(AlLi)$ is suppressed. Under equilibrium conditions, A1-Mg-Li alloys with a Mg/Li ratio in the range of 2.5 to 1.5 form the phase Al_2MgLi.

Conclusively, the significant reduction in density and enhancement of the elastic modulus by Li addition have generated and maintained a large interest in the A1-Li family of alloys. However, until now not a single casting alloy was developed. There is only one report of Saurman et al. *[SAU05]* on the development of Al-Li casting alloy for transportation applications. It was found that the static properties in the as-cast condition are comparable to the conventional AlSi7Mg0.3 semi-solid standard alloy in T6 heat treatment condition, but related to the density the investigated Al-Li alloys have better strength to weight ratios. Therefore further potential in improving mechanical properties can be expected after heat treatment of the Al-Li-Mg precursor material.

A disadvantage is, that the addition of Li to established Al-Si casting alloys could lead to the formation of undesired silicides (for example, Li_6Si_2), as found for the transition element (Ti, Zr). However, the Al-Mg-Si system, considered in chapters 4, 5 and 6, has only a small Si content (less than 0.10 wt.%) in solid solution and therefore it could be a potential candidate for developing casting alloys with reduced density.

Germanium

Despite of the exotic nature and small industrial application, Ge now is considered as the prospective alloying element for aluminum alloys. This statement is based on the similarity of Ge to Si and its ability to form strengthening precipitates after addition to Al-Si or Al-Mg alloys.

Authors, *[MUK00]* reported that such successful alloys are age hardenable. Their advantage is the ease of formation and the stability of the solute-rich clusters/G-P zones. The

concept, called the "± effect" in aluminum alloy design, is, that in a ternary alloy where one solute atom is smaller and the other larger than the matrix atom, less lattice strain is produced by the formation of clusters containing both solute atoms.

In the early 1990s, Hornbogen et al. *[HOR93]* utilized this concept to come up with ternary Al-Ge-Si alloys. Radmilovich et. al. *[RAD03]* showed, that binary Al-Si and Al-Ge and ternary Al-Si-Ge systems are interesting choices for studying the crystallography of precipitation, since the hardening precipitates have a diamond cubic structure and exhibit a variety of shapes and orientation relationships including complex, twinned morphologies.

In the work of Marioara et. al., *[BJO10]* two ternary Al-Mg-Ge alloys were analysed using TEM and HR-TEM. It was shown that the hardness of Al-Mg-Ge alloys is achieved mostly through precipitate phases that are finer than usually in the Al-Mg-Si system. It was concluded that the hardening effect of a precipitate depends more on its coherent interface with the Al matrix than on the precipitate structure itself. They also pointed out that coherency depends strongly on the content of Ge or Si, whereas the precipitate structure seems to remain the same.

Development of commercial Al-Mg-Ge alloys is yet in the progress. Combining information's of the established ternary Al-Mg-Ge phase diagram, namely the high eutectic melting temperature of 626.0°C and the ability of precipitation strengthening, these alloys could provide strong competition to existing commercial casting materials.

Aluminum+Magnesium+Silicon

The alloys of the Al-Mg-Si system are the most popular ones for wrought materials. Two main reasons of their popularity are low cost due to low content of alloying elements (usually up to 1.00 wt.% of each Mg and Si) and the ability to be precipitation strengthened. The last decade showed growing interest from the foundry industry for this Al-Mg-Si system. Therefore the current investigations have high industrial relevance.

The history of Al-Mg-Si casting alloys dates back to the 1938 when they were used for casting air cooled diesel engine blocks. However, since that there were no information about neither successful nor unsuccessful application of this casting alloy in practice and hence, the 6XX.Xth series of aluminum casting alloys was not very popular. Only little research in this field can be found from literature *[PIR90], [PIR93]*. The renaissance of the Al-Mg-Si casting alloys began in 1996 when the "Aluminium Rheinfelden GmbH" represented to the market on Al-Mg-Si-type alloy under the brand name Magsimal®-59 *[KOC96], [KOC03], [KOC06]*. After this, every producer of aluminum castings worldwide designed at least one casting alloy with a similar composition. The compositions of existing Al-Mg-Si

casting alloys are summarized in Table 2.3. Foundry alloys usually contain five to six weight percent Mg and two percent of Si. Alloying by Mn is also used.

Table 2.3: Composition of commercial aluminum casting alloys based on Al-Mg-Si system, [KOC00], [RHE07], [RHE08], [JOR08], [SAG05]

nominal composition	average elements content, wt.%						
	Si	Mg	Mn	Cu	Zn	Ti	Fe
Aural 11 (Rio Tinto Alcan), *[JOR08]*	2.00	5.00	0.50	0.03	-	0.05	0.17
Maxxalloy-59 (Salzburger Aluminium Group SAG), *[JOR08]*	2.00	5.00	0.80	0.02	0.10	0.20	0.20
Maxxalloy-ULTRA* (Salzburger Aluminium Group SAG), *[SAG05]*	2.60	5.90	0.70	0.02	0.07	0.10	0.20
Magsimal 59 (Aluminium Rheinfelden GmbH), *[RHE07]*	2.00	5.00	0.65	0.05	0.07	0.20	0.20

* - contains rare earth elements and 0.10 - 0.30 wt.% Cr

It was reported that together with high ductility, yield strength and ultimate tensile strength (see Section 1.2), Al-Mg-Si alloys display several advantages in comparison to commercial Al-Si-Mg casting alloys, *[KOC03]*. There are:

- high corrosion resistance even in sea water;
- ability to be connected to surrounding parts by gluing, selfpiers-riveting and MIG-welding;
- good fluidity, no sticking to die;
- alloys subjected to high pressure die casting (HPDC) are ‘naturally hard’. The cast parts can be assembled with the other structures in temper F without additional heat treatment.

To satisfy increasing demands for light weight constructions, several variations of the AlMg5Si2 alloy were developed. It was reported that addition of Co, Cr and rare earth elements to AlMg5Si2Mn alloy (Maxxalloy-ultra) lead to improved tensile properties comparable with forged products. In 2006, the AlMg3SiMn alloy containing Sc was patented, *[KOC06]*.

However, in spite of the advanced use of Al-Mg-Si alloys in foundry shops, the mechanisms responsible for their ‘natural hardening’ and the change of the properties during heat treatment are yet uncovered and will be investigated in present work.

To sum up, there are many aluminum alloys used in foundry today - over 200 casting

alloys are currently registered worldwide and until now Al-Si-Mg are the most popular one. Table 2.4 summarizes the chemical and phase compositions of Al-based casting alloys, their eutectic melting temperatures and the strengthening phases formed after heat treatment. A further improvement of their properties via additional saturation of the solid solution is rather difficult because it simultaneously reduces the applicability of the alloys for casting by different processes. Under this aspect, the relatively young Al-Mg-Si system is the most promising candidate for advanced use in foundry shops.

Table 2.4: Chemical and phase composition of commercial casting alloys and their strengthening phases formed after solution heat treatment, quenching and aging

	system	Si wt.%	Mg wt.%	Cu wt.%	Zn wt.%	phase composition	T_e, °C	strengthening phases
1	Al-Si	4.5-13	-	-	-	(Al) + (Si)	577	-
2	Al-Si-Mg	6-11	0.1-0.6	-	-	(Al) + (Si) + Mg_2Si (β)	555	β", β'
3	Al-Mg-Si	1.0-2.5	2.5-5.5	-	-	α – Al + (Al) + (Mg_2Si)	595	β", β'
4	Al-Si-Cu	7-13	-	1.5-5	-	(Al) + (Si) + $CuAl_2$ (Θ)	525	Θ", Θ'
5	Al-Si-Cu-Mg	4-23	0.2-1.1	0.5-8	-	(Al) + (Si) + $CuAl_2$ (Θ) + $Al_5Cu_2Mg_8Si_6$ (W)	505	Θ", Θ', β", β', S(Al_2CuMg)
6	Al-Si-Cu-Mg-Zn	6-10	0.1-0.5	0.3-1.5	5-12	(Al) + (Si) + $CuAl_2$ (Θ) + $Al_5Cu_2Mg_8Si_6$ (W)	505	Θ", Θ'
7	Al-Cu	-	-	3.5-11	-	α – Al + Al_2Cu	548	Θ", Θ'
8	Al-Mg	-	2,5-12	-	-	α – Al + Al_8Mg_5	450	
9	Al-Mg-Zn	-	0.5-2.4	-	2.5-6.5	α – Al + Mg_2Zn (η) + Al_3Mg_2Zn (T)	475	η, η', T'
10	Al-Mg-Zn-Cu	-	1.5-2.5	0.4-1.5	5-8	α – Al + M – phase *+ Al_3Mg_2Zn (T)	475	η, η',

* - M – phase is quaternary solid solution between CuMgAl and Mg_2Zn (η)

2.3 Strengthening mechanisms in aluminium casting alloys

Al alloys for structural applications are rarely strengthened by one hardening mechanism only. Table 2.5 gives a summary of the elementary strengthening mechanisms operating in Al.

Table 2.5: Elementary strengthening mechanisms in Al

	mechanism	obstacle	designation	mathematical term	dimension of density	geometric dimension
(i)	Solid solution strengthening	Solute atom	C	$\Delta\sigma_0 = \Delta\sigma_{SS}$	m^{-3}	0
(ii)	Work hardening, substructure hardening	Dislocation	ρ_D	$\Delta\sigma_1 = \Delta\sigma_D$	m^{-2}	1
(iii)	Grain size strengthening	Grain boundary	GSS*	$\Delta\sigma_2 = \Delta\sigma_{GRS}$	m^{-1}	2
(iv)	precipitation strengthening	Particle, pore	f_P	$\Delta\sigma_3 = \Delta\sigma_p$	m^0	3
(v)	Texture strengthening	Crystal anisotropy		$\Delta\sigma_A$	-	-
(vi)	Fibre reinforcement	Discontinuous and continuous fibres (eutectic lamellas)		$\Delta\sigma_M$	-	-

* - Grain Size Strengthening (GSS)

The main difference between wrought and casting alloys is that the casted part can not be subjected to deformation. Thus reduction of grain size by plastic deformation, work hardening, substructure hardening and texture strengthening are not mechanisms operating in cast parts.

The final properties of a certain cast alloy are exclusively the result of the cooling of the melt in the mold cavity and the following heat treatment. Thus the number of strengthening mechanisms available for casting alloys is the combination of four mechanisms only: (i), (iii), (iv) and, for eutectic-type alloys, (vi).

The four major strengthening mechanisms can be classified according to Table 2.5 by the obstacles which impede gliding (and/or climbing) of dislocations. The resulting tensile yield strength σ_y is the sum of these mechanisms together with the yield strength of pure aluminum $\sigma_\perp$:

$$\sigma_y = \sigma_\perp + \sum \Delta\sigma_i = \sigma_\perp + \Delta\sigma_0 + \Delta\sigma_2 + \Delta\sigma_3 + \Delta\sigma_M \qquad (2.4)$$

$\Delta\sigma_0$ comes from solid solution strengthening, $\Delta\sigma_2$ from grain size strengthening, $\Delta\sigma_3$ from precipitation strengthening and $\Delta\sigma_M$ from the eutectic (intermetallic) lamellae.

The quantitative understanding of the high yield strength σ_y of aluminum alloys was developed by Hornbogen et al. *[BLA93], [HOR93], [STA92]*. It is based on the differentiation between "hard" and "soft" obstacles (Table 2.6). The criterion for the classification is whether glissile dislocations are bent to semicircles or not. They are not bent to semicircles in pure aluminum, aluminum solid solutions and alloys containing only shearable precipitates. The addition of "hard" obstacles causes dislocations to loop and bypass the nonshearable particles.

Table 2.6: Examples of "hard" and "soft" obstacles in Al, [HOR93]

"hard" obstacles	"soft" obstacles
particles having dimensions $d^{1} > d_C{}^{2}$	particles having dimensions $d < d_C$ short range order, clusters
pores	solute atoms, vacancies
sessile dislocations	antiphase domain boundaries

1- particle diameter,

2- critical diameter of particle

An illustration of the different strengthening mechanisms operating in casting alloys, obtained by tensile tests combined with scanning microscopy, is given in Figure 2.7. The initial structure of the commercial A356.0 (AlSi7Mg) casting alloy solidified in a permanent mold and T6 heat treated consists of $\alpha - Al$ and $(Al) + (Si)$ eutectic, in form of rounded Si particles. At the points 1, 2 and 3, the tests were paused and the structure condition was imaged.

The spheroidisation of (Si) took place during solution treatment and will be considered in the Chapter 5. At point 2, σ=184 MPa, (Si) particles are already 'cracked' (Figure 2.7 b) confirming that they are brittle. Beyond this stress level, only the strength of the dispersion strengthened matrix $\alpha - Al$ defines the final properties of the alloy. This example shows that two strengthening mechanisms are most important for eutectic-type aluminum casting alloys, namely solid solution and dispersion strengthening. These will be briefly considered in following sections.

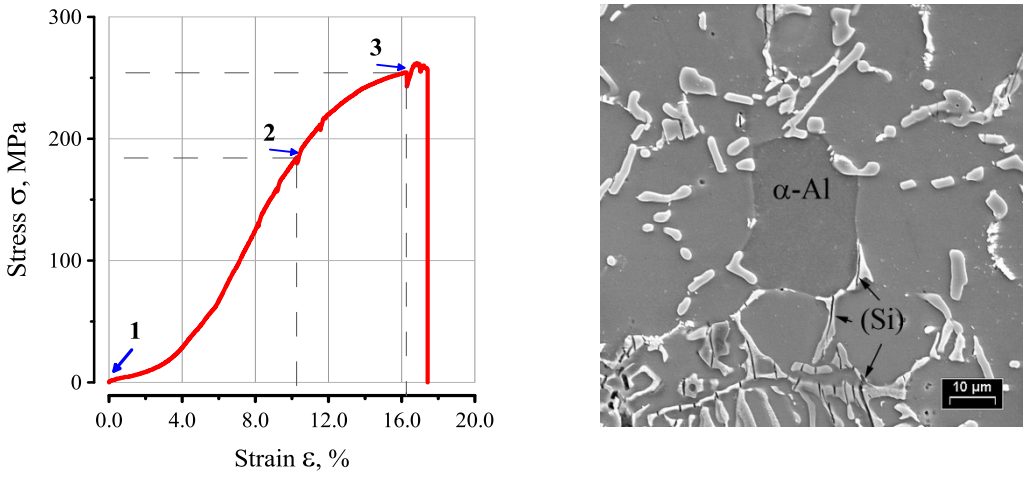

a. *b.*

Fig. 2.7 Stress-strain curve of T6 A356.0 (AlSi7Mg) casting alloy (a) and structure condition at point 2 (b) (cracking of eutectic Si is marked by arrows), (present work)

Grain size strengthening is also operating in casting alloys, but for eutectic alloys with relatively high eutectic volume fraction, the contribution of this mechanism is less pronounced.

2.3.1 Solid solution strengthening

Solid solution strengthening has mostly to do with the composition, not with casting. Individual atoms of the alloying element, which are dissolved in the melt lead to lattice distortion during solidification.

If the alloyed atom takes the place of a normal atom, it is called a 'substitutional defect'; smaller atoms put the crystal lattice into tension, larger atoms into compression. Atoms much smaller than the majority atoms take positions between the lattice points and are called 'interstitial defects'.

The solid solution hardening is the result of an interaction between the mobile dislocations and the solute atoms. In any case, the distortions of the crystal lattice act as 'pinning points', i.e. restrict the motion of dislocations, thus strengthening the material. A huge amount of work was done on the solid solution hardening of Al alloys in the 1950's and 1960's. Classic reviews on solution hardening are represented by Fleischer *[FLE61], [FLE63]* and more recently by Haasen, *[HAA96]* and Nes, *[RYE06]*. Table 2.7 gives a summary of Al-based binary systems, the solubility of the main alloying elements at different temperatures and the type of solid solution formed.

According to Ryen et al., *[RYE06]* the most relevant mechanisms for substitutional alloying of aluminum are the elastic interactions, having two reasons. (1) The size misfit: the size of the solute atom differs from the size of the matrix atoms and creates a strain field around the

atom. (2) The modulus misfit: the difference in the binding force between the solute atoms and the matrix atoms results in a hard or soft ‘‘spot’’ in the matrix.

Table 2.7: Summary of major alloying elements used for aluminum alloys, their solubility at different temperatures and their classification, [MON76]

system	eutectic (e) or peritectic (p) temperature, °C	maximum solubility, at.%	
		at eutectic/peritectic melting point	at 293 K
		high soluble	
Al-Zn	380.0 (e)	88.70	66.40
Al-Mg	450.0 (e)	16.26	37.30
Al-Cu	548.0 (e)	17.39	2.40
Al-Si	577.0 (e)	12.16	1.60
Al-Mn	660.0 (p)	0.97	0.90
Al-Ge	425.0 (e)	29.50	2.30
Al-Li	600.0 (e)	30.0	13.90
		low soluble	
Al-Ti	665.0 (p)	0.084	0.50
Al-Zr	660.0 (p)	0.033	0.09
Al-Cr	660.0 (p)	0.21	0.40
Al-Sc	660.0 (e)	0.31	0.20
Al-Fe	655.0 (e)	0.91	0.03

2.3.2 Strengthening due to decrease of grain size

It is commonly accepted that a structure consisting of fine equiaxed grains gives the best combination of strength and ductility. First, because fine grains result in a high grain boundary surface area. Second, because fine grains cause a more uniform distribution of grain boundary precipitates. Coarse grain structure and columnar grains, forming in a high thermal gradient, are no favorable structures. At room temperature, hardness, yield strength, tensile strength, fatigue strength and impact strength, all increase with decreasing grain size. Machinability is also affected; rough machining favors coarse grain size while finish machining favors fine grain size.

E.O.Hall and N.J.Petch have derived the following relation, famously known as Hall-Petch relation, between yield strength σ_y and grain size d:

$$\sigma_y = \sigma_i + Kd^{-\frac{1}{2}} \tag{2.5}$$

where σ_i is the ‘friction stress’, representing the overall resistance of the crystal lattice to dislocation movement, i.e. the stress needed to move unlocked dislocations along the slip plane, K is the ‘locking parameter’ that measures the relative hardening contribution of the grain

boundaries. It is important to note that the above relation is not valid for both, very large grains and extremely fine grains, *[CAN12]*.

The grain size strengthening mechanism is based on the fact that crystallographic orientation changes abruptly in passing from one grain to the next across the grain boundary. Thus it is difficult for a dislocation moving on a slip plane in one crystal to pass over to a regarding slip plane in the other grain, especially if the orientation is very misaligned. As an example dislocations fixed by a grain boundary are represented on Figure 2.8.

Grain refinement of Al alloys is a conventional foundry practice. Applied to casting alloys, it gives not only an improvement of the mechanical properties but also improves feeding during solidification, reduces porosity and makes it more evenly distributed and finally reduces hot tearing.

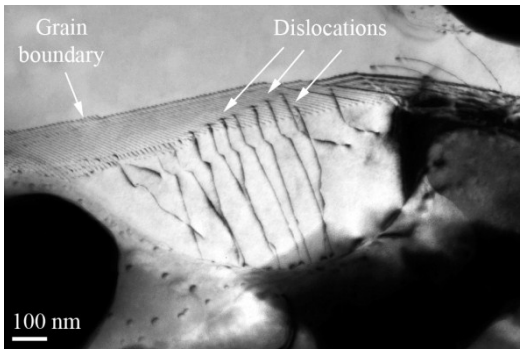

Fig. 2.8: Sticking of dislocations on the grain boundary in AlMg7Si3Mn casting alloy in as-cast state, (present work)

Strengthening associated with reduction of grain size is very important for single phase casting alloys such as Al-Cu and Al-Mg. Reduction of grain size can be achieved through the chemical grain refinement via addition of Al-Ti-B master alloys to the melt which brings potent TiB_2 nucleation particles to the melt.

For eutectic alloys with eutectic volume fractions in the range of 35 - 50 vol.%, the grain boundary is rather small. The grains of $\alpha - Al$ are decorated by eutectic colonies.

2.3.3 Precipitation strengthening

By Alfred Wilm, strengthening of Al alloys due to the formation of small particles during natural aging has been discovered.

The present understanding of precipitation hardening is that small second-phase particles distributed in a ductile matrix can hinder the dislocation motion and thus increase the strength of a material. Second-phase particles either can be introduced by mixing and consolidation (dispersion strengthening) or precipitated in solid state (precipitation hardening). Precipitation hardening or age hardening is produced by solution treating and quenching an alloy. The term 'Age hardening' is used to describe the process because strength develops with time. Prerequisite for precipitation hardening is that the second phase must be soluble at an elevated temperature but that it precipitates upon quenching and aging at a lower temperature. If the precipitation occurs at normal ambient temperatures, it is called natural aging. Some alloy systems need to be

aged at higher temperatures and this process is known as artificial aging.

Dislocations moving through the matrix, which is precipitation hardened, have two alternatives. They can either cut through the precipitate particles or bend around and bypass them. The first alternative is possible only when the slip plane is continuous from the matrix through the precipitate particle and when the stress to move a dislocation in the precipitate is comparable to that in the matrix. Cutting of particles is easier for small particles which can be considered as segregated solute atoms. Cutting is not possible if there is an interface or an abrupt change in orientation. Under such instances, dislocations have to bend around the particle and bypass. This situation is known as the bypass mechanism or the so-called Orowan mechanism which is sketched on Figure 2.9. The stress, required to bend a dislocation, is inversely proportional to the average interspacing λ of the particles in the matrix. A simple expression for the interspacing λ of particles is:

$$\lambda = \frac{4(1-f)r}{3f} \tag{2.6}$$

where f is the volume fraction of spherical particles with radius r.

The two segments of the dislocation line at either end of the precipitate attract each other and finally this constriction leads to the advancement of the dislocation line and a dislocation loop around the particle.

The critical shear stress can be given:

$$\tau_c = \frac{2E_L}{bL} \tag{2.7}$$

where τ_c is the shear stress, E the dislocation line energy necessary for the dislocation to bulge between two obstacles, L the obstacle spacing, and b is Burgers vector.

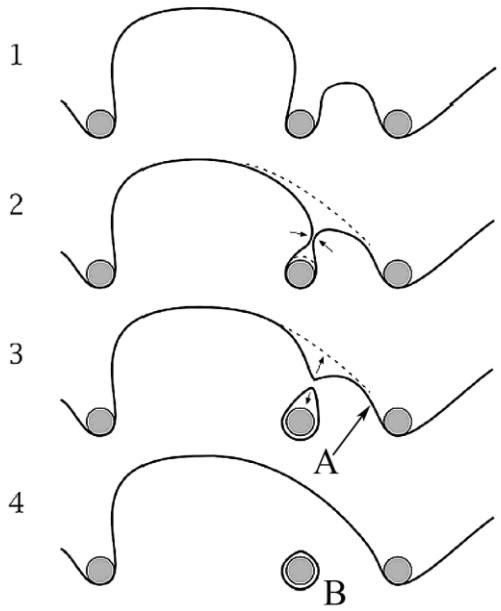

Fig. 2.9: The Orowan mechanism. Labels 1, 2, 3, and 4 show the dislocation bulging out between the precipitates, [FRE12]

The two segments of the dislocation line at either side of the precipitate attract each other, join and annihilate. So the dislocation splits into a line, which proceeds (A) and a line (B), which is fixed by the obstacle.

A typical one-peak precipitation-strengthening curve consists of two stages, as shown in Figure 2.10. In Stage I, the resistance of a precipitate against dislocation cutting results in strength increase. In Stage II, over aging leads to an increase of L. Now the dislocation is forced to loop around the precipitate and the yield strength decreases. The term

'strengthening' is used to describe the strength increase in Stage I — the underaging period, and 'softening' for Stage II — the overaging period.

Precipitate growth and coarsening both need solutes from the surrounding matrix. The coarsening of larger precipitates takes place by dissolving smaller particles.

Age hardening occurs in alloys for which the solubility of the alloying element in the matrix material increases with increasing temperature. When, for example, the Al-Cu alloy contains 2.00 at.% Cu and the alloy is kept at a temperature of 540.0°C (the eutectic temperature in the Al-Cu system is 548.0°C), all copper atoms will eventually dissolve in aluminum. On macroscale, this can be seen in Figure 2.2, namely the transformation from a two phase structure in as-cast state to a one-phase structure after quenching. When this solid solution is cooled down slowly, the formation of $CuAl_2$ precipitates will start at a temperature of around 500.0°C. When room temperature is reached, the system will contain very large $CuAl_2$ precipitates in thermal equilibrium with the aluminum matrix. However, if the solid solution is quenched very rapidly from 550.0°C to room temperature, there will be not sufficient time for precipitation and a super saturated solid solution (SSSS) is obtained. This super saturated solid solution is not energetically stable and it decomposes initially to clusters where solute atoms are segregated. This process leads to G-P zones and represents the early stage of aging. A detailed review about the structure of G-P zones for the Al-Mg-Si system is given by *[MAT98]* and for the Al-Cu system by Fine, *[FIN75]*.

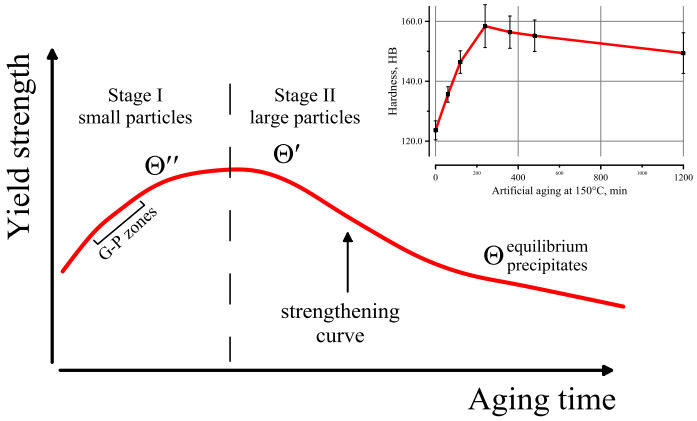

Fig. 2.10: A typical one-peak aging curve. Evolution of precipitates is shown for a Al-Cu alloy where $\Theta - CuAl_2$ forms during aging, [FIN75]. Inserted frame is the change of hardness of A201.0 commercial casting alloy during artificial aging at 150.0℃

When the time is sufficient for diffusion, Cu in Al-Cu alloys or Mg and Si in Al-Mg-Si alloys will eventually form copper aluminide or magnesium silicide precipitates. In the Al-Cu and Al-Mg-Si systems, the sequence of precipitation is different, but they have certain common features which are summarized in Table 2.8. The decomposition of a supersaturated solution starts with clustering of silicon atoms. Coherent G-P zones are forming, which are rather stable and can exist up to 260.0ºC. The next stage of ageing is the formation of a rod like intermetalic phase, so-called β" and β' particles. These particles are semi-coherent and the

rod axes are parallel to ⟨001⟩. As final stage, the Mg_2Si phase (β) is formed as incoherent platelets. In Al-Cu systems, four stages of crystal structure transformation can be observed *[GIE06], [GUO05]*. The density of G-P zones can be up to 10^{17} - 10^{18} for cm^{-3}.

Table 2.8: Precipitation sequence established for Al-Cu alloys, [FIN75] (All tetragonal lattice)

$\alpha - Al_{SSSS}$	⇨	vacancy-rich G-P zones	⇨	Θ"	⇨	Θ'	⇨ Θ
				disk-like precipitates		disk-like precipitates	$CuAl_2$
				coherent		coherent/incoherent	equilibrium

Natural aging in Al-Mg-Si wrought alloys is still a matter of many controversies (see for example Banhart, *[BAN10]*). The aging of casting alloys directly from as-cast state is represented in literature by single publications, for example by *[CHA77]*.

2.4 Summary

The presented review shows the current understanding of the effect of alloying elements on the properties of casting alloys together with an analysis of the possible strengthening mechanisms relevant for these alloys.

A large quantity of research was published on the effect of processing and heat treatment of Al-Si-Mg casting alloys, showing that the maximum strength can be achieved only after heat treatment. Recently developed Al-Mg-Si casting alloys became very popular in foundry since they can be used in as-cast state and sometimes referred as ‘naturally hard’. In this case the term ‘naturally hard’ means that their solid solution matrix tends to decompose at room temperature and forms secondary precipitates which act as strengthening phase. However, experimental proof of this effect has not been presented yet. It has to be noticed, that these alloys are subjected usually to high pressure die casting. This is interesting, because the high cooling rates typical for HPDC provide the best mechanical properties of the material. With conventional casting such properties cannot be attained after solution treatment, quenching and aging in spite of intensive research.

From the other hand, the decomposition of the solid solution and the formation of precipitates in wrought alloys, especially during heat treatment, are well established. The formation of secondary phases in casting alloys should not differ strongly from that in wrought alloys since the alloying elements are the same. It was shown that Sc addition provides effective strengthening of the Al alloys but it is not applied for casting alloys yet. The situation is similar

regarding the alloying of Al alloys by Li. Until now, no Li-containing casting alloy was developed. The established ability of Al-Mg-Ge alloys to precipitation strengthening together with the high eutectic melting temperature indicates the high potential of this system for the design of new casting alloys, especially for elevated temperature applications.

Combining the information from the 1st and 2nd Chapters the goals of the present research can be summarized as follows:

- analysis of the structure of Al-Mg-Si and Al-Mg-Ge casting alloys in as-cast state together with its change during solution treatment and aging;
- measurement of the composition of solid solution in as-cast state and its variation during solution treatment and artificial aging;
- finding the reason of the high mechanical properties of Al-Mg-Si casting alloys in as-cast state and discovering their changes during solution treatment and aging;
- investigation of the morphology and type of the secondary precipitates in Al-Mg-Si and Al-Mg-Ge during heat treatment.

3 Materials and Methods

3.1 Alloys selection and alloys composition

The promising potential of Al-Mg-Si and Al-Mg-Ge systems was briefly represented in Chapters 1 and 2.

3.1.1 Al-Mg-Si phase diagram

The most substantial overviews on Al-Mg-Si phase diagram were represented by Mondolfo *[MON76]*, Kumar et al. *[KUM00]*, Barabash *[LIS97]* and Fan et al. *[ZHA01]*. The aluminum rich side of the Al-Mg-Si phase diagram is shown in Figure 3.1 and Table 3.1 represents the invariant phase equilibria. According to *[KUM00]*, exclusively Al solid solution and Mg_2Si intermetallic phase equilibrium phases were observed, but no ternary phases.

The most important feature of the Al-Mg-Si system is the existence of a pseudobinary section. This line in the ternary phase diagram can be defined as a vertical section between a congruently melting binary compound, Mg_2Si on one face and Al on the other, where congruent melting defines that the composition of liquid and solid phase is the same. In other words, the ternary system might be considered as binary.

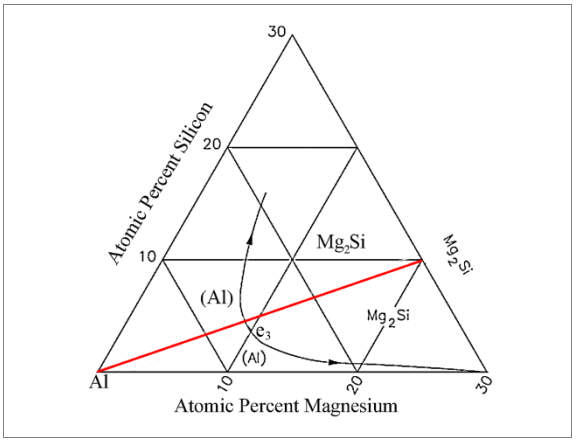

Fig. 3.1: Al-Mg-Si diagram with pseudobinary line (red) and experimentally established invariant line of L → (Al) + Mg_2Si (dashed), *[BAR01]*

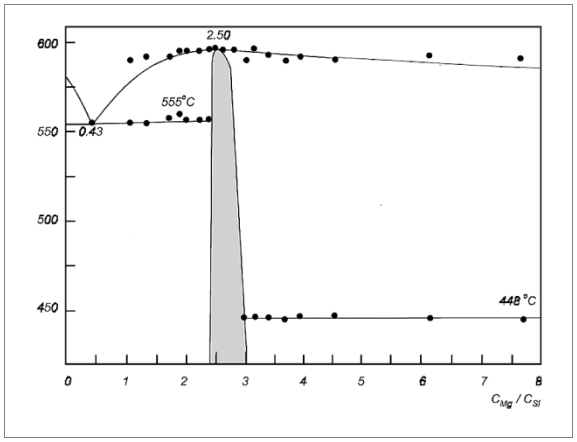

Fig. 3.2: Conditions of the eutectic transformation L → (Al) + Mg_2Si. The area of the two-phase eutectic is restricted by $\text{at.\%Mg}/\text{at.\%Si} = 2.4-3.0$ *(grey area), [BAR00]*

As shown by Barabash *[BAR01]*, the point where the solidification range of $\alpha(\text{Al})-Mg_2Si$ eutectic equals zero does not lie on the pseudobinary line of $\text{Al}-Mg_2Si$ (Figure 3.1, red line), defined by the composition ratio $\text{at.\%Mg}/\text{at.\%Si} = 2$, but is shifted to the Mg-rich side (Figure 3.1, dashed line). The temperature of the pseudobinary eutectic is 597°C according

to *[BAR01]*. For the eutectic alloy, the Mg/Si ratio is 2.49. All alloys having Mg/Si ratios between 2.40 to 2.48 are hypoeutectic. Their phase composition should be $\alpha - Al$ and $\alpha - Al + Mg_2Si$ eutectic. Hypereutectic alloys have the Mg/Si range of 2.51 to 3.00 and their structure consists of α-Al solid solution matrix, eutectic and primary Mg_2Si crystals.

Table 3.1: Invariant phase equilibrium in Al-Mg-Si system, [KUM00]

reaction	temperature, °C	type	phase	composition, at.%		
				Al	Mg	Si
$L \rightarrow (Al) + Mg_2Si$	594	e_3	L	85.30	10.80	3.90
			(Al)	97.10	2.70	0.20
			Mg_2Si	0	66.70	33.30

Based on the presented analysis, for further elaboration the two hypereutectic alloys (namely A1 and A2 in Table 3.3) and one hypoeutectic alloy (namely A3) were selected in order to establish the behavior of all three phase constituents during solidification, solution treatment and aging. The compositions of the Al-Mg-Si alloys selected for the investigation are presented in Table 3.3.

Alloying of casting alloys by manganese provides a solution strengthening effect and is the common practice in foundry shops. Simultaneously, it was found that during heat treatment of 6XXX wrought alloys, they tend to form Mn-containing dispersoids (section 2.2, *[LOD00]*). This effect was not considered for casting alloys up to now. In order to establish this effect for Al-Mg-Si alloys, the addition of Mn was included into the research program (alloys A2 and A3, Table 3.3).

It was shown in chapter 2 (section 2.2) that Li addition to Al-based alloys, effectively improves their strengths by formation of fine precipitates. Established Li-containing alloys are commonly based on Al-Mg and Al-Cu binary systems and are used for extrusion or rolling. Until now there were no commercial Li-containing casting alloys developed. Hadian et al., *[HAD08]* found that Li addition to a Al-15.00 wt.% Mg_2Si alloy provides a reduction of the size of the primary Mg_2Si crystals, changes the eutectic morphology and increases the of UTS and elongation. According to Pan *[LIS01]*, Li additions widen the range for $Al(Li) - Mg_2Si$ eutectic, which suppresses the appearance of ternary eutectic efficiently.

Because the formation of undesirable silicides is less probable in Al-Mg-Si alloys than in Al-Si alloys, Li was added to Al-Mg-Si alloys. Two Li-containing alloys (namely B1 and B2 in Table 3.3) were investigated with a Li level of 0.50 and 1.00 wt.%.

The double effect of Sc+Zr on the structure formation of aluminum alloys is well known and established for wrought alloys. As it was shown in section 2.2, the addition of Sc without Zr to Al-Si casting alloys is not effective as grain refiner. In the work of Mykhalenkov et al. *[MYK10]* it is shown that the addition of Sc+Zr to the Al-7.70at.%Mg-2.80at.%Si-0.30at.%Mn

casting alloy promotes the formation of a fine grained structure due to the nucleation of $\alpha-Al$ grains by a $Al_3(Sc_{1-x}Zr_x)$ primary compound. Annealing of the alloy at 300°C during 10 hours resulted in the formation of fine cube shaped $Al_3(Sc_{1-x}Zr_x)$ precipitates indicating the ability of the alloy to be age hardened. Based on the strong potential of Sc+Zr addition for the strength of aluminum alloys, two alloys containing 0.20 wt.%Sc + 0.20 wt.% Zr, and 0.22 wt.%Sc + 0.14 wt.% Zr were subjected to the research program (C1 and C2 in Table 3.3).

3.1.2 Al-Mg-Ge phase diagram

The ability of Al-Mg-Ge alloys to form strengthening particles during the decomposition of the solid solution was shown by Marioara et al. *[BJO10]*, as presented in section 2.2.

Exceptional however is, as recent studies of Islam et al. *[ISL06]* showed, that this system is rather similar to Al-Mg-Si: it belongs to the eutectic type with an calculated eutectic melting point of 632°C (Table 3.2), which is almost the highest melting temperature among commercial Al-based alloys. Likewise the Al-Mg-Si system, the Al-Mg-Ge system (Figure 3.3) has a pseudobinary section in the aluminum corner, i.e. the structure of potential casting alloys can be predicted as: $\alpha-Al$ and $\alpha-Al+Mg_2Ge$ eutectic. Because of the high eutectic melting temperature and the ability to form nano-scale precipitates, two Al-Mg-Ge alloys were investigated, one with Mn addition, and the other one with Mn and Li additions (D1 and D2 in Table 3.3).

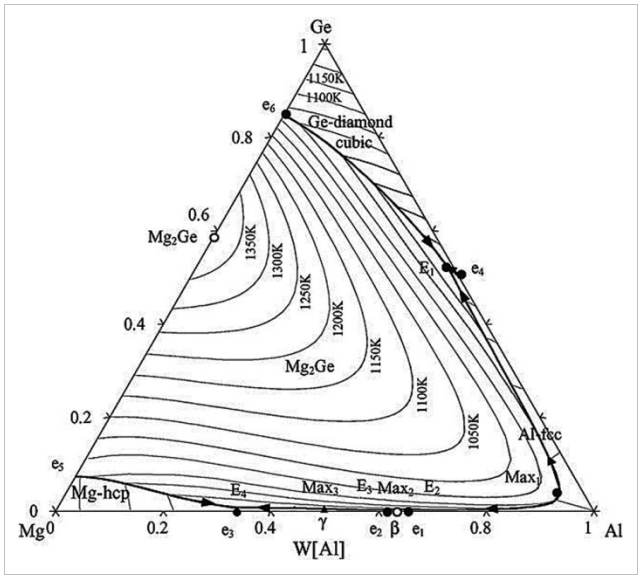

Fig. 3.3: Al-Mg-Ge ternary equilibrium phase diagram, [ISL06]

Table 3.2: Invariant phase equilibrium in Al-Mg-Ge system, [ISL06]

reaction	temperature, °C	type	phase	composition, at.%		
				Al	Mg	Ge
$L \rightarrow (Al) + Mg_2Ge$	632	e_1	L	92.50	5.00	2.50
			(Al)	99.10	0.60	0.30
			Mg_2Ge	0	66.70	33.30

For comparison three commercial casting alloys (see Tabable 3.3) were included into the research program, namely:

- A356, a commercial casting alloy with the nominal composition AlSi7Mg containing 0.32 wt.% Mg;
- A201, a high strength commercial casting alloy with the nominal composition AlCu4.5MnMg;
- Magsimal®59, a commercial casting alloy with the nominal composition AlMg5Si2Mn supplied by "Aluminium Rheinfelden GmbH" (Rheinfelden, Germany)".

Table 3.3: Specimen's nomenclature used throughout the work

specimen	nominal composition of alloys, at.%/wt.% (Al-balance)							
	Mg	Si	Mn	Li	Sc	Zr	Ge	Cu
A1	7.72/7.00	2.86/3.00	-	-	-	-	-	-
A2	7.72/7.00	2.86/3.00	0.29/0.60	-	-	-	-	-
A3	6.62/6.00	2.86/3.00	0.29/0.60	-	-	-	-	-
B1	7.72/7.00	2.86/3.00	0.29/0.60	1.90/0.5	-	-	-	-
B2	7.72/7.00	2.86/3.00	0.29/0.60	3.75/1.0	-	-	-	-
C1	7.72/7.00	2.86/3.00	0.29/0.60	-	0.12/0.20	0.06/0.2	-	-
C2	7.72/7.00	2.86/3.00	0.29/0.60	-	0.13/0.22	0.04/0.14	-	-
D1	5.00/4.34	-	0.29/0.60	-	-	-	2.50/6.49	-
D2	5.00/4.34	-	0.29/0.60	1.90/0.50	-	-	2.50/6.49	-

	commercial casting alloys, at.%/wt.% (Al-balance)							
	Mg	Si	Mn	Li	Fe	Ti	Ag	Cu
A356	0.36/0.32	6.71/6.97	0.01/0.02	-	0.03/0.06	-	-	-
A201	0.33/0.30	0.02/0.05	0.15/0.30	-	0.05/0.10	0.06/0.10	0.15/0.60	2/4.50
AlMg5Si2Mn	6.04/5.47	2.10/2.20	0.34/0.69	-	0.06/0.12	-	-	-

3.2 Melting procedure

The alloys were melted in clay graphite crucibles in an electric resistance furnace. For each alloy series, individual crucibles were used to avoid contamination from different alloying elements.

As starting materials high purity aluminum (A99,997) was used. The alloying elements were added via master alloys, namely AlSi25, AlMn26, AlMg50, AlSc2, AlZr10, AlGe20 master alloys. The exact chemical composition of the aluminum and master alloys are presented in Tables 1 and 2, Appendix 1. Microstructure and phase constituents are given in Appendix 2. Both, aluminum and master alloys were cut into small pieces and weighted in appropriate proportions before charging. The batch weight was about 250 g as a reference rate for all melts.

First just aluminum was melted and maintained the 720°C, than AlSi25 and AlMn26 master alloys were added into the melt and stirred using a graphite rod. After complete dissolution

of the master alloys, the melt was heated up again to the 720°C and its surface was covered by flux powder. As a flux powder, carnallite ($Mg[H_2O]_6KCl_3$) was used. Prior to addition it was dried for 24 hours at 250°C. Between different castings, the flux powder was stored in the preheated furnace to avoid its interaction with air and moisturizing. Mg and/or Li was made added then in the following manner: pieces of Mg- and Li-containing master alloys were wrapped in aluminum foil and added in small increments by plunging them under the melt surface using a titanium instrument. The prior to addition of Li, the melt surface was flushed by dry argon using a specially designed lance (see Appendix 3). Flushing protects the melt surface from interaction with the environment and decreases the probability of Li and/or Mg to be oxidized.

After addition of Mg and Li, argon fluxing was used to remove non-metallic impurities and soluble gases from the melt. Fluxing was performed by immersing the lance under the melt surface. Prior to fluxing the lance was preheated up to 400°C and before immersing the argon flow was opened.

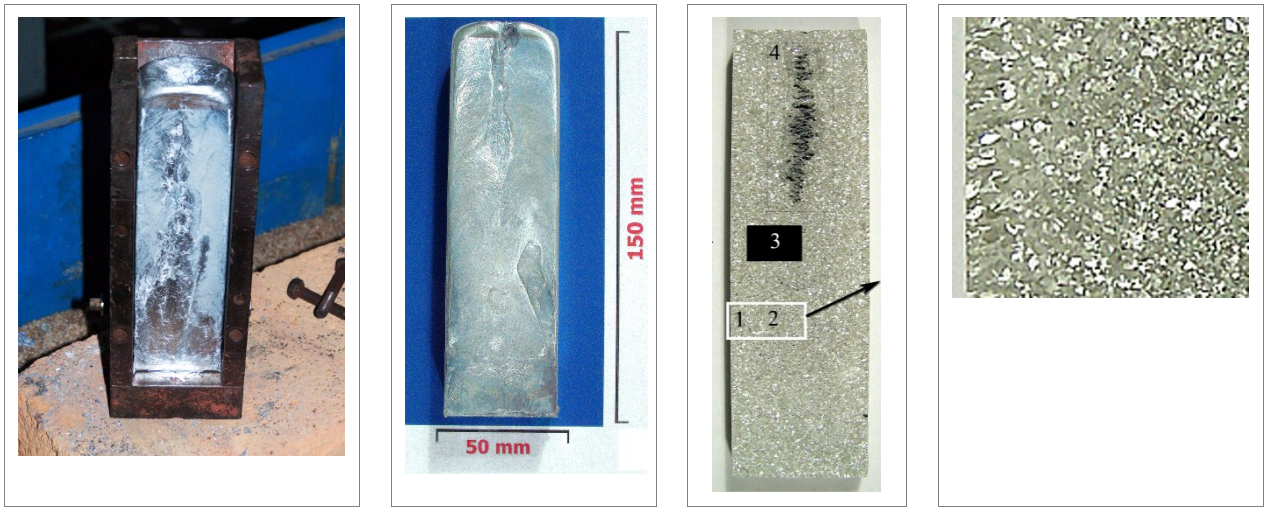

a. b. c. d.

Fig. 3.4: Steel mould filled with alloy (a), ingot dimensions (b) and different zones of cast ingot (c), enlarged part of the area 1,2 representing columnar and equiaxed crystal zones (d)
1 – columnar crystal zone; 2 – equiaxed grains zone; 3 – place where metallographic specimens were cut; 4 – position of gas and shrinkage porosity

Fluxing time was 10 min and kept constant for all melts. After fluxing the melt surface was skimmed to remove dross and after reaching the temperature of 700°C, the alloys were cast into a steel mold. The mold temperature was 25°C for all casting to produce similar cooling conditions for all alloys. Preliminary tests showed that such conditions result in a cooling rate of 2 K s^{-1} prior solidification. Figure 3.4 shows the opened mould after filling with the alloy, dimensions of the ingot, a vertical section of the etched ingot and an enlarged part where the areas of columnar and equiaxed grains are visible. The position from where specimens for metallographic examinations were extracted, is specified. The obtained ingots were cut on two

halves. One was used for macroetching and the other one for cutting the specimens for metallographic examinations.

3.3 Heat treatment

Two types of heat treatment were applied. The first one is the solution treatment (see Table 2.2), which was conducted in an electrical resistance furnace. Before treatment the furnace was heated up to the solution treatment temperature and kept for 12 hours at this temperature.

Than the specimens were positioned in the central part of the preheated furnace to ensure equal heating rate and temperature distribution around the specimens. Temperature was controlled by a K-type thermocouple placed directly at the surface of the specimens. The melting temperature of each specimen was determined from differential scanning calorimetry runs individually for each alloy, as presented in Chapter 5. Times from 20 min up to 24 hours were used for the solution treatment studies. The time for reaching the solution treatment temperature was 10-15 min and is excluded from the presented times. After solution treatment the specimens were quenched in 25°C water.

After quenching one part of each specimen was stored in liquid nitrogen to slow down diffusion processes and prevent premature decomposition of the solid solution before artificial aging. This was the first type of heat treatment.

The second type of heat treatment was T6, which combines solution treatment, quenching and artificial aging. Artificial aging was conducted in a forced circulation air furnace at 175°C for various times. The time needed for heating the specimens up to the artificial aging temperature was 20 min and is excluded from the presented times. The specimens were taken out of the furnace and cooled in still air after artificial aging.

3.4 Differential scanning calorimetry

Differential scanning calorimetry (DSC) is a technique determining the heat flow between the sample and the surrounding as a function of temperature or time. At heating or cooling, the phase transformations in the material are accompanied by heat consumption or emission, called endo- or exothermic. DSC determines the temperatures of these transformations and quantifies their heat exchanges, i.e. the enthalpy changes in the alloys. The most recent review about DSC analysis of phase transformations in aluminum alloys is given by Starink, *[STA04]*.

The measurements were performed using a NETZSCH DSC 404 device (heat flux type DSC) with disc shaped specimens with a weight of approximately 20 mg encapsulated in an alumina pan. Alumina pans were used as a reference (210.1 - 220.5 mg). Specimens and pans

were weighted using a Sartorius analytical balance with an accuracy of 0.0001 mg. During DSC studies the chamber was protected by purified argon gas (99,99% purity) with 10-20 cm^3/min flow rate. Temperature scans were made in the range from room temperature ~ 25 to 710°C with computer controlled heating and cooling. The obtained results were processed with the software Proteus Analysis. After each set of specimens, the pans were cleaned in 5 ml 65%HNO_3 + 5 ml 37%HCl solution for 2 hours in an ultrasonic cleaning equipment.

Before the measurement, the DSC was calibrated using the standard calibration program and tools supplied by NETZSCH. In order to check the reliability of the melting onset temperature, aluminium specimens of different purities were heated and cooled down at a rate of 10 K min^{-1}, (Figure 3.5). It was found that melting is displayed as a sharp endothermic peak on the DSC curve and that for Al with 99.9999 purity, the melting onset temperature is 659.5°C, which is only 0.82°C lower than the theoretical Al melting temperature of 660.32°C. Slight deviation from this temperature were obtained for aluminum with 99.999 and 99.997 purity.

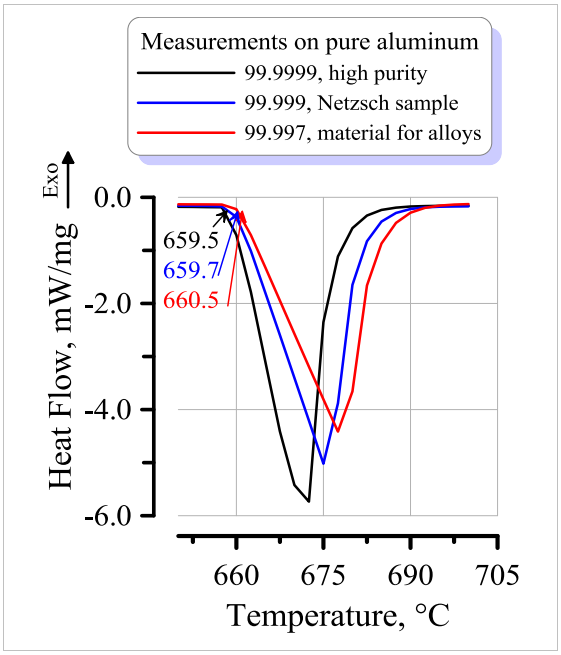

Fig. 3.5: DSC curves of aluminium with different purities, scanning rate 10 K min^{-1}

Several DSC runs were performed on binary alloys with the nominal compositions Al-7.00 wt.% Mg, and Al-7.00 wt.% Si in order to compare the measured melting onset temperatures with those taken from phase diagrams. For Al-7.00wt.% Mg, DSC gave 448.6°C, the phase diagram 450°C, *[MUR82]* for Al-7.00 wt.% Si 575.4°C, the phase diagram 577.0°C, *[MUR84]*. The observed onset temperatures for pure Al and binary alloys indicate the reliability of the DSC runs.

3.5 Structure characterization

The microstructure characterization of the alloys was carried out by light optical, scanning electron and transmission electron microscopy.

3.5.1 Specimens preparation

The specimens for metallographic investigations were prepared using standard metallographic procedures. They include several steps:

1) cutting;

2) mounting;
3) grinding;
4) polishing;
5) etching.

Metallographic specimens were cut from the ingots using a Woco-high speed saw. Water cooling was applied to protect the alloy from heating. The size of the specimens were kept constant 10×10×10 mm. For handling, it was necessary to embed the specimens in a polymer block. For this purpose cold embedding was used.

Next, the specimens were grinded using rotating grinding discs, covered with silicon carbide paper, under permanent water flow. The sequence of papers used was: 220, 500, 800, 1200, 2500, 4000 SiC-grit. For the final grinding, water and liquid soap lubricant was used. At last, the samples were washed in water with soap, then by alcohol and finally dried.

The dry specimens were polished using 6, 3 and 1 μm diamond suspensions and lubricant. After each polishing step, the specimens were ultrasonically cleaned with alcohol for 3 min and then dried.

To achieve the highest surface quality, vibration polishing in oxide polishing suspension (colloidal silica, 0.04 μm) was used. As a polishing cloth, OP-Chem cloth from STRUERS was used. The duration of vibration polishing was about 1 hour. The quality of the polished surface was controlled after each step by light microscope. A light microscope image of the microstructure of the AlMg7Si3Mn alloy is represented on Figure 3.6, confirming the quality of the metallographic preparation.

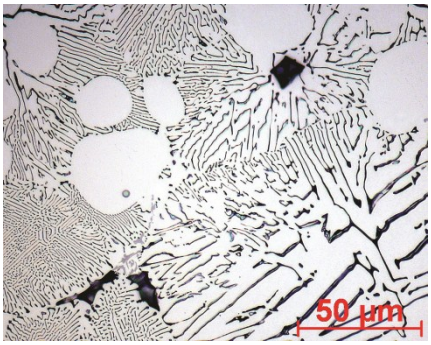

Fig. 3.6: Check of the light microscopy preparation quality. α-Al matrix of the AlMg7Si3Mn alloy white, eutectic colonies black

For visualization of the dendritic structure, an etchant of 6 g NaOH + 100 ml H_2O was used.Thin foil preparation for transmission electron microscopy (TEM) studies were carried out in a twin jet STRUERS Tenupol 3 electropolishing machine. Disks with diameter 3 mm and a thickness of about 150 μm were electropolished using an electrolyte with 70% methanol, 20% glycerol and 10% perchloric acid kept at -27 °C and a voltage of 20 V.

3.5.2 Light and scanning electron microscopy

An optical microscope Zeiss Axioskop with a MR MC80 digital camera with the software program AxioVision Rel. 4.7 was used for metallographic analysis. The

interlamellar spacings were measured in ten areas of the specimen using software tools. They are represented as average values.

The SEM's used in this work are Zeiss EVO and ULTRA, Zeiss FIB-SEM CrossBeam 1540ESB, and JEOL JSM-6490. All microscopes were equipped with Energy Dispersive Spectrometry systems (EDS). At the same time, the JSM-6490 is equipped with a wave length dispersive spectroscopy system. Both, the inlens backscattered electron (BSE) and inlens secondary electrons (SE) detectors are used to obtain material contrast (BSE) and topological contrast (SE). Both, EDS and WDS spectrometry are used in this work to obtain the composition of solid solution grains and intermetallics.

3.5.3 Transmission electron microscopy

All TEM investigations were carried out using a Philips CM 30 TEM operated at 250 kV accelerating voltage and equipped with Energy Dispersive Spectrometry system (EDS) (Noran System Six EDS. Thermo Scientific). Bright field (BF) images were used for observing the morphology of solid solution grains, intermetallics and precipitates. Element concentrations were measured using spot sizes of 4-10 nm. The given concentrations are averaged over measurements in 10 individual grains for HPDC casting or dendrite arms in case of laboratory melted and cast into permanent mould specimens.

3.6 Hardness and microhardness measurements

Hardness measurements were performed using a Brinell hardness testing machine with a ball diameter of 2.5 mm and a load of 62.5 kg. They were performed for as-cast, solution treated and aged specimens. For each specimen, 10 individual measurements were performed and the resulting hardness is presented as the average value.

Microhardness was used in this work for two purposes: first, for measuring the hardness of the solid solution of the base AlMg7Si3 alloy after, and additional alloying with Mn (A2), Li (B1 and B2), Sc+Zr (C1 and C2) and for the Al-Mg-Ge alloys (D1 and D2), second, for measuring the change of the hardness of the solid solution during solution treatment and natural or artificial aging for all alloys.

Microhardness is determined from the relation of applied load to contact area of the indentation. Vicker's tests were performed by pressing a diamond pyramid against the specimen with uniformly increasing load. By measuring the diagonals d_1 and d_2 of the indentation, as shown in Figure 3.7, the hardness of the specimen can be obtained from the following equation:

$$H_V = \frac{2P \sin\frac{\theta}{2}}{\overline{d^2}} \qquad (3.1)$$

where H_V is the Vicker's microhardness, P is the load (kgf), θ=136° is the angle between two facets of the Vicker's pyramid and $\bar{d}$ is the average value of d_1 and d_2 (mm).

Microhardness tests were carried out on polished non-etched specimens on a Duramin-2 microhardness tester. These Vickers microhardness measurements were performed on primary α-Al grains for HPDC alloy or dendrite arms for permanent mould casting using 0.05 Kgf load for 10 seconds. 10 indentations are performed on each sample and then averaged.

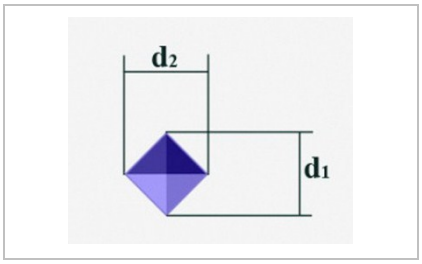

Fig. 3.7: Schematic illustration of the indentation mark and the measured diagonals

3.7 Summary

The chapter gives an overview of the alloys included to the research program and all techniques applied to investigate their heating and cooling behavior, microstructure features, phase compositions and precipitates formed during aging as well as changes of hardness and microhardness associated with alloying additions, solution treatment and aging. Chapter 3 can be summarized as follows:

- on the base of the analysis of Al-Mg-Si phase diagram, as base materials two alloys with hypereutectic and one with hypoeutectic composition were selected. For the Al-Mg-Ge system, the concentrations of Mg and Ge were selected such as their concentrations in the liquid phase at eutectic temperature;
- a combination of DSC and microscopical studies is used to study the phase formations in Al-base alloys, especially when precipitation from solid solution is considered. From DSC the temperature of phase transformations can be recorded and TEM investigations supply informations about morphology, type and size of these precipitates;
- it was confirmed that the metallographic techniques chosen for specimens preparation provide a good polish quality, i. e. all phases present in the alloy can be distinguished;
- hardness and microhardness test allow to measure the effect of aging on the hardness of the Al alloys.

4 As cast state of Al-Mg-Si and Al-Mg-Ge alloys

4.1 Introduction

The term “as-cast state” designates the structure in an alloy after complete solidification in a mould cavity. Solidification begins when the first portions of the melt come into direct contact with the mold walls and it finishes when the last portions of liquid metal disappear. At this time interval two processes are running simultaneously, namely nucleation of solid phase and its subsequent growth. The fundamentals of these processes with reference to the structure formation were represented in Chapter 1 (section 1.3). Chapter 4 presents the final structure of the alloys A1 - D2 (Table 3.3) formed during solidification and cooling down to room temperature.

As discussed in section 1.3.2, in contrast to pure aluminum, alloys containing a relatively high amount of alloying additives solidify in form of equiaxed grains.

In Figure 4.1 the macrostructure of specimen A2 in comparison to aluminum 99.998 purity is shown. In the pure Al, the grains nucleate on the mold walls and grow towards the center until their tips impinge one another. At the beginning of solidification, the driving force for nucleation is usually thermal undercooling ΔT_t in the melt at the mold wall. Thermal undercooling is quickly dissipated by the evolution of latent-heat. In case of pure aluminum, there can be no further nucleation and columnar grains will grow until solidification is completed (Figure 4.1 a). However, when the melt contains foreign atoms, the growing chill crystals reject these atoms, resulting in a solute-rich layer over the crystal surfaces. Here constitutional undercooling ΔT_c may reach a level sufficient for the nucleation of equiaxed grains on particles of insoluble impurities present in this layer. As these new grains, which formed in the constitutional zone, grow, they also promote the nucleation of new grains in front of them. This cyclical mechanism produces continuously equiaxed grains advancing towards the center of the melt. Such a situation is clearly seen from the

Fig. 4.1: Macrostructure of Al high purity (99.998) (a) and A2 ingot (b)

macrostructure of the A2 specimen where a high amount of solute atoms is present in the melt before solidification begins. The length of the columnar crystal zone for specimen A2 is about 700 µm at a cooling rate of 2 K s^{-1} (Figure 1.12). In Table 4.1 this parameter is represented for all specimens included in the program.

Table 4.1: Average length of the columnar crystal zones for all alloys included in the research program

alloy	A1	A2	A3	B1	B2	C1	C2	D1	D2
Length of the columnar crystal zone, µm	1000	800	1000	750	700	600	600	600	500

In Figure 4.2, the average element distribution along the columnar crystal zone in alloy A2 is illustrated.

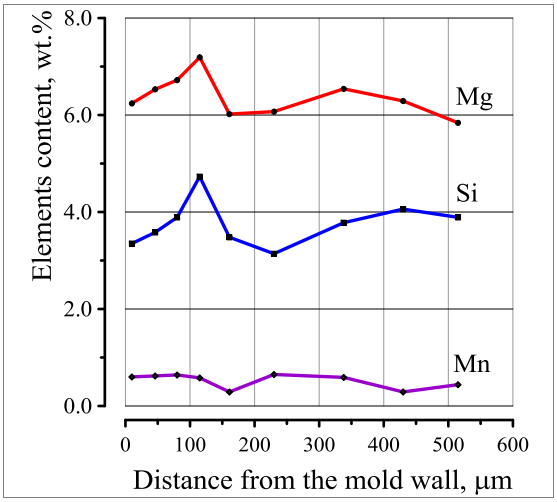

Fig. 4.2: Distribution of Mg, Si and Mn along the columnar crystal zone in A2

It can be seen that the relatively high initial Mg and Si content decreases at a distance of about 150-200 µm and then stabilizes. The Mn distribution is nearly constant from the surface to the center of the ingot.

The length of columnar crystal zone for the A1 - D2 specimens varies in the range from 1000 to 500 µm. From this observation one can conclude that the macrostructure of the specimens consists mostly of equiaxed grains and that additional alloying with Li (B1 and B2) and Sc+Zr (C1 and C2) has little effect on the nucleation and growth of both, columnar and equiaxed crystals at a given cooling rate. For comparison, the A356.0 alloy cast under the same conditions gives a columnar crystal zone of about 900 µm. For the commercial AlMg5Si2Mn HPDC alloy solidified at a cooling rate of 70 - 100 K s^{-1}, a zone of columnar crystals still exist but its length is only about 100 µm.

Columnar dendritic growth develops in a positive temperature gradient. Due to this gradient a preferred orientation of the dendrites is obtained, which results in arrays with a typical spacing. The size of the columnar zone depends on the solute level, pouring temperature, thermal gradient and nuclei density present in the melt. It is known that when effective grain refiner is added prior to casting, the fully equiaxed structure can be obtained. This is true not only for wrought alloys but also for casting ones. In the latter, due to the high solute content, the growth

rate of the solid phase is high and the width of the constitutionally undercooled zone ahead of the dendrite tips, where potent nucleation particles are present, is small, *[CHA09]*. The observed structures of A1 - D2 together with AlMg5Si2Mn HPDC and A356 PM show that the high solute content and even the high temperature gradient in the case of HPDC cannot provide such conditions where the formation of a columnar zone is avoided. Formation of a fully equiaxed structure is very important for casting alloys because this structure is less anisotropic than the mixed columnar+equiaxed type. Thus for Al-Mg-Si casting alloys, appropriate grain refiners have to be used for achieving a complete equiaxed structure. As an example, during laboratory tests, addition of 0.10 wt.% Ti to A2 gives a pronounced grain refinement. In the as-cast structure, a columnar zone was not observed. However, even when a high cooling rate is applied further investigation is needed to establish the optimum conditions to obtain a fine grained structure of these casting alloys.

4.2 Differential scanning calorimetry (DSC)

Differential scanning calorimetry (DSC) is used in the present study to determine the melting and solidification characteristics, such as the onset temperatures of phase transformations. In a DSC experiment the specimen under investigation and a reference are heated up, respectively, cooled down simultaneously. The difference in energy consumption or production per time and mass between specimen and reference is measured during such a heating cycle. This so-called heat flow is plotted as a function of temperature. A positive peak indicates an exothermic reaction, namely solidification. A negative peak stands for an endothermic reaction, i.e. melting. In the present study, as reference an empty alumina pan was used. The heating/cooling rate was kept constant at 10 $K\ min^{-1}$. For some cases different heating/cooling rates were applied in the range 1 - 50 $K\ min^{-1}$, which will be specified in the text.

4.2.1 Calorimetric study of the Al-Mg-Si alloys A1 - A3

The DSC experiments were performed for a A1, A2 and A3 specimens at cooling/heating rates of 10 $K\ min^{-1}$. The sample masses were in the range from 0.01663 to 0.02134 g. The DSC curves obtained by heating and cooling of as-cast specimens of A1 are shown in Figure 4.3. They demonstrate the heat effects appearing during heating and solidification.

In the most general case, one endothermic and two exothermic reactions can be clearly distinguished. Reaction 1 represents the combined heat effect of melting of eutectic and α-Al. There were no other reactions observed during heating, especially, in the low temperature part of the curve. On cooling, reaction 2 is associated with the nucleation and growth of the aluminum matrix and reaction 3 is due to eutectic growth.

In this simple case, the reaction sequence detected from heating and cooling curves represents conventional melting and solidification processes in two phase alloys.

As mentioned in section 3.1.1 the Al-Mg-Si alloys A1 and A2 were selected to be hypereutectic. This means that together with the α-Al solid solution and (Al)+(Mg_2Si) eutectic, primary Mg_2Si crystals have to be present in the alloy structure. However, there were no separate heat effects observed during melting or cooling, which could be attributed to the melting or formation of such crystals. From the Al-Mg-Si phase diagram follows, that in case of hypereutectic alloys at first primary Mg_2Si crystals precipitates from the melt. Than the rest of the melt solidifies, having the binary eutectic structure α-Al and (Al)+(Mg_2Si) eutectic. Consequently, the first exothermic effect of the cooling curve (Figure 4.3, denoted 2) is not only caused by the nucleation and growth of α-Al but it is combined with the nucleation and growth of primary Mg_2Si crystals.

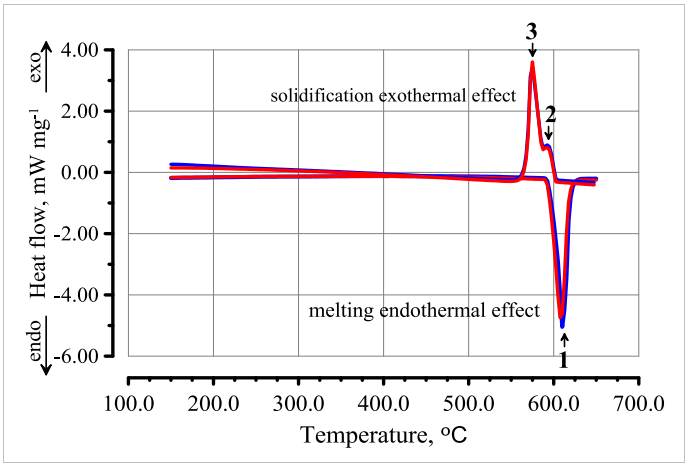

Fig. 4.3: DSC curves of as-cast A1 specimen: 1 – endothermic effect associated with melting; 2 – exothermic effect associated with nucleation and growth of α-Al; 3 – exothermic effect associated with eutectic growth

During heating of the A1 - A3 specimens, only one sharp endothermic peak was detected (Figure 4.4 a), which and can be characterized by three specific temperatures, namely:

- melting onset temperature T_{m_onset} (denoted 1);
- peak temperature T_{m_peak} (denoted 2);
- melting outset temperature T_{m_outset} (denoted 3).

From Figure 4.4 a it can be seen that the shapes of the peaks for all three alloys are similar. In A2 and A3, the high temperature part of the DSC traces is slightly bulged out. The DSC experiments on A1 at different heating rates show that even here the endothermic effect observed at a heating rate of 10 $K\,min^{-1}$ is the superposition of two heat effects (Figure 4.4 b). At a heating rate of 1, 2 and 3 $K\,min^{-1}$, the peak of the first endothermic effect is extended by a small plateau. For the higher heating rates of 5 and 10 $K\,min^{-1}$, this effect is less pronounced.

The exact values of the three temperatures for A1 - A3, recorded in heating experiments with heating rate 10 $K\,min^{-1}$, are summarized in Table 4.2. For the base alloy A1, the onset melting temperature is 587.4°C and corresponds well with the eutectic $(Al)+(Mg_2Si)$

temperature from the equilibrium Al-Mg-Si phase diagram (Figure 3.2) which is according to *[KUM00]*, equal to 594.0°C. Thus the first endothermic effect is attributed to the (Al) + $Mg_2Si \rightarrow L$ reaction. Further heating resulted in the appearance of the second endothermic peak related to the melting of α-Al. The peak onset of the second peak for a heating rate of 1 K min^{-1} was detected at 591.3°C, increasing heating rate up to 5 K min^{-1} shifts this temperature to a higher value of 606.4°C. The end of melting is specified by melting outset temperature. For A1 alloy it was found to be 619.8°C.

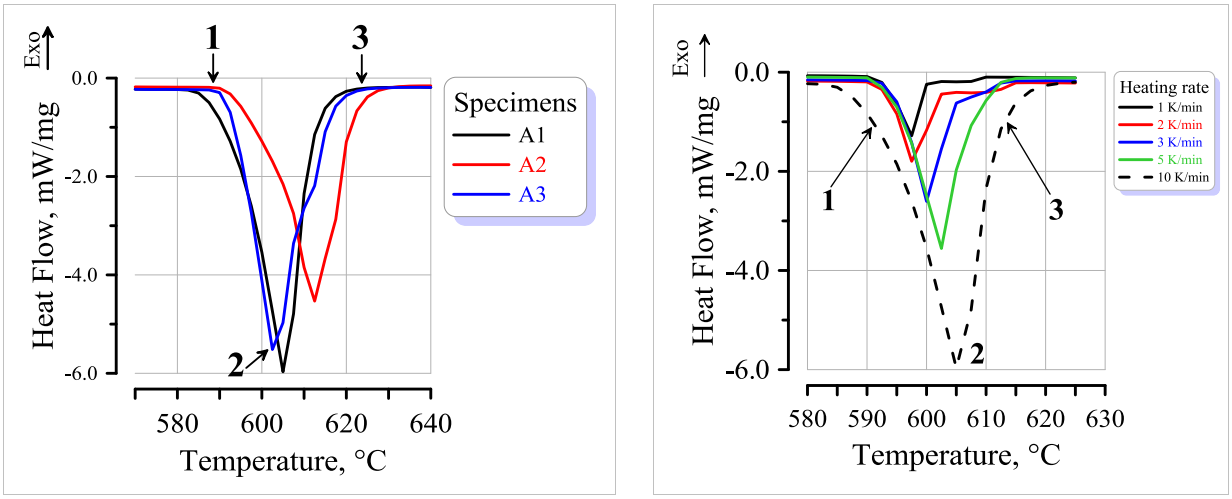

a. b.

Fig. 4.4: Enlarged parts of the DSC heating curves for A1, A2, and A3 for heating rate 10 K min^{-1} (a) and DSC traces for A1 obtained at different heating rates (b)

Table 4.2: Temperature details for heating of A1, A2 and A3 heated at a rate of 10 K min^{-1}

temperature, °C	specimens A1	A2	A3
T_{m_onset}	587.4	592.4	591.1
T_{m_peak}	604.4	611.5	600.9
T_{m_outset}	619.8	625.3	620.1

Alloy A2 is additionally alloyed with 0.60 wt.% Mn. From Table 4.2 follows that the presence of Mn has no significant effect on the eutectic melting temperature and the melting of aluminum matrix. A similar tendency was observed for A3, containing less Mg than A1 and A2. Therefore the DSC data allow to conclude the following reaction sequence for A1 - A3:

reaction	temperature, °C
(Al) + $Mg_2Si \rightarrow L$	595.0
(Al) $\rightarrow L$	607.0

The described effects can be observed when the specimens are heated up. When cooled down with a rate of 10 K min^{-1}, the DSC curves for all three alloys are nearly identical (Figure 4.5). This confirms that both – lower Mg content (A3) or alloying with Mn (A2) has an insignificant effect on the reactions occurring during the solidification of Al-Mg-Si alloys.

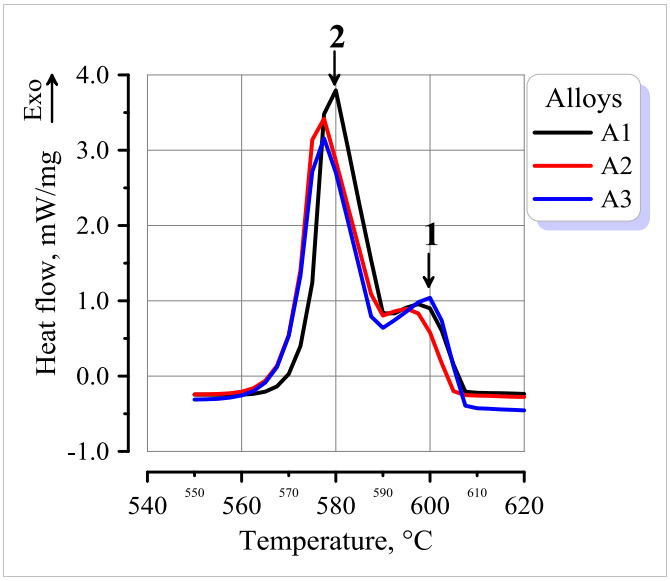

Fig. 4.5: DSC cooling curve for A1, A2, and A3 at a cooling rate of 10 K min^{-1}:
1 – exothermic effect associated with solidification of α-Al;
2 – exothermic effect associated with eutectic reaction

4.2.2 DSC study of the Al-Mg-Si alloys B1 - C2

Two types of alloying additions were used for the Al-Mg-Si alloys (see Table 3.3). For the first one, Li was added in an amount of 0.50 wt.% in B1 and 1.00 wt.% in B2. For the second one Sc and Zr, 0.20 wt.% Sc+0.20 wt.% Zr in C1 and 0.22 wt.% Sc +0.14 wt.% Zr in C2.

In Figure 4.6, the high temperature part of the DSC heating curves of C1 and C2 are shown for a heating rate of 10 K min^{-1} in comparison with A2. The different melting temperatures are specified in Table 4.3. The shapes of the DSC curves obtained from Sc+Zr containing alloys and their positions are similar to that of A2 indicating that alloying of Al-Mg-Si alloys with Sc+Zr does not affect the phase equilibrium. Preliminary tests of Li-containing alloys (B1 and B2) showed that heating under argon atmosphere results in a complete oxidation of the material. Hence, the DSC data for B1 and B2 specimens were recorded under the vacuum.

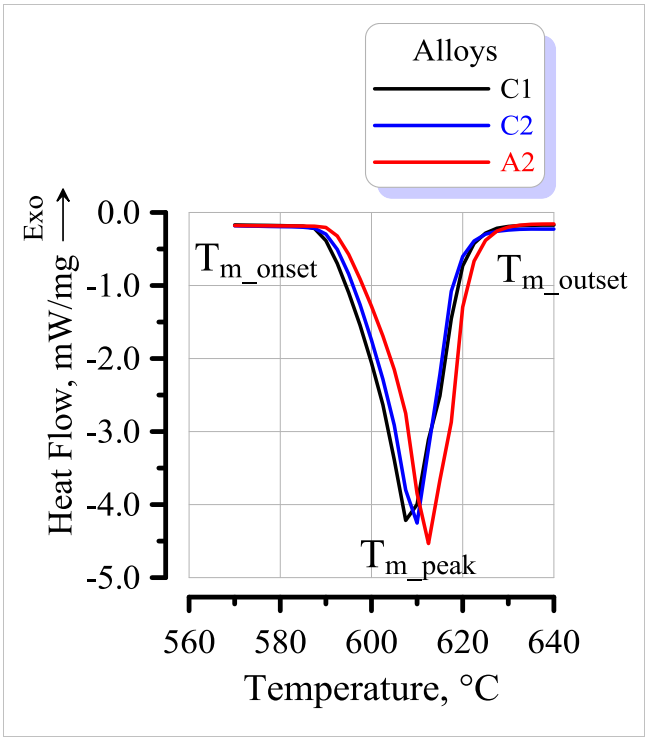

Fig. 4.6: DSC heating curve for as-cast C1, C2, and A2, heating rate of 10 K min^{-1}

The DSC traces for B1 and B2 are very similar to that of A2 (Figure 4.7). Onset, peak, and outset temperatures were very close to that obtained for A2, thus confirming that addition of up to 1.00 wt.% Li has no effect on the eutectic melting temperature and melting of the α-Al solid solution. To summarize the results of the DSC studies of the Al-Mg-Si alloys, it was found that the eutectic melting temperature of 595.0°C is very close to that of the established ternary phase diagram. No noticeable other effects in the DSC-curves were observed for alloys alloyed with Mn, Sc+Zr or Li.

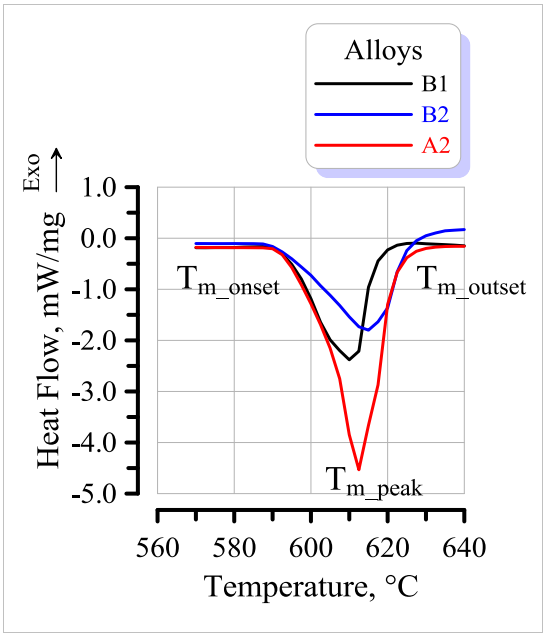

Fig. 4.7: DSC heating curve for as-cast B1, B2 and A2, at a heating rate of 10 K min^{-1}

Table 4.3: Temperature details for heating of C1, C2 and A2

temperature, °C	specimens		
	C1	C2	A2
T_{m_onset}	593.9	594.2	594.9
T_{m_peak}	604.3	605.1	607.8
T_{m_outset}	616.8	616.3	617.2

4.2.3 Comparison of DSC studies of A356.0, A201.0 and AlMg5Si2Mn with A2

In Figure 4.8, the DSC heating curves obtained from the commercial A356.0 (Al-Si), A201.0 (Al-Cu) and AlMg5Si2Mn HPDC casting alloys are shown together with that of A2. The enlarged part of the curves shows the low temperature heat effect (Figure 4.8 b) and the melting behavior (Figure 4.8 c).

This first heat effect (denoted 1) is exothermic and was detected during heating of A356.0 and A201.0. The onset temperature for A356.0 alloy is 192.4°C, peak temperature 247.8°C and outset 262.1°C. For the A201.0 alloy this heat effect was less pronounced and has an onset temperature of 236.4°C, peak temperature 246.7°C and outset 260.0°C. For AlMg5Si2Mn HPDC, the low temperature heat effect has an onset temperature of 183.0°C and a peak temperature 201.0°C. The low temperature heat effect was not observed in A2.

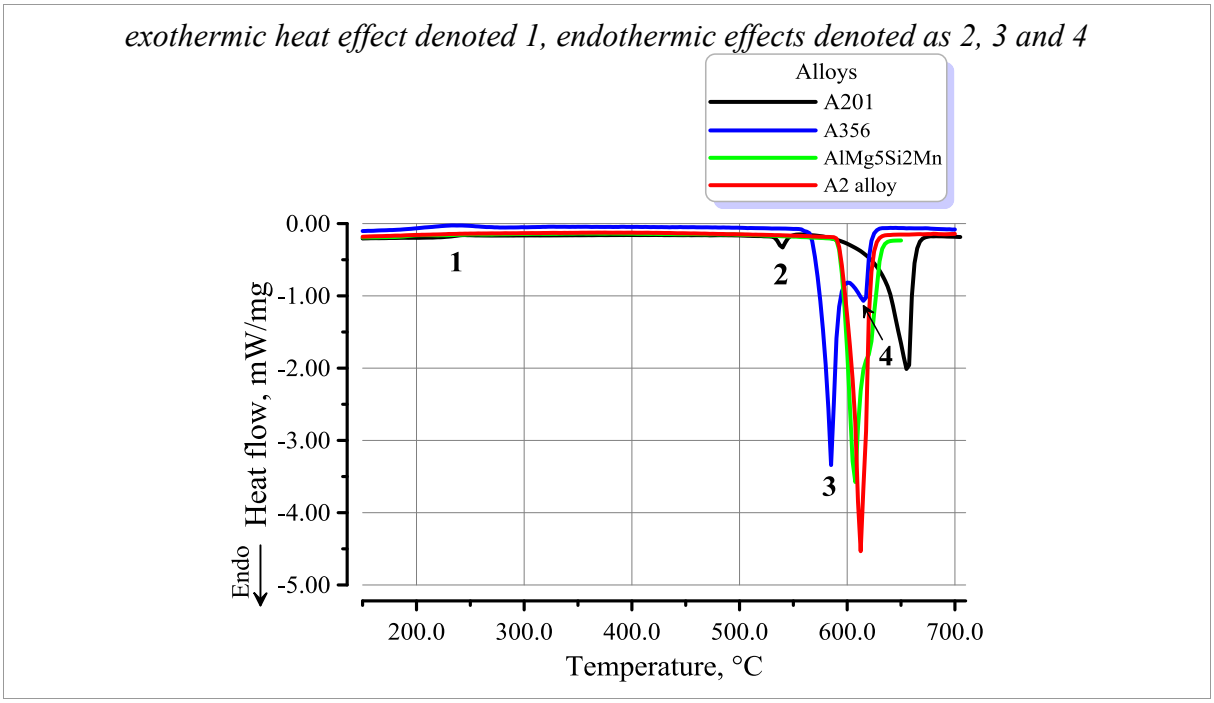

a. DSC heating curves obtained from A356.0, A201.0 and AlMg5Si2Mn commercial casting alloys in comparison to A2

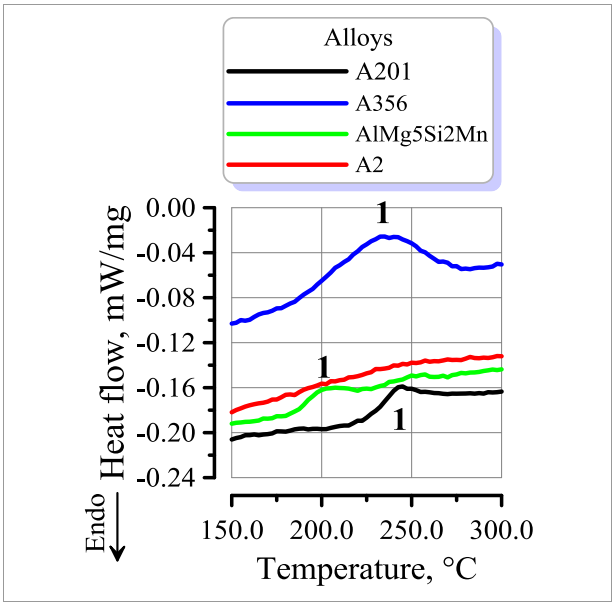

b. low temperature part of DSC curve

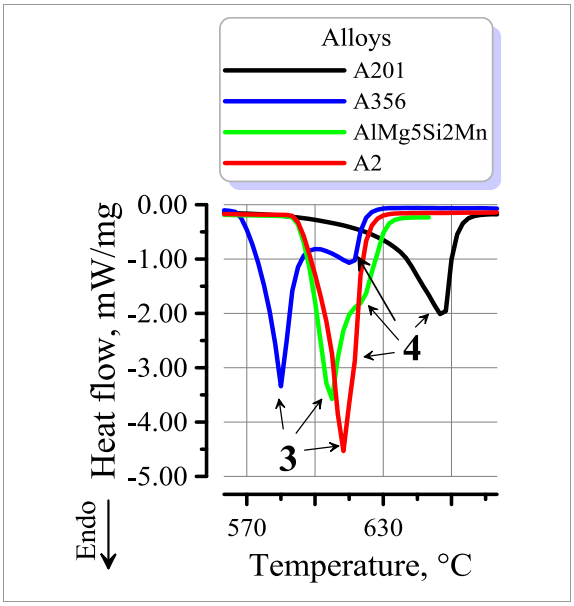

c. high temperature part of DSC curve

Fig. 4.8: DSC traces obtained from A201.0, A356.0, AlMg5Si2Mn commercial alloys in comparison to A2

Low temperature exothermic effects are usually attributed to a precipitation process. It was reported by Wang et al. *[WAN11]*, that the A356.0 alloy (Al-Si) cast into a permanent mold, tends to form precipitates during aging directly from as-cast state at the temperature close to 230.0°C. They observed an exothermic heat effect in the same temperature range as it was shown in Figure 4.8 b TEM investigations showed the formation of β' precipitates.

The endothermic heat effect denoted 2 was exclusively found in A201.0. It has an onset

temperature of 546.1°C and a peak temperature of 548.0°C. Comparing the measured temperature with that in an established Al-Cu phase diagram, this heat effect can be attributed to the melting of $CuAl_2$ (the eutectic temperature in the Al-Cu system is 548.0°C). Due to the low volume fraction of primary $CuAl_2$ phase in A201.0 containing 4.50 wt.% Cu, this heat effect is small. Alloys of the Al-Cu system, i.e. A201.0, are usually subject of T6 heat treatment. However, their aging from as-cast state is not considered for further practical implementation. The obtained results show that in Al-Cu casting alloy $CuAl_2$-precipitation takes place even without solution treatment. However, this effect is not strong enough to possess commercial significance.

The sharp endothermic peak denoted 3 for Al-Mg-Si alloys is attributed to the melting of (Al)+(Mg_2Si) eutectic as discussed above. The DSC curves for AlMg5Si2Mn HPDC and A2 are nearly identical showing eutectic melting temperatures of 596.2°C for AlMg5Si2Mn and 594.9°C for A2. For A356.0 which belongs to the hypoeutectic Al-Si alloys, an onset melting temperature of 571.3°C was measured which represents the melting of (Al)+(Si) eutectic and is close to what is defined by the equilibrium Al-Si phase diagram.

Further heating results in the appearance of an endothermic peak denoted 4, (Fig. 4.8 c). A peak onset temperature of 618.0°C was measured for AlMg5Si2Mn, while for A2 only a slight bulge on the right slope of the peak is visible as discussed before (Fig. 4.4 a and 4.4 b). For A356.0 the onset temperature of heat effect 4 is 612.1°C, for A201.0 alloy onset is 612.1°C. This effect is related to the melting of α-Al.

Summarizing the DSC results obtained for commercial alloys one can say that the AlMg5Si2Mn HPDC alloy and A2 alloy behave in a similar way, i.e. all detected heat effects are practically the same.

4.2.4 DSC study of the Al-Mg-Ge alloys D1, D2

Two alloys, namely D1 and D2, were subject of the research program (see Table 3.2). D1 is the base Al-Mg-Ge alloy, D2 was alloyed with Li. DSC heating curves of these two alloys are shown in Figure 4.9 where alloy A2 is also represented for comparison. It can be seen that T_{m_onset} for D1 and D2 has been shifted to higher temperatures.

For D1, the melting onset temperature was found to be 629.3°C and for D2 624.0°C (Table 4.4). The DSC data confirm that for the Al-Mg-Ge system the eutectic melting temperature is about 25.0°C higher than that of Al-Mg-Si. This fits well with the model of Islam et al. *[ISL06]*, where they calculated an eutectic melting temperature of 632.75°C what is about 3.0°C higher than that of D1.

Careful examination of the heating and cooling DSC curves did not show any additional heat effects. Hence the sequence of melting reaction can be represented as follows:

reaction	temperature, °C
(Al) + Mg_2Ge → L	629.0 – 632.0
(Al) → L	~ 640.0

As in Al-Mg-Si alloys, the heat effect associated with the reaction (Al) → L is not exclusively the melting of the Al solid solution but it is combined with the melting of Mg_2Ge primary crystals.

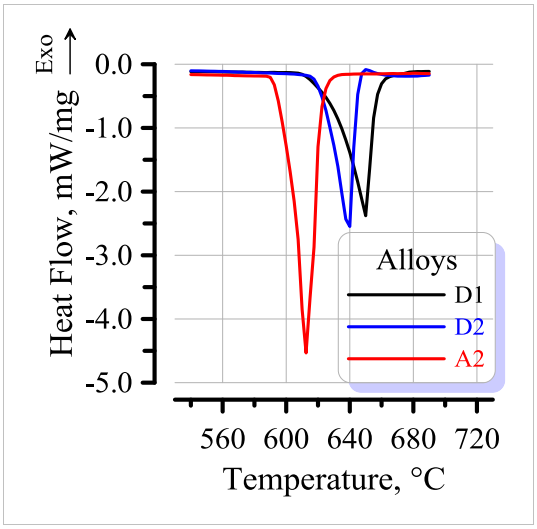

Fig. 4.9: DSC heating curve for as-cast D1, D2 and A2 alloys, heating rate 10 K min^{-1}

To sum up, the experimental Al-Mg-Si and Al-Mg-Ge systems exhibit higher eutectic melting temperatures than the commercial systems hypoeutectic Al-Si (A356.0, T_e=571.0°C), eutectic Al-Cu (A201.0, T_e=548.0°C) and Al-Mg (AlMg5Si2Mn, T_e=596.0°C) HPDC casting alloys.

Table 4.4: Temperature details for heating of D1, D2 and A2 specimens

temperature, °C	specimens		
	D1	D2	A2
T_{m_onset}	629.3	624.0	594.9
T_{m_peak}	650.6	639.3	607.8
T_{m_outset}	655.6	645.4	617.2

In the selected concentration interval of Mg, Si and/or Ge, both systems show two reactions which take place during melting or solidification. The first one is the eutectic melting and the second one is the melting of the Al-based solid solution. The same sequence of reactions is true for the solidification where α-Al grains nucleate at higher temperature and grow until the eutectic temperature is reached. For the experimental alloys, there were no additional heat effects observed in the high temperature part of the DSC curves as well as in the low temperature part verifying the absence of any other phase transformations in these alloys. After alloying with Li or Sc+Zr, no additional heat effects were observed thus confirming that in the selected concentration interval these additions have no effect on the phase equilibria in both systems Al-Mg-Si and Al-Mg-Ge.

4.3 Structure of Al-Mg-Si casting alloys

The microstructural characterization of A1 - D2 is of fundamental importance for the alloys development. Under interest are: phase morphology, phase identification, microanalysis of the chemical composition and its change due to the presence of additional alloying elements.

4.3.1 Structure of base alloy and after Mn addition

The structures of the base alloy without Mn, A1, and the alloys with Mn addition A2 and A3, are shown in Figure 4.10. All alloys exhibit equiaxed grain structure and 3 phase constituents can be distinguished in the Al matrix. They are represented in Figure 4.10 as:

- dendrite arms of the α-Al solid solution (white, denoted 1);
- (Al)+(Mg_2Si) eutectic (dark, denoted 2);
- Mg_2Si primary crystals (dark, denoted 3);
- α-Al(Mn,Fe)Si phase (gray, denoted 4).

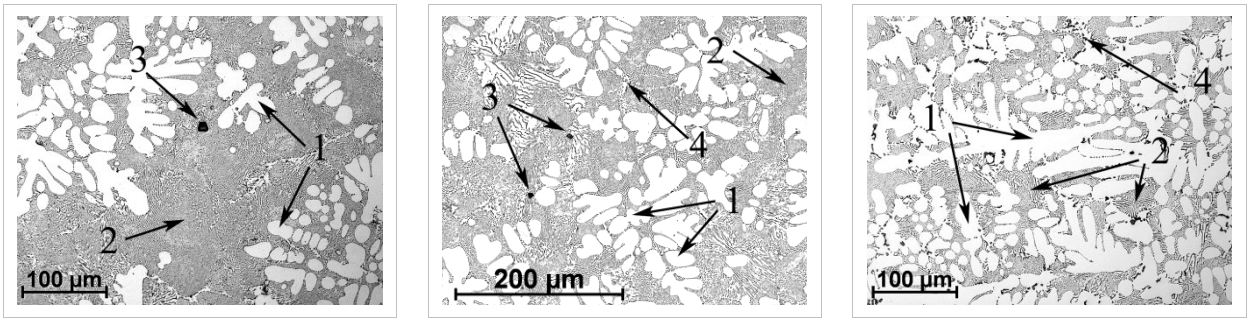

a. ×200 b. ×200 c. ×200

d. ×1000 e. ×1000 f. ×1000

Fig. 4.10: Microstructure of A1 (a, d), A2 (b, e) and A3 (c, f) obtained at different magnifications

The preferential morphology of α-Al is dendrite with long primary arms for all three alloys. The (Al)+(Mg_2Si) eutectic has lamellar morphology, where long Mg_2Si plates alternate with α-Al. Primary Mg_2Si crystals have a regular polyhedral shape and are situated in the centers of eutectic colonies. Magnesium silicide primary crystals were observed in A1 and A2 since these alloys are hypereutectic. In A3 primary Mg_2Si crystals were not observed. Solidified under the same conditions, i.e. melt temperature, mold temperature, cooling rate, all three alloys show much the same phase morphology.

In A2 and A3, containing 0.60 wt.% Mn, an additional phase was observed. It appears in the field of α-Al in, form of dark irregular shaped particles (denoted 4). EDX measurements showed that this is a Mn-containing primary phase (α-Al(Mn,Fe)Si). Due to its low volume fraction there was no heat effect traced during the DSC studies of A2 and A3.

The composition of the phases was measured by EDX analysis using SEM and TEM microscopes. The dendrite arms of α-Al solid solution of alloy A1 contains nearly exclusively Mg (Table 4.5). The Mg content in the solid solution measured in SEM, using 10 kV acceleration voltage, is 2.59 wt.% what is similar to that measured in TEM. The small Si content measured in case of SEM-EDX analysis obviously originated from surrounding Mg_2Si lamellas or from those lying beneath the surface.

Table 4.5: Average composition of α-Al solid solution in A1 measured by SEM- and TEM-EDX analysis

element	line	SEM wt. %	TEM wt. %
Mg	K_α	2.59	2.61
Al	K_α	97.11	97.39
Si	K_α	0.30	-
Mn	K_α	-	-
Fe	K_α	-	-
Sum		100	100

According to *[KUM00]*, the α-Al solid solution contains at the eutectic temperature of 2.44 wt.% Mg and 0.21 wt.% Si. These values are slightly lower than determined in the A1 alloy at room temperature. Since the composition of A1 alloy is hypereutectic and since it solidifies under non-equilibrium conditions, this may cause a slight deviation from the equilibrium composition of the primary and secondary dendrite arms of an α-Al solid solution.

Table 4.6: Average composition of the dendrite arms of α-Al solid solution in A2 and A3 alloys

element	alloy			
	A2		A3	
	SEM, wt.%	TEM, wt.%	SEM, wt.%	TEM, wt.%
Mg	2.76	2.44	2.63	1.76
Al	96.52	97.07	96.55	97.71
Si	0.30	-	0.30	-
Mn	0.41	0.49	0.51	0.53

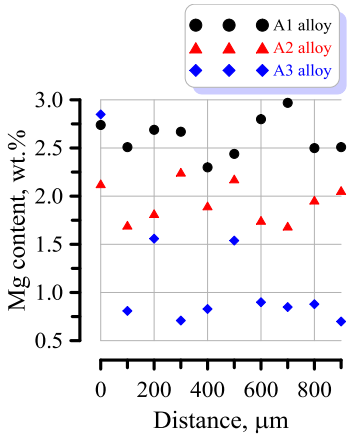

Fig. 4.11: Distribution of Mg across the dendrite arm in A1, A2 and A3 measured using TEM-EDX

For A2 and A3 alloys the EDX measurements of dendrite arms of the α-Al solid solution shown a similar average Mg content, and the Mn additions can be detected and measured. The results of the EDX analysis of A2 and A3 are summarized in Table 4.6. In Figure 4.11, the distribution of Mg across the dendrite arms in A1, A2 and A3 alloys is shown.

It was found that for all three alloys that the Mg content in the solid solution measured by SEM-EDX is higher than that measured in TEM. Because of the lower spatial resolution of the EDX measurement in the SEM, this could be due to the Mg-rich surrounding of the α-matrix.

The Mg distribution across the dendrite arm is not homogeneous and varies in the range from 2.20 to 3.00 wt.% for A1 alloy and between 1.70 to 2.30 wt.% for A2 alloy. The most inhomogeneous Mg distribution was found for A3. In addition, there was no difference found between the Mg content in the dendrite arm and in the area between eutectic Mg_2Si lamellas.

The Mn content, measured by both methods, is in the range from 0.35 to 0.55 wt.% what is almost equal to the Mn addition to A2 and A3 alloys (see Table 3.3). It is distributed nearly homogeneously inside the dendrite arms of α-Al solid solution.

The morphology of the primary Mn-containing phase, observed in A2, is shown in Figure 4.12. Its chemical composition is: Al - 74.45 at.%, Mn - 15.78 at.%, Si - 4.73 at.%, Fe - 0.04 at.%. This phase can be identified as $\alpha - \mathrm{Al(Mn, Fe)Si}$, what is often observed in commercial aluminum casting alloys after Mn alloying, *[WAN01]*.

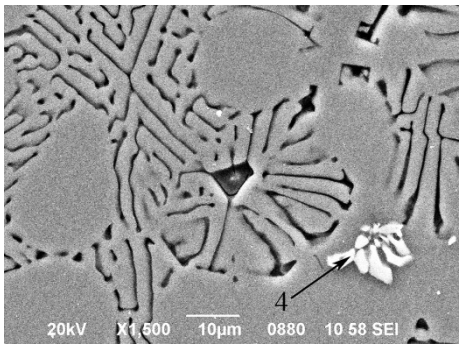

Fig. 4.12: Morphology of the Mn-containing phase in A2 alloy

The morphology of the (Al)+(Mg_2Si) eutectic is visible in Figure 4.12 and in Figure 4.13. In Figure 4.13 the Mg_2Si - lamella tips are shown and the points of the EDX SEM analysis are marked. The average element content is: Mg - 18.30 wt.%; Si - 34.10 wt.%, Al - 18.70 wt.%. The spectra show a relatively high oxygen content of 28.10 wt%, which makes the identification of the composition difficult.

In various EDX measurements, the oxygen content in the spectra was in the range from 20.00 to 40.00 wt.%. Even when oxide polishing suspension was not applied in the final polishing stage, the oxygen content of the lamellas remains on the high level. EDX measurements in TEM show similar results, with oxygen content of about 10.00 wt.%. This result implies that the Mg and Si containing intermetallics in the matrix of each alloy A1 - A3 exhibit a strong tendency for oxidising. The lowest oxygen concentration was measured in TEM EDX when the lamella was covered by a thin layer of Al matrix. In this case the quantification gives a lamella composition close to the stoichiometric composition of Mg_2Si. The measured

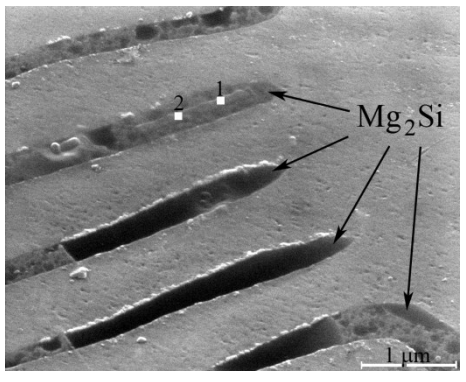

Fig. 4.13: Morphology of Mg_2Si lamellas in A2 alloy. Points of EDX analysis are specified as 1 and 2

composition was: Mg - 64.56 at.% and Si - 31.17 at.% which is very close to the Mg_2Si compound.

The explanation of the oxidation effect is that during electrolytic thinning of Al-Mg-Si alloys, Mg_2Si reacts with perchloric acid by the reaction:

$$Mg_2Si + 4HClO_4 = 2Mg(ClO_4)_2 + SiH_4 \qquad (4.1)$$

The presence of a small amount of O_2 causes further oxidation of the silane SiH_4 by the reaction:

$$SiH_4 + 2O_2 = SiO_2 + 2H_2O \qquad (4.2)$$

SiO_2 remains in the thin foil whereas $Mg(ClO_4)_2$ can dissolve in the electrolyte. Thus the origin of oxygen in EDX spectra's is a side-effect of the specimen preparation. In spite of this, the observed intermetallic lamella can be identified as Mg_2Si.

The polyhedral-shaped phase, denoted 3 in Figure 4.10, situated in the centers of eutectic colonies, has to be considered more in detail. According to the Al-Mg-Si phase diagram, the composition of alloy A1 is hypereutectic and lies in the two phase region where (Al)+(Mg_2Si) are in equilibrium. This Mg_2Si phase exists in two forms, namely as eutectic lamellas and as primary crystals.

The analysis of several crystals in the centers of eutectic colonies showed that they consist mostly of Mg and Si. In Figure 4.14, the morphology of such a primary phase in A2 is shown. Its composition measured by SEM EDX is: O - 28.17 at.%, Mg - 46.97 at.%, Al - 4.34 at.%, Si - 30.72 at.%. Considering that the oxygen originated from the oxidation of Mg_2Si and that Al comes from the matrix, these crystals can be identified as Mg_2Si intermetallic. Their position in the centers of eutectic colonies confirms that these crystals act as nucleation sites for eutectic growth. From Figure 4.14, the initiation of eutectic lamellas on the primary phase can be seen clearly.

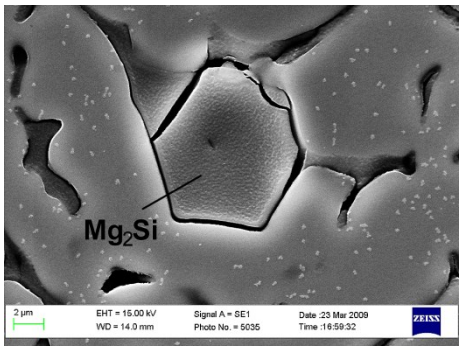

Fig. 4.14: Morphology of the primary Mg_2Si crystals observed in A2 alloy

SEM examinations of A1 and A2 alloys show that almost all primary Mg_2Si crystals contain a white particle in the center, Figure 4.15. From the position of the particle one can conclude that it is the nucleation site of the crystals. SEM - EDX analysis shows that the particles are enriched by oxygen and also contain Mg and Si in amounts of: O - 43.41 at.%, Mg - 14.55 at.%, Al - 18.30 at.%, Si - 2.89 at.%.

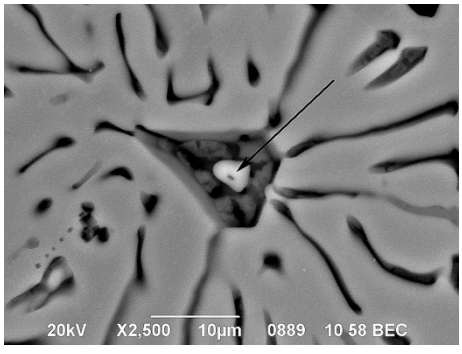

Fig. 4.15: Nucleation particle in the center of primary Mg_2Si crystal (marked by arrow) observed in A2

It is obvious that Al alloys, containing a relatively high amount of Mg (5.00 - 9.00 wt.%), will be saturated with oxides. Due to the high affinity between oxygen and Al alloy, at high temperatures surface oxidation of Al alloy melts is inevitable in case they are exposed to oxygen containing atmospheres. The oxides formed at the surface are readily entrained into the castings by turbulences during stirring of the melt and pouring. In addition, alloying elements in Al alloys, in particular Mg, will affect the oxidation mechanism and thus alter the structure and morphology of the resultant oxide particles. These particles play an important role for the subsequent solidification. The presence of Mg increases the oxidation tendency of Al alloys, and this has to be taken into account of course for alloys with relatively high Mg concentration. The oxidation reaction starts with the formation of amorphous MgO, $MgAl_2O_4$ or Al_2O_3 particles, depending on the magnesium content, which then transform into crystalline MgO, spinel $MgAl_2O_4$ or α-Al_2O_3 films. It has been reported by Fan et al. *[FAN09]*, that the oxide bifilms are favorable sites for the nucleation of a wide variety of intermetallics in many matrices. The results obtained in our Al-Mg-Si alloys show that the nucleation of primary Mg_2Si intermetallic starts on the surface of oxide particles and that these particles have most probably spinel structure because they contain Mg, Al and O.

So it was experimentally confirmed, for a cooling rate of 2 K s^{-1}, which is common for permanent mold casting (see Table 1.1), that the structure of hypereutectic Al-Mg-Si alloys consists of three phases, such as: dendrite arms of the α-Al, primary Mg_2Si crystals and (Al) + (Mg_2Si) eutectic. For the hypoeutectic A3 alloy, dendrite arms of the α-Al and (Al) + (Mg_2Si) eutectic are the phases constituents.

Considering the commercial AlMg5Si2Mn alloy, the specimen was cast using high pressure die casting, where the cooling rate is one order higher than for permanent mold casting (Table 1.1). In Figure 4.16 the microstructure of this alloy after PM and HPDC is shown. The microstructure of both samples consists of the primary α-Al grains (light areas) and (Al) + (Mg_2Si) eutectic (grey). In the PM alloy the dendrite arms of the α-Al exhibit a dendritic morphology surrounded by eutectic colonies. For the HPDC alloy α-Al prefers an equiaxed, globular-rosette morphology.

The average grain size in the HPDC specimen is about 15 - 35 μm, i.e. much smaller than in the PM alloy where the average length of the primary dendrite arms is well above 150 μm, varying from smaller columnar crystals close to the fast cooling surface to large equiaxed grains in the central part of the casting. Average grain sizes of AlMg5Si2Mn HPDC were reported by *[OTA09]*. There it was shown, that for 3 mm thick HPDC specimens the average grain size is about 12 to 25 μm, which is similar to what was measured in the present work.

The element distribution in the AlMg5Si2Mn HPDC alloy was measured using a TEM.

There is the widespread opinion, *[KOC96]* that increasing cooling rate respectively short solidification time could preserve more solute in the α-Al solid solution. Quantification of the EDX spectra however, reveals that the Mg and Mn content in α-Al grains is nearly the same as it was measured for dendrite arms in A2 alloy.

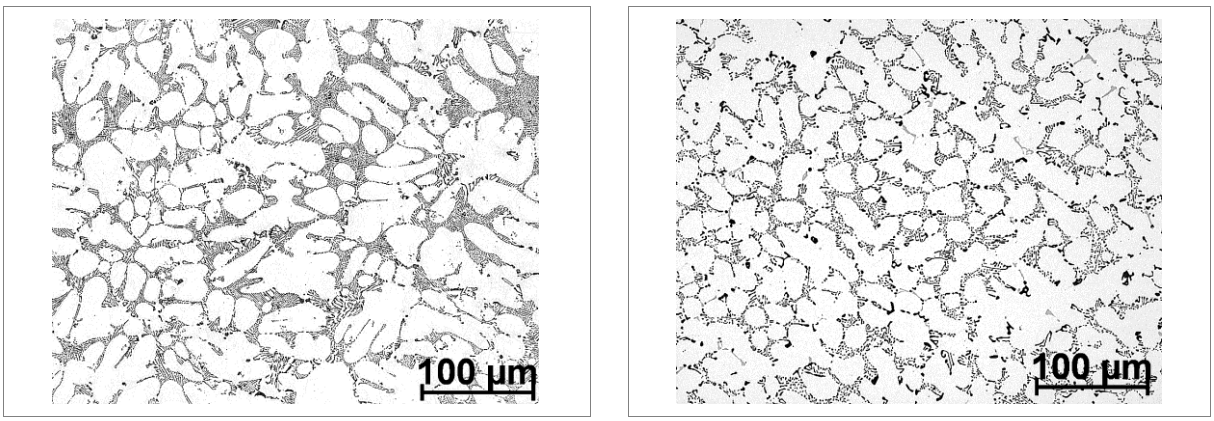

a. *b.*

Fig. 4.16: Microstructure of commercial AlMg5Si2Mn alloy cast into permanent mold (PM) (a) and after high pressure die casting (HPDC) (b)

The element distribution across the grain in Figure 4.17 shows that the average Mg content 1.90 wt.% varies in the range between 1.20 and 2.70 wt.%. A lower Mg content was detected in the area close to grain center and it gradually increases towards the grain periphery. The average Mn content was measured to be 0.45 wt.% with Mn homogeneously distributed across of the grain. A similar behavior was observed for Ti. For comparison, in A2 the Mg concentration was 2.76 wt.% and the Mn concentration 0.41 wt.% (Tabale 4.6). Hence an increase of the cooling rate cannot shift the saturation of the Al-based solid solution towards higher levels of foreign atoms.

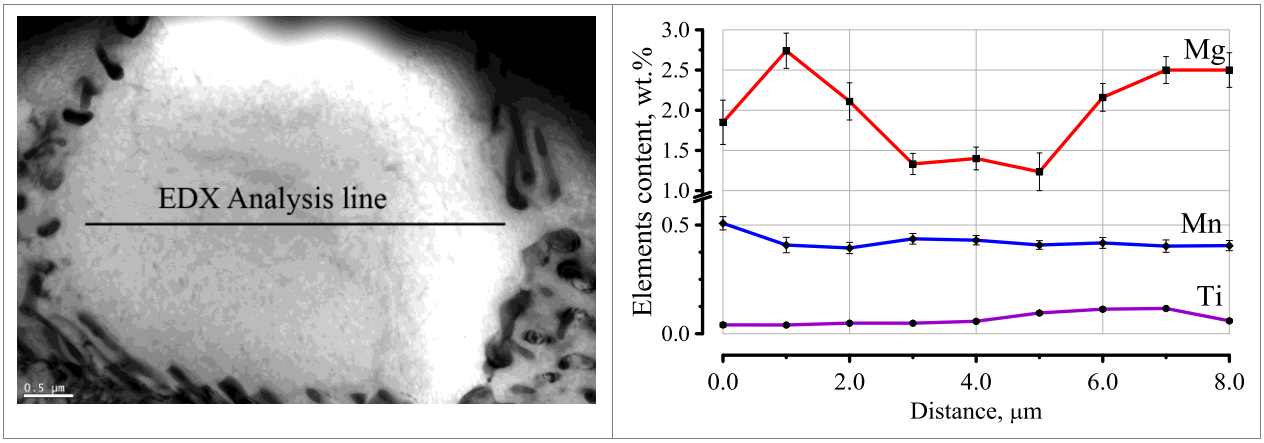

a. b.

Fig. 4.17: Bright field image of a separate grain in AlMg5Si2Mn HPDC commercial alloy (a) and distribution of Mg, Mn and Ti across the grain (b)

4.3.2 Effect of Li and Sc+Zr addition

The alloys of the B and C series differ from the series A by the presence of Li, respectively, Sc+Zr. In Figures 4.18 and 4.19 the microstructures of the alloys of the B and C series are shown. The microstructures of B1 and B2 alloys are similar to those of the A series and consist of four phases denoted as 1 - α-Al solid solution, 2 - (Al)+(Mg_2Si) eutectic, 3 - primary Mg_2Si crystals, and 4 - $\alpha - Al(Mn, Fe)Si$ phase. The same phases were detected in C1 and C2 alloys. No additional phases were detected.

There were no differences in the phase morphologies between B1 and B2 alloy (Figure 4.18). However, some features have to be noticed. The first one is that the size of primary Mg_2Si crystals decreases after addition of Li. The mean size of Mg_2Si in the Li-free A2 alloy particles was in the range from 15 to 20 μm, but after addition of 1.00 wt.% Li it fell below 10 μm (B2 alloy). The presence of Li changes the eutectic morphology from longer to shorter plates. Such a microstructural refinement could be due to an increased constitutional undercooling. The addition of any alloying element to the system causes a higher value of ΔT_c, which induces an instability in the Al–Mg_2Si binary system. This destabilizes the eutectic planar front, as it happens in systems with low G_L/V_{growth} ratio.

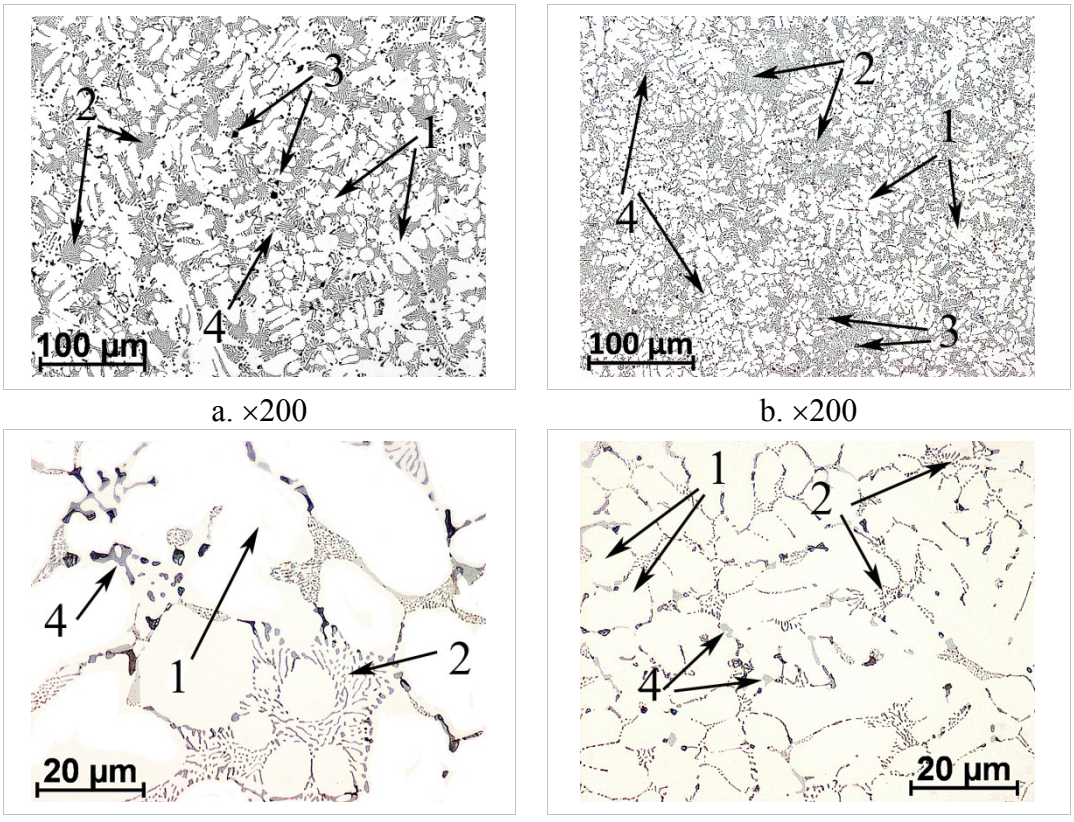

a. ×200 b. ×200

c. ×1000 d. ×1000

Fig. 4.18: Microstructure of B1 (a, c), B2 (b, d) obtained at different magnifications

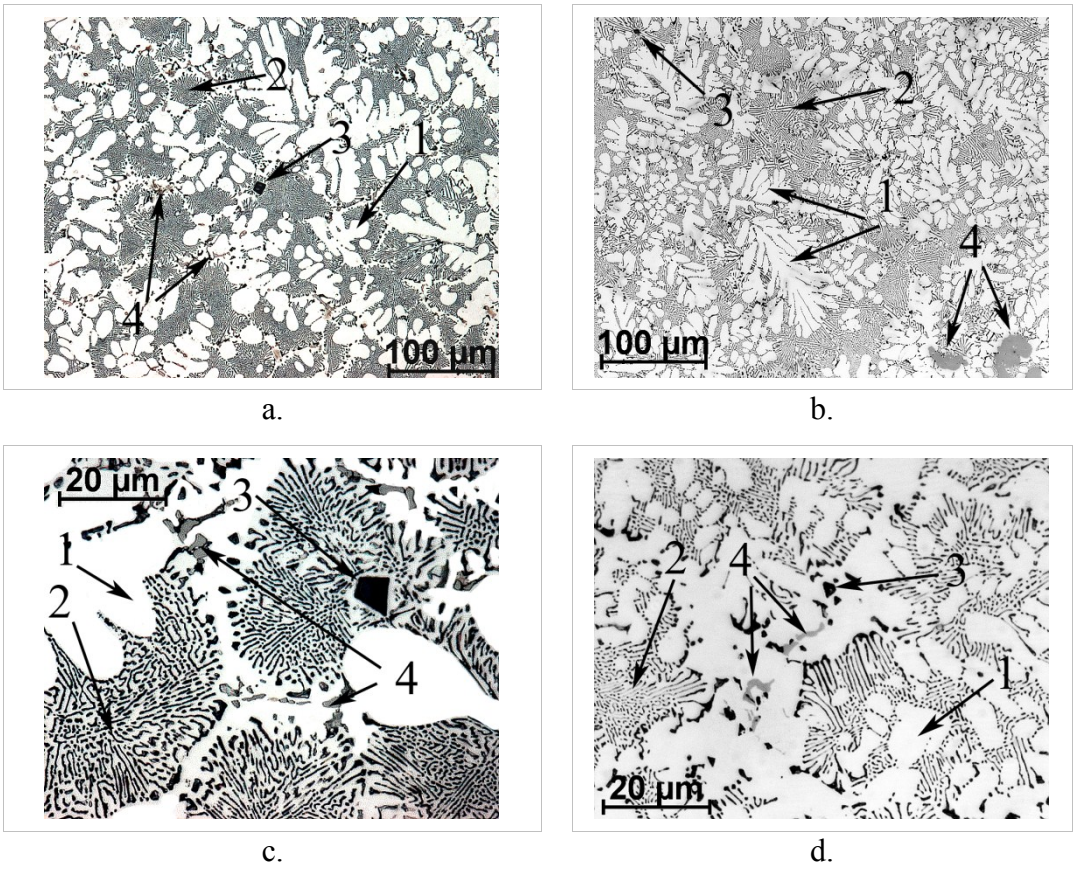

Fig. 4.19: Microstructure of C1 (a, c) and C2 (b, d) obtained at different magnifications

EDX analysis of B1 and B2, performed along the α-Al dendrite arms, showed that the Mg and Mn content is higher in the B2 alloy in comparison to B1 and A2. This distribution in the solid solution is shown on Figure 4.20. It can be seen that in presence of 1.00 wt.% Li, the average Mg concentration in the matrix is about 2.50 wt.% (B2 alloy) in comparison to 1.90 wt.% for A2 alloy.

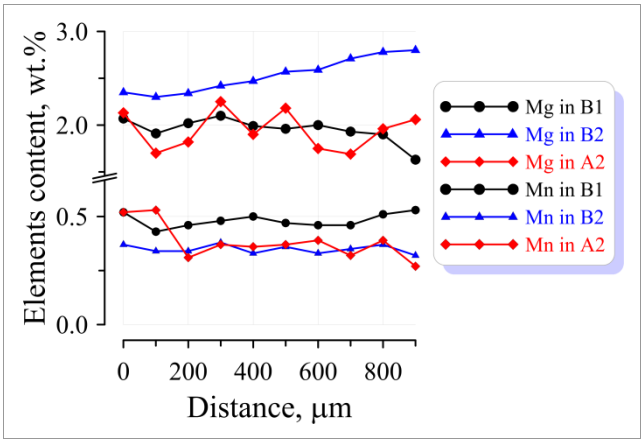

Fig. 4.20: Distribution of Mg and Mn in the dendrite arm in B1, B2 in comparison to A2

The Mn content in B1 in the solid solution is about 0.30 wt.% and on the same level as for A2 alloy. The Si content in α-Al for B1 and B2 is below the limit of detection.

For the Sc+Zr containing alloys C1 and C2, no pronounced refinement of the phase constituents was observed. However, EDX analysis of the aluminum matrix shows a significant reduction of the average Mg content down to 1.40 wt.%, as shown in Figure 4.21.

The Mn content remains the same for both alloys and is about 0.40 wt.%. The average Sc content in the matrix was measured to be 0.18 wt.% for C1 and 0.20 wt.% for C2 alloy.

These values are very close to the amount of Sc added to the C1 and C2 alloys and confirm that no Sc-containing primary phases formed during solidification.

Summarizing the obtained results one can state that Li or Sc+Zr within the investigated limit both do not change the phase equilibrium in the Al-Mg-Si system, just produce an additional saturation of the solid solution. This, however, could enhance the mechanical properties by solid solution strengthening. Indeed hardness and microhardness tests of as-cast alloys shows that Li and Sc+Zr containing alloys have the highest values of HB and $HV_{0.05}$. They approach the hardness of the high strength A201.0 casting alloy (Figure 4.26) and are higher than the commercial A356.0 alloy.

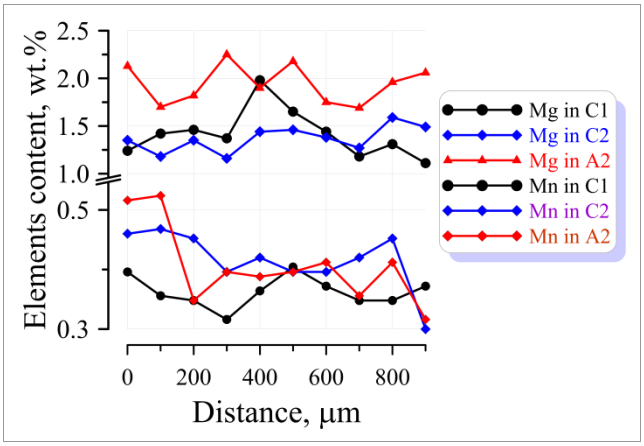

Fig. 4.21: Distribution of Mg and Mn in the dendrite arm in the C1, C2 alloys and in comparison to A2 alloy

4.3.3 Structure of Al-Mg-Ge alloy

The structure of D1 and D2 is given in Figure 4.22. Similar to the Al-Mg-Si-Mn alloys A2 and A3 alloys, four phases can be distinguished in the alloy structure. The first one is the aluminum matrix which appears white. For the selected composition, the fraction of matrix is lower than in A2 alloy and can be seen as thin layers between eutectic grains. In D2 alloy, the area occupied by α-Al is slightly larger than in D1 alloy. The second phase is the $(Al)+(Mg_2Ge)$ eutectic which has the morphology of fine short rods. In D2 alloy, which contains Li, the Mg_2Ge rods are shorter than in D1 alloy.

The third phase consists of primary Mg_2Ge crystals positioned inside of eutectic colonies. Their size is different for D1 and D2 alloys. For D1 alloy the average size is in the range between 60 and 100 µm, the Li-containing alloy D2 shows a smaller size of the primary crystals in the range between 15 and 30 µm. This decrease of the size of the Mg_2Ge compound confirms the modification effect of Li on the primary crystals, as found in chapter 4.3.2 for B1 and B2.

Light microscopy images show that not all these crystals are monolithic. In Figure 4.23 two different morphologies of Mg_2Ge in D1 are shown, namely dendritic and polyhedral. According to Li et al. *[LIC11]*, primary intermetallic compounds such as Mg_2Si may grow from the parent melt with four different morphologies, such as: complete octahedron, hopper crystal, truncated octahedron and dendrite. Presumably Mg_2Ge grows in a similar mode as magnesium silicide, which takes place as follows. At a early stage of growth, Mg_2Ge particles exhibit a multibranch-like morphology, i.e. they are dendritic.

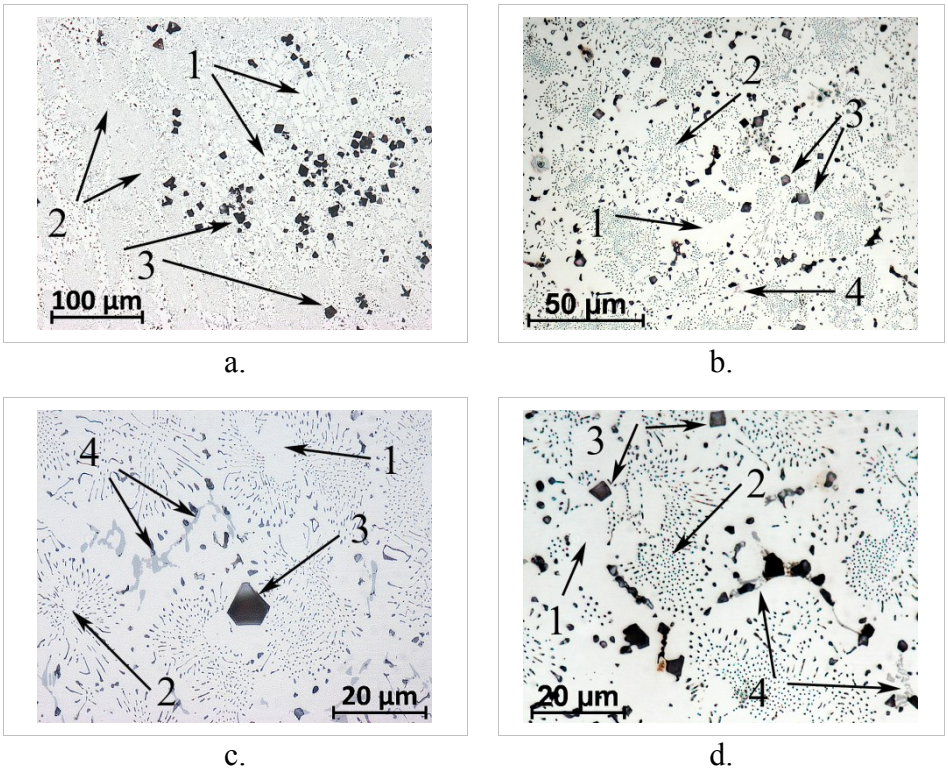

Fig. 4.22: Microstructure of D1 (a, c) and D2 (b, d) obtained at different magnifications

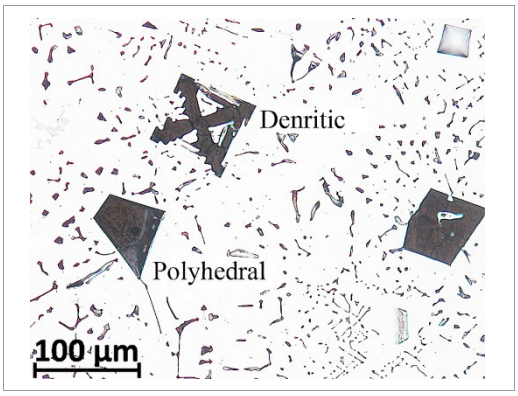

Fig. 4.23: Morphologies of Mg_2Ge primary crystals observed in D1

As the growth proceeds, the multi-branch particles subsequently change their shape by crystal growth filling the spaces between the branches, which lead to an octahedral outline, disturbed by symmetric hollows in the center of the surfaces. Particles with symmetric hollows are typical characteristics of the Mg_2Ge crystals. This means, however, that the primary crystal growth was terminated. It has been confirmed that impurities, in case of D2 this is Li, can be adsorbed on the crystal surface, leading to a retardation of the growth rate of the face which explains the observed hallows, *[BUC51]*.

The fourth phase is the Mn-containing phase distributed in the solid solution area between eutectic grains. It has uneven morphology, as found in the alloys A1 - A3. The TEM EDX analysis shows that the average Mg content in the α-Al solid solution is in the range between 0.30 and 0.60 wt.% for D1 and D2. The measured Mg distribution in the dendrite arm for both alloys in comparison to A2 is represented in Figure 4.24.

The average Ge content was measured to be 0.60 - 1.00 wt. % for D1 and somewhat lower in D2 (0.30-0.50 wt.%). The Mn content in α-Al is very close the added amount 0.60 wt.%.

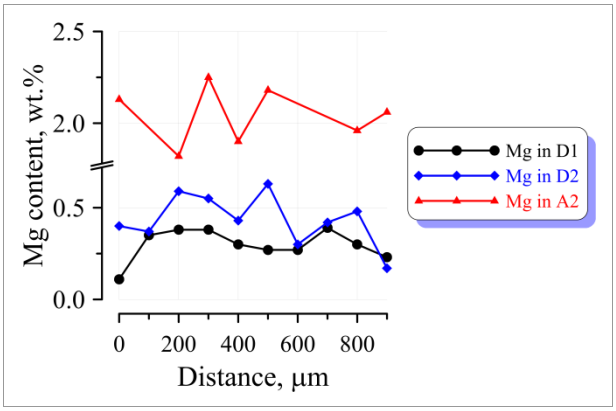

Fig. 4.24: Distribution of Mg across the α-Al dendrite arm in D1 and D2 in comparison to A2

The Mg_2Ge compound consists of Mg - 65.00 at.%, Ge - 35.00 at.% from the equilibrium Mg-Ge phase diagram, *[NAY84]*. The result of the EDX analysis of the Mg_2Ge lamella is: Mg - 46.60 at.%, Ge - 25.90 at.%, Mn- 0.10 at%, Al - 20.00 at%, O - 7.10 at.%. The measured Ge content is close to the concentration in the equilibrium Mg_2Ge compound, whereas the Mg content is lower than the equilibrium concentration. This corresponds to the EDX results of the Mg_2Si lamella in A1 and A2 alloys, where this effect was explained by the oxidation of Mg. The measured Al and Mn concentrations probably originate from the surrounding matrix.

4.3.4 Conclusions of the investigations of the as-cast materials

All alloys subjected to the research program behave similarly during melting and solidification. The measured eutectic melting temperatures are close to the established equilibrium eutectic temperatures taken from phase diagrams. Based on these DSC results, a temperature for solution treatment can be defined, taking into account that it should be as close as possible to the liquidus temperature in order to obtain the best solution of the constituents. Overheating i.e. exceeding the initial eutectic melting temperature must be avoided.

For commercial casting alloys such as A356.0 and A201.0, the parameters of solution treatment (temperature, time) are well known. It was reported by *[SHI90]*, that the optimum temperature for A356.0 is 540.0°C, which is about 30.0°C lower than the eutectic melting temperature in the Al-Si system. Increasing the solution treatment temperature up to 560.0°C resulted in melting of ternary eutectics which are predominantly Fe-rich phases, which decreases the mechanical properties of the alloy dramatically. The solution treatment temperature of Al-Mg-Si casting alloys is specified in literature by a single publication, *[PET12]* where 570.0°C was used for an AlMg5Si2Mn alloy casted in a permanent mold. This temperature is about 25.0°C lower than the eutectic melting temperature.

The structure of the alloys confirms that they belong to a quasi-binary type of the equilibrium phase diagram. Additional alloying with Li or Sc+Zr does not change the phase equilibrium in both Al-Mg-Si and Al-Mg-Ge systems.

No additional phases were detected, but both additives produced a modification of the interlamella spacing λ as presented in Figure 4.25. It shows, that all alloys containing Li (B1, B2, D2) or Sc+Zr (C1, C2) have a finer eutectic structure than those, without these additives (A1, A2, A3, D1). The D2 alloy shows an interlamellar distance of 0.65 µm and, in general, Li causes a finer structure.

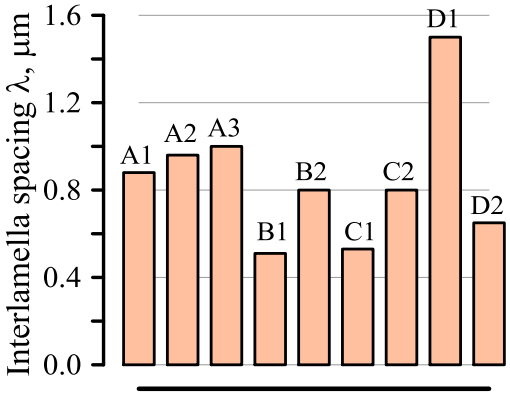

Fig. 4.25: Interlamellar spacing in A1 - B2 alloys

4.3.5 Hardness of the as-cast material

The mechanical properties of the base alloys and after addition of Mn, Li and Sc+Zr were measured by Brinell hardness (HB) and microhardness ($HV_{0.05}$).

The results are summarized in Figure 4.26. HB of A2 alloy containing 0.60 wt.% Mn is higher than that of the A1 base alloy, which is typical for solid solution strengthening. Reducing the Mg content from 7.00 to 6.00 wt.% (A3) results in a drop of both, HB and $HV_{0.05}$. The Li and Sc+Zr addition in B1-C2 show an significant effect on the hardness compared to the Al-Mg-Si alloys A1, A2.

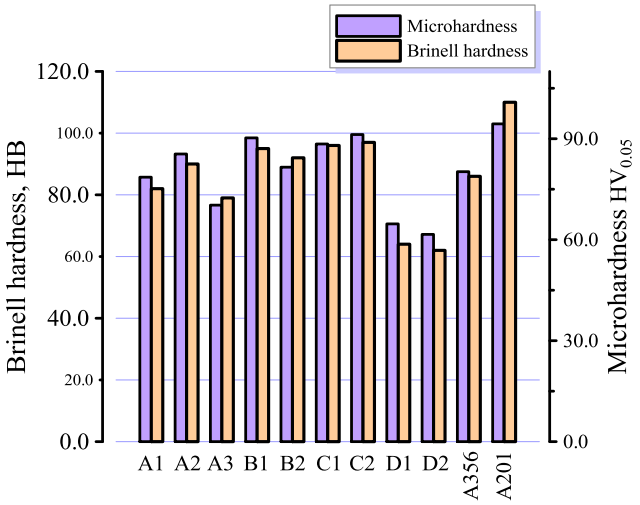

Fig. 4.26: Brinell hardness and microhardness of Al-Mg-Si casting alloys in as-cast state in comparison to commercial A356.0 and A201.0 alloys

4.4 Precipitates in as-cast Al-Mg-Si and Al-Mg-Ge alloys

The TEM examinations of all experimental alloys showed that the α-Al solid solution is not homogeneous. The α-Al dendrite arms contain plate-like precipitates. The plates are elongated along a certain direction and they are arranged parallel to each other's resulting in a pattern like a zebra crossing, as can be seen best in Figs. 4.27 g and i. On one side of this pattern a curved black line is visible (Figs. 4.27 b and 4.28), which could be identified as a dislocation. This generalization is true for all studied alloys as can be seen in Figure 4.27. There the fan-shaped, respectively zebra crossing shaped, pattern is denoted 1, the eutectic lamella 2.

The exact chemical composition of the precipitates in the specimens could not be measured, because the plates are so thin, that the surrounding matrix material contributes much

more to the EDX spectrum than the precipitate. Qualitatively, spectra collected from such areas showed an enrichment by Mg and Si.

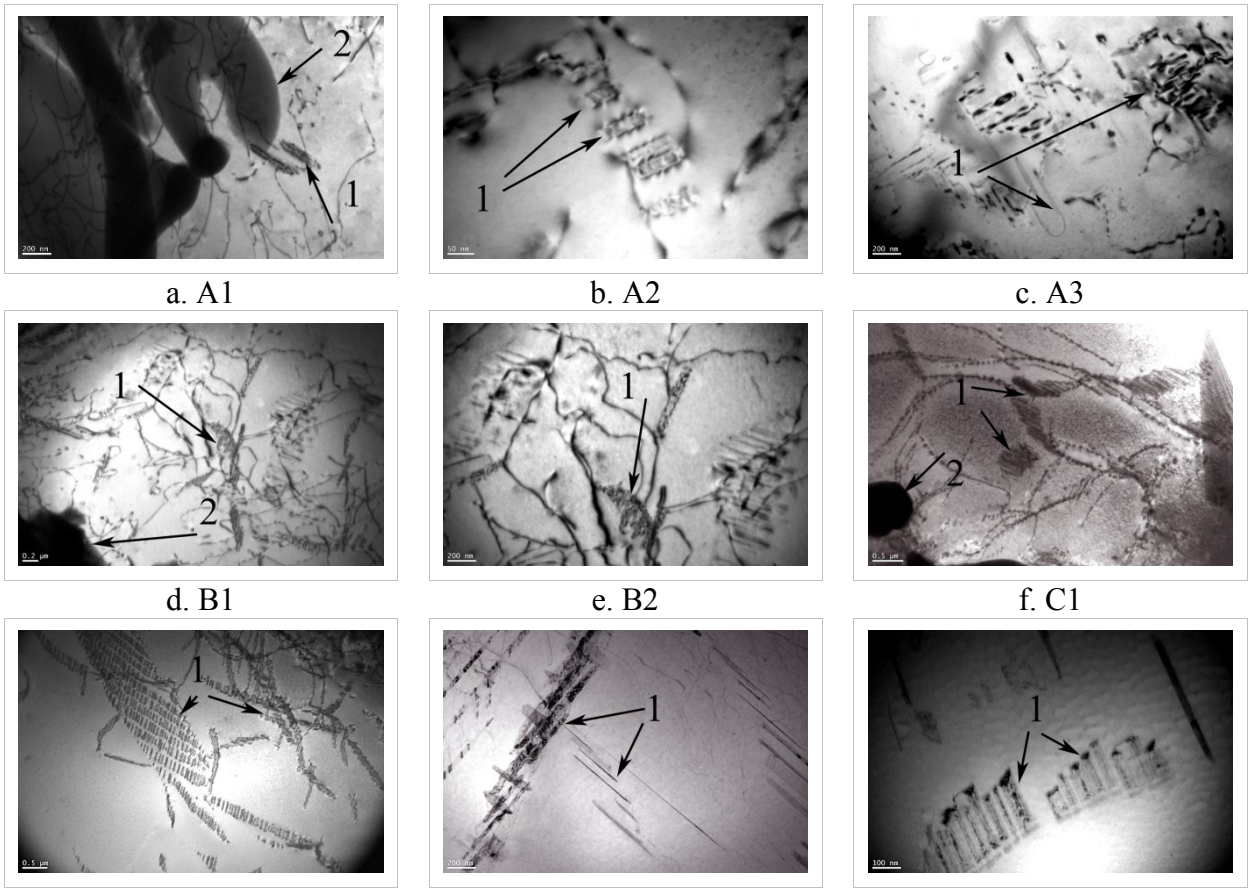

a. A1 b. A2 c. A3

d. B1 e. B2 f. C1

g. C2 h. D1 i. D2

Fig. 4.27: Bright field images of precipitates observed in all studied alloys

This fan-shaped structure is an effect of natural aging. The TEM investigation of A1 and A2 performed 3 hours after casting showed that there are no precipitates inside the α-Al matrix. They appear in alloys examined after 3 days aging at room temperature. Their growth could be observed sometimes directly in the TEM, when the TEM-foil heated up by inelastic scattering. The average size of the precipitates was in the range between 80 and 120 nm. The alloy composition has no effect on the precipitate size.

An enlarged view of the precipitates in C1 is shown in Fig. 4.28 a. The schematic presentation of the zebra crossing structure is given in Fig. 4.28 b. Tilting the specimen to different zone axes and using different reflections for diffraction contrast, allowed to reconstruct the geometry of this structure and the nature of the dislocation. The plates are lying in (100) planes; their long axis is [010]. The dislocation has the Burgers vector $\vec{b} = \pm\frac{1}{2}[10\bar{1}]$.

It connects the plates on the right side in a curved line which can be described by the average direction $[\bar{6}\ \bar{2}\ \bar{8}]$ or simplified [101].

So the plates are not lying in one (100) – plane, but are shifted in [100] and [001] direction. The dislocation forms a loop around each precipitate. Along the long side of the precipitate the dislocation segment has the line vector [010] and the Burgers vector $\vec{b} = \pm\frac{1}{2}[10\bar{1}]$ i.e. it is an edge dislocation. The TEM micrograph in Figure 4.28 c shows the existence of a solute depleted zone around the precipitates.

Additional information about the precipitations in as-cast state were obtained by TEM examinations of the commercial A201.0 (Al-Cu) and AlMg5Si2Mn alloys in as-cast state. It could be shown that the solid solution in A201.0 also contains such plate-like precipitates aligned along dislocation (Figure 4.29 a). The fraction of precipitates is not very high and comparable to that in A1. The most intriguing results were observed in TEM investigations of the high pressure die cast alloy AlMg5Si2Mn.

Bright field images of the precipitates are shown in Figs. 4.29 b and c, which give an impression of the high precipitation density. The precipitates in AlMg5Si2Mn HPDC are found in the α-Al dendrite arms in the center and close to the eutectic as well. They form without any heat treatment.

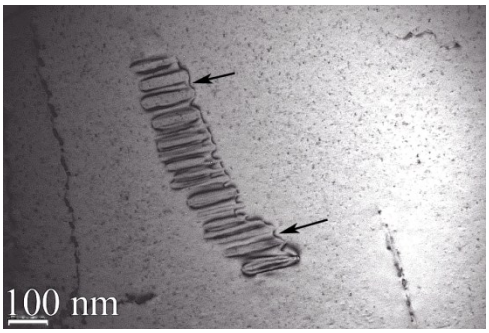

a.

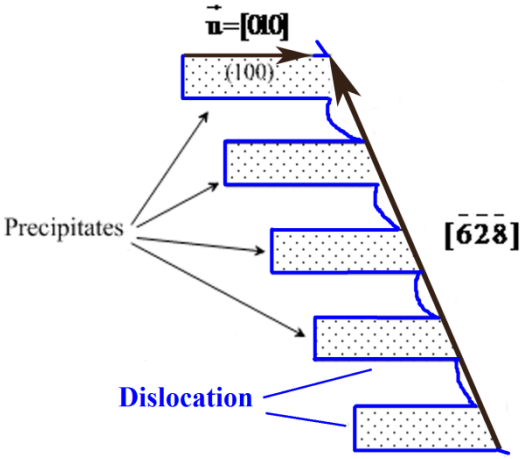

b.

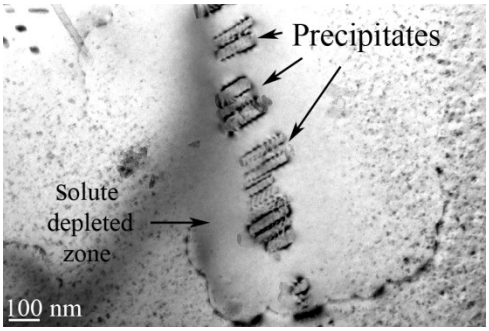

Fig. 4.28: Enlarged view of precipitates in C1, dislocation marked by arrows (a), schematic presentation of precipitates and dislocation (b) and solute depleted zone around precipitates (c)

In summary, the TEM investigation gave:

1. for all alloys, precipitates are aligned along dislocations and show a similar plate-like morphology;
2. the precipitation density is higher in C1 and C2 than in all other alloys;

3. the precipitates are preferentially distributed in the solid solution area, however they can be found also between the eutectic lamellas;
4. the precipitates are not formed earlier than 2 days after casting;
5. the precipitates contain mostly of Mg and Si.

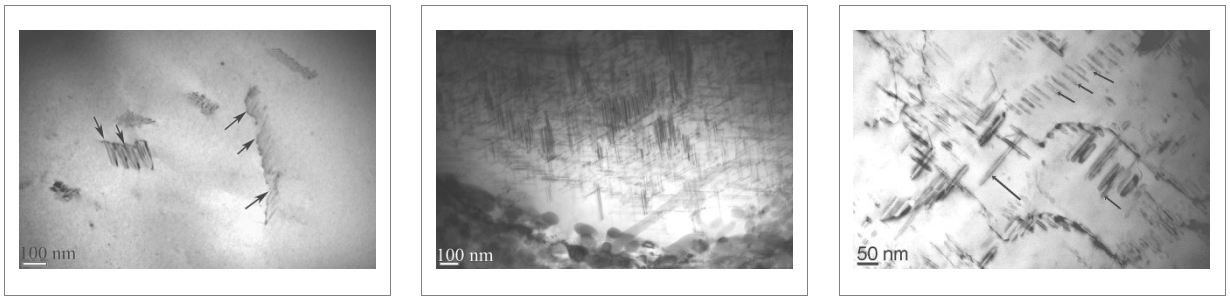

a. b. c.

Fig. 4.29: Bright field images of precipitates observed in as-cast state in A201.0 (a) and in AlMg5Si2Mn HPDC (b, c)

From the alignment of the precipitates along dislocations, it is most likely that they form via heterogeneous nucleation and that dislocations provide nucleation sites for their growth. Heterogeneous nucleation of precipitates in Al-Mg_2Si alloys on dislocations is a well established mechanism during the decomposition of the solid solution. However, in most cases this effect was considered for wrought alloys undergoing artificial aging. For casting alloys in cast condition however, the direct formation of such a type of precipitates was not established yet. The observation, that the high dislocation density in AlMg5Si2Mn HPDC alloy is connected with a high density of precipitates supports the presumption, that the precipitates nucleation on dislocations. In AlMg5Si2Mn HPDC, the density of dislocations is much higher than that for all specimens cast into permanent mold, i.e. A1 - D2. Probably, the reason for the dislocations are extrusion stresses during the HPDC process and thermal stresses between α-Al and Mg_2Si intermetallics. When no pressure is applied, as during mould filling and solidification, the precipitates density is much lower. So obviously pressure plays a more important role for dislocation generation than thermal stress. It has also to be mentioned that the different cooling rate doesn't influence to growing and the size of this precipitates.

4.5 Discussion

4.5.1 Nucleation of Mg_2Si primary crystals

It is well accepted that a fine grain size of aluminum alloys usually results in an increase of the in mechanical properties, such as ambient temperature strength, toughness and ductility. An effective method to achieve a fine grain structure is controlled solidification using grain

refiner to promote heterogeneous nucleation. A typical example is the inoculation in Al alloys, with particles based on the Al-Ti-B, *[DAV70]* and Al-Ti-C, *[BAN86]* systems. The phases TiB_2 and TiC are believed to be potent substrates on which Al grains nucleate heterogeneously. However, studies of Greer et al. *[GRE03]*, show that nucleation of α-Al doesn't start by direct attachment of atoms to the surface of TiB_2 particles, but on an intermediate Al_XTi layer. So it is a multistep nucleation. Such a multistep nucleation was first described by Fan et al. *[FAN09]*, investigating the reduction of the size of primary grains in a Mg-based casting alloy and a Al-Zn-Si alloy. Such a multistep mechanism was found not only for the nucleation of α-aluminum but also for some intermetallic compounds present in conventional Al-based alloys. Examples of multistep nucleation were already given in section 1.3.1 (Figures 1.9 and 1.11) and additional prove was given in Section 4.3.1 where the oxide particle was observed in the center of primary Mg_2Si crystals (Figure 4.15). Another example with an oxide inclusion situated in the center of a AlScZr primary particle is presented in Figure 4.30 a. The presence of an oxygen peak is an indication that the particle is an oxide inclusion. Fig 4.30 b shows the corresponding EDX spectrum.

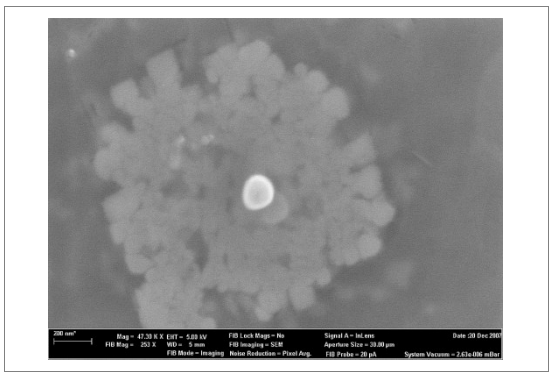

a.

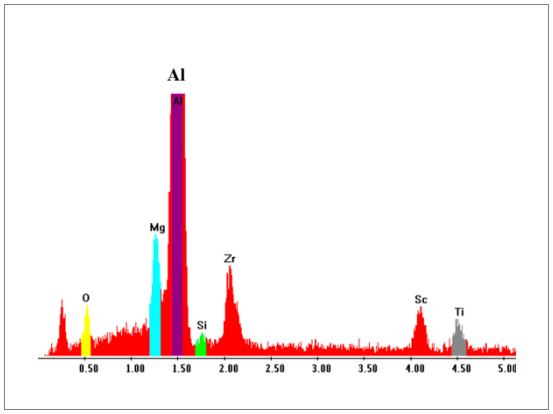

b.

Fig. 4.30: AlScZr primary phase in C1 alloy containing an oxide inclusion in the center (a) and EDX spectrum of the particle (b)

Fan et al. observed oxide particles inside of Al_3Ti crystals and Al_8Mn_5 primary intermetallic particles. Thus one can conclude, when the oxide particles are dispersed in the melt they promote the heterogeneous nucleation via a multi-step nucleation mechanism. Since oxides are always present in aluminum alloy melts, this refinement of primary intermetallic phases by multistep nucleation is expected to be the leading mechanism for of their formation.

4.5.2 Formation of the precipitates

Investigations performed by Norman et al. *[NOR98]* on the solidification behavior of dilute Al-Sc alloys showed that in Al-Sc and Al-Cu-Sc alloys in as-cast state the grain boundaries migrate during cooling, leaving behind a fan-shaped array of precipitates. The widely accepted mechanism for the formation of this type of precipitates is discontinuous precipitation. The supersaturated solid solution decomposes behind a migrating grain boundary, pushed

forward by the developing precipitates. This particular process is called cellular precipitation. In the following, this term will be used instead of discontinuous precipitation, which is a more general term for phase transformations *[DOH96], [FOU72], [SUN72]*.

The explanation of the formation of fan-shaped arrays of precipitates in Al alloys comes from the early works of Blake et al. *[BLA85]*, Nes *[NES77], [NES72]* and Williams *[WIL81]*, where the precipitation of Al_3Zr from solid solution was studied. The image in Figure 4.31a was selected from the work of Norman et al. *[NOR98]* and illustrates the fan-shaped array of these precipitates in comparison to the ones observed in C1. In *[HOR84]* the formation of the fan-shaped precipitates is described: if the mismatch between precipitate and matrix lattice exceeds a critical value, the precipitates arrange themselves in rows, which may coalesce to form rods. The preferential orientation of the rods is determined by the elastic anisotropy of the matrix.

In as-cast state the average grain size in the alloy Al does not fall below 60 - 100 μm even if it was well grain refined. Therefore the distance, which a grain boundary moves, when leaving behind the fan-shaped arrays of precipitates, is in average half of this value. However, it was observed by Williams et al. *[WIL76]* that the grain boundary in Al-Li alloys migrates only a distance less than 1 μm leaving discontinuous precipitates behind. Though the initiation of the precipitation process starts immediately after the first fraction of solid has formed, i.e. the precipitates should be present in the matrix immediately after complete solidification. This explanation is not consistent with our observations of the precipitation process in the alloy A1-D2, because, as mentioned above, three hours after casting no precipitates were observed in the structure of all studied alloys. They appeared only after two days delay and this time period can be taken as the incubation time for natural aging. Thus the most likely formation mechanism of the precipitates is nucleation on dislocations.

According to Doherty *[DOH96]*, in a precipitation reaction there is a change from a single phase structure, α, to a two phase structure, $\alpha+\beta$, similar to a cellular precipitation reaction. The thermodynamic explanation of the driving force for this solid state transformation is the same as represented in Chapter 1 for the liquid-solid transition (Section 1.3), namely the reduction of the Gibbs free energy from the original to the final structure.

In the first step of the transformation, a thin platelet of the new phase, called β, forms within the matrix. This new crystal, the nucleus, has a completely different composition and structure from the parent phase α.

However, for solid state transformations, the heterogeneous nucleation is also possible on defects in the parent phase. Such defects are grain boundaries, dislocations, stacking faults or the interfaces of previously formed precipitates. The reason is that the energy of nucleus formation is reduced by that amount of defect energy, which was consumed by the nucleus during its

formation. It was shown by Cahn that dislocations are strong nucleation sites for heterogeneous nucleation, *[DOH96]* and such a nucleation on dislocations is discussed by Nes *[NES74]* for NbC in steels.

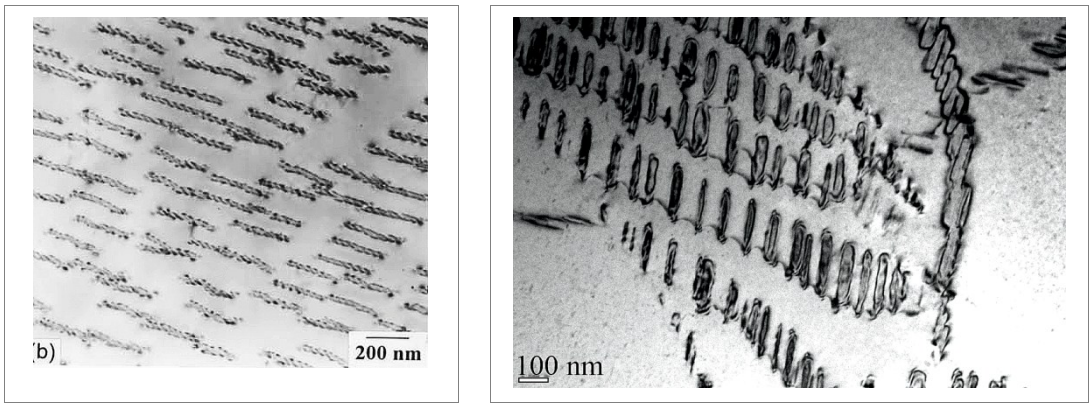

a. b.

Fig. 4.31: Bright field images of discontinuous precipitates observed in Al-0.7 wt.% Sc, [NOR98] (a) and in C1 (b)

The edge dislocations found (Figure 4.28 b) one can illustrate as extra half planes of atoms in the crystal lattice. This gives rise to lattice strains around the dislocation. These local stress fields attract foreign atoms. It was demonstrated by Jacobs, *[JAC69]* that needle-shaped precipitates in Al-Mg_2Si alloys form via heterogeneous nucleation on dislocations and grow along a <100> matrix direction in heat treated material. It was reported by Guyot et al. *[GUY74]* that the precipitate nuclei in Al-Cu alloy formed on the expanded side of a dislocation.

In Al-Mg_2Si, heterogeneous nucleation of precipitates alloys on dislocations is a well established mechanism during the decomposition of the solid solution. However in most cases this effect was considered for wrought alloys undergoing artificial aging or at least after solution heat treatment. For casting alloys the precipitation reaction in as-cast condition was not reported earlier and now this effect is experimentally confirmed. In the following sections it is called natural aging.

4.6 Summary

The results of Chapter 4 can be summarized as follows:

- From DSC runs the eutectic melting temperatures of Al-Mg-Si and Al-Mg-Ge alloys were determined. They are 595.0°C and 629.0°C, respectively. These data fit well to the eutectic temperatures obtained from equilibrium phase diagrams. Alloying of Al-Mg-Si alloys by Li or Sc+Zr and Al-Mg-Ge by Li does not change the sequence of the reactions observed during heating and cooling, i.e. the phase equilibrium remains unchanged. This was confirmed by microstructural analysis, where no additional phases were detected.

- The structure of Al-Mg-Si and Al-Mg-Ge alloys consists of four phases. The first one is the α-Al in form of dendrites with long primary arms. The second phase is (Al)+(Mg_2Si) eutectic in form of long Mg_2Si lamellas separated by α-Al. The third phase are primary Mg_2Si crystals, respectively Mg_2Ge. The fourth phase is AlMnSi in A1-C2, in D1-D2 the composition is not known.
- The average Mg content in the α-Al solid solution for all alloys was about 2.00 wt.%. The highest average Mg content was detected in alloy B2 (2.70 wt.%) and the lowest in alloy C2 (1.50 wt.%) indicating that the alloying with Li conserves Mg in the matrix. This is probably due to the fact that Li decreases the size of primary Mg_2Si crystals. For all studied alloys Mn is evenly distributed in the aluminum grains. Its content was detected to be 0.40-0.50 wt. %, which is nearly equal to its addition to the melt.
- It was established that the initiation of the growth of primary Mg_2Si crystals in Al-Mg-Si alloys takes place heterogeneously on the surface of oxide inclusions, which are either alumina or spinel for Mg-rich alloys. These results support the multistep nucleation hypothesis: first, nucleation of primary intermetallic on the surface of oxide particles, second, nucleation of primary α-Al or eutectic phases.
- During natural aging, in casting alloys the decomposition of the solid solution takes place, resulting in the formation of plate-like precipitates. These precipitates are most probably, β'' Mg_9Si_5 phase. This supposition is based on the literature data. In case of particles having two large dimensions and on very small X-ray diffraction can't give direct prove of the precipitate type. EDX measurements also cannot give an answer about precipitates composition because of the analyzer resolution. The mechanism of their formation is heterogeneous nucleation on dislocations. Similar precipitates were found in A201.0 (Al-Cu) and AlMg5Si2Mn HPDC alloys confirming that aluminum casting alloys tend to natural aging without preliminary heat treatment.

5 Solution treatment of Al-Mg-Si and Al-Mg-Ge alloys

5.1 Introduction

Solution treatment is the first step of heat treatment applied for casting alloys and the main purposes are:

- saturation of the solid solution with alloying elements via dissolution of primary phases;
- homogeneous distribution of the alloying elements inside of the α-Al dendrites.

From the other hand, solution treatment of casting alloys, especially Al-Si, produces side effect such as the spheroidization of eutectic lamellas. It was reported by Shivkumar et al. *[SHI90]* that an increase of the solution treatment temperature of the commercial alloy A356.0 up to 560.0°C resulted in a very quick spheroidization. Such a effect can be expected also in Al-Mg-Si and Al-Mg-Ge systems containing (Al)+(Mg_2Si)/(Mg_2Ge) eutectics. The solution treatment temperature for the alloys under consideration was chosen to be 575.0°C. This is 20.0°C lower than eutectic melting point for Al-Mg-Si, respectively 50.0°C for Al-Mg-Ge alloys.

It can be expected, that the precipitates having formed during natural aging from the as-cast state, may dissolve during high temperature treatment, resulting in a precipitates free matrix. Thus this chapter considers the structural changes, which occurred in the specimens A1 - D2 during solution treatment.

5.2 Calorimetric studies of the homogenization of Al-Mg-Si and Al-Mg-Ge alloys

Before a large piece of a specimen was solution treated, a very small piece of each alloy was tested using isothermal DSC. The specimens were heated up to 575.0°C with the rate of 10 K min^{-1} and held for 24 hours.

From a theoretical point of view, during solution treatment two processes are expected to occur, namely:

- spheroidization of eutectic lamellas what is established for Al-Si alloys, but not yet confirmed experimentally for Al-Mg-Si and Al-Mg-Ge;
- dissolution of plate-like precipitates formed during natural aging.

DSC traces for alloys A1 - C2 are shown on Figure 5.1. Li containing alloys were not subjected to DSC experiments due to their strong tendency to oxidation.

Preliminary investigations showed a strong exothermic heat effect at the solution treatment temperature even under vacuum. This effect is attributed to the oxidation of the very small specimen (~ 0.002 g), which are always used for DSC studies and thus the Li containing alloys B1, B2 and D2 were excluded from the isothermal DSC runs. From these observations one can conclude that for practical purpose homogenisation of Li-containing alloys it is necessary to use furnaces with protective atmosphere to reduce the oxidation and degassing effects.

It was found that all obtained isothermal DSC traces are similar: they do not show any substantial heat effects over a whole period of solution treatment, Figure 5.1. The difference of the heat flow values for different alloys is very small. The vary between -0.18 and -0.08 mW mg^{-1}.

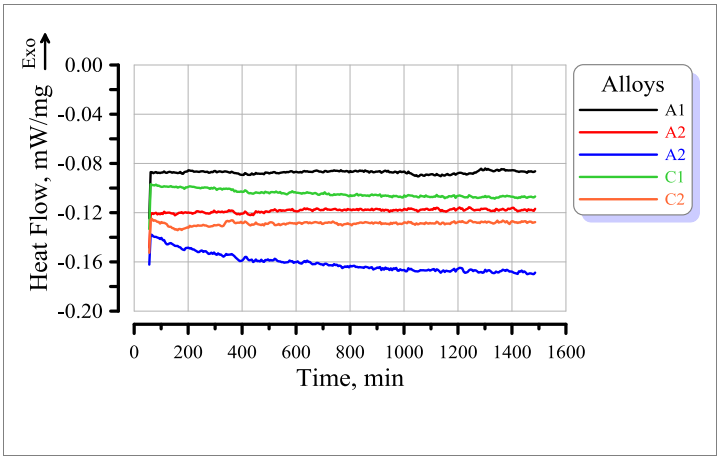

Figure 5.1: DSC traces of the alloys A1 - C2 held at 575.0℃ for 24 hours

It is obvious that the fraction of precipitates in as-cast state is not very high, (Figure 4.27), so they do not produce a pronounced heat effect during their dissolution. The fraction of eutectic in Al-Mg-Si alloys, however, is high, about 45%, so if spheroidization of Mg_2Si would show a heat effect it would be visible in the DSC curves. However, no heat effect from spheroidization was detected.

Thus, based on the DSC runs, it can be concluded that all studied alloys do not undergo any phase transformation over a time period of 24 hours heating at 575.0°C. Heat effects related to incipient melting were not detected too, specifying that the applied solution treatment temperature was reasonably selected and does not cause overheating of the material. On the other hand, hardness measurements show a significant decrease of HB and $HV_{0.05}$ even after 60 minutes heating and this will be considered in the next section.

5.3 Hardness of Al-Mg-Si and Al-Mg-Ge alloys

As it was specified in Section 3.6, two types of hardness measurements were used. One is the Brinell hardness (HB), where a ball with a diameter of 2.5 mm is pressed into the specimen. From a microstructural point of view the Brinell hardness is the average of the hardnesses of solid solution, eutectic and primary Mg_2Si or Mg_2Ge crystals. By using Vickers microhardness it is possible to measure the hardness of the α-Al solid solution. Thus the formation or dissolution

of precipitates taking place inside the matrix can be detected with a higher sensitivity than with the Brinell method.

5.3.1 Brinell hardness of Al-Mg-Si and Al-Mg-Ge alloys

In Figure 5.2, the changes of HB for A1 - C2 are plotted against the solution treatment time. The enlarged part of the graph shows the HB changes at the early stage of solution treatment. The first 15 minutes of heating were excluded from the total heating time because this time is needed to heat up a specimen from room temperature to 575.0°C. Oxidation effects are restricted to the surface of the specimens (1x1x1 cm^3). The strongest drop of hardness for all alloys occurred within the first 20 minutes of solution treatment. Further heating results in continuously decreasing hardness which is virtually stabilized after 2 hours. The highest HB was measured in Li and Sc+Zr containing alloys.

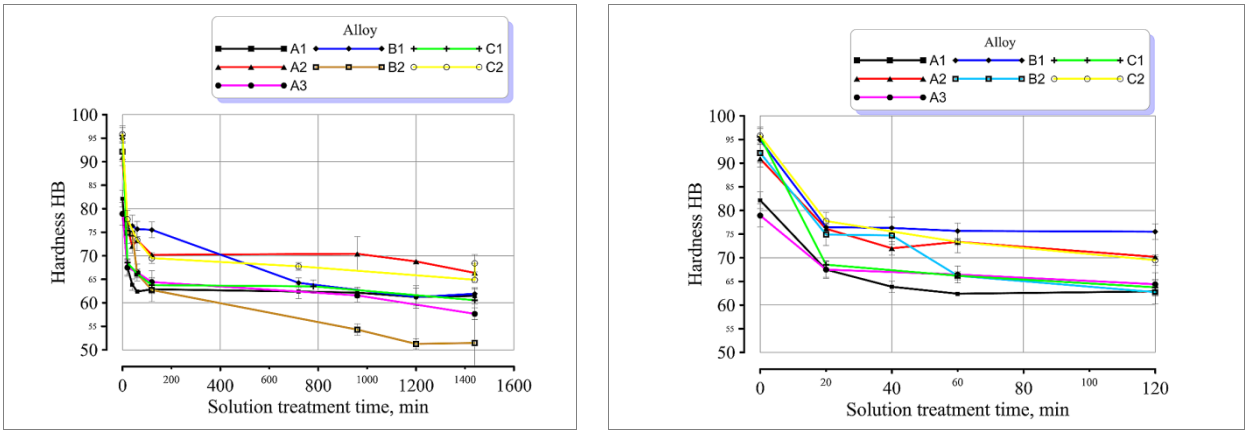

Fig.5.2: Changes of Brinell hardness during solution treatment of A1 - C2 specimens(a) and enlarged part of the graph showing the changes of HB during the first two hours of solution treatment (b)

The reduction of hardness in Al casting alloys during solution treatment is usually associated with:

(i) dissolution of primary intermetallic phases, e.g. Mg_2Si in Al-Si-Mg and $CuAl_2$ in Al-Cu alloys;

(ii) spheroidization of eutectic lamellas in Al-Si alloys.

According to Wang et al. *[WAN01]*, the dissolution of the primary Mg_2Si particles in the commercial Al-Si-Mg casting alloy A356.0 during solution treatment at 540.0°C needs only 15 min. Fe- and Mn- containing intermetallics, such as $\alpha - Al_8Fe_2Si$, $\beta - Al_5FeSi$ or, in presence of Mn, $Al_{15}(Fe,Mn)_3Si_2$, dissolve in α-Al after one hour heating. In Al-Cu alloys the dissolution of the eutectic (Al)+($CuAl_2$) takes place by fragmentation of the Al_2Cu particles into smaller segments that spheroidise and finally dissolve by radial diffusion of Cu atoms into the surrounding matrix, which takes about 12 hours solution treatment at 500.0°C, *[SJO10]*.

In the case of Al-Mg-Si casting alloys, there were no data found concerning the effect of solution treatment on mechanical properties. As it was shown in Chapter 4, the structure of A1 - C2 alloys consists of α-Al, (Al)+(Mg_2Si) eutectic, primary Mg_2Si crystals and a small fraction of $\alpha - Al(Mn, Fe)Si$ phase. Simultaneously, it was established that α-Al solid solution contains precipitates formed during natural aging. Hence the change of HB should be due to either spheroidization of eutectic lamellas or dissolution of precipitates.

Spheroidization of eutectic and dissolution of $\alpha - Al(Mn, Fe)Si$ can be detected as a change in macrohardness, whereas it is difficult to detect the behavior of the precipitates by HB measurements, as explained before.

D1 and D2 show a strong HB decrease during the early stage of solution treatment (Figure 5.3) similar to A1 - C2 (Figure 5.2). For D1, heating up to the solution treatment temperature causes a dramatic decrease of HB. After 20 minutes holding, it falls down to the level of pure Al. Alloy D2, containing Li, keeps its HB on a higher level for a longer time. But after 700 minutes heating the values of HB become equal for both, D1 and D2.

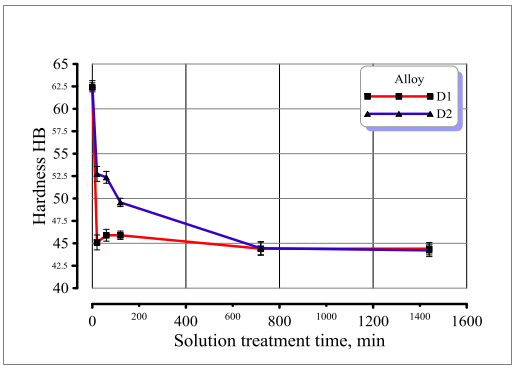

Figure 5.3: Changes of Brinell hardness during solution treatment of D1 and D2

Conclusively, it can be said, that due to the similar nature of A1 - C2 and D1 - D2, they show a similar behavior during solution treatment. The next section will consider the structural transformations in relation to the mechanical properties.

5.3.2 Microhardness of Al-Mg-Si and Al-Mg-Ge alloys

The change of microhardness during solution treatment is illustrated in Figure 5.4.

$HV_{0.05}$ starts to decrease rapidly after the beginning of the solution treatment and stabilizes after 20 - 40 minutes. Because the indentations were placed in the α-Al matrix, these results indicate the softening of the matrix, so the measured effect is most likely due to the dissolution of the β″-phase, formed in A1 - C2 alloys during natural aging. This explanation is also valid for D1 and D2, as will be shown in the

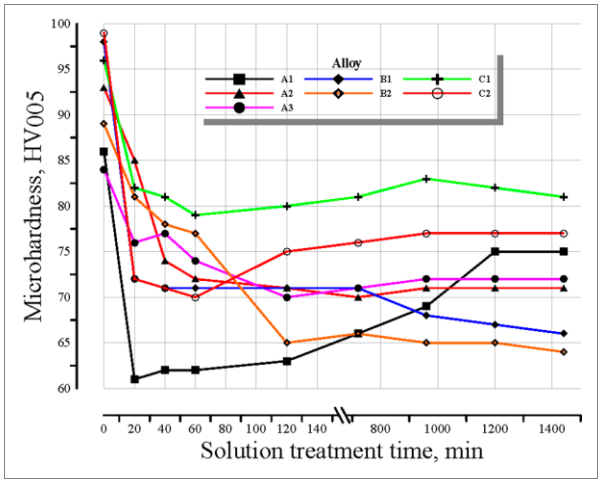

Figure 5.4: Changes of microhardness of A1 - C2 during solution treatment

following section.

In addition, in the time period between 600 and 1200 min HV gradually increased but does not reach the level of as-cast state.

This effect is attributed to the changes taking place inside of solid solution such as increasing of Mg content in solid solution and formation of Mn-rich dispersoids and will be discussed in the following section more in detail. The highest level of microhardness was achieved for C2 and C1 alloys.

This effect originate from the precipitation of $Al_3(Sc,Zr)$ phase, which takes place in the time of homogenisation and the confirmative results of TEM investigations will be presented in the next section. From the other hand, lowest values of HV was measured for A1 alloy, where only strengthening by solute Mg taking place.

5.4 Structure of Al-Mg-Si and Al-Mg-Ge alloys after solution treatment

Structural investigations of the specimens A1 - D2 confirmed, that both, eutectic spheroidization and precipitates dissolution, takes place. As an example, in Figure 5.5 three micrographs of C2 are shown, solution treated 20, 120 and 1440 minutes, respectively.

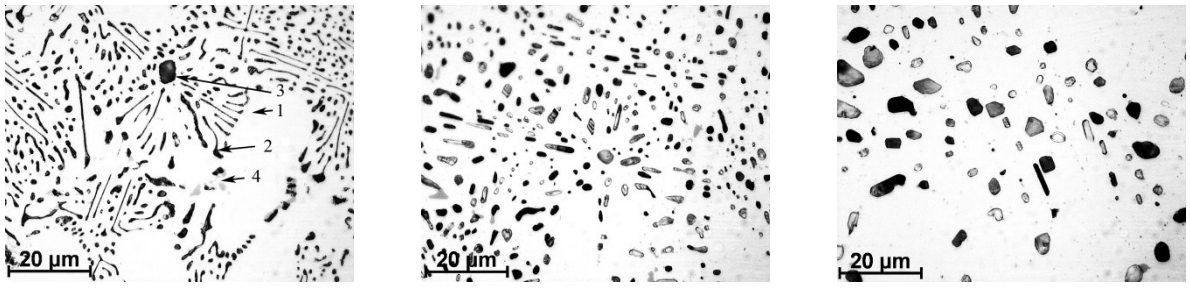

a. 20 min b. 120 min c. 1440 min

Fig. 5.5: Changes of eutectic lamella morphology during solution treatment of C2, α-Al matrix denoted 1, (Al)+(Mg_2Si) eutectic denoted 2, Mg_2Si primary crystals denoted 3, AlMnSi phase denoted 4

After 20 min solution treatment spheroidization of (Al)+(Mg_2Si) eutectic starts and after 120 min only a small part of elongated lamellas remains. After 120 min, larger Mg_2Si intermetallic particles grow on expense of smaller ones.

This change in eutectic Mg_2Si morphology was observed in all studied alloys confirming that the main reason for the decrease of HB and HV is the spheroidization of eutectic lamellas.

Solution treatment of the Al-Mg-Ge alloys D1 and D2 results in a spheroidization of the Mg_2Ge lamellas too. A micrograph of the solution treated D1 specimen is shown in Figure 5.6 from where one can see that lamellas changes their morphology from plates to spherical

particles. Small primary Mg_2Ge crystals can join and form very big ones.

Additionally to light microscopy, specimens were studied using TEM with EDX. These investigations provide more detailed information about structural and compositional changes taking place during solution treatment. In general, the following facts were observed:

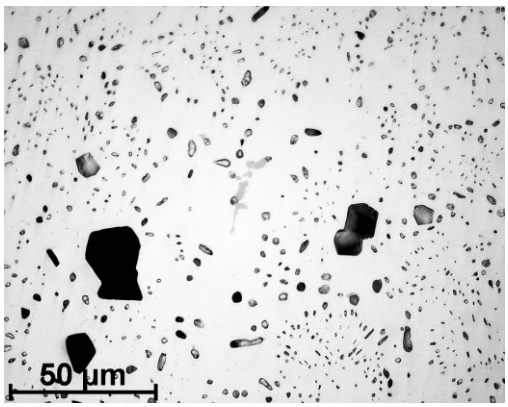

Figure 5.6: Microstructure of D1 solution treated for 1440 min

- the α-Al solid solution contains no precipitates. They were dissolved during solution treatment. In all specimens, the precipitates, having formed on dislocations during natural aging, were no more observed after 20 min heating, showing their quick dissolution;
- the TEM investigations confirmed the spheroidization of the Mg_2Si lamellas in specimens A1 - C2 and Mg_2Ge in specimens D1 - D2. EDX analysis of lamellas indicated that no change of chemical composition of the lamella takes place during solution treatment;
- the composition of the α-Al solid solution changes during heating;
- in Mn containing alloys, a new phase forms during solution treatment. This phase appeared in specimens A2 - C2 and D1 - D2 after 20 min heating;
- in the Sc and Zr containing alloys C1 and C2, new precipitates were observed. They formed in α-Al after heating for two hours.

In Figure 5.7 a, a bright field image of the α-Al solid solution in A2 after 20 min solution treatment is presented indicating the absence of precipitates on dislocations, in contrast to what was observed in as-cast state, (Figure 4.27 b). Thus one can conclude that the solution treatment results in a quick dissolution of the precipitates. The decrease of $HV_{0.05}$, (Figure 5.4) confirms this statement. This result indicates that the strengthening role of precipitates decreases during solution treatment (Figure 5.4).

In the alloys A201.0 and AlMg5Si2Mn HPDC after solution treatment no precipitates were found too, which supports the hypothesis of precipitate dissolution.

In Figure 5.7 b, a bright field image of a Mg_2Si lamella in A2 after 20 min solution treatment is shown.

EDX measurements performed on several lamellas gave the composition: Mg - 57.44 at.%, Si - 32.71 at.%, O - 13.11 wt.% and traces of Al, Fe and Mn, which is very close to the equilibrium

Mg_2Si composition. The oxygen originates from the oxidation of the compound during electrolytic thinning (see Section 4.3).

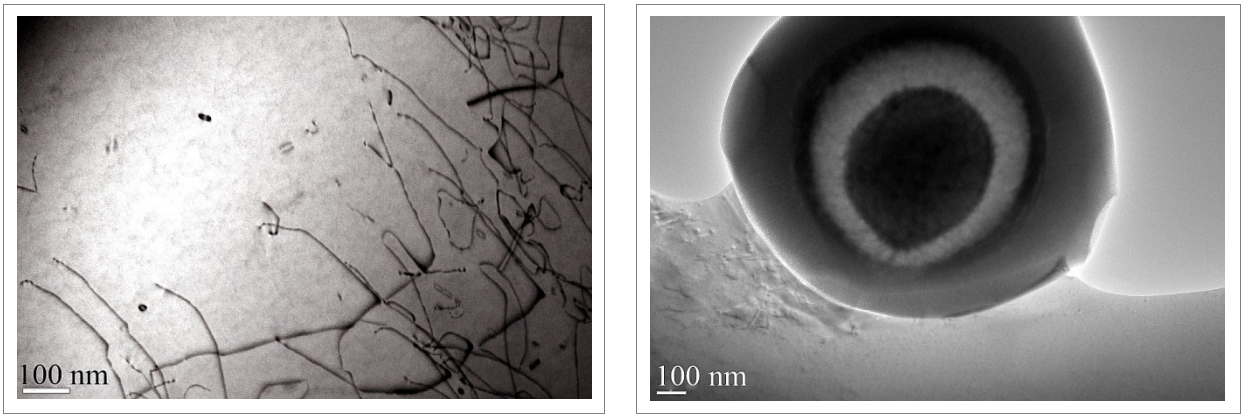

a. b.

Fig. 5.7: Bright field images of A2 after solution treatment at 575.0 °C for 20 min (a) and spheroidized Mg_2Si lamella (b)

Additionally, the micrograph shows a non monolithic structure of the lamella.

The results of the EDX analysis of the aluminium solid solution, performed for all alloys, are summarised in Figure 5.8. Likewise HB and microhardness, the Mg content in α-Al decreases during the first 20 min of solution treatment. After this, however, the Mg content in the solid solution gradually increases. This cannot be the result of precipitate dissolution, because the EDX measurement is an average of the Mg-content of the α-matrix, while does not change. A reason might be the eutectic spheroidization.

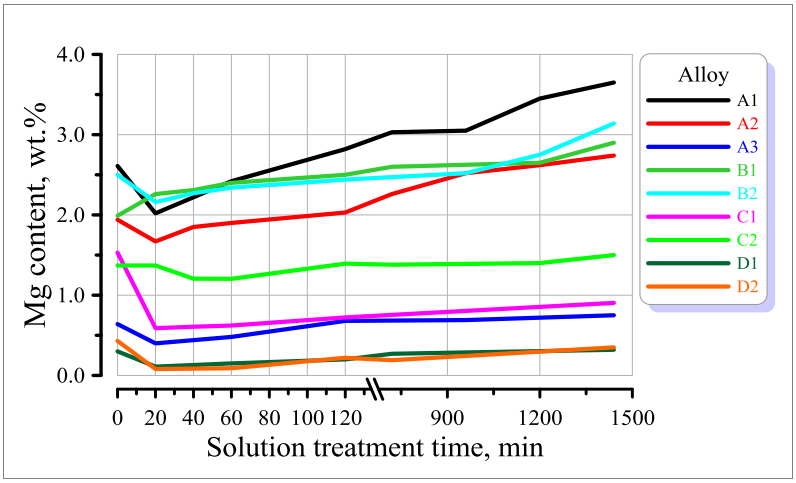

Figure 5.8: Changes of Mg content in solid solution during solution treatment of A1 - D2 alloys

Likewise Mg in A2, D2 shows a decrease of the Mn content in α-Al after 20 min heating and afterwards a clear increase as illustrated in Figure 5.9. However, solution treatment for 600 - 800 min resulted in a lowering of the Mn content. This tendency was observed for all studied alloys. TEM examination of solution treated specimens reveals the nature of the non-monotonous change of the Mn content. In Figure 5.10 bright field images of A2 solution treated for 20, 120 and 1200 min are shown.

After 20 min heating, in the area of the α-Al solid solution new particles were observed, close to the Mg_2Si lamellas. During heating, the size and volume fraction of these particles becomes larger. The development of these particles, also called dispersoids, is illustrated by the example of A2. 20 min, the microstructure after 575.0°C is shown in (Figure 5.10 a).

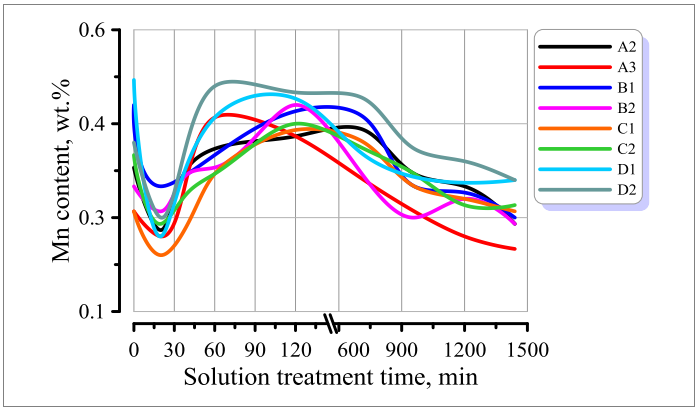

Figure 5.9: Changes of Mn content in solid solution during solution treatment of A2 - D2

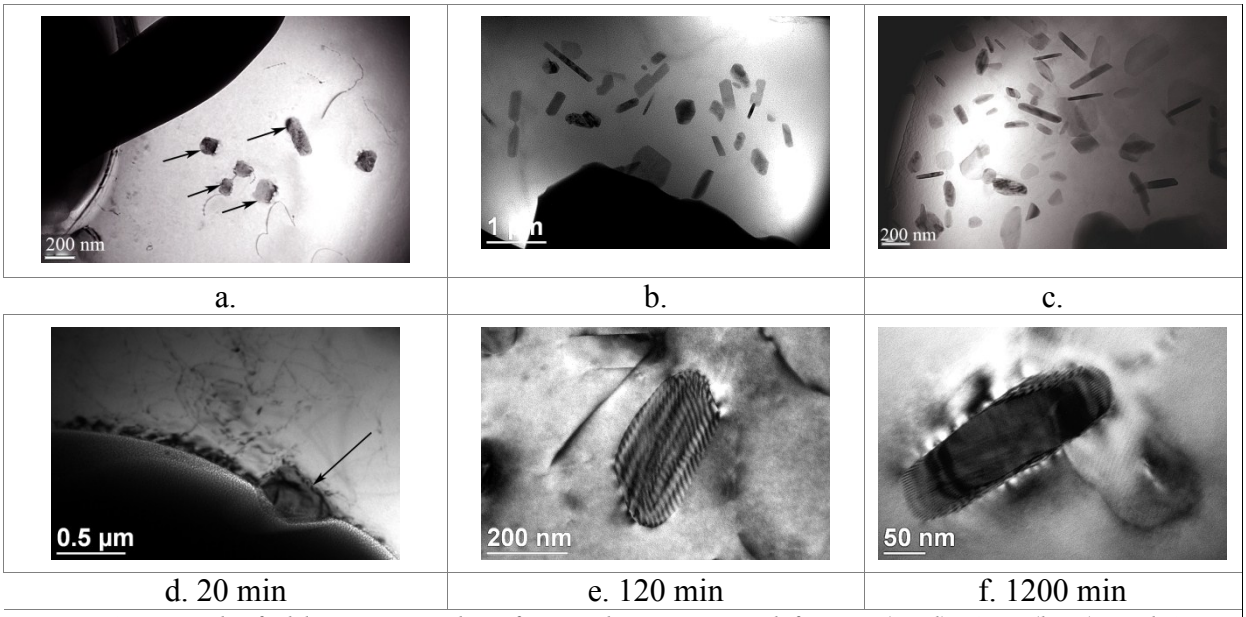

Fig. 5.10: Bright field micrographs of A2 solution treated for 20 (a, d), 120 (b, e) and 1200 (c. f) min

Dispersoids, marked by arrows, grow in the interface between Mg_2Si and α-matrix. Heating for 120 min produces more dispersoids (Figure 5.10 b). The density of dispersoids has increased and they are distributed in the matrix, but preferentially close to the eutectic Mg_2Si lamellas. Prolonged solution time results in the formation of relatively large dispersoids having length between 150 to 250 µm and a width between 50 to 100 µm (Figure 5.10 c). The morphologies of the dispersoids after 20, 120 and 1200 minutes are shown in Figures 5.10 a - f.

The EDX analysis performed on 30 individual dispersoids gave the average concentrations of the elements summarised in Table 5.1. The dispersoids contain mainly Mn, Si and Al. In some cases small concentrations of Mg were detected, which is not surprising because A2 contains 7.20 wt.% Mg. The measured Fe content was not higher than 0.70 wt.%. The main sources of the iron contamination are certainly the AlSi26 and AlMn25 master alloys. For commercial alloys, using low grade aluminium, the Fe content should be even higher.

Table 5.1: Change of the composition of the dispersoids during solution treatment of A2

element	solution treatment time, min (temperature 575.0°C)						
	20	40	60	120	720	960	1440
	content, wt.%						
Mg	0.08	0.30	1.60	1.20	-	-	-
Si	4.60	5.20	2.30	1.90	6.60	4.90	5.10
Mn	21.20	24.50	24.50	25.40	30.30	31.50	33.40
Fe	0.50	0.30	0.60	0.70	0.60	0.80	0.70
Al	73.62	69.70	71.00	70.80	62.50	62.80	60.80

The Si content in the dispersoids is 2.30 - 6.60 wt.% and does not change during solution treatment whereas the Mn content continuously grows from 21.20 wt.% after 20 min up to 33.40 wt.% after 24 hours heating.

The appearance of the dispersoids produced a decrease of the Mn and Si content in the solid solution. This decreases the solid solution hardening of the matrix but produces precipitation hardening. This could explain the slight increase of the Vickers hardness, shown in Figure 5.4.

From the composition and morphology, the observed dispersoids were identified as $\alpha-\mathrm{Al(Mn, Fe)Si}$ phase. Their precipitation behavior is well established for 3XXX (Al-Mn-Fe-Si system) wrought alloys. According to Li et al. *[LIY12]*, $\alpha-\mathrm{Al(Mn, Fe)Si}$ is the dominant dispersoid in the 3XXX family of wrought alloys. It was shown that dispersoids precipitate nearly in all commercial wrought alloys containing Si and Fe/Mn, for instance 3XXX, 4XXX, 5XXX and 6XXX alloys, especially, during heating at low and intermediate temperatures, *[LIY03]*. These dispersoids are always considered as most important for the mechanical properties of commercial aluminum alloys.

For Al-Si casting alloys the prevailing option is that the addition of Mn plays a leading role in neutralization of the harmful effect of Fe. It changes the morphology of Fe-rich primary intermetallics which form during solidification. A number of Fe-rich intermetallic phases, including $\alpha-\mathrm{Al_8Fe_2Si}$ or $\alpha-\mathrm{Al_{15}(Fe,Mn)_3Si_2}$, $\beta-(\mathrm{Al_5FeSi})$, $\pi-(\mathrm{Al_8Mg_3FeSi_6})$ and $\delta-(\mathrm{Al_4FeSi_2})$, have been identified in Al-Si casting alloys.

Among them, the $\beta-(Al_5FeSi)$ phase was reported to be particularly deleterious to the castability and mechanical properties, *[LUL05]*. The platelet-like morphology of this phase is expected to cause severe feeding difficulties during solidification, and eventually to increase the tendency to porosity formation. It was reported by Lu and Dahle that alloying by Mn modifies the platelet-like morphology of coarse $\beta-(Al_5FeSi)$ to a less harmful, more compact form of $\alpha-(Al_{15}(Fe,Mn)_3Si_2)$ phase, *[LUL05]*. However, there was no information concerning re-precipitation of a Mn-containing phase in casting alloys during solution treatment found in literature. So this effect is established in present work on the example of Al-Mg-Si and Al-Mg-Ge casting alloys.

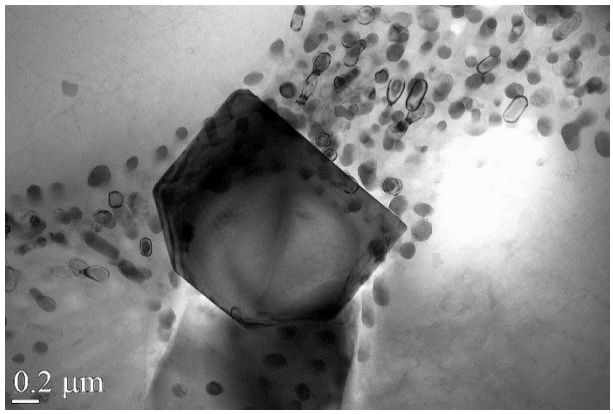

Figure 5.11: Bright field image of blocky-type Fe-containing phase in AlMg5Si2Mn alloy

During the TEM examination of the AlMg5Si2Mn HPDC alloy, blocky shaped primary intermetallic particles were found as shown in Figure 5.11.

The particle is positioned inside the eutectic colonies and has an average size of about 1.5 to 2.5 µm. EDX measurements performed on 15 separate particles showed that this phase is enriched with Fe, Mn and Si. The average composition is: Fe - 4.00 at.%, Mn - 13.34 at.%, Si - 4.90 at.%, Mg - 1.22 at.%, Al - 76.54 at.%. In some particles small amounts of V and Cu were detected.

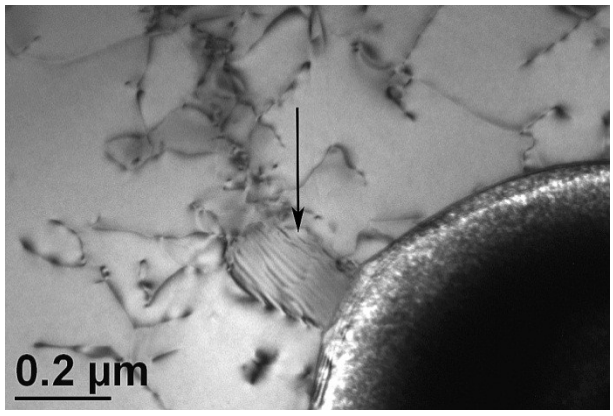

Figure 5.12: Bright field image of a Al(Mn, Fe)Ge *dispersoid growing from a Mg_2Ge lamella (marked by arrow) in D1 alloy*

In a single measurement the overlap of matrix and eutectic material could be avoided. It gave: Fe - 4.01 at.%, Mn - 14.20 at.%, Si - 3.23 at.%, but no Mg. On base of these measurements the Fe containing phase was identified as $\alpha-$Al(Mn, Fe)Si phase.

Concerning the ability of AlMg5Si2Mn HPDC to be heat treated, one can conclude from the observations above, that the solution treatment of the alloy may result in the dissolution of the $\alpha-$Al(Mn, Fe)Si primary phase, followed by the decomposition of the solid solution by the formation of large $\alpha-$Al(Mn, Fe)Si dispersoids. So the solution treatment of the commercial alloy AlMg5Si2Mn HPDC could be reasonable.

Decomposition of the solid solution by precipitation of $\alpha - Al(Mn, Fe)Si$ dispersoids, as described for alloy A2, were also observed in all the others Al-Mg-Si-Mn alloys subjected to the research program.

A similar mechanism of dispersoid formation was found in Al-Mg-Ge-Mn alloys. As an example the growth of a dispersoid from a Mg_2Ge lamella is shown in Figure 5.12. In Table 5.2 results of the EDX analysis of Mn-rich dispersoids in D1, heat treated for 20 minutes, are shown together with a typical EDX spectrum (Figure 5.13). The main difference from the $\alpha - Al(Mn, Fe)Si$ phase is that Si is replaced by Ge.

Table 5.2: Chemical composition of the Mn-rich phase in D1

element	content	
	at.%	wt.%
Mg	0.29	0.24
Ge	0.50	1.31
Al	95.71	91.48
Mn	3.29	6.50
Fe	0.04	0.09
Cu	0.17	0.38

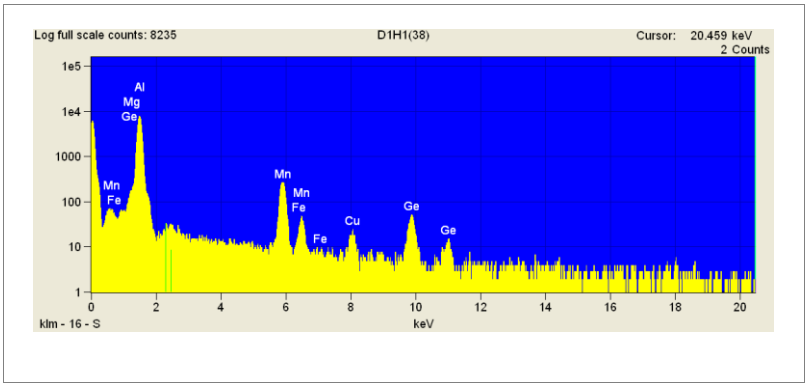

Fig. 5.13: EDX spectrum of the Mn-rich phase in D1, (logarithmic scale)

The low Fe content is the result of using pure materials for melting. In some analyzed dispersoids, the Fe content was somewhat higher up to 0.17 wt.%. From this one can conclude that a higher Fe content in the alloy would lead to $Al(Mn, Fe)Ge$ dispersoids.

Conclusively, the obtained results show, that Mn has not only the established function to change the morphology of Fe-rich intermetallics, but also to cause the precipitation of dispersoids which can play a strengthening role. This statement seems to be true not only for alloys of the Al-Mg-Si and Al-Mg-Ge system, but also for Al-Si alloys, where Mn is also one of the main alloying elements.

It was already mentioned in Chapter 2 that dilute Al–Sc alloys have excellent mechanical properties at room temperature, due to the presence of elastically hard and coherent Al_3Sc precipitates, which can be obtained in high volume density. These Al_3Sc precipitates remain coherent up to a diameter of 20 – 30 nm, since the lattice parameter mismatch is 1.25% at room temperature, *[MAR01]*. The Al_3Sc phase decomposes from the α-Al supersaturated solid solution as a stable phase without forming any intermediate phases, *[IWA04]*.

Sc diffuses relatively fast in Al and the addition of this element leads to a rapid and homogeneous nucleation of coherent and stable Al_3Sc-precipitates (cubic $L1_2$-structure), but the

high diffusivity of Sc also implies that these dispersoids may coarsen relatively fast.

This, however, has been slowed down by adding Sc in combination with Zr. Combined Sc/Zr-additions lead to the formation of $Al_3(Sc_{1-x}Zr_x)$-precipitates with very attractive properties, as they nucleate rapidly at high volume densities, are homogeneously distributed and coarsen quite slowly, *[FOR04]*.

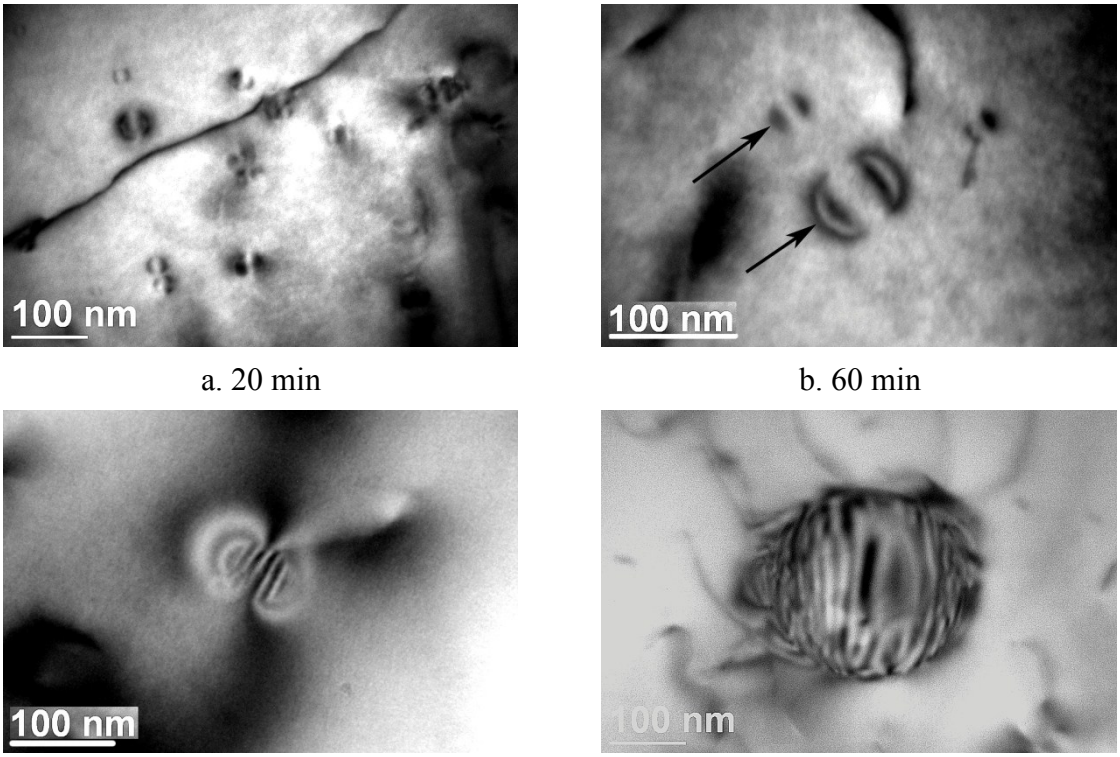

a. 20 min b. 60 min

c. 120 min d. 1440 min

Fig. 5.14: Bright field images of Sc-containing precipitates formed in C1 during solution treatment at 575.0°C for 20 (a), 60 (b), 120 (c) and 1440 (d) min

Therefore, in the present work a combination of Sc and Zr was used. It should be mentioned that no Sc-containing casting alloy has been developed yet. The main reason to utilize the Al-Mg-Si system as base material for a Sc-containing alloy is the very low Si content in the solid solution, which minimizes the formation of undesirable Sc or Zr silicides.

Figure 5.14 illustrates the formation of precipitates in C1 during solution treatment soaking at 575.0°C. After 20 min, the decomposition of α-Al has resulted in the formation of precipitates. The stress field around the particle is visible as two semi-circles. This so-called Ashby-Brown contrasts *[ASH63] and [TAN66]* is usual for TEM observation of small particles and indirectly confirms that they are coherent. Due to the small size of the precipitates, the exact chemical composition could not be measured by EDX analysis even when a spot size of 3 nm was used. However, it was found that the precipitates are enriched with Sc and Zr and hence they were designated as $Al_3(Sc_{1-x}Zr_x)$ precipitates.

From the bright field images in Figure 5.14 one can see, that after 20 min 2 semicircles are separated by a line of no contrast. This is an indication of a coherent particle. After 60 min these regular semicircles still exist, after 120 min they are irregular and after 1440 min they are strongly distorted. According to Iwamura et al. *[IWA04]*, this can be interpreted as a transition from coherent to semi-coherent. This means that $Al_3(Sc_{1-x}Zr_x)$ loses its coherency with the α-Al matrix after about 120 min heating at 575.0°C. Further heating results in a growth of the precipitates and after 24 hours they have reached a size of about 100 nm (Figure 5.14 d). The obtained results fit well with the heating experiments of Iwamura, *[IWA04]*.

A typical precipitation temperature for Sc-containing aluminum alloys is about 300.0°C – 350.0°C. In the present work a temperature of 575.0°C was used, which is too high to produce finely dispersed coherent precipitates. Publications show, that Sc has the same positive effects in Al-Mg-Si casting alloy, as it has for Al-based wrought alloys, *[BLA85]*, as long as moderate temperature are considered.

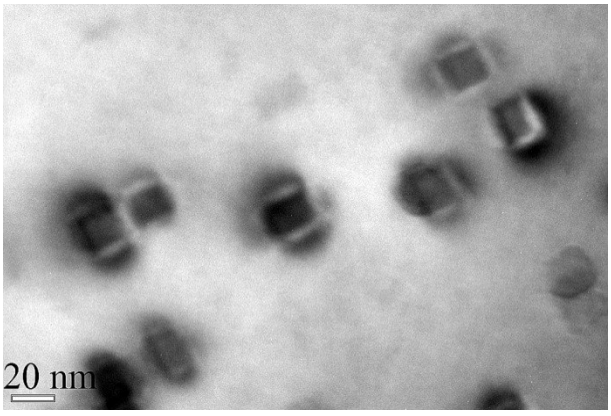

Figure 5.15: Bright field image of $Al_3(Sc_{1-x}Zr_x)$ *precipitates in C1 obtained after heating at 300.0°C during 8 hours*

A preliminary test, performed on C1, shows, that after heating at 300.0°C for 8 hours, the solid solution decomposes, forming cubic-shaped precipitates homogeneously dispersed in α-Al (Figure 5.15). The average size of the precipitates is about 15-20 nm. The strain contrast is visible on all four sides of the precipitate indicating its coherency with the matrix. The presented results in combination with the possibility of grain refinement by Sc+Zr addition (see Chapter 2, Figure 2.6) show, that a aluminum casting alloy with Sc and Zr addition is a promising candidate for the production of castings with enhanced mechanical properties.

5.5 Eutectic spheroidization in Al-Mg-Si and Al-Mg-Ge alloys during solution treatment

In a series of publications of Ogris et al. *[OGR02]*, an analytic model of the eutectic Si spheroidization in Al-Si casting alloys was developed on the base of a model designed by Stuwe and Kolednik, *[STU88]*.

The eutectic plates of Mg_2Si spheroidize during high temperature treatment. The evolution of the change of Mg_2Si eutectic during high temperature treatment can be roughly

divided into three steps:

- breaking of lamellas in pieces called disintegration;
- pieces transform into spheres, called spheroidization;
- growth of the Mg_2Si spheres in the matrix.

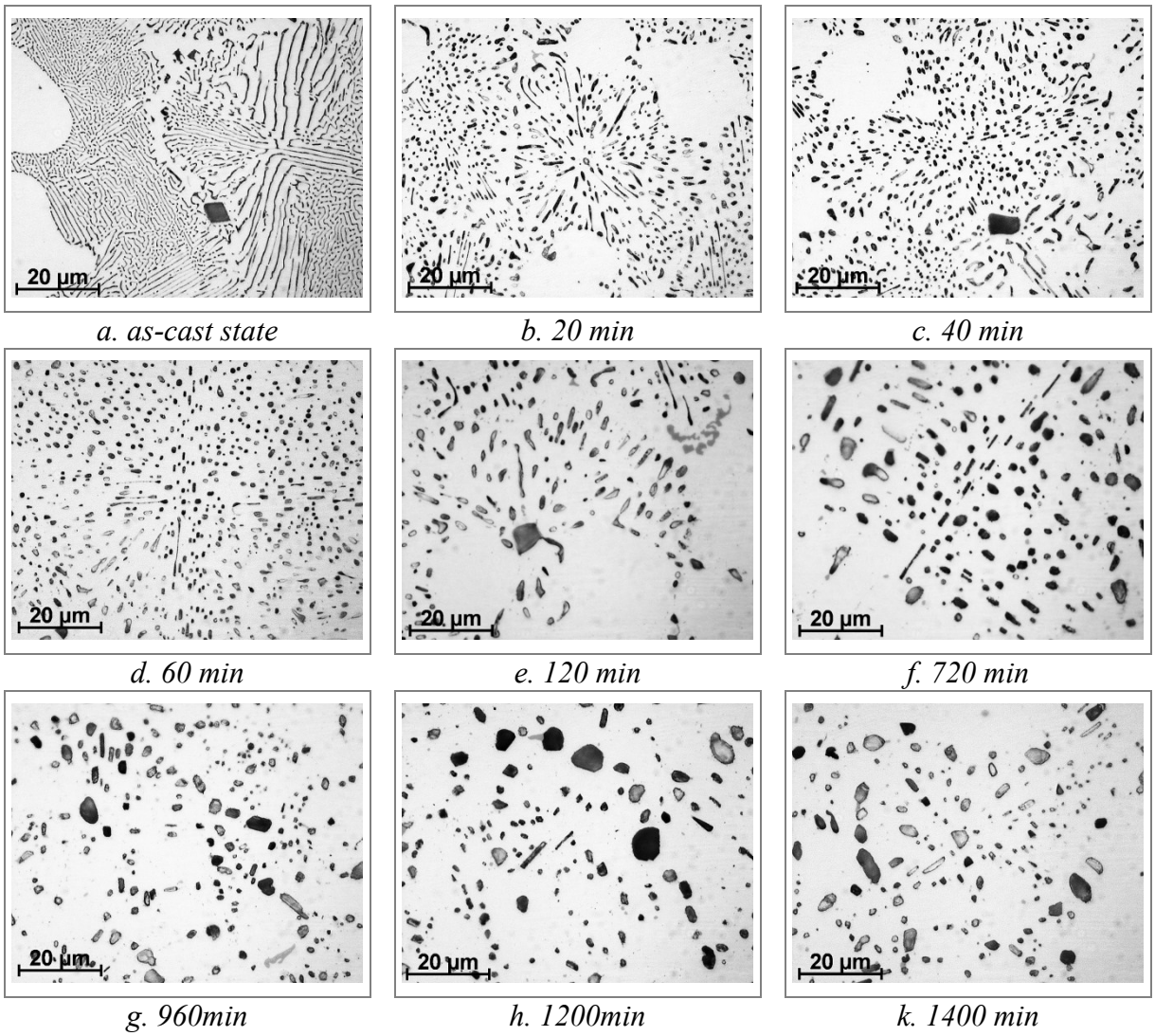

Fig. 5.15: Spheroidization of Mg_2Si particles during solution treatment of A2 alloy at 575.0 °C

The original model calculates the time, which a potassium filled cylinder needs to transform into a sphere in tungsten. The same model was later successfully used to calculate the disintegration time; it has long been know that lamella can break into many small spheres during solution treatment, *[WER89]*. The driving force of spheroidization is the same as for the disintegration and, namely the minimization of surface energy under the effect of surface tension. In the following, an adapted version of the model was applied to describe the disintegration of eutectic silicon corals in Al–Si alloys, *[OGR02]*. It was proposed *[WER89]*, to apply this model to the spheroidization of Mg_2Si lamellas in Al-Mg-Si

alloys (Figures 5.5 and 5.15).

In Section 5.4, it was presented, that in Al-Mg-Si and Al-Mg-Ge the eutectic lamellas also tend to spheroidization and that this process takes less than 20 min which is very close to the result obtained by Ogris for Si spheroidization. Prolonged soaking for 24 hours results just in an increase of the sphere diameter.

5.6 Summary

The results of this chapter can be summarized as follows:

1. At the early stage of solution treatment two processes are taking place, namely spheroidization of eutectic Mg_2Si lamellas and dissolution of precipitates formed during natural aging in as-cast state. Both of them need not longer than 120 min for completion at a temperature 575.0°C. The same results were obtained for the Al-Mg-Ge system. This metallographic conclusion is confirmed by HB- and microhardness measurements and by DSC runs.
2. During heating a precipitation process takes place, namely the formation of $\alpha - \mathrm{Al(Mn, Fe)Si}$ dispersoid together with spheroidization of eutectic lamellas in A2-C2. The dispersoids grow on the surface of Mg_2Si lamella and after a certain time they occupy the interlamellar areas. Similar Mn-rich dispersoids are observed in D1 and D2. The appearance of these dispersoids uncovers the double importance of Mn addition for the casting alloys:

   -First, the change of the morphology of Fe-rich primary intermetallics formed during solidification;

   - Second, the reprecipitation of the Mn-rich phase during solution treatment. The Mn-rich dispersoids act as a strengthening phase for the alloy, which is confirmed by the slight increasing of HV after 600 min soaking.
3. In C1 and C2 a different precipitation process was observed, namely the formation of $Al_3(Sc_{1-x}Zr_x)$ precipitates. The decomposition of the solid solution starts after 20 min soaking and further heating results in the growth of the precipitates up to a size where they lose their coherency with the matrix. The size for coherency loss is reached after about 120 min soaking.
4. Metallographic examinations of A2, solution treated for different times, show that during the first 20 minutes the Mg_2Si lamellas transform into separate spheres, which grow within 24 hours from 1 μm diameter to 3 - 3.5 μm.

6 Aging of Al-Mg-Si and Al-Mg-Ge alloys

6.1 Introduction

Solution treatment and quenching produces a supersaturation of the α-Al matrix, i.e. it contains alloying elements in solution above their solubility limits. In Chapter 5 it was shown that heating of A1 - D2 leads to an increased Mg content in α-Al dendrite arms together with the precipitation of $\alpha - \mathrm{Al(Mn, Fe)Si}$ dispersoids in Mn-containing specimens, respectively, $\mathrm{Al_3(Sc_{1-x}Zr_x)}$ precipitates in specimens alloyed with Sc+Zr. So in all investigated alloys, decomposition of the solid solution and precipitation already starts at the stage of solution treatment, except in A1 alloy where no precipitates were observed. However, at the time of quenching no thermodynamically stable condition is reached and therefore further storing of the alloys at room temperature, called natural aging, or low temperature heating, called artificial aging, results in further decomposition. This topic of solid state transformations was extensively studied over the last 100 years starting from the accidental discovery of "strong aluminum" up to now, *[SIM11]*. The most profound reviews on the aging of metallic alloys can be found in books of Martin *[MAR98]*, Chuistov *[CHU03]*, Khachaturyan *[KHA83]* etc. and magazine publications, *[FIN75]*, *[POL04]* etc. Most of the published research considers the precipitation from a supersaturated solid solution of wrought materials, not casting alloys. For both alloy groups the same alloying elements are used. So one could expect that the type, morphology and composition of precipitates in cast alloys should not be much different from that of wrought ones. However, the production process plays also an important role, for instance the grain size of the extruded product is about 3.0 to 5.0 μm whereas in permanent mold casting it can not be lower than 100 μm. Indeed one can see that the structure of casting alloys in as-cast state and after solution treatment and quenching is not similar to that of wrought ones.

The importance of aging for casting alloys was already considered in Chapter 2 (see for example Figure 2.4) and can be again illustrated on the examples of the commercial alloy A201.0. In A201.0 the Brinell hardness after artificial aging is more than twice as high as in as-cast condition (Figure 6.1). Starting with the investigations of Guinier, *[DUP10]* and Preston, *[PRE38]* and continued with detailed research of Vaughan and Silcock *[VAU67], [RIN00]*, the precipitation of the so called Θ phase in Al-Cu alloys during aging was established. Vaughan

showed that this phase has 159 possible orientations relative to the α-Al lattice. Its orientation depends also on the applied cooling rate.

As discussed in Chapters 2, 4 and 5, the structure of the most widespread Al-Si-Mg and newly developed Al-Mg-Si-Mn casting alloys consists of the dendrite arms of the α-Al solid solution together with eutectic and primary intermetallics. This complex microstructure affects precipitation, such as nucleation of $\alpha - \mathrm{Al(Mn, Fe)Si}$ dispersoids on the eutectic lamellas (Figure 5.10) and decomposition of the aluminum matrix even during solution treatment, as observed in Sc+Zr containing alloys (Figure 5.13). So one could expect, that the effect of structure on precipitation, revealed in A1 - C2 and D1 - D2 casting alloys, should occur also during aging.

Regarding the effect of heat treatment on mechanical properties, the published results for Al-Mg-Si-Mn alloys are controversial and scanty.

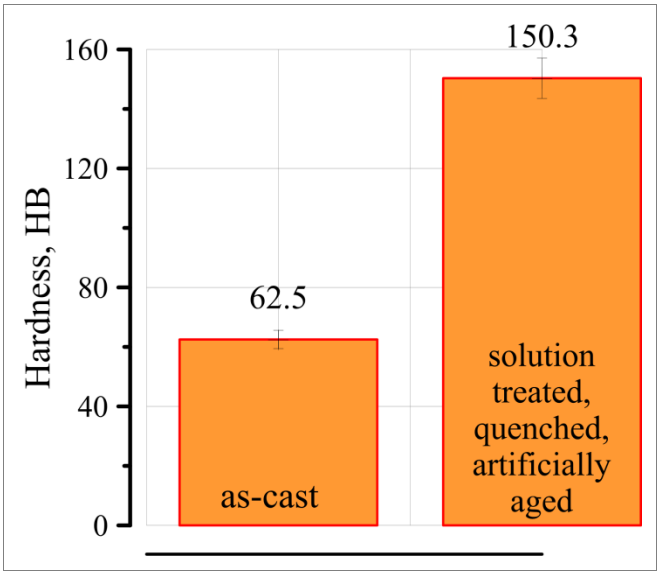

Fig. 6.1: Changes of HB of A201.0 alloy (Al-Cu-Mg-Ag system) from as-cast state to peak aged condition

From the work of Petkow et al., *[PET12]* it can be seen that the AlMg5Si2Mn alloy, cast into permanent mold, shows only a slight increase of tensile and ultimate tensile strength after T6 treatment together with a dramatically low fracture elongation of about 2.5% for temper F, decreasing down to 1.4% after artificial aging. In relation to as-cast state, solution treatment for 8 hours at 570.0°C, quenching and artificial aging at 190.0°C for 8 hours result in an ultimate tensile strength of only 263 MPa, which is lower than that of A356.0 T6. Preliminary studies show that the ultimate tensile strength of A356.0 T6 may reach a level up to 300 MPa and an elongation to fracture of 6%. These data are in agreement with results obtained by Shabestari, *[SHA04]*.

Comparable to A356.0 is the permanent mold cast AlMg5Si2Mn *[PIR91]*, where the ultimate tensile strength varies from 255 to 298 MPa and the elongation in the range between 1.2 and 3.2%. The elongation is one order lower than that of AlMg5Si2Mn HPDC where it can reach 18%.

The combination of high strength and elongation of AlMg5Si2Mn HPDC is the result of natural aging, which leads to the room temperature decomposition of the solid solution and the formation of plate-like precipitates growing from dislocations (Section 4.4). Since the dislocation

density in a HPDC alloy is higher than in a alloy cast into permanent mold (PM), the fraction of precipitates is higher in the first one (Figure 4.29 c). Thus the mechanical properties of a PM Al-Mg-Si alloy will be certainly lower than those of HPDC alloys in temper F (see Table 2.2). However, if both alloys are subjected to a solution treatment, which results in the dissolution of the precipitates, no difference between PM and HPDC alloys remains.

Theoretically, further aging should result in recurring decomposition of the solid solution and the formation of precipitates. This is confirmed by the results of Hu et al., *[HUZ13]* who observed an increase of tensile properties and hardness of the AlMg5Si2Mn HPDC alloy after age treatment for 1 hour at 250.0°C. They reported for this alloy an ultimate tensile strength in as-cast condition of 324 MPa and after artificial aging it raises up to 369 MPa. The elongation at fracture was on the same level for F and T6 conditions. It is worth noting that the temperatures for heat treatment of Al-Mg-Si casting alloys can not be considered as established yet. The applied time-temperature-conditions are almost always based on practical experience and only sometimes on the results of DSC measurements as presented in the following chapter.

6.2 Calorimetric studies of the precipitation process in Al-Mg-Si and Al-Mg-Ge alloys

Due to the limited research on Al-Mg-Si casting alloys, e.g. *[OTA09]*, *[DRA10]*, *[PET12]*, *[HUZ13]*, the effect of aging on precipitation in this group of material needs additional investigations. Only one publication presents results of DSC studies on the AlMg5Si2Mn alloy, *[PET12]*. Here Petkov et al. obtained DSC curves, which show heat effects in the low temperature part of the curve. The first exothermic reaction was detected at the temperature of 100.0°C and represents the formation of G-P-zones. Further heating results in the appearance of a second exothermic effect with an onset temperature of 244.0°C and a peak temperature of 262.0°C indicating the formation of $\beta''-$ or $\beta'-$precipitates. The next exothermic effect has a onset temperature of 383.8°C and a peak temperature of 416.0°C. Petkov et al. stated that this heat effect is related to the formation of stable $\beta-Mg_2Si$ precipitates. This sequence of heat effects matches well with numerous studies of the precipitation process in wrought 6XX.X (Al-Mg-Si) alloys; see f. e. the review of Starink, *[STA04]* and publications, such as *[WOO99]*, *[VED07]*, *[BIR08]*. In the work of Birol, *[BIR08]* on the AA6005 (Al-Mg-Si) wrought alloy, seven enthalpic signals were identified in the DSC spectrum, five of which are exothermic. Heating starts with a small exothermal effect centered around 80.0°C, which is close to the observation of *[PET12]* for a casting alloy, Birol found a second exothermic peak in the temperature range between 122.0°C and 212.0°C, which is related to the formation of GP-I.

Further heating leads to the strongest exothermic effect at 275.0°C, clearly linked to the precipitation of the most important hardening phase, β". Heating up to 340.0°C shows the next effect caused by the transformation of β" to β'. The last peak at a temperature as high as 400.0°C is associated with the precipitation of a stable $\beta - Mg_2Si$ phase.

This sequence of thermal effects detected by Birol, *[BIR08]* is in reasonable consistency with the precipitation sequence reported for Al-Mg-Si alloys:

$$SSSS \rightarrow GP-I \rightarrow \beta'' \rightarrow \beta' \rightarrow \beta - Mg_2Si \qquad (6.1)$$

where SSSS means super saturated solid solution, *[BAN10]*.

In order, to understand, which effect the aging temperature has on precipitates, having formed during the solution treatment, DSC measurements for different solution times and different alloys were performed. The DSC curves obtained in the present study are shown in Figure 6.2 a and b. From Figure 6.2 a obtained of A1 preheated at 575.0°C in the time interval from 20 to 1440 min, two exothermal effects can be distinguished. The first one, denoted as 1, appeared in the temperature range between 200.0 and 270.0°C with a peak onset of 224.1°C and a peak temperature of 248.0°C for A1, solution treated for at 575.0°C for 720 min. Similar peak positions were detected for all specimens solution treated for different times (thin black lines).

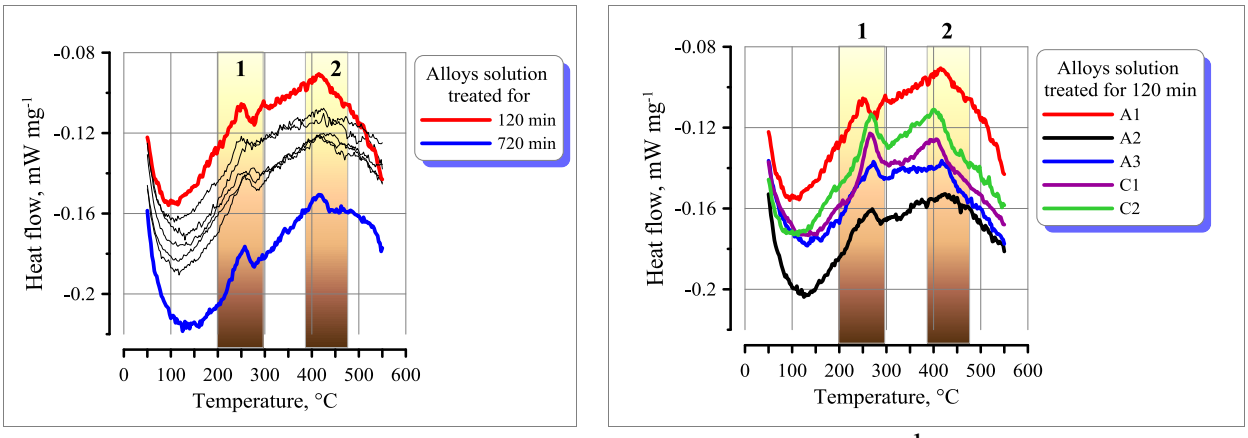

Fig. 6.2: DSC of A1 specimens, solution treated for different times and quenched, black lines: solution times between 20 and 1440 min, (a) DSC curves for A1 - A3, C1, C2 solution treated for 120 min and quenched (b)

Comparison of DSC results for heating up the A1 - A3, C1, C2 specimens, solution treated for 120 min, shows that in Mn-containing alloys, the position of the first peak is slightly shifted towards a higher temperature as can be seen by comparison of the A1 curve with the curves for A2, A3, C1 and C2. These alloys exhibit an onset temperature of peak 1 of about 245.0°C and a peak temperature of about 260.0°C. For the D1 and D2 alloys no significant heat

effects were observed. According to Starink, *[STA04]*, many reactions in Al based alloys cause relatively small heat flows, which could be an explanation of the absence of peaks in this case. The relatively low sensitivity for heat flow changes of the differential scanning calorimeter (DSC) used in the present work, restricts the ability to detect precipitation heat effects in Al-Mg-Ge alloys and heat effects associated with the formation of additional precipitates expected to be present in C1, C2, B1, B2 and D2 alloys.

The results of the DSC runs performed on solution treated and quenched specimens fit well to the data of numerous investigations on Al-Mg-Si alloys and can be summarized as follows:

- the first exothermic heat effect (denoted 1) is observed at temperatures between 220.0°C and 260.0°C. From comparison of these temperatures with literature one can conclude that they are related to the precipitation of the β" phase;
- the second exothermic effect appears at temperatures between 370.0°C and 440.0°C and can be attributed to the precipitation of the stable $\beta - Mg_2Si$ phase;
- the heat effects expected for the precipitation of Li- or Sc+Zr-containing phases, were not detected in DSC runs.

Since the observed heat effects are in good agreement with literature data, the artificial aging temperature for Al-Mg-Si alloys can be selected in a similar way as for the A356.0 casting alloy. In the most advanced investigations of Wang and Davidson *[WAN01]*, the precipitation temperature interval was found to be 200.0°C – 400.0°C. Zhu et al. *[ZHU12]* used an artificial aging temperature of 160.0°C to achieve an ultimate tensile strength of 285 MPa for PM A356.0 and an elongation at fracture of 5.5%, despite the precipitation temperature for the β" phase of about 216.0°C would allow a higher temperature, *[WAN01]*. Kaiser et al. *[KAI12]* detected on the DSC curve of A356.0 alloyed with Sc just two exothermal heat effects, which were related to the precipitation of β" and $\beta - Mg_2Si$ phase. Heat effects which could be associated with the precipitation of a Sc-containing phase, were not observed.

In order to be able, to compare the results of the present work with literature, a temperature of 175.0°C was used for the artificial aging experiments. It is clearly below the dissolution temperature of the precipitates, but high enough to attain hardening within reasonable times.

6.3 Hardness of Al-Mg-Si and Al-Mg-Ge alloys

6.3.1 Brinell hardness of Al-Mg-Si and Al-Mg-Ge alloys

Precipitation hardening of A1 - D2 was confirmed by Brinell hardness measurements performed on specimens artificially aged for different times.

As an example, in Figure 6.3 a, HB for A1 - C2 is plotted against artificial aging time. Already the first measured point after 30 min of artificial aging gives an increase of HB and it continues up to 180 min, where HB reaches its maximum. The peak hardness of A1 is nearly the same as it was measured for A356.0 aged for the same time. For the Mn-containing alloys A2 and A3, HB is somewhat higher indicating the sum effect of precipitation and $\alpha - Al(Mn, Fe)Si$ dispersoids. From the graph in Figure 6.3 b, it is clear that the precipitation process in A356.0, where the solid solution decomposes with the formation of β″ and later β′ phases, is similar to that of A2 where same precipitates are expected at different aging stages, but different from that in A201, which reaches a much higher microhardness.

Additional alloying with Li (B1 and B2) and Sc+Zr (C1 and C2) shows even lower HB values than that of A1 - A3.

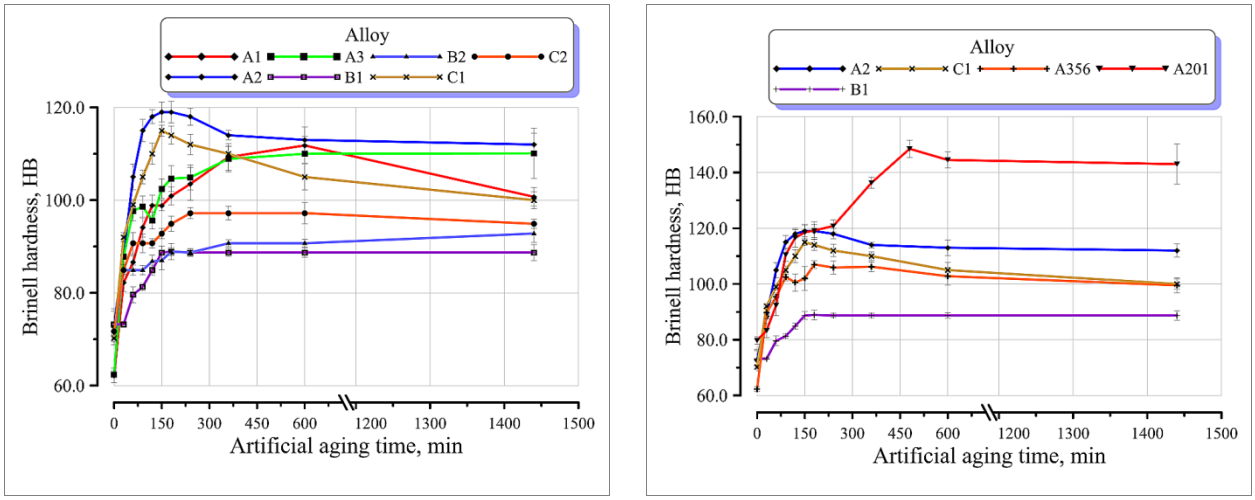

a. b.

Fig. 6.3: HB of A1 - C2 as a function of artificial aging time (a) and for comparison with A2, C1, B1 and commercial A356.0, A201.0 alloys (b)

From Fig. 6.3 follows that HB of the commercial alloy A201.0 is the highest from all alloys tested. This result is not surprising, because A201.0 (Al-Cu system) belongs to the class of high strength alloys, as mentioned in Chapter 2. For sand casting (slow cooling rate), UTS reachea a level up to 440 MPa with an elongation up to 10% in T6 condition, *[DIN96]*. These are the highest values one can achieve for Al-based casting alloys subjected to conventional casting techniques. Such unique properties have two origins of, namely:

- high solute content in solid solution. EDX measurements show that in T6 condition the Al matrix contains 5.50 wt.% Cu, 3.50 wt.% Ag and 0.26 wt.% Mn which is much higher than in the alloys A1 - C2 and even in the commercial alloy A356.0;

- precipitation of strengthening phase during aging.

The main contributor to the high HB values are the precipitates of θ-$CuAl_2$ phase as shown in Fig. 2.4. On the other hand however, poor castability, susceptiblity to solidification cracking and interdendritic shrinkage and the low corrosion resistance strongly restrict a widespread application of the A201.0 alloy in foundry industry. These are the reasons, why Al-Si and Al-Mg-Si are preferable for casting.

The lowest HB was measured for the Li-containing alloys B1 and B2 and for the Sc+Zr-containing alloys C1 and C2 HB was only somewhat higher. The decrease of HB indicates that alloying by precipitate-forming elements has on unfavorable effect on the mechanical properties of Al-based alloys. As it was discussed in Chapter 4, addition of Li makes the interlamellar spaces larger in the (Al)+(Mg_2Si) eutectic. This result in a large distance between the Mg_2Si particles after spheroidisation, therefore the absolute values of HB are lower than for A1 - A3.

HB for D1 and D2 in as-cast state is the lowest one among all alloys tested. After solution treatment, the HB values of the Al-Mg-Ge specimens fall down to the hardness of pure aluminum (Figure 5.3). During artificial aging at 175.0°C, the maximum hardness was achieved after 120 - 360 min (Figure 6.4). No difference between HB of D1 and of Li-containing D2 was detected.

Prolonged ageing results in a slight decrease of HB for both D1 and D2.

The highest values of HB were measured for the A201.0 alloy artificially aged at 150.0°C for 420 min, showing the leading position of Al-Cu alloys among casting alloys (Figure 6.3 b). Its strength originates from of needle shaped Ω-precipitates (Table 2.4, Figure 2.4).

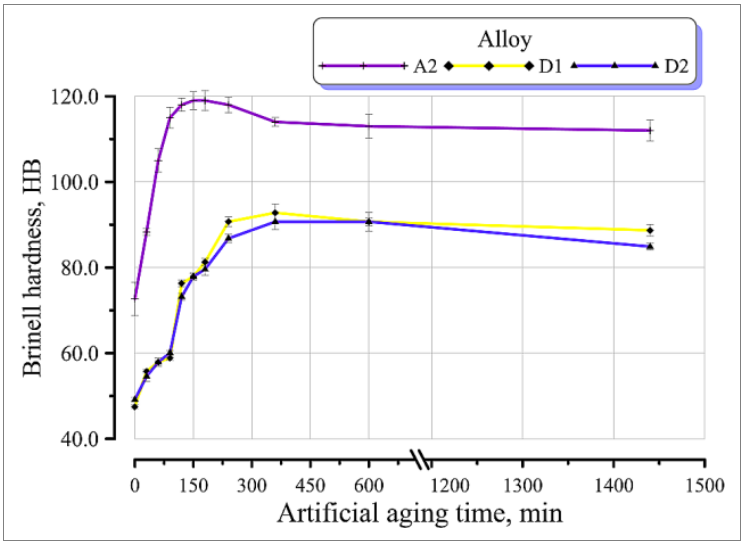

Fig. 6.4: Hardness of D1 and D2 as a function of artificial aging time

Thus for Al-Mg-Si, the increase of HB can be mainly attributed to the precipitation process during aging, as known from the commercial A356.0 and A201.0 alloys.

6.3.2 Microhardness of Al-Mg-Si and Al-Mg-Ge alloys

It is clear that macrohardness such as HB is less sensitive to the structural changes taking place inside the solid solution.

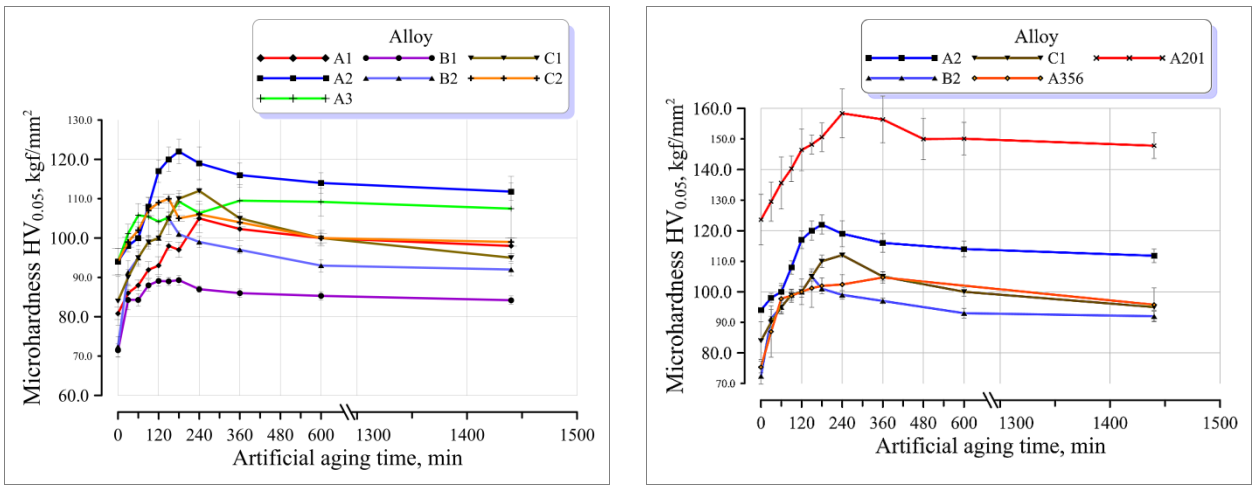

a. b.

Fig. 6.5: Microhardness of A1 - C2 as a function of artificial aging time (a) and comparison of artificial aging kinetic for A2, B2, C1 and the commercial A356.0 and A201.0 alloys (b)

Therefore, $HV_{0.05}$ measurements were applied to detect the changes of mechanical properties of the α-Al solid solution during aging. The results are summarized in Figure 6.5.

For the base alloys A1 - A3 $HV_{0.05}$ significantly rises after 60 min of artificial aging and reaches its maximum after 180 min. Further heating can not significantly improve microhardness, i.e., the $HV_{0.05}$ values keep nearly the same level up to 24 hours artificial aging. For A2 and A3 the microhardness is higher than in A1, similar as observed for HB in Figure 6.3 a. The reason is the formation of Mn-containing $\alpha - Al(Mn, Fe)Si$ dispersoids.

In the Li-containing alloys B1 and B2, $HV_{0.05}$ was much lower than for the base alloys A1 - A3. Similar as HB in Fig. 6.5 a, $HV_{0.05}$ of, C1 and C2 reaches its maximum after 300 min artificial aging, but the values are still lower than for A1 - A3. It was shown in Chapter 5 (Section 5.4), which the Mg content in the solid solution of C1 and C2 is the lowest one. After solution treatment at 575.0°C for 1 h, the Mg content in solid solution was about 1.20 wt.% in C1, which is dramatically lower to that measured in A1, where the solid solution contains 2.50 wt.% Mg.

It has to be noticed that the most unfavorable point for C1 and C2 is that the solid solution already decomposes during solution treatment and precipitates are formed (Figure 5.13). It can be expected that no much precipitation will take place during aging, mostly growth of precipitates. Consequently, the volume fraction of precipitates should remain constant, only their size should increase. This has to be directly established by TEM examinations.

$HV_{0.05}$ for the commercial casting alloys A201.0 and A356.0 is included in Figure 6.5 b for comparison. The microhardness of A1 - A3 is lower than that of A201 alloy aged at 150.0°C for 120 to 1440 min but higher than for A356.0 alloy aged at 175.0°C during 30 to 1440 min.

Similar to HB, D1 and D2 alloys show the lowest microhardness in as-cast state. Measurements of $HV_{0.05}$ after solution treatment, quenching and artificial aging show that it gradually increases and reaches a maximum after 360 min exposure. The obtained data indicate the ability of Al-Mg-Ge system to be age hardened. The microhardness of the Li-containing D2 alloy increases at a earlier stage of aging than for D1 (Figure 6.6). However, the absolute values of $HV_{0.05}$ are on the same level for both, D1 and D2.

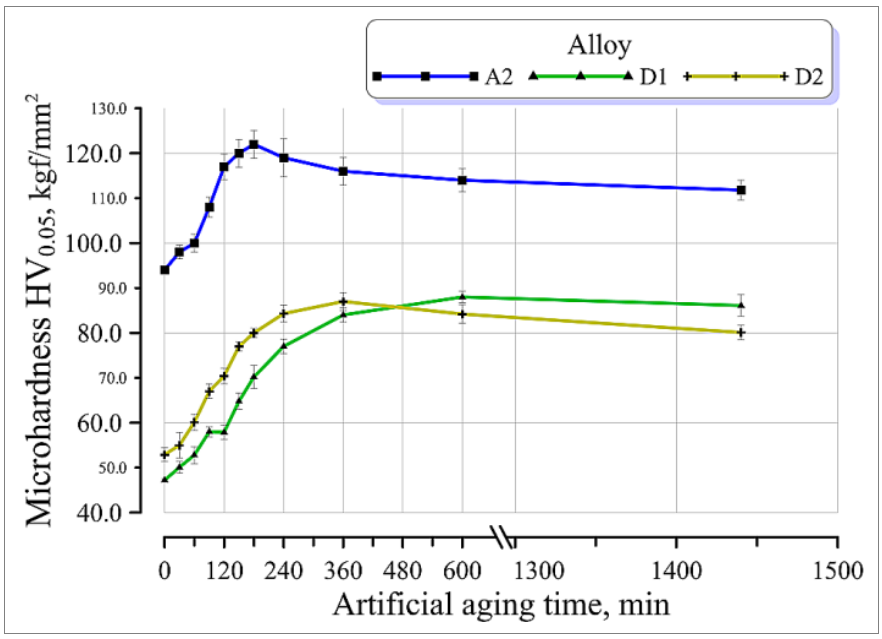

Fig. 6.6: Microhardness of D1 and D2 as a function of artificial aging time in comparison to A2

In conclusion, the indirect methods DSC and hardness measurement gave indications for solid state transformations. The final prove of precipitation processes in A1 - D2 are examinations of thin foils using TEM, as presented in the following section.

6.4 Precipitates formed in of Al-Mg-Si and Al-Mg-Ge alloys

Specimen with different artifical aging times were investigated by transmission electron microscopy. The following effects were found:

- formation of precipitates in the α-Al solid solution;
- change of the chemical composition of the α-Al solid solution due to the formation of precipitates.

DSC traces obtained during heating of solution treated and quenched specimens show exothermal peaks which could indicate a precipitation process. Therefore in specimens where clear exothermic effects were detected, TEM examinations were performed to confirm that precipitation took place.

6.4.1 Precipitates in Al-Mg-Si alloys without and with addition of Li and Sc+Zr

In Figure 6.7 bright field images of A1 - C2, aged for different times, are shown. After 30 min of artificial aging, no precipitates were observed in A1 (Figure 6.7 a). The increase of hardness is still low at this time. So the density and /or size of the precipitates is low, which makes it very difficult to detect in a nonideal crystal precipitates in a nano-scale.

After aging for 180 min, strong precipitation has taken place in A1, visible as fine black dots which are randomly distributed in the field of solid solution. No precipitation free zone (PFZ) is observed at the parallel area grain boundary visible as a band of parallel fingers. This finding is in line with the observations of Mariorara et al. *[MAR05]*, who reported that in Mg-rich Al-Mg-Si alloys after short aging times no precipitates can be found. After aging for 240 min, where HB and $HV_{0.05}$ are maximal, the matrix contains needle-shaped precipitates (Figure 6.7 c), which are β″-phase, according to introduction of paragraph 6.2. Such a sequence of precipitation was observed in A2. After aging for 90 min only fine black dots are visible (Figure 6.7 e). Further aging for 120 min results in the precipitation of needles of β″ phase (Figure 6.7 e), which increase their volume fraction after 600 min aging.

The decomposition of the solid solution was proved by EDX measurements in the alloys matrix of A2 alloy. The average composition in as quenched condition is: 2.00-2.30 wt.% Mg and 0.25-0.35 wt.% Mn. After aging for 30 min, the Mg content decreases to 1.10-1.20 wt.%. but simultaneous Si intensity appears in the EDX spectrum. 10 measurements of different α-Al give a Si content of about 0.15-0.25 wt.%, which remains unchanged during 24 hours artificial aging.

The Li-containing alloys B1 and B2 show a similar precipitation behavior. After 90 min artificial aging of B1, only dotlike contrasts were detected (Figure 6.7 g). After 240 min these dots have become somewhat larger, (Figure 6.7 h), but after 600 min (Figure 6.7 k) the matrix contains precipitates of 3 types:

(i) needle-shaped β″-phase;

(ii) cubic-shaped precipitates parallel oriented to the needles;

(iii) small black cubic-shaped precipitates, 45° rotated to the needles

Alloy B2 confirms these results (Figs. 6.7 l, m, n). The sequence of the precipitate formation is even better visible than in Figs. 6.7 g, h, k. Comparing the morphology of the precipitates of the type (ii) with those, observed by Ohmori et al. *[OHM02]*, *[MAT06]* in Al-Mg-Si alloy containing 1.48 at.% Mg and 0.48 at.% Si, they can be identified as equilibrium β-Mg_2Si cuboid particles. Extensive research on the precipitation reactions in Al-Mg-Si are represented in the following works *[TAK98]*, *[OHM02]*, *[MOS12]*. There it is was shown that the heat effect corresponding to the formation of the β-Mg_2Si cuboid phase, has a temperature of about 290.0°C. This is only slightly higher than that for β″ and therefore both effects can be separated only by using DSC with high sensitivity. In the work of Mossad et al. *[MOS12]* it was stated that the heat effect of the formation of β-Mg_2Si cuboid particles is often overlayed by the precipitation of β″. As can be seen from Figures 6.7 k, β-Mg_2Si cuboid particles are randomly distributed in the matrix and have dimensions of about 40×40 nm.

Artificial aging time, min (specified below each image) Artificial aging temperature 175.0°C

A1

a. 30 min b. 180 min c. 240 min

A2

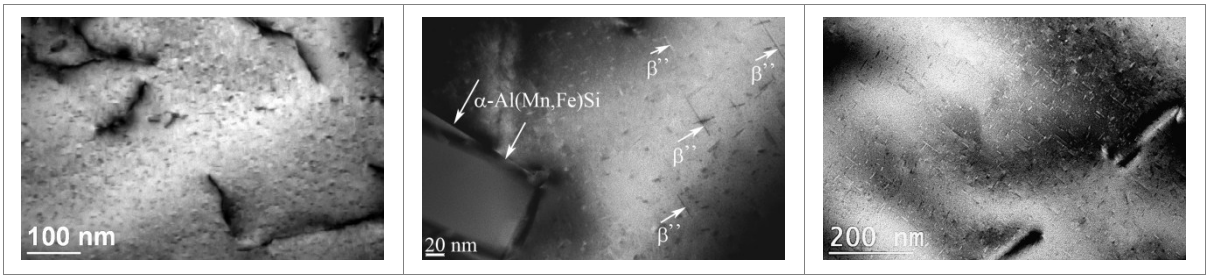

d. 90 min e. 120 min f. 600 min

B1

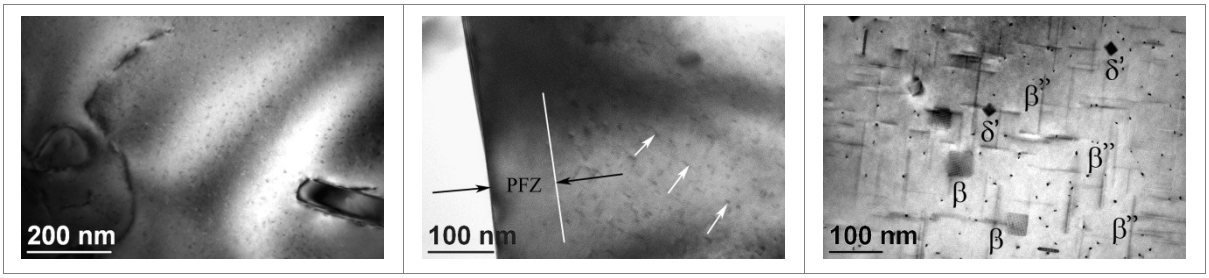

g.90 min h. 240 min k. 600 min

B2

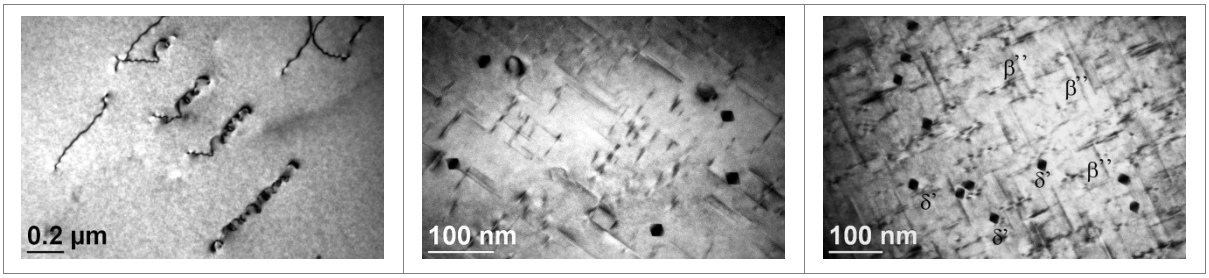

l. 30 min m. 240 min n. 1440 min

C1

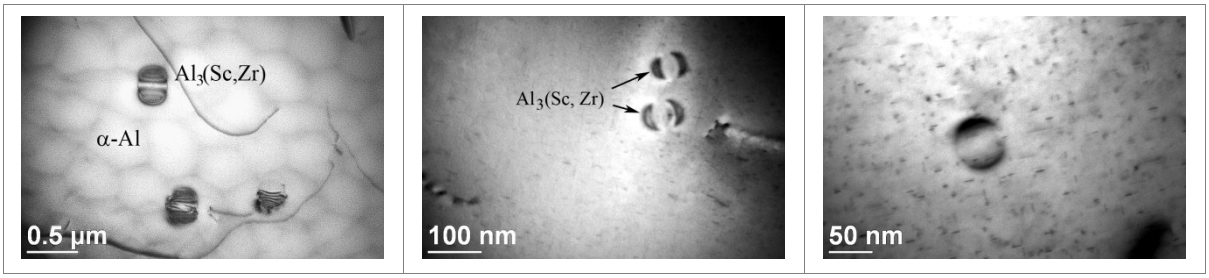

o. 30 min p. 90 min q. 240 min

Fig. 6.7: Precipitation process in A1-C1 alloys: bright field images of the α-Al matrix after different aging times

Their enlarged view represented in Figure 6.8 shows two separate particles marked β1 and β2. Obviously, a quadratic, thin plate is positioned one time on its large face (β1), the other time it is in edge on position (β2).

EDX analysis of these particles showed that they are enriched by Mg and Si simultaneously, which is an additional confirmation that these particles are Mg_2Si. It was reported that addition of Li decreases the solubility of Mg in solid solution, *[CHU03]*. This obviously can be one of the reasons for the formation of the cuboid phase.

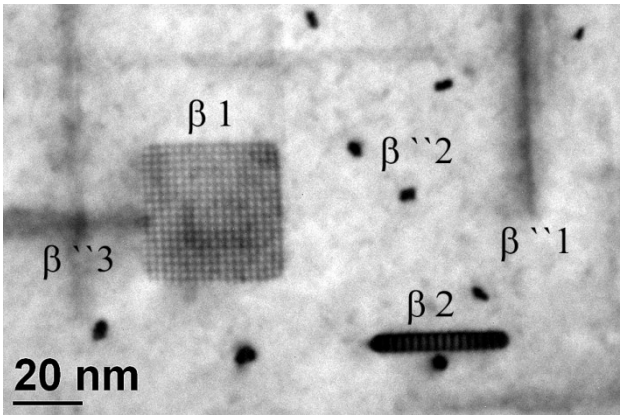

Fig. 6.8: Bright field image of β1 Mg_2Si particles and β" needles after artificial aging at 175.0 ℃ for 600 min

Additionally, in Figure 6.8, lines in two perpendicular directions can be seen, marked as $\beta"_1$ and $\beta"_3$. Fine spots are marked as $\beta"_2$. From this observation it can be concluded, that the β" phase has in deed needle morphology and that the needles are oriented in 3 perpendicular directions.

The third kind of precipitates are small black cuboids, which are randomly distributed in the α-Al. Comparing the TEM images of B1 and B2 with literature about Li-containing alloys *[CHE00]*, *[WEI00]*, *[MUR03]*, the third precipitate can be identified as δ′ Al_3Li phase, which coexists with two types of Mg_2Si compounds. A confirmation of the particle composition by EDX measurements is not possible because the light element Li can not be detected by energy dispersive analysis. In some publications δ′ Al_3Li precipitates are considered as spherical shaped, see for example *[CAB12]*. However, the image quality in those works is not sufficient to exactly reveal the precipitate morphology. Further precipitate identification needs advanced methods, such as high resolution TEM or analytical STEM, which is beyond this working program.

For C1 and C2 the only process expected to take place, is the formation of Mg_2Si precipitates, since the Sc- and Zr precipitates already formed during solution treatment. As can be seen from Figure 6.7 o after 30 min of artificial aging, the α-Al matrix contains $Al_3(Sc,Zr)$ precipitates. Aging for 90 min leads to the appearance of dotlike contrast and after 240 min small needles are visible in the matrix indicating the formation of β″.

6.4.2 Precipitates in the Al-Mg-Ge alloy and after Li addition

It is well known that the precipitation sequence of Al-Mg-Ge alloys is similar to that of Al-Mg-Si alloys *[MUN05]*, *[MUR12]*, *[BJO10]*. The recent work of Murakami et al. *[MUR12]*

showed that precipitates in an Al-1.10 wt.% Mg_2Ge are formed after conventional T6 heat treatment. Bjorge et al. *[BJO10]* showed that alloys of the Al-Mg-Ge system are strengthened by needle-shaped or a lath-shaped partially coherent precipitates which have a structure similar to the β′-phase in the Al-Mg-Si system. It was proposed to name this β′-like phase β′-Ge, [BJO12]. The presence of β′-Ge was confirmed by using a high angle annular dark field scanning TEM (HAADF STEM) in an alloy containing 0.87 at.% Mg and 0.43 at.% Ge *[BJO12]*. Bjorge et al. found that the hardness of a Ge-rich alloy reaches its maximum after 10 hours artificial aging at 200.0°C which is 9 h later than it was detected for a Mg-rich alloy *[BJO12]*. In the present study, the microhardness of D1 reached its maximum after 6 h aging at 175.0°C, which is not far from the measurements of Bjorge and the absolute values of HV are very similar.

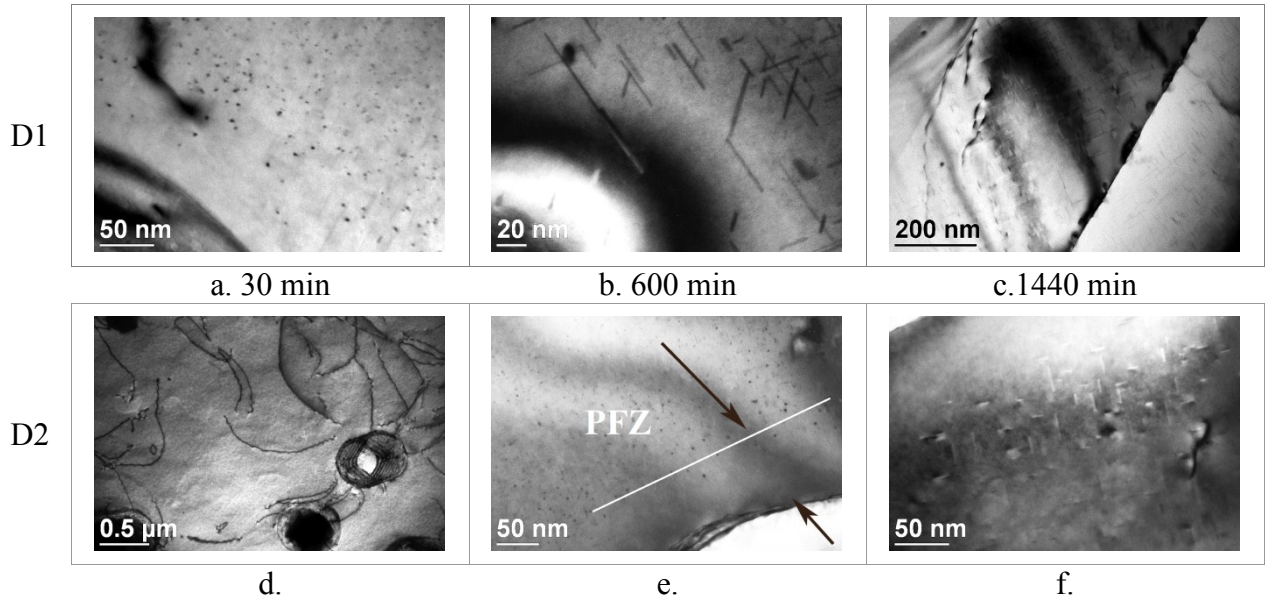

Fig. 6.9: Precipitation process in D1 - D2 alloys: bright field images of the α-Al matrix after at different aging times

The composition of the solid solution after quenching of D1 was measured by EDX and contains 0.13 at.% Mg and 0.35 at.% Ge. Comparing the composition of D1 with that of the alloy studied by Bjorge et al. *[BJO12]*, it can be concluded that, the precipitates observed after 600 min aging have the structure of a trigonal U1 phase (a = b = 0.405 nm, c = 0.674 nm), as it occurs in Al-Mg-Si alloys. Therefore it was proposed to call this phase $U1_{Ge}$.

TEM examinations of D1 and D2 showed that after 30 min the α-Al matrix in both alloys exhibits dotlike contrasts similar to A1 - A3 (Figures 6.9 a and d). After 600 min aging the needles of the $U1_{Ge}$ phase appeared. Continuous aging up to 24 h does not change the size or

precipitation density. As can be seen from Figure 6.9 a, the precipitates are positioned very close to the grain boundary, i.e. a precipitation free zone (PFZ) does practically not exist.

In general, PFZs are regions adjacent to grain boundaries which are depleted of precipitates. It is usually assumed that the PFZ result from the depletion of vacancies and solutes in this region. This is the standard interpretation for wrought alloys where PFZs are often observed.

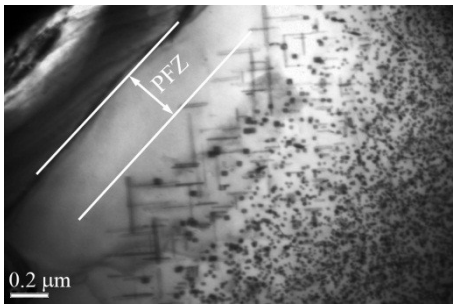

Fig. 6.10: Bright field image of B2 alloy after homogenization for 20 h at 300.0℃

Since only few TEM investigations of casting alloys exist, there the appearance of PFZs is not well established. As an example, in specimen B1 (Figure 6.7 h) precipitates are close to the grain boundary. However, in preliminary investigations performed with the B2 alloy with Li, after homogenization for 20 h at 300.0°C, PFZs were found. They are positioned between the area, where the α-Al matrix is occupied by needle-shaped and the cubic-shaped precipitates and eutectic lamella as illustrated in Figure 6.10. The most obvious case obviously, the relatively low homogenization temperature, is the reason for the formation of PFZ it results in a decreasing supersaturation of α-Al, but also in the lamella spheroidisation. Supposing, the spheroidisation leaves a concentration gradient behind the lamella then solute content in this region could be to low for further precipitation.

The precipitation process in D2 is not much different from that in D1 but aging for 600 min leads to the precipitation of a long needle-shaped β″-phase. Such precipitates were observed in an alloy of the Al-Mg-Si system with Li addition, *[BOJ12]*. From Figure 6.6 one can see that the maximum microhardness is reached somewhat earlier for the Li-containing alloy D2 than for D1. Obviously, this Li – containing δ′ phase precipitates much faster than the $U1_{Ge}$ phase (compare Fig. 6.9 d with Fig. 6.9 b). So the δ′ phase seems to be the hardening phase in the Li-containing D2 alloy. The precipitation kinetics in the Li – containing alloys B1, B2 is much faster than in D2, as can be concluded from the hardening curves in Figs. 6.5 and 6.6. So it seems that the precipitation processes change totally, when Si is substituted by Ge.

6.5 Summary

The central question of Chapter 6 was, whether Al-Mg-Si and Al-Mg-Ge alloys are able to form precipitates during aging which are acting as strengthening phase. This question rises from the composition of the solid solution prior to aging. As it was shown in Chapter 5, in as-quenched specimens the α-Al solid solution contains about 1.50 - 2.50 wt.% Mg. The Si content

is too low to be measured by EDX. Hence after quenching, the solid solution has not the fitting composition to form Mg_2Si.

Comparing the experimental alloys with commercial casting alloys one finds, that the solid solution of the commercial Al-Si-Mg casting alloy A356.0 contains enough solutes after solution treatment to form intermediate β" or stable β-Mg_2Si phases in contrary to the experimental casting alloys A1 - C2. TEM EDX measurements gave for PM A356.0 in solution treated and quenched state up to 0.27 wt.% Mg and about 1.00 wt.% Si, in α-Al for A1 - C2, solution treated, quenched and 24 hours annealed up to 2.70 wt.% Mg and no Si.

Results of hardness and microhardness measurements clearly show that strengthening of A1 - D2 and their matrices occurs. Especially, the increase of $HV_{0.05}$ is certifying the appearance of a new strengthening phase inside the aluminum solid solution. This is supported by DSC measurements where exothermal effects were detected.

A microstructural prove was obtained by TEM examinations of aged specimens. Different types of precipitates were found:

- in the base alloys A1/A2 needle-shaped β" precipitates;
- Li additions to the base alloy promote the formation of two additional phases: δ′ Al_3Li and β Mg_2Si. They have cuboidal shape;
- Sc+Zr promotes the formation of a ternary $Al_3(Sc,Zr)$ phase during solution treatment. Artificial aging adds the phase β".

One can conclude that Al-Mg-Si and Al-Mg-Ge casting alloys can be strengthened via precipitation hardening.

7 Conclusion

The thesis demonstrated that Al-Mg-Si and Al-Mg-Ge can play an integral role in developing a new generation of Al-based casting alloys, which offer promising potentials as the materials with good strength and ability to be used in as-cast and heat treated conditions. According to the goals of the research plan at the end of Chapter 2, the obtained results are summarized below.

(i) From the structural point of view it was established that in as-cast state the structure of Al-Mg-Si casting alloys consists of three phases, namely the α-Al solid solution, the (Al)+(Mg_2Si) eutectic and the primary Mg_2Si crystals. For the Al-Mg-Ge system corresponding constituents were detected, namely (Al)+(Mg_2Ge) eutectic and primary Mg_2Ge crystals in a α-Al solid solution. Addition of Mn leads to the formation of the primary $\alpha - AlFeMnSi$ phase, which is randomly distributed inside the solid solution grains. The eutectic melting temperatures for the Al-Mg-Si and the Al-Mg-Ge systems were measured by DSC. They are 587.4°C, respectively 629.0°C, which is in good agreement with equilibrium phase diagrams. These temperatures are the highest among commercially utilized casting alloys. The heat effects corresponding to the melting and solidification of the primary α-Al phase and the eutectic were clearly visible in the DSC curve. However, a heat effect associated with the formation of the primary AlFeMnSi phase was not observed due to its low volume fraction. The multistep nucleation, taking place during the solidification of these alloys, was experimentally confirmed. As shown in Chapter 4, the primary intermetallic crystals nucleate on the surface of oxide particles followed by the eutectic growth of the crystals. A similar nucleation sequence was observed for primary $Al_3(Sc,Zr)$ particles, nucleating on the surface of the oxide agglomeration, followed by the nucleation of the α-Al solid solution grains. Additional alloying with Li produces a modification effect on the primary intermetallics, making them smaller. Addition of Sc+Zr does not produce any a remarkable effect on the as-cast structure of the Al-Mg-Si alloys. During solution treatment in Al-Mg-Si and Al-Mg-Ge systems, the eutectic lamellas undergo a spheroidization as shown in Chapter 5. At a early stage of heating, the lamellas break into separate pieces and further treatment results in the coagulation and growth of intermetallic spheres. The primary crystals also tend to coagulate during solution treatment. After artificial aging, the additional precipitation was investigated by TEM in Chapter 6.

(ii) From the compositional point of view, EDX measurements of all alloys indicate that in as-cast state the α-Al solid solution in the Al-Mg-Si alloys contains about 2.40 at.% Mg. Si is below the detection limit. In the Al-Mg-Ge alloys, the α-Al solid solution contains 0.29 at.% Mg and about 1.00 at.% Ge. The composition of the intermetallics fits well to the stable Mg_2Si and Mg_2Ge compounds. In the Mn-containing alloys, the Mn content in α-Al was in the range between 0.20 - 0.29 at.%, which is very close to the Mn amount of the melt. Hence, only a small part of the Mn remains for the formation of the primary AlFeMnSi phase and therefore its fraction is rather low. During solution treatment, the Mg content increases gradually from 2.00 at.% in as-cast state up to 3.00 at.% after 24 hours soaking, producing a super saturation of the α-Al. The changes of the Mn content were not monotonous. At the initial stage of the solution treatment it decreases, prolonged soaking results in a slight increase of the Mn content, but after 600 min heating it decreases again. Artificial aging does not show any pronounced changes in the composition of the solid solution as well as of the other intermetallics.

(iii) Regarding the precipitation processes, it was shown in Chapter 4 that in Al-Mg-Si and Al-Mg-Ge alloys natural aging starts directly from the as-cast state. It was established in the Al-Mg-Si alloys that after a certain time the solid solution decomposes and plate-like precipitates are formed. These plates are β''-Mg_5Si_6 phase. The plates are lying in (100) planes and they are elongated in [010] direction. The dislocation connecting the plates has the average direction [101], so the plates are not lying in one (100)–plane, but are shifted in [100] and [001] direction. The dislocation forms a loop around each precipitate. Hence, the main mechanism of precipitate formation is heterogeneous nucleation on dislocations. This mechanism is also valid for the Al-Mg-Ge system, where similar precipitates in the shape of a zebra crossing were observed. Aging in as-cast condition was also detected in the commercial A201 and AlMg5Si2Mn alloys. The unique combination of the mechanical properties of the AlMg5Si2Mn alloy is based on the formation of fine-scale β''-Mg_5Si_6 precipitates, which are nucleated on dislocations during natural aging. The high dislocation density in an alloy subjected to the HPDC provides more nucleation sites for precipitates formation and this is the main reason for high mechanical properties of the AlMg5Si2Mn HPDC alloy. Solution treatment of the Al-Mg-Si and Al-Mg-Ge alloys results in a simultaneous dissolution of the precipitates formed during natural aging. This process takes several minutes time and causes a drop of the hardness and microhardness, which is completed after 60 minutes heating. The second process accompanying the solution treatment is the spheroidization of the eutectic lamellas, as described in Chapter 5. Spheroidization starts after 15 - 20 min solution treatment, after 30 min the lamellas are completely disintegrated. Mn plays different roles in solidification and solution treatment. During solidification one part of the

Mn atoms dissolves in the α-Al matrix, the other part forms primary intermetallics together with Si and Fe. Solution treatment results in the dissolution of the primary particles and the formation of new secondary dispersoids. Their growth starts on the surface of Mg_2Si or Mg_2Ge eutectic lamellas. These dispersoids occupy such areas in the matrix, which have become vacant by the lamella spheroidization.

Aging of Al-Mg-Si alloys leads to the formation of needle-shaped precipitates of the β″-phase in Al-Mg-Si and $U1_{Ge}$-phase in Al-Mg-Ge alloys. In Li-containing alloys two additional types of precipitates were found, namely the Mg_2Si β-phase having a plate-like morphology and small cubic-shaped Al_3Li particles, the δ′ phase. In the Sc+Zr containing alloys, $Al_3(Sc,Zr)$ precipitates are forming during solution treatment which remain stable during artificial aging.

In conclusion, that Al-Mg-Si and Al-Mg-Ge systems have promising potential for a novel generation of casting alloys, such as a Li-containing casting alloys with reduced density, which is not established yet. The Sc+Zr containing casting alloys are usually considered as 'principal addition', which effectively improve the properties of aluminum alloys. However, until now no casting alloy containing Sc or Sc+Zr was designed. The present work shows that these elements can be added successfully to Al-Mg-Si alloys. The formation of precipitates starts already during solution treatment as shown in Chapter 5.

Thus, the obtained results clearly show, that the four goals of the research, namely:

- analysis of the structure of Al-Mg-Si and Al-Mg-Ge casting alloys in as-cast state together with its change during solution treatment and aging;
- measurement of the composition of solid solution in as-cast state and its variation during solution treatment and artificial aging;
- finding the reason of the high mechanical properties of Al-Mg-Si casting alloys in as-cast state and discovering their changes during solution treatment and aging;
- investigation of the morphology and type of the secondary precipitates in Al-Mg-Si and Al-Mg-Ge during heat treatment;

were achieved and it was shown, that Al-Mg-Si and Al-Mg-Ge systems can be used to develop novel casting alloys, which are able to be precipitation strengthened in as-cast condition as well as in heat treated state. Further research is needed to attain more detailed information about the relation between dislocation density and precipitates volume fraction and how this volume fraction could be increased by Ti, Zr and/or Cr additions.

Appendixes

Appendix 1

Chemical composition of aluminum and Al-based master alloys used throughout work

nominal composition	content, wt.%[1]								
	Si	Mn	Sc	Zr	Ti	Fe	Mg	Li	Ge
Al-25.00%Si	25.30	-	-	-	0.01	0.09	-	-	-
Al-26.00%Mn	-	25.8	-	-	-	0.13	-	-0.04[3]	-
Al-6.00%Ti[4]	0.04	-	-	-	6.20	0.07	-	-	-
Al-50.00%Mg	0.01		-	-	-	0.08	50.8	-	-
Al-5.00%Li[2]	0.08				0.01	0.08		5.40	
Al-10.00%Zr	0.05	-	-	10.10	0.003	0.09	-	-	-
Al-20.00%Ge	-	-	-	-	-	0.09	-	-	20.20
Al-2.00%Sc	0.021	-		0.023	0.002	0.08	-	-	-

[1] - Al balance;
[2] – Al-5.00%Li also contains 0.03%Na (supplied by **KBM Master Alloys B.V.,** Delfzijl);
[3] – V content;
[4] – C content 0.05 wt.%;

Chemical composition of aluminum Al 99.997 (supplied by Norsk Hydro)

	impurities, ppm*									
	Si	Fe	Cu	Mg	Ti	Cr	Mn	Zn	V	P
A99.997	5.20	3.90	9.00	0.90	0.20	0.10	0.10	2.70	0.10	2.00

* - ppm = 0.0001 wt.%

Appendix 2

Microstructure of master alloys used throughout the work and their structure characterization

Al – 26.00 wt.% Si master alloy

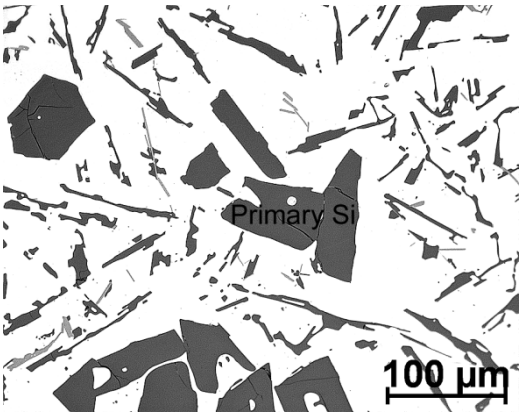

Fig. 2.1: Microstructure of Al-26.00 wt.% Si master alloy and morphology of primary Si crystals

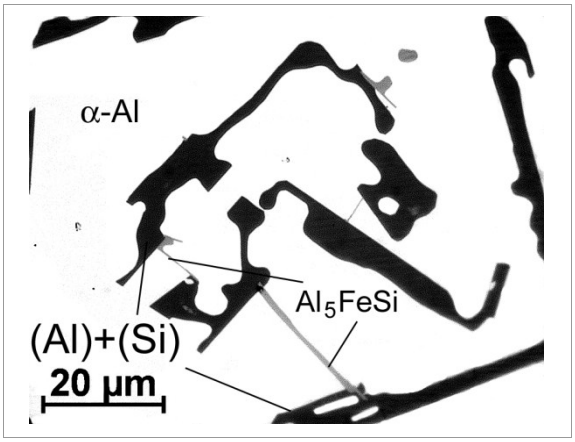

Fig. 2.2: Morphology of (Al)+(Si) eutectic (dark needles) and of β (Al_5FeSi) (thin light needles)

The constituents of the system are Al and Si, forming a eutectic at 11.70 wt.% Si, 577.0°C. Aluminum and silicon do not form any compound.

According to the chemical composition and phases present in the master alloy Al-26.00 wt.% Si is the main source of Fe impurity in the experimental alloy.

Al – 25.00 wt.% Mn master alloy

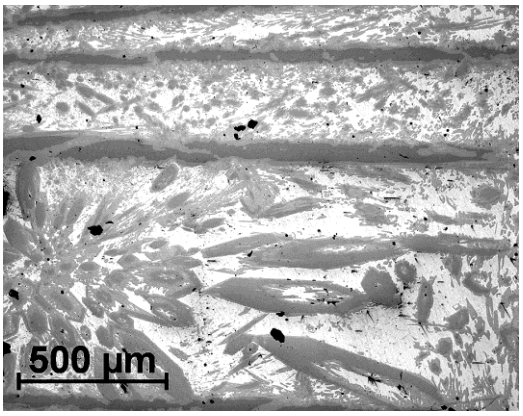

Fig. 2.3: Microstructure of binary Al – 25.00 wt.% Mn master alloy

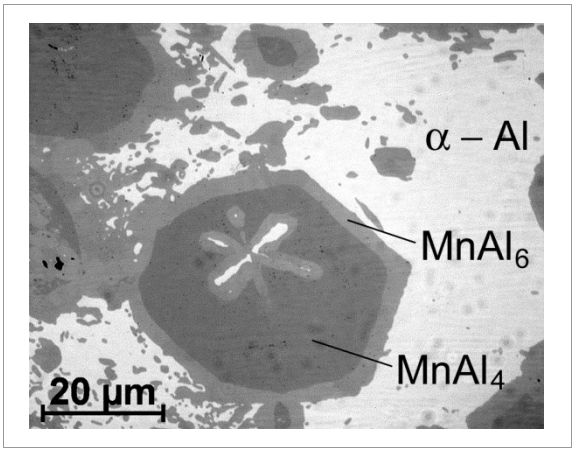

Fig. 2.4: Morphology of primary $MnAl_4$ crystals surrounded by shell of $MnAl_6$

The equilibrium compound at the aluminum end of Al-Mn equilibrium phase diagram is $AlMn_6$ intermetallic compound. It forms a eutectic with Al at 1.95 wt. % Mn, 658.0°C.

In turn, primary crystals of $MnAl_6$ are form up to 4.00 wt.% Mn. Primary crystals $MnAl_6$ is formed at 710.0°C by peritectic reaction from $MnAl_4$ and the liquid ($L + MnAl_4 = MnAl_6$). $MnAl_4$ is hexagonal with lattice parameters a = 2.84 nm, c = 1.24 nm, and forms primary crystals from 4.00 to 12.00 wt.% Mn; then it is formed by peritectic reaction from $MnAl_3$ at 820.0°C. The peritectic reactions $MnAl_3 + L \rightarrow MnAl_4 + L \rightarrow MnAl_6$ are slow, and in non-equilibrium conditions usually are not completed.

Table 2.1: Invariant reactions in the Al terminal of Al-Mn phase diagram, *[LIU99]*

Reaction	Reaction type	Temperature °C	Composition, at. % Mn		
$L + Al_4Mn \rightarrow Al_6Mn$	Peritectic	705.20	1.82	20.00	14.29
$L \rightarrow (Al) + Al_6Mn$	Eutectic	658.50	0.96	0.71	14.29

Al – 50.00 wt.% Mg master alloy (supplied by KBM Master Alloys B.V., Delfzijl)

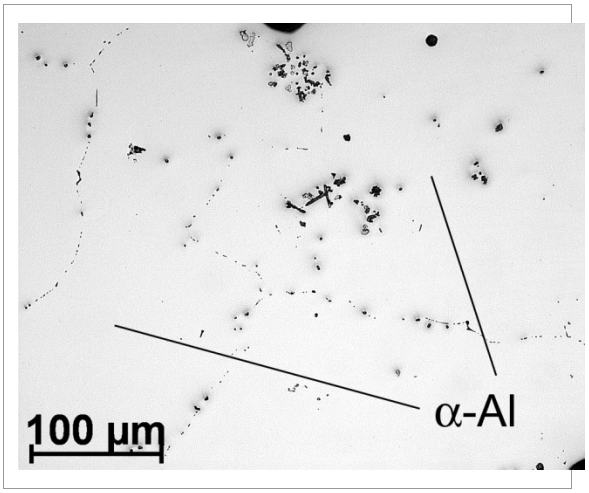

Fig. 2.5: Microstructure of Al – 50.00 wt.% Mg binary master alloy

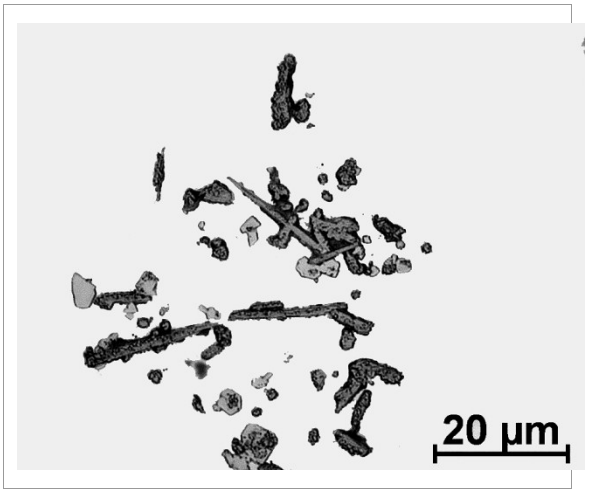

Fig. 2.6 Microstructure of Al – 50.00 wt.% Mg binary master alloy

Magnesium and aluminum form four compounds. The first at the aluminum end is Mg_5Al, hexagonal, with lattice parameters a = 1.14 nm, c = 1.79 nm, and a magnesium content of 35.00 to 36.20 at.%.

Another crystal structure of Mg_5Al_8 is formed by precipitation from a supersaturated solid solution of magnesium in aluminum. Mg_5Al_8 forms a eutectic with Al at about 33.00 at. % Mg, melting at 449.00°C.

Al – 10.00 wt.% Zr master alloy (supplied by KBM Master Alloys B.V., Delfzijl)

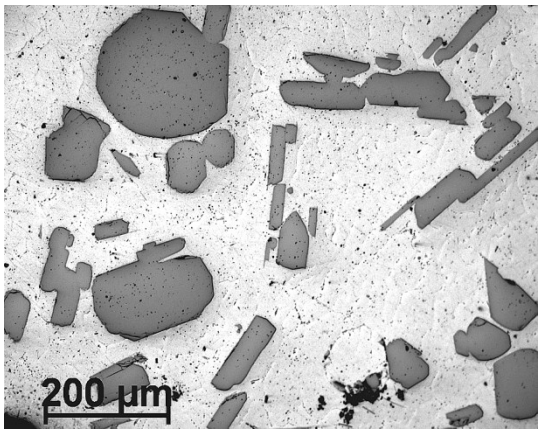

Fig. 2.7: Microstructure of Al – 10.00 wt.% Zr binary master alloy

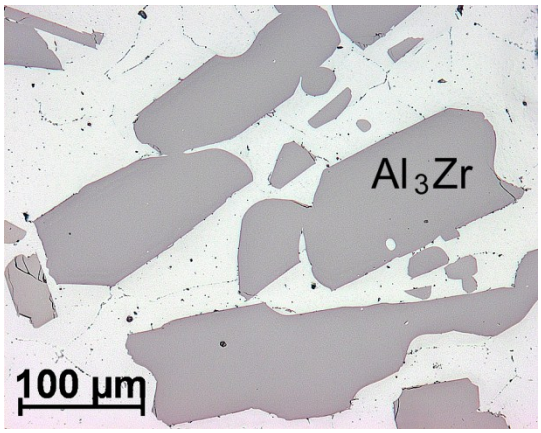

Fig. 2.8: Morphology of Al_3Zr crystals in Al – 10.00 wt.% Zr binary master alloy

Al – 2.00 wt.% Sc master alloy ("Vostgok", Zheltiye Vody, Ukraine)

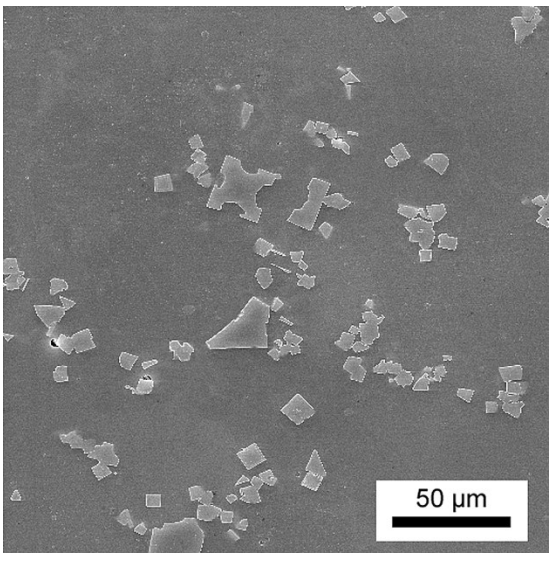

Fig. 2.9: Microstructure of Al – 2.00 wt.% Sc binary master alloy

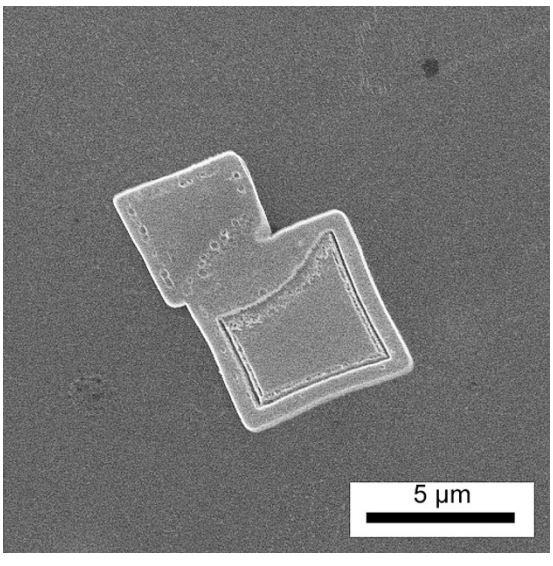

Fig. 2.10: Morphology of Al_3Sc primary particles in Al – 2.00 wt.% Sc binary master alloy

Al – 5.0 wt.% Li master alloy (supplied by KBM Master Alloys B.V., Delfzijl)

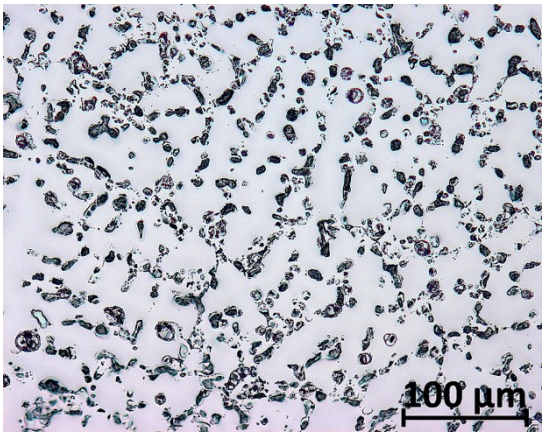

Fig. 2.11: Microstructure of Al – 5.00 .% Li binary master alloy

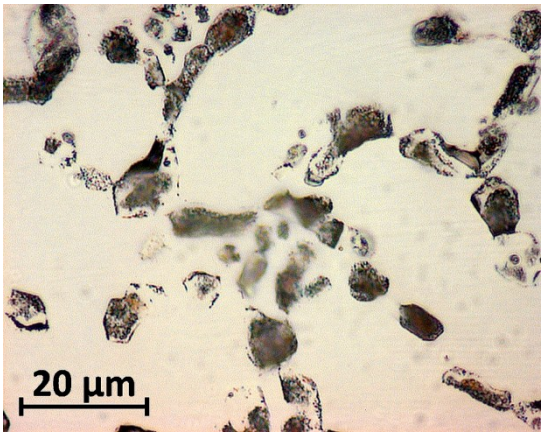

Fig. 2.12: Morphology of primary Al_3Li particles in Al – 5.00 wt.% Li binary master alloy

Al – 20.0 wt.% Ge master alloy (laboratory melted)

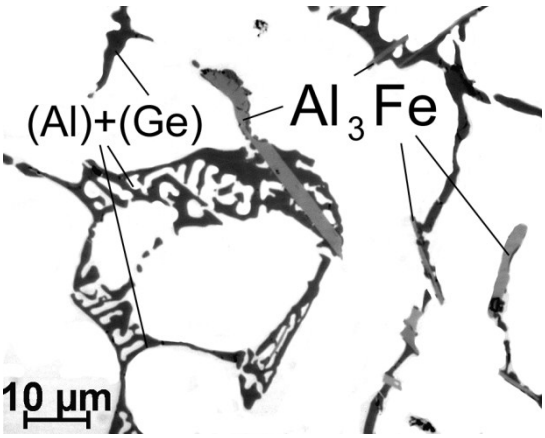

Fig. 2.13: Microstructure of Al – 20.00 wt.% Ge binary master alloy

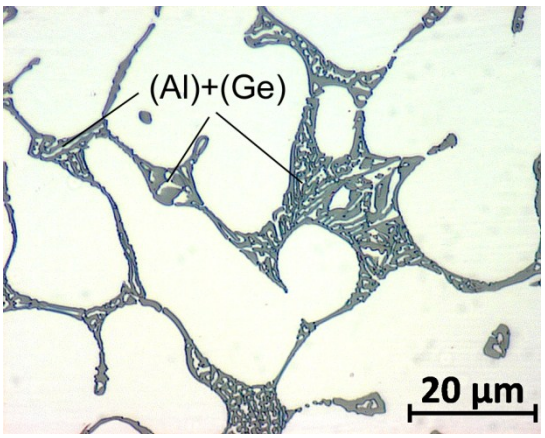

Fig. 2.14: Morphology of (Al)-(Ge) eutectic in Al – 20.00 wt.% Ge binary master alloy

Appendix 3

Melting and macroetching techniques used throughout the work. Figure 3.1 displays the melting set up, and tools used for melting of the alloys subjected to research program. Graphite bell was used for addition of alloying elements. Pieces of master alloys were wrapped into aluminum foil and putted inside of the bell and then added to the melt by immersing the bell below the melt surface. Prior casting each melt was treated by argon blowing. Application of the system for melt blowing is the common industrial practice and has three main reasons such as:

- to achieve homogeneous temperature and alloying elements distribution in the melt;
- to clean the melt from dissolved gases (mainly hydrogen);
- to clean the melt from nonmetallic impurities (mainly oxides and spinels).

a. Melting set up

b. graphite bell used for alloying additions

c. Testing of the lance

d. Graphite lance designed for melt blowing

Fig. 3.1: Melting set up and tools used to prepare experimental alloys

Macroetching of alloys under investigation

Cast ingots were cut on two parts and one part was grinded and polished using standard metallographic procedure. Final grinding performed on 1200 GRIT silicon carbide paper and after this specimens were etched using modified M2, *[PET01]* etching liquid: 215 ml HCl+150 ml HNO_3+15 ml HF. To avoid overheating of etching liquid specimens were immersed into etchant several times. Water flushing was used between immersions. After revealing the macrostructure and specimens reached sufficient contrast final water flushing was used. For removing reaction products from the specimen service solution of 80% HNO_3+20% H_20 was applied. As the final step etching in 1% HF solution applied for improving specimens' contrast.

References

[ALU98] The Aluminium Association. Aluminium Alloy: Selection and Applications, The Aluminum Association, Inc., Washington DC, USA, 1998

[ALU12] the European Aluminium Association, http://www.alueurope.eu/

[AND04] Andresen, W., Die Cast Engineering: A Hydraulic, Thermal, and Mechanical Process, CRC Press, 2004, 400

[ASH63] Ashby, M. F., Brown, L. M., Diffraction contrast from spherically symmetrical coherency strains, in: Philosophical Magazine, 1963, 1083-1103

[ASK87] Askeland, D. R., The Science and Engineering of Materials, PWS-Kent Publishing Co., 1987

[ASM88] ASM Metals Handbook Ninth Edition, Volume 15, *Casting*, ASM International, 1988

[ASM04] Introduction to Aluminium-Silicon Casting Alloys. Aluminium-Silicon Casting Alloys: Atlas of Microfractographs, 2004, www.asminternational.org/bookstore

[BAN86] Banerji, A., Reif, W., Development of Al-Ti-C Grain Refiners Containing TiC, in: Metallurgical Transactions A, Vol. 17A, 1986, 2127-2137

[BAN10] Banhart, J., Chang, C. S. T., Liang, Z., Wanderka, N., Lay, M. D., Hill, A. J., Natural ageing in Al-Mg-Si alloys - a process of unexpected complexity. Natural aging in Al-Mg-Si alloys - a process of unexpected complexity, in: Advanced Engineering Materials, Vol. 12, No. 7, 2010, 559-571

[BAR00] Barabash, O., M., Legkaya, T. N., Korzhova, N. P., Sulgenko, O. V., Thermodynamic analysis and experimental study of composite structure formation in eutectic alloys α-Al+Mg_2Si, in: Powder metallurgy and Metal Ceramics, Vol. 39, No. 9-10, 2000, 458-461

[BAR01] Barabash, O. M., Sulgenko, O. V., Legkaya, T. N., Korzhova, N. P., Experimental Analysis and Thermodynamic Calculation of the Structural Regularities in the Fusion Diagram of the System of Alloys Al-Mg-Si, in: Journal of Phase Equilibria, Vol. 22, No. 1, 2001, 5-11

[BIR08] Birol, Y., DSC analysis of the precipitation reaction in AA6005 alloy, in: Journal of Thermal Analysis and Calorimetry, Vol. 93, No. 3, 2008, 977-981

[BJO10] Bjorge, R., Marioara, C. D., Andersen, S. J., Holmestad, R., Precipitation in Two Al-Mg-Ge Alloys, in: Metallurgical and Materials Transactions A, Vol. 41A, 2010, 1907-1916

[BJO12] Bjorge, R., Dwyer, C., Weyland, M., Nakashima, P. N. H., Marioara, C. D., Andersen, S. J., Etheridge, J., Olmestad, R., Aberration-corrected scanning transmission electron microscopy study of β'-like precipitates in an Al-Mg-Ge alloy, in: Acta Materialia, Vol. 60, 2012, 3239-3246

[BLA85] Blake, N., Hopkins, M. A., Constitution and age hardening of Al-Sc alloys, in: Journal of Material Science, Vol. 20, 1985, 2861-2867

[BLA93] Blankenship, C. P. A., Hornbogen, E., Starke, E. A., Predicting slip behaviour in alloys containing shearable and strong particles, in: Materials Science and Engineering, Vol. 169A, 1993, 33-41

[BRO12] Brock, H., Franc, P., Annual Report 2012, in: The Aluminium Association. Arlington, Virginia, 2012, 28

[BUC51] Buckley, H. E., Crystal growth, John Wiley & Sons, Inc., New York, 1951, 571

[BUN99] Bunn, A. M., Schumacher, P., Kearns, M. A., Boothroyd, C. B., Greer, A. L., Grain refinement by Al-Ti-B alloys in aluminium melts: a study of the mechanisms of poisoning by zirconium, in: Materials Science and Technology, Vol. 15, 1999, 1115-112

[CAB12] Cabibbo, M., Partial dissolution of strengthening particles induced by equal channel angular pressing in an Al-Li-Cu alloy, in: Materials Characterization, Vol. 68, 2012, 7-13

[CAM04] Campbell, I., Castings practice the 10 rules of castings, Elsevier Butterworth-Heinemann, 2004, 199

[CAN79] Cantor, B., Doherty, R. D., Heterogeneous nucleation in solidifying alloys, in: Acta Metallurgica, Vol. 27, 1979, 33-46

[CAN03] Cantor, B., Heterogeneous nucleation and adsorption, in: Philosophical Transactions of the Royal Society A., Vol. 361, 2003, 409-417

[CHA63] Chadwick, G. A., Eutectic Alloy Solidification, Pergamon Press, 1963, 86

[CHA64] Chalmers, M., Principles of Solidification, John Wiley & Sons Inc., New York, 1964, 120-180

[CHA77] Chamberlain, B., Wayanabe, S., Zabek, V. J., A Natural Aging Aluminium Alloy Designed for Permanent Mold Use, in: AFS Transactions, Vol. 85, 1977, 133-142

[CHA09] Chandrashekar, T., Muralidhara, M. K., Kashyap, K. T., Raghothama, R. P., Effect of growth restricting factor on grain refinement of aluminium alloys, in: The International Journal of Advanced Manufacturing Technology, 2009, 234-241

[CHE00] Chen, R., Huang, Z., Chen, C. Q., Shen, J. Y., Zhang, Y. G., Thermodynamic calculated and TEM observed microstructure of Al-Li-Mg-Si alloys, in: Materials Science and Engineering, Vol. 280A, 2000, 146-150

[CHU03] Chuistov, K. V., Aging of Metallic alloys, Second ed. Kiev, Academperiodika, 2003, 568

[CON92] Conserva, M., Donzelli, G., Trippodo, R., Aluminium and its applications, Edimet, 1991, 408

[CZE06] Czerwinski, F., The Basics of Modern Semi-Solid Metal Processing, in: JOM, 2006, 17-20

[DAV70] Davies, I. G., Dennis, I. M., Hellawell, A., The Nucleation of Aluminium Grains in Alloys of Aluminium with Titanium and Boron, in: Metallurgical Transactions, Vol. 1, 1970, 275-280

[DAV93] Davis, J. R., Aluminium and Aluminium Alloys, ASM Specialty Handbook, ASM International, Materials Park, OH, 1993, 784

[DOH96] Doherty, R. D., Diffusive Phase Transformations in the solid state, in: Physical Metallurgy, Elsevier Science BV, 1996, 1363-1505

[DRA10] Dragulin, D., Belte, M., Hoffmann, O., AlMg5Si2Mn – Aliminiumdruckgusslegierung unter dem Aspekt einer Wärmebehandlungsperspektive, in: Druckguss, Vol. 3, 2010, 49-51

[DUP10] Duparc, H. O. B. M., The Preston of the Guinier-Preston Zones. Guinier, in: Metallurgical and Materials Transactions B, Vol. 41B, 2010, 925-934

[FAN02] Fan, Z., Semisolid metal processing, in: International Materials Reviews, Vol. 47, No. 2, 2002, 1-37

[FAN09] Fan, Z., Wang, Y., Zhang, Z. F., Xia, M., Li, H. T., Xu, J., Granasy, L., Scamans, G. M., Shear enhanced heterogeneous nucleation in some Mg- and Al-alloys, in: International Journal of Cast Metals Research, Vol. 22, No. 1-4, 2009, 1-5

[FAR10] Faraji, M., Katgerman, L., Distribution of trace elements in a modified and grain refined aluminum-silicon hypoeutectic alloy, in: Micron, Vol. 41, No. 6, 2010, 554-559

[FAV08] Favvas, E. P., Mitropoulos, A. C., What is spinodal decomposition?, in: Journal of Engineering Science and Technology Review, Vol. 1, 2008, 25-27

[FIN75] Fine, M. E., Precipitation Hardening of Aluminium Alloys, in: Metallurgical and Materials Transactions A, Vol. 6A, No. 4, 1975, 625-630

[FLE61] Fleischer, R. L., Solution hardening, in: Acta Metallurgica, Vol. 9, 1961, 996-1000

[FLE63] Fleischer, R. L., Substitutional solution hardening, in: Acta Metallurgica, Vol. 11, 1963, 203-209

[FLE74] Flemings, M. C., Solidification Processing, McGraw Hill, New York, 1974, 245

[FLE86] Flemings, M. C., Solidification Processing, Trans Tech Publications, Switzerland, 1986, 97

[FLE91] Flemings, M. C., Behaviour of Metal Alloys in Semisolid state, in: Metall. Trans. A, Vol. 22A, 1991, 957-962

[FOR04] Forbord, B., Lefebvre, W., Danoix, F., Hallem, H., Marthinsen, K., Three dimensional atom probe investigation on the formation of $Al_3(Sc,Zr)$-dispersoids in aluminium alloys, in: Scripta Materialia, Vol. 51, 2004, 333-337

[FOU72] Fournelle, R. A., Clark, J. B., The Genesis of the Cellular Precipitation Reaction, in: Metallurgical Transactions, Vol. 3, 1972, 2757-2767

[FRE12] Fredricsson, H., Akerlind, U., Solidification and Crystallisation Processing in Metals and Alloys, John Wiley & Sons, Ltd., 2012, 816

[GAL87] Galbrith, J. M., Tosten, M. H., Howell, P. R., On the nucleation of Θ' and T_1 on Al_3Zr precipitates in AI-Li-Cu-Zr alloys, in: Journal Material Science, Vol. 22, 1987, 27-36

[GIE06] Geier, H., Rockenschaub, H., Pabel, T., Variation of the precipitation mechanisms for high pressure die casting alloy AlSi9Cu3(Fe), in: Giessereiforshung, 58, No. 3, 2006, 2-18

[GLI11] Glicksman, M. E., Principles of Solidification: An Introduction to Modern Casting and Crystal Growth Concept, Springer Science+Business Media, LLC, New York, 2011, 520

[GRE03] Greer, A. L., Cooper, P. S., Meredith, M. W., Schneider, W., Schumacher, P., Spittle, J. A., Tronche, A., Grain Refinement of Aluminium Alloys by Inoculation, in: Advanced Engineering Materials, Vol. 5, No. 1-2, 2003, 81-91

[GUO05] Guo, Z., Sha, W., Quantification of precipitate fraction in Al–Si–Cu alloys, in: Materials Science and Engineering A, Vol. 392, No. 1-2, 2005, 449-452

[GUY74] Guyot, P., Wintenberger, M., Repeated θ' precipitation at dislocations in Al-4wt.%Cu, in: Journal of Materials Science, Vol. 9, 1974, 614-618

[HAA96] Haasen, P., Physical Metallurgy, 4th ed., Elsevier Science BV, 1996, 2009-2068

[HAD08] Hadian, R., Emamy, M., Varahram, N., Nemati, N., The effect of Li on the tensile properties of cast Al–Mg_2Si metal matrix composite, in: Materials Science and Engineering A, Vol. 490, No. 1-2, 2008, 250-257

[HIE96] Hielscher, U., Sternau, H., Koch, H., Franke, A. J., Magsimal-59: An AlMgMnSi-Type Squeeze-Casting Alloy Designed for Temper F , W. Hale, ed., TMS, Warrendale, PA, 1996, 933-937

[HIR04] Hirsch, J., Automotive Trends in Aluminium - The European Perspective, in: Materials Forum, Vol. 28, 2004, 15-23

[HOR84] Hornbogen, E., On the micristructure of alloys, in: Acta Metallurgica, Vol. 32, No. 5, 1984, 615-627

[HOR93] Hornbogen, E., Starke, E. A., Theory assisted design of high strength low alloy aluminium, in: Acta Metallurgica et Materialia, Vol. 41, No. 1, 1993, 1-16

[HUZ13] Hu, Z., Wan, L., Wu, S., Wu, H., Liu, X., Microstructure and mechanical properties of high strength die-casting Al–Mg–Si–Mn alloy, in: Materials and Design, Vol. 46, 2013, 451-456

[ISL06] Islam, F., Thykadavil, A. K., Medraj, M., A Computational Thermodynamic Model of the Mg-Al-Ge System, in: Journal of Alloys and Compound, Vol. 425, 2006, 129-139

[IWA04] Iwamura, S., Miura, Y., Loss in coherency and coarsening behaviour of Al_3Sc precipitates, in: Acta Materialia, Vol. 52, 2004, 591-600

[JAC65] Jackson, K. A., Hunt, J. D., Transparent compounds that freeze like metals, in: Acta Metallurgica, Vol. 13, No. 11, 1965, 1212-1215

[JAC66] Jackson, K. A., Hunt, J. D., Lamellar and rod eutectic growth, in: Trans. Metall. Soc. AIME, 1966, 1129-1142

[JAC69] Jacobs, M. H, The nucleation and growth of precipitates in aluminium alloys, PhD thesis at the University of Warwick, 1969, 184

[JAC04] Jackson, K. A., Constitutional supercooling surface roughening, in: Journal of Crystal Growth, Vol. 264, 2004, 519 -529

[JOR08] Jorstad, J. L., Excellent die casting alloy system made better by rheocasting. Die Casting Engineer, 2008, 18-20

[KAI11] Kaiser, M. S., Kurny, A. S. W., Effect of Scandium on the grain refining and aging behavior of cast Al–Si–Mg alloy, in: Iranian Journal of Materials Science & Engineering, Vol. 8, No. 4, 2011, 1-8

[KAI12] Kaiser, M. S., Basher, M. R., Kurny, A. S. W., Effect of Scandium on Microstructure and Mechanical Properties of Cast Al-Si-Mg Alloy, in: Journal of Materials Engineering and Performance, Vol. 21, No. 7, 2012, 1504-1508

[KAU02] Kaufman, M., Principles of Thermodynamic, Marcel Dekker, Inc., New York, Basel, 2002, 309

[KAU04] Kaufman, J. G., Rooy, E. L., Aluminum Alloy Castings: Properties, Processes, and Applications, ASM International, 2004, 321

[KHA83] Khachaturyan, A. G., Theory of Structural Transformations in Solids, Wiley, New York, 1983, 240

[KIM94] Kim, T. W., Cantor, B., An adsorption model of the heterogeneous nucleation of solidification, in: Acta metallurgica et materialia, Vol. 42, No. 9, 1994, 3115-3127

[KIN01] King, J., The aluminium industry, Woodhead Publishing Ltd., 2001, 340 p

[KOC96] Koch, H., Hielscher, U., Sternau, H., Franke, A. J., Magsimal-59, an Al MgMnSi-Type Squeeze-Casting Alloy designed for temper F, in: TMS, Light Metals, 1996, 933-937

[KOC00] Koch, H., Krug, P., Franke, A. J., Ductile high pressure die casting parts for automotive application - alloy development and experience from practice, in: Proc. 11th Biennial Die Casting Conf., Australian Die Casting Association, Melbourne, Australian, 2000, 26-25

[KOC03] Koch, H., Eigenschaften und Anwendung der Legierungen vom Typ Magsimal (AlMg5Si2Mn) - ein Statusbericht, in: Konferenz-Einzelbericht zum 24. Aalener Gießereisymposium, 2003, 1-18

[KOC06] Koch, H., Lenczowski, B., Al-Mg-Si cast aluminum alloy containing scandium // C22C 21/02 (2006.01), C22C 21/08 (2006.01) PCT/DE2004/002425, WO/2005/047554

[KUM00] Kumar, H., Chakraborti, K. C., Hans-Leo, N., Bodak, O., Rokhlin, L., Al-Mg-Si (Aluminium-Magnesium-Silicon), in: Light Metal Ternary Systems: Phase Diagrams, Crystallographic and Thermodynamic Data, Landolt-Börnstein New Series IV/11A3, MSIT, 2000

[KUR84] Kurz, W., Fisher, D., J., Fundamentals of Solidification, Trans. Tech. Publications, Ltd., Aedermannsdorf, Switzerland, 1984, 242

[KUR92] Kurz, W., Fisher, D. J., Fundamentals of solidification, Trans. Tech. Publication, 4th ed., 1992, 305

[LAV87] Lavernia, E. J., Grant, N. J., Aluminium-lithium alloys, in: Journal of Material Science, Vol. 22, 1987, 1521-1529

[LEI07] Leis, W., Aluminiumlegierungen: Legierungen und Festigkeitseigenschaften, in: Giesserei, Vol. 94, No. 2, 2007, 48-59

[LIC11] Li, C., Wu, Y., Li, H., Liu, X., Morphological evolution and growth mechanism of primary Mg_2Si phase in Al-Mg_2Si alloys, in: Acta Materialia, Vol. 59, 2011, 1058-1067

[LIS97] Li, S., Zhao, S., Pan, M., Zhao, D., Chen, X., Barabash, O., Barabash, R., Solidification and Structural characteristic of α-(Al)-Mg_2Si Eutectic, in: Materials Transaction, JIM, Vol. 38, No. 6, 1997, 553-559

[LIS01] Li, S.-P., Zhao, S.-X., Pan, M.-X., Zhao, D.-Q., Chen, X.-C., Barabash, O., M., Eutectic reaction and microstructural characteristics of Al (Li)-Mg_2Si alloys, in: Journal of Materials Science, Vol. 36, 2001, 1569-1575

[LIU92] Liu, J. M., Zhou, Y. H., Shang, B. L., Theory and experiments on irregular eutectic growth: Investigation on Al-Si eutectic growth, in: Journal of Material Science, Vol. 27, 1992, 2067-2074

[LIY03] Li, Y. J., Arnberg, L., Quantitative study on the precipitation behaviour of dispersoids in DC-cast AA3003 alloy during heating and homogenization, in: Acta Materialia, Vol. 51, 2003, 3415-3428

[LIY12] Li, Y. J., Muggerud, A. M. F., Olsen, A., Furu, T., Precipitation of partially coherent α-Al(Mn,Fe)Si dispersoids and their strengthening effect in AA 3003 alloy, in: Acta Materialia, Vol. 60, 2012, 1004-1014

[LOD00] Lodgaard, L., Ryum, N., Precipitation of dispersoids containing Mn and/or Cr in Al-Mg-Si alloys, in: Materials Science and Engineering, Vol. 283A, 2000, 144-152

[LUL05] Lu, L., Dahle, A. K., Iron-Rich Intermetallic Phases and Their Role in Casting Defect Formation in Hypoeutectic Al-Si Alloys, in: Metallurgical and Materials Transactions A, Vol. 36A, 2005, 819-835

[MAG91] Magnin, P., Trivedi, R., Eutectic growth: A modification of the Jackson and Hunt theory, in: Acta metallurgica et Materialia, Vol. 39, No. 4, 1991, 453-467

[MAR98] Martin, J. W., Precipitation Hardening, Second Edition: Theory and Applications. Butterworth-Heinemann, 1998, 240

[MAR01] Marquis, E. A., Seidman, D. N., Nanoscale structural evolution of Al_3Sc precipitates in Al(Sc) alloys, in: Acta Materialia, Vol. 49, 2001, 1909-1919

[MAR05] Marioara, C. D., Andersen, S. J., Zandbergen, H. W., Holmestad, R., The Influence of Alloy Composition on Precipitates of the Al-Mg-Si System, in: Metallurgical and Materials Transactions A, Vol. 36A, 2005, 691-702

[MAT98] Matsuda, K., Gamada, H., Fujii, K., Uetani, Y., Sato, T., Kamio, A., Ikeno, S., High-Resolution Electron Microscopy on the Structure of Guinier–Preston Zones in an Al-1.6wt.%Mg_2Si Alloy, in: Metallurgical and Materials Transactions A, Vol. 29A, No. 4, 1998, 1161-1167

[MAX75] Maxwell, I., Hellawell, A., A simple model for grain refinement during solidification, in: Acta Metallurgica, Vol. 23, 1975, 229-237

[MCD04] McDonald, S. D., Nogita, K., Dahle, A. K., Eutectic nucleation in Al–Si alloys, in: Acta Materialia, Vol. 52, 2004, 4273-4280

[MIL00] Miller, W. S., Zhuang, L., Bottema, J., Wittebrood, A. J., De Smet, P., Haszler, A., Vieregge, A., Recent development in aluminium alloys for the automotive industry, in: Materials Science and Engineering, Vol. 280A, 2000, 37-49

[MIN74] Minkoff, I., Lux, B., On spiral eutectic growth., in: Journal of Material Science Letters, Vol. 9, 1974, 1365-1367

[MON76] Mondolfo, L. F., Aluminium Alloys, Structure and Properties, Butterworth and Co, Ltd, London and Tonbridge, 1976, 971

[MOS12] Mossad, A. A., Gaber, A.-F., Matsuda, K., Ikeno, S., The Structure and Kinetics of the Nanoscale Precipitation Processes in Al-1.0wt.%Mg_2Si-0.4wt.%Mg-0.5wt.%Ag Alloy, in: Metallurgical and Materials Transactions A, 2012, 1-7

[MUK00] Mukhopadhyay, A. K., Ghosal, P., Prasad, K. S., Rama, R. V., Nature of precipitates and constituent particles present in ternary Al-Ge-Si alloy, in: Metallurgical and Materials Transactions A, Vol. 31A, 2000, 2093-2097

[MUN05] Munekata, T., Matsuda, K., Uetani, Y., Ikeno, S., TEM observation of rod-shaped precitates in Al-Mg-Ge Alloy, in: Microsc. Microanal 11 (Suppl2), 2005, 1860-1861

[MUR82] Murray, J. L., The Al-Mg (Aluminium-Magnesium) System, in: Bulletin of Alloy Phase Diagrams, Vol. 3, No. 1, 1982, 60-73

[MUR84] Murray, J. L., McAlister, A. J., The Al-Si (Aluminium-Silicon) System, in: Bulletin of Alloy Phase Diagrams, Vol. 5, No. 1, 1984, 74-84

[MUR03] Murken, J., Höhner, R., Skrotzki, B., Strain path dependence of the precipitate size evolution of an Al-Mg-Li alloy under combined thermal and mechanical loading, in: Materials Science and Engineering, A363, 2003, 159-170

[MUR12] Murakami, T., Matsuda, K., Nagai, T., Nakamura, J., Kawabata, T., Ikeno, S., Aging Behavior of Al-Mg-Ge Alloys with Different Mg_2Ge Contents, in: Advanced Materials Research, Vol. 409, 2012, 63-66

[MYK96] Mykhalenkov, K. V., Chernega, D. F., Mogilatenko, V. G., Molyar, A. G., On the adsorption of nitride particles by molten aluminium alloys, in: Casting processes, No. 1, 1996, 3-9

[MYK99] Mykhalenkov, K., Lysenko, S., Reif, W., Application of TiN particles for Grain Refinement of Aluminium. Zeitschrift für Metallkunde, Vol. 90, No. 9, 1999, 664-668

[MYK10] Mykhalenkov, K., Boyko, V., Link, T., Korzhova, N., Legkaya T., Nano-Size Precipitates in Al-Mg-Si Casting Alloys After Additional Alloying, in: World Journal of Engineering, Vol. 7, No. 2, 2010, 308-313

[NAY84] Nayeb-Hashemi, A. A., Clark, J. B., Olesinski, R. W., Abbaschian, G. J., The Ge-Mg (Germanium-Magnesium) System, in: Bulletin of Alloy Phase Diagrams, Vol. 5, No. 4, 1984, 359-365

[NEF04] Neff, D. V., Evaluating Molten Metal Cleanliness for Producing High Integrity Aluminium Die Castings, in: Die casting engineer, 2004, 2-6

[NES72] Nes, S., Precipitation of the metastable cubic Al3Zr-phase in subperitectic Al-Zr alloys, in: Acta Metallurgica, Vol. 20, 1972, 499-506

[NES74] Nes, E., The mechanism of repeated precipitation on dislocations, in: Acta Metallurgica, Vol. 22, 1974, 81-87

[NES77] Nes, E., Billdal, H., The mechanism of discontinuous precipitation of the metastable Al_3Zr phase from an Al-Zr solid solution, in: Acta Metallurgica, Vol. 25, 1977, 1039-1046

[NIE98] Nie, J. F., Muddle, B. C., Microstructural Design of High-Strength Aluminium Alloys, in: Journal Phase Equilibria, Vol. 19, No. 6, 1998, 543-551

[NOG01] Nogita, K., Dahle, A. K., Eutectic solidification in hypoeutectic Al–Si alloys: electron backscatter diffraction analysis, in: Materials Characterization, Vol. 46, 2001, 305-310

[NOR98] Norman, A. F., Prangnell, P. B., McEwen, R. S., The solidification behaviour of dilute Aluminium-Scandium alloys, in: Acta materialia, Vol. 46, No. 16, 1998, 5715-5732

[OGR02] Ogris, E., Wahlen, A., Lüchinger, H., Uggowitzer, P. J., On the silicon speroidization in Al-Si alloys, in: Journal of Light Metals, Vol. 2, 2002, 263-269

[OHM02] Ohmori, Y., Doan, L. C., Nakai, K., Ageing Processes in Al-Mg-Si Alloys during Continunous Heating, in: Materials Transactions, Vol. 43, No. 2, 2002, 246-255

[OTA09] Otarawanna, S., Gourlay, C. M., Lauki, H. I., Dahle, A. K., Microstructure Formation in AlSi4MgMn and AlMg5Si2Mn High-Pressure Die Castings, in: Metallurgical and Materials Transactions A, Vol. 40A, 2009, 1645-1659

[PAC21] Pacz, A., US Patent No. 1387900, Aluminium-Silicon Alloy, 1921

[PAC35] Pacz, A., US Patent No. 2013926, Modification of aluminium, aluminium alloys and alloys containing aluminium, 1935

[PAT08] Patel, J. B., Liu, Y. Q., Shao, G., Fan, Z., Rheo-processing of an alloy specifically designed for semi-solid metal processing based on the Al-Mg-Si system, in: Materials Science and Engineering A, Vol. 476, No. 1-2, 2008, 341-349

[PAT12] Patakham, U., Kajornchaiyakul, J., Limmaneevichitr, C., Grain refinement mechanism in an Al-Si-Mg alloy with scandium, in: Journal of Alloys and Compounds, Vol. 542, 2012, 177-186

[PER05] Perez, M., Gibbs–Thomson effects in phase transformations, in: Scripta Materialia, Vol. 52, 2005, 709-712

[PET94] Petzow, G., Metallographisches, keramographisches, plastographisches Ätzen, 6. vollständig überarbeitete Auflage, Gebrüder Borntraeger, Berlin, Stuttgart, 1994, 298

[PET12] Petkov, T., Künster, D., Pabel, T., Faerber, K., Kneiβl, C., Schumacher, P., Optimierung der Wärmebenhandlung einer AlMgSi-Gusslegierung, in Druckguss, Vol. 6, 2012, 268-274

[PIR90] Pirs, J., Zalar, A., Investigations of the distribution of elements in phases present in G-AlMg5Si cast alloy with EDX/WDX spectrometers and AES, in: Microchimica Acta, Vol. 101, No. 1-6, 1990, 295-304

[PIR91] Pirs, J., Zalar, A., Investigations of the distribution of elements in phases present in G-AlMg5Si cast alloy with EDX/WDX spectrometers and AES, in: Fresenius' Journal of Analytical Chemistry, Vol. 341, 1991, 145-149

[PIR93] Pirš, J., Distribution of elements in phases present in G-AlMg5Si cast alloy, in: Aluminium, Vol. 69, No. 5, 1993, 462-465

[POL95] Polmear, I. J., Light alloys: metallurgy of the light metals, John Wiley & Sons Australia, Limited, 1995, 362

[POL04] Polmear, I. J., Aluminium Alloys - A Century of Age Hardening, in: Materials Forum, Vol. 28, 2004, 1-14

[PRE38] Preston, G. D., The diffraction of X-rays by an age hardening alloy of aluminium and copper: The structure of intermediate phase, in: Philosophical Magazine, Vol. 26, 1938, 855-870

[QIU07] Qiu, D., Taylor, J. A., Zhang, M., Kelly, P. M., A mechanism for the poisoning effect of silicon on the grain refinement of Al–Si alloys, in: Acta Materialia, Vol. 55, 2007, 1863

[QUE04] Quested, T. E., Greer, A. L., The effect of the size distribution of inoculant particles on as-cast grain size in aluminium alloys, in: Acta Materialia, Vol. 52, 2004, 3859-3868

[RAD03] Radmilovich, V., Mittin, D., Tolley, A. J., Dahmen, U., Morris J., W., Resistance to Shape Refinement of Precipitates in Al-(Si, Ge) Alloys during Thermal Cycling, in: Metallurgical and Materials Transactions A, Vol. 34A , 2003, 543-551

[RHE07] Aluminium Rheinfelden GmbH brochure, DG-Hanbuch 07, Primary Alloys for Die Casting, 2007

[RHE08] Ductility in Aluminium Pressure Die Casting, Aluminium Rheinfelden GmbH brochure, 2008

[RIN00] Ringer, S. P., Hono, K., Microstructural Evolution and Age Hardening in Aluminium Alloys: Atom Probe Field-Ion Microscopy and Transmission Electron Microscopy Studies, in: Materials Characterization, Vol. 44, 2000, 101-131

[RYE06] Ryen, O., Nijs, O., Sjolander, E., Holmedal, B., Ekstrom, H.-E.,. Nes, E, Strengthening Mechanisms in Solid Solution Aluminium Alloys, in: Metallurgical and Materials Transactions A, Vol. 37A, 2006, 1999-2006

[SAG05] Progress in Aluminium, SAG Aluminium Lend GmbH & Co KG brochure, 2005

[SAT03] Sato, T., Hirosawa, S., Hirose, K., Maeguchi, T., Roles of Microalloying Elements on the Cluster Formation in the Initial Stage of Phase Decomposition of Al-Based Alloys, in: Metallurgical and Materials Transactions A., Vol. 34A, No. 12, 2003, 2745-2755

[SAU05] Sauermann, R., Arnold, A., Friedrich, B., Hallstedt, B., Schneider, J. M., Development of Al-Li-based Alloys for thixoformed Automotive Parts, in: Proceedings of European Metallurgical Conference "EMC 2005", Dresden Germany, 2005, 1471-1484

[SAU06] Sauermann, R., Friedrich, B., Grimmig, T., Buenk, M., Buhring-Polaczek, A., Development of Aluminium-Lithium alloys processed by Rheo Container Process, in: Solid State Phenomena, Vol. 116-117, 2006, 513-517

[SCH94] Schumacher, P., Greer, A. L., Heterogeneously nucleated α-Al in amorphous aluminium alloys, in: Materials Science and Engineering A, Vol. 178A, 1994, 309-313

[SEK68] Sekerka, R. F., Morphological Stability, in: Journal of Crystal Growth, Vol. 3-4, 1968, 71-81

[SHA04] Shabestari, S. G., Shahri, F., Influence of modification, solidification conditions and heat treatment on the microstructure and mechanical properties of A356 aluminum alloy, in: Journal of Materials Science, Vol. 39, 2004, 2023-2032

[SHI90] Shivkumar, S., Ricci, S., Keller, C., Apelian, D., Effect of Solution Treatment Parameters on Tensile Properties of Cast Aluminum Alloys, in: Heat Treating Journals, Vol. 8, No. 1, 1990, 63-70

[SHI11] Shimosaka, D., Kumai, S., Casarotto, F., Watanabe, S., Effect of cooling rates during solidification of Al-5.5%Mg-2.3Si-0.6Mn and Al-13%Mg_2Si pseudo-binary alloys on their secondary particle morphology and tear toughness, in: Materials Transactions, Vol. 52, No. 5, 2011, 920-927

[SIM11] Simcoe, C. R., The Discovery of Strong Aluminium, in: Advanced Materials & Processes, 2011, 35-36

[SJO10] Sjölander, E., Seifeddine, S., Optimisation of solution treatment of cast Al-Si-Cu alloys, in: Materials and Design, Vol. 31, 2010, 44-49

[STA92] Starke, E. A., Hornbogen, E., Blankenship, C. P., Theory and design of ideal microstructures in particle hardened aluminium alloys, in Aluminium Alloys, Their Physical and Mechanical Properties ICAA3, Vol. 1, Trondheim, Norway, 1992, 279

[STA04] Starink, M. J., Analysis of aluminium based alloys by calorimetry: quantitative analysis of reactions and reaction kinetics, in: International Materials Reviews, Vol. 49, No. 3-4, 2004, 191-226

[STE09] Stefanescu, D. M., Science and Engineering of Casting Solidification, Second Edition. Springer Science+Business Media, LLC, New York, 2009, 413

[STU88] Stüwe, H. P., Kolednik, O., Shape instability of thin cylinder, in: Acta Materialia, Vol. 36, No. 7, 1988, 1705-1708

[SUN61] Sundquist, B. E., Mondolfo, L. F., Heterogeneous Nucleation in the Liquid-to-Solid Transformation in Alloys, in: Trans. AIME, Vol. 221, 1961, 157-164

[SUN72] Sundquist, B. E., Cellular Precipitation, in: Metallurgical Transactions, Vol. 4, 1973, 1919-1934

[TAK98] Takeda, M., Ohkubo, F., Shirai, T., Stability of metastable phases and microstructures in the ageing process of Al-Mg-Si ternary alloys, in: Journal of Materials Science, Vol. 33, 1998, 2385-2390

[TAM25] Tamman, G., State of Aggregations, D. Van Nostrand Co., New York, 1925, 173

[TAN66] Tanner, L. E., Diffraction contrast from elastic shear strains due to coherent phases, in: Philosophical Magazine, 1966, 111-130

[TIL53] Tiller, W. A., Jackson, K. A. , Rutter, J. W., Chalmers, B., Redistribution of solute atoms during the solidification of metals, in: Acta Metallurgica, Vol. 1, 1953, 428-437

[TIL58] Tiller, W. A., Liquid Metals and Solidification, ASM, Cleveland, OH, 1958, 276-318

[TIM12a] Timpel, M., Wanderka, N., Schlesiger, R., Yamamoto, T., Isheim, D., Schmitz, G., Matsumura, S., Banhart, J., Sr-Al-Si co-segregated regions in eutectic Si phase of Sr-modified Al-10Si alloy, in: Ultramicroscopy, 2012, 1-12

[TIM12b] Timpel, M., Wanderka, N., Schlesiger, R., Yamamoto, T., Lazarev, N., Isheim, D., Schmitz, G., Matsumura, S., Banhart, J., The role of strontium in modifying aluminium–silicon alloys, in: Acta Materialia, Vol. 60, 2012, 3920-3928

[TOT03] Totten, G. E., Mackenzie, D. S., Handbook of Aluminium, Vol.1, Physical Metallurgy and Processes, Marcel Dekker, Inc., UK, 2003, 1296

[TUR61] Turnbull, D., The Liquid State and the Liquid-Solid Transition, Trans. AIME, Vol. 221, 1961, 422

[VAU67] Vaughan, D., Silcock, J. M., The Orientation and Shape of θ Precipitatates Formed in an Al-Cu Alloy, in: Physical Status Solid, Vol. 20, 1967, 725-736

[VIN03] Vinarcik, E. L., High integrity die casting processes, J.Wil. & Sons, Inc., New York, 2003, 232

[VED07] Vedani, M., Angella, G., Bassani, P., Ripamonti, D., Tussi, A., DSC analysis of strengthening precipitates in ultrafine Al-Mg-Si alloys, in: Journal of Thermal Analysis and Calorimetry, Vol. 87, 2007, 277-284

[WAN01] Wang, Q. G., Davidson, C. J., Solidification and precipitation behaviour of Al-Si-Mg casting alloys, in: Journal of Material Science, Vol. 36, 2001, 739-750

[WAN05] Wang, S. C., Starink, M. J., Precipitates and intermetallic phases in precipitation hardening Al-Cu-Mg-(Li) based alloys, in: International Materials Reviews, Vol. 50, 2005, 193-215

[WAN11] Wang, G., Yan, L., Ren, G., Zhao, Z., Analyzing As-Cast Age Hardening of 356 Cast Alloy, in: Journal of Materials Engineering and Performance, Vol. 20, No. 3, 2011, 399-404

[WEI00] Wei, B. C., Chen, C. Q., Huang, Z., Zhang, Y. G., Aging behavior of Li containing Al-Zn-Mg-Cu alloys, in: Materials Science and Engineering, Vol. 280A, 161-167

[WER89] Werner, E., The speroidization of thin plates, in: Acta Mat., Vol. 37, No. 7, 1989, 2047-2053

[WIL76] Williams, D. B., Edington, J. W., The discontinuous precipitation reaction in dilute Al-Li alloys, in: Acta Metallurgica, Vol. 24, 1976, 323-332

[WIL81] Williams, D. B., Butler, E. P., Grain boundary discontinuous precipitation reactions, in: International Metals Reviews, No. 3, 1981, 153-183

[WIL11] Wilm, A., Physical-Chemical study of Mg-containing Aluminium alloys (Physikalisch-metallurgische Untersuchungen über magnesiumhaltige Aluminiumlegierungen), in: Metallurgie, Vol. 8, No. 7, 1911, 225-227

[WOO99] Woo, K. D., Lee, J. S., Kim, S. W., Calorimetric Investigation of Precipitation Kinetics in Al-Mg-Si-X(Cr, Be) Alloys, in: Metals and Materials, Vol. 5, No. 4, 1999, 363-368

[WUT00] Wuth, M. C., Koch, H., Franke, A. J., Production of steering wheel frames with an AlMg5Si2Mn alloy, in: Casting Plant and Technology International, Vol. 16, No. 1, 2000, 12-24

[YAM08] Yamagata, H., Kasprzak, W., Aniolek, M., Kurita, H., Sokolowski, J., H., The effect of average cooling rates on the microstructure of the Al-20%Si high pressure die casting alloy used for monolithic cylinder blocks, in: Journal of materials processing technology, Vol. 203, 2008, 333-341

[ZHA01] Zhang, J., Fan, Z., Wang, Y. Q., Zhou, B. L., Equilibrium pseudobinary Al-Mg_2Si phase diagram, in: Materials Science and Technology, Vol. 17, 2001, 494-496

[ZHU12] Zhu, M., Jian, Z., Yang, G., Zhou, Y., Effects of T6 heat treatment on the microstructure, tensile properties, and fracture behavior of the modified A356 alloys, in: Materials and Design, Vol. 36, 2012, 243-249

[ZOL07] Zolotorevskiy, V., Belov, N. A., Glazoff, M. V., Casting aluminium alloys**,** Oxford, Elsevier Science, 2007, 478

Curriculum Vitae

Private address:
Oleny Teligy St. 13/14, apt. 11
Kiev, 04112, Ukraine
Phone: (+380 – 44) 458 – 30 – 54
E-mail: viktoriya.boyko@mailbox.tu-berlin.de
mobile (8 063) 388 50 50

Viktoriya Boyko

1 Personal Data	Date and place of birth	August 3, 1981, Kiev, Ukraine
	Present Citizenship	Ukrainian
	Marital Status	married, 2 children
2 Academic Degree	2005, July	National Technical University of Ukraine, Kiev
	Bachelor	
	Material Science and Engineering Number of semesters - 8, Date of attendance – July 15th, 2005	
	2007, June	National Technical University of Ukraine, Kiev
	Master	
	Physical Science of Materials Number of semesters – 4, Date of attendance – June 30th, 2007	
3 University education	September 2005 – June 2007	Master courses (National Technical university of Ukraine and Technical University Berlin)
	Major area of concentration – Characterization of structure and mechanical properties of Al-Zn-Mg foamed alloy Minor area of concentration: Determination of mechanical properties of intermetallic phases formed in foamed 7075 alloy under different foaming process Number of semesters – 4, planned date of attendance – June 2007	
	September 1999 – July 2005	Bachelor Course (National Technical University of Ukraine, Kiev, Ukraine)
	Adjunct area of concentration – Material science	
4 Practice	I (after 2nd year)	Duration: 4 weeks
	Topic: Determination of mechanical properties by using local loading method (LLM) Under supervision of Professor D. V. Lotsko, Institute for Problem of Material Science National Academy of Science of Ukraine	
	II (after 3rd year)	Duration: 4 weeks
	Topics: - Plasticity characteristics obtained in hardness measurements;	

		- Construction of stress - strain curves by indentation method. Under supervision of Corresponding member of National academy of science, Professor Y. V. Milman, Institute for Problem of Material Science National Academy of Science of Ukraine
5	Professional background	July 2005 – 2007 Engineer Institute for Problem of Material Science National Academy of Science of Ukraine September 1999 – May 2007 Student National Technical University of Ukraine, Kiev, Ukraine
6	Research publications, contributions to books	Application of solar energy for making Al foams Published in proceedings of the 4th International conference "Materials and Coatings for Extreme Performances: Investigations, Applications, Ecologically Safe Technologies for Their Production and Utilization" 18 - 22 September, 2006 Zhukovka, Crimea, Ukraine
7	Thesis's	Masters thesis's: Mechanical properties of intermetallic phases formed in foamed 7075 alloy under different foaming process
8	Postgraduate study	September 2009 – PhD student in Physical-and-Technological Institute of Metals and Alloys, Department of Casting and Structure Formation, Kiev, Ukraine October 2010 – granted a DAAD scholarship for PhD position in Technical University in Berlin, Institut für Werkstoffwissenschaften und Technologien, Berlin, Germany
9	Current research activities	➢ Development of the method of determination of the mechanical properties by local loading of materials, especially for brittle materials ➢ Al-Mg-Si(6XX.X) aluminium casting alloys after alloying ➢ Intermetallics: Mechanical properties of aluminides ➢ TEM investigation of aluminum alloys

21.01.2014

(signature)

Publications and contribution to the conferences

2008

Mykhalenkov, K. V., Ivanchenko, V. G., Reif, W., Boyko, V. V., On the grain refinement of hypoeutectic Al-Si alloys with B-containing additives, in: Metal Science & Treatment of Metals, Vol. 2, 2008, 18-15, UDC[1] – 669.715(031)

Mykhalenkov, K., Boyko, V., Link, T., Korzhova, N., Legkaya, T., Microstructure characterisation of new Al-Mg-Si casting alloy containing Sc+Zr, in: Proceedings of the 3rd Conference ″Special metallurgy: tomorrow, today and in future″, Edit. by K.Mykhalenkov, Polytechnica, Kiev, Ukraine, 2008, 166-173, UDC – 669.714

2009

Boyko, V., Korzhova, N., Mykhalenkov, K., Link, T., Micro- and macrostructure characterization of novel casting aluminium alloys based on the Al-Mg-Si system, International scientific and technical conference "Materials for extreme conditions -4", Engineering Physics Department "KPI", Ukraine, 2009, 144-147, UDC – 669.218:539.434.62

Kazarin, D., Boyko, V., Mykhalenkov, K., Effect after alloying by Ti+Sc and Zn+Cu on the microstructure in Al-Mg-Si-Mn aluminium alloys, Proceedings of the 4rd Conference ″Special metallurgy: tomorrow, today and in future″, Edit. by K.Mykhalenkov, Polytechnica, Kiev, Ukraine, 2009, 243-263, UDC – 669.715:621.74.043

2010

Boyko, V., Link, T., Korzhova, N., Legkaya, T., Mykhalenkov, K., Nano-Size Precipitates in AlMgSi Casting Alloys After Additional Alloying, in: World Journal of Engineering, Vol. 7, No. 2, 2010, 308-313

Mykhalenkov, K., Boyko, V., Link, T., Korzhova, N., Legkaya, T., Microstructure features of Al-Mg-Si casting alloys after additional alloying, XIII Konferencja naukowo-techniczna Odlewnictwa Metali niezelaznych "Naukai Technologia" Zwierrzhyniec, Poland, 2010, 77-82, ISBN 978-83-60958-58-2

2011

Boyko, V., Mykhalenkov, K., Link, T., Precipitates in Al-Mg-Si alloys, International scientific and technical conference "Materials for extreme conditions", Kiev, Ukraine, 2011, 165-171, UDC – 669.715:721.782.74

Mykhalenkov, K., Boyko, V., Link, T., Korzhova, N., Legkaya, T., Microstructiral studies of Al-Mg-Si-Mn and Al-Mg-Ge-Mn casting alloys, XIV Konferencja naukowo-techniczna Odlewnictwa Metali niezelaznych "Naukai Technologia", Zacopanie, Poland, 2011, 4-8, ISBN 978-83-60958-80-3

Boyko, V., Link, T., Mykhalenkov, K., Microstructiral studies of Al-Mg-Ge-Mn casting alloys, Proceedings of the 5rd Conference ″Special metallurgy: tomorrow, today and in future″, Edit. by K.Mykhalenkov, Polytechnica, Kiev, Ukraine, 2011, 243-263, UDC – 669.715:621.74.043

2012

Mykhalenkov, K., Boyko, V., Link, T., Strengthening particles in Aluminum casting alloys , in: Proceedings of International conference "Foundry production: Technology, Materials, Equipment and Ecology", Edit. V.Naidek, Kiev, Ukraine, 2012, 39-41

Boyko, V., Link, T., Mykhalenkov, K., Microstructural Studies Of AlMg5Si2Mn High Pressure Die Casting Alloy, Proceedings of X International Scientific Conference "Special Electric Metallurgy: Yesterday, Today and Tomorrow", Edit. by D. Chernega, Kiev, Ukraine, 2012, 101-109, UDC – 619-714

Boyko, V., Link, T., Mykhalenkov, K., Structural characterization of Al.-Mg-Ge alloys,

Proceedings of XIII Scientific Conference “Casting of Non-ferrous Metals and Alloys: Science and Technology”, Edit. by Z.Bonderek, Stary Wisnicz, Poland, 2012, 32-29, ISBN 978-60958-97-1
Boyko, V., Link, T., Mykhalenkov, K., Characterization of structure of AlMg5Si2Mn high pressure die casting Aluminum alloy, Proceedings of XIII Scientific Conference “Casting of Non-ferrous Metals and Alloys: Science and Technology”, Edit. by Z.Bonderek, Stary Wisnicz, Poland, 2012, 24-31, ISBN 978-60958-97-1
Boyko, V., Link, T., Mykhalenkov, K., Strengthening particles in Aluminum casting alloys, Proceedings of International conference “Foundry production: Technology, Materials, Equipment and Ecology”, Edit. V.Naidek, Kiev, Ukraine, 2012, 39-41, UDC –669.218:539.434
Boyko, V., Link, T., Mykhalenkov, K., Nano-particles in Aluminum Casting Alloys, Proceedings of International Scientific conference “Materials for extreme applications”, Edit. by P.Loboda, Kiev, Ukraine, 2012, 45-51, UDC –669.714
Boyko, V., Prach, O., Trudonoshin, O., Mykhalenkov, K., Novel Al-Mg-Si casting alloys. Overwiev, Proceedings of International Scientific conference “Materials for extreme applications”, Edit. by P.Loboda, Kiev, Ukraine, 2012, 40-44, UDC –669.725:721.782

2013

Boyko, V., Link, T., Mykhalenkov, K., Precipitation Hardening in Aluminum Casing Alloys, in: Equipment and Tools For Professionals of Technical Magazine, Metalworking, Vol. 1, Kharkov, Ukraine, 2013, 18-20, UDC– 669.714
Boyko, V., Link, T., Prach, O., Trudonoshyn, O., Mykhalenkov, K., Natural aging of aluminum casting alloys of 6XX.X series and precipitation hardening in as cast condition, in: IX International special exhibition “Foundry 2013”, Zaporizhia, Ukraine, 2013, UDC – 669.714
Boyko, V., Prach, O., Trudonoshyn, O., Mykhalenkov, K., Eutectic spheroidization in Al-7Mg-3Si casting alloys during solution treatment, in: Konferencja Naukowo-technicznaja Odlewnictwa Metali Niezelaznych „Naka i Technoogia”, 6 – 8 Czerwiec 2013 r, Muszyna – Złockie, Poland, 2013, 21-25, ISBN 978-83-63663-21-6
Boyko, V., Link, T., Korzhova, N., Mykhalenkov, K., Structure and „natural hardening” of commercial AlMg5Si2Mn casting Alloy, in: Konferencja Naukowo-technicznaja Odlewnictwa Metali Niezelaznych „Naka i Technoogia”, Muszyna – Złockie, Poland, 2013, 29-34,
ISBN 978-83-63663-21-6
Boyko, V., Prach, O., Trudonoshyn, O., Mykhalenkov, K., Natural hardening and precipitates in novel AlMg5Si2Mn casting alloy, in: The XXIII international scientific conference for young scientists, Karpenko Institute of Physics and Technology National Academy of Sciences in Ukraine, Lviv, October 23-25, 2013, 292-295, UDC – 669.714
Boyko, V., Link, T., Korzhova, N., Mykhalenkov, K., Microstructure characterization of AlMg5Si2Mn casting alloy, in: Materials Science and Technology (MS&T) 2013, October 27-31, Montreal, Quebec, Canada, 2013, 1331-1338, ISBN-13: 978-0-87339-762-9

[1]- (UDC - *Universal Decimal Classification*)